Free surface dynamics and non-contact radar sensing in a partially filled pipe

Jiayi Wu

Supervisor: Andy Nichols
Anton Krynkin

Department of Civil and Structral Engineering
University of Sheffield

This dissertation is submitted for the degree of
Doctor of Philosophy

June 2023

Acknowledgements

The author would like to express sincere gratitude to my supervisors, Dr Andy Nichols and Dr Anton Krynkin who guided me through this PhD project, for their invaluable advice, continuous support and patience.

Deep gratitude goes to Dr Giulio Dolcetti from University of Trento who helped me in free surface analysis. I would like to thank Dr Yan Liu from UCL for his valuable comments when discussing the hydrodynamics in partially filled pipes.

I would like to thank Dr Viktor Doychinov from University of Leeds, Dr Jonathan Davidson from University of Sheffield EEE department, Daniel Fernando from Texas Tech University who helped me a lot in radar signal processing. Also, the author is thankful to Dr Wei Liu and Mr Edward A Ball from University of Sheffield EEE department for advice on radar selection and purchase.

I wish to acknowledge the help provided by numerous technical staff of the University of Sheffield who provided essential assistance and advice regarding laboratory setup, most notably Mr Paul Osborne, Dr Paul Bentley, Mr Alex Cargill, Mr Mark Foster and Dr Robin Mills.

Also. the author would like to thank all members of the water group in University of Sheffield and in STREAM IDC which was a pleasure to work with during all these years. I am grateful to the UK's Engineering and Physical Sciences Research Council and Dynamic Flow Technologies for the financial support towards this work.

My person thanks and deep admiration are for my family and friends who showed love and support through these last years.

Abstract

Buried drainage systems are ageing and facing challenges due to climate change, population growth and urbanisation. Non-contact measurement techniques have the potential to determine the hydraulic properties remotely, requiring less maintenance compared to traditional intrusive techniques. A new class of sensor aims to measure the free surface dynamics remotely and infer flow properties from this the flow conditions. Unfortunately, research in partially filled pipes is very limited because of the limitation in measurement techniques. This study aimed to understand the free surface dynamics in partially filled turbulent pipe flows, and the signal response of a remotely radar sensor with the water surface fluctuations.

This study has set up several measurement equipment over a 290 diameter pipe, including both surface, sub-surface, intrusive and non-intrusive measurement equipment. A Digital Image Correlation system was novel applied for stereoscopic measurement of water surface and validated against the conventional intrusive conductance wave probes. Acoustic Doppler Velocimetry (ADV) was used to measure three dimensional velocity at individual spatial locations below the free surface. To objectively quantify the properties of coherent structures from ADV data, a modified phase-space detection method was proposed. The proposed method provides similar statistics with the traditional U-level method while better considering the physical reality of what constitutes a coherent structure.

Experimental data has shown that the velocity dip phenomenon occurs when the pipe is more than 35 % filled, which is caused by secondary currents. The free surface roughness and size of free surface features are also found to be influenced by the two main secondary currents. An oscillatory spatial correlation in the streamwise direction was observed in the free surface data for flows less than 43 % filled. This oscillation frequency at the free surface links to the bursting frequency beneath, which proves the linkage between the free surface pattern and the sub-surface turbulence. A lateral sloshing motion was found in this study, linked to the width of free surface, and caused by the meandering of secondary currents.

A novel application of a 24 GHz Doppler radar sensor (DRS) is proposed in this study to measure water surface fluctuations. It is shown that the sensor is capable of accurately recovering the instantaneous large gravity water waves using a non-linear demodulation technique. For small random water surface waves, the sensor response is linked with the

surface roughness by using the small angle approximation, but recovery of the precise free-surface shape was not achieved.

This study demonstrates that the free surface behaviour can be accurately measured by a radar sensor, and hence the underlying bulk flow conditions can be non-intrusively monitored. This research contributes to the wider knowledge in the field of buried drainage systems by addressing a significant knowledge gap in the understanding of free surface dynamics in partially filled turbulent pipe flows. Furthermore, the findings of this study have practical implications for the development of efficient and non-intrusive methods for monitoring flow conditions in such systems.

Keywords: ADV; coherent structures; DIC; Doppler radar sensor; free surface dynamics; non-contact sensing; turbulence; partially filled pipe; pipe flow

List of publications

Journal Publications

Nichols, A., Rubinato, M., Cho, Y. and Wu, J., 2020. Optimal Use of Titanium Dioxide Colourant to Enable Water Surfaces to Be Measured by Kinect Sensors. *Sensors*, 20(12), p.3507.

Wu, J., Nichols, A., Krynkin, A. and Croft, M., 2022. Digital Image Correlation for stereoscopic measurement of water surface dynamics in a partially filled pipe. *Acta Geophysica*.

Wu, J., Nichols, A., Krynkin, A. and Croft, M., 2022. Objective phase-space identification of coherent turbulent structures in 1D time series data. *Journal of Hydraulic Research*, in press.

Wu, J., Nichols, A., Krynkin, A. and Croft, M., 2022. Free surface dynamics in partially filled turbulent pipe flows. *Journal of Hydraulic Research,* in preparation.

Wu, J., Nichols, A., Krynkin, A. and Croft, M., 2022. Non-intrusive water surface dynamics measurement using a Doppler radar sensor. *Sensors*, in preparation.

Conference Publications

Wu, J., Nichols, A., Krynkin, A. and Croft, M., 2022. Non-contact measurement of gravity waves based on a 24GHz quadrature FMCW Doppler radar. *25th European Junior Scientists Workshop on Monitoring Urban Drainage systems and rivers*, Saint Maurice en Valgaudemar, France.

Wu, J., Nichols, A., Krynkin, A. and Croft, M., 2022. Experimental measurement of free surface and sub-surface properties in a partially filled pipe. *39th IAHR World Congress*, Granada, Spain.

Table of contents

List of figures

List of tables

Nomenclature

Roman Symbols

$\bar{u}$	Mean local streamwise velocity
$\bar{u}_B$	Mean local streamwise velocity measured by downward-looking ADV
$\bar{u}_S$	Mean local streamwise velocity measured by side-looking ADV
$\bar{v}$	Mean local lateral velocity
$\bar{w}$	Mean local vertical velocity
$\triangle T$	Individual event duration
σ_{uB}	Standard deviation of streamwise velocity measured by downward-looking ADV
σ_{uS}	Standard deviation of streamwise velocity measured by side-looking ADV
$\vec{V_{err}^k}$	Error vector representing the difference between $\vec{V_{means}^k}$ and $\vec{V_{ref}^k}$
$\vec{V_{means}^k}$	The vector from the circle center to the k$^{\text{th}}$ measured signal point
$\vec{V_{ref}^k}$	k$^{\text{th}}$ reference vector from the center to the ideal circle
A	Cross-sectional area of the occupied area
a_1	1$^{\text{th}}$ order coefficient in baseband transfer function denominator
A_e	Amplitude imbalance
A_I	Amplitude of I channel
a_k	k$^{\text{th}}$ order coefficient in baseband transfer function denominator
A_m	Amplitude of mechanical motion

A_Q Amplitude of Q channel

A_s Baseband gain factor

Ar integration constant

B Baseband signal

b_k k^{th} order coefficient in baseband transfer function numerator

c Speed of electromagnetic wave

$C1$ Capacitance of high pass filter capacitor

$C2$ Capacitance of low pass filter capacitor

C_{in} Input signal before the high pass filter

D Pipe diameter

d Water depth

d_0 Nominal distance between the transmitter and the target

DC_I DC offset of I channel

DC_Q DC offset of Q channel

e_a Median axis for ellipsoid

e_j Minor axis for ellipsoid

e_u Major axis for ellipsoid

f Darcy-Weisbach friction factor

f_0 Temporal frequency of oscillation of the free surface pattern

f_B Bursting frequency

f_c Cut-off frequency

f_{LO} Carrier frequency

f_m Frequency of mechanical motion

f_{shm} Frequency of simple harmonic motion

f_s	Sampling frequency
g	Acceleration due to gravity
H_{B1}	Baseband amplifier transfer function with 1st order
H_B	Baseband amplifier transfer function
H_{D1}	Compensation transfer function with 1st order
H_D	Compensation transfer function
H_{HP}	High pass filter transfer function
I'/Q'	Imbalances corrected I/Q signals
I/Q	Quadrature I/Q channels
I_1	First integral for velocity-dip position from bottom
I_2	Second integral for velocity-dip position from bottom
I_n	Modified Bessel function of order n
k	Phase-space scaling factor
k_0	Stationary wave wavenumber
k_s	Hydraulic roughness
k_U	U-level threshold value
k_x	Streamwise wavenumber
k_y	Lateral wavenumber
L	Turbulent length scale
l	Correlation function correlation radius
L_0	Characteristic spatial period
L_w	Free surface width, indicated in Fig. 2.1
m_t	Turbulence mask function
m_w	Wave mask function

N	Depth of influence factor
n	Index number
N_B	Normalised mean bursting period
p	Correlation function wavelength
P_w	Wetted perimeter
Q	Flow rate
q	Turbulent velocity
q_0	Spatial correlation function wavenumber
Q_f	Flow rate for the fully filled pipe flow
R	Pipe radius
$R1$	Resistance of high pass filter resistor
$R2$	Resistance of low pass filter resistor
R^2	Coefficient of determination
R_D	Hydraulic diameter
R_h	Hydraulic radius
R_{mw}	Received signal
S	Ratio of surface tension and fluid density
S_f	Slope of pipe
S_u	streamwise turbulence root-mean square velocities
S_v	Lateral turbulence root-mean square velocities
S_w	Vertical turbulence root-mean square velocities
T	Surface tension
t	Time domain
T_e	Individual event period

T_{mw}	Transmitted signal
u	Instantaneous streamwise velocity
$u^{'}$	Instantaneous streamwise velocity fluctuation
U^{+}	Normalised depth-local mean streamwise velocity
U_{*c}	Centreline shear velocity
U_{*}	Average shear velocity
U_{b}	Bulk flow velocity (mean velocity)
U_{max}	Maximum streamwise velocity
U_{s}	Surface velocity
v	Instantaneous lateral velocity
$v^{'}$	Instantaneous lateral velocity fluctuation
W	Correlation function
w	Instantaneous vertical velocity
$w^{'}$	Instantaneous vertical velocity fluctuation
X	Auxiliary variable in model of Guo et al. (2015)
x	Streamwise direction coordinate
x_{m}	Mechanical movement
Y	Auxiliary variable in model of Guo et al. (2015)
y	Lateral direction coordinate, indicated in Fig. 2.1
y^{+}	Normalised depth-wise location
y_{b}	Boundary coordinate indicated in Fig. 2.1
y_{e}	Probability density function of exponential fit
y_{g}	Probability density function of gamma fit
z	Vertical direction coordinate, indicated in Fig. 2.1

z_0 Zero-velocity position

A_{mDRS} Motion amplitude measured by DRS

A_{mLDS} Motion amplitude measured by LDS

Fr_{BP} Froude number defined by Brocchini and Peregrine (2001)

f_{cH} Cutoff frequency of high pass filter

f_{cL} Cutoff frequency of low pass filter

U_{bf} Bulk flow velocity for the fully filled pipe flow

We_{BP} Weber number defined by Brocchini and Peregrine (2001)

Fr Froude number

Re Reynolds number

We Weber number

Greek Symbols

α U-level sign to distinguish between ejections and sweeps

β The angle of the vector $\boldsymbol{\rho}$-$\boldsymbol{U_s}\tau$ measured from the direction of U_s

δ Velocity dip position from bottom

$\Delta\phi(t)$ Residual oscillator phase noise

η Time-dependent water surface fluctuation

κ Von Kármán constant

λ Wavelength of the wireless signal

λ_0 Stationary wave wavelength

λ_s Ratio of centreline to average shear velocity

λ_{UN} Universal threshold

μ fitting parameter for exponential distribution

μ_f Dynamic viscosity of the fluid

ω	Angular frequency
ω_0	Intrinsic frequency of gravity-capillary waves in still water
Φ	Demodulated phase of the motion
ϕ	Phase noise of the transmitter
ϕ_e	Phase imbalance
ϕ_I	Residual phase in I channel
ϕ_Q	Residual phase in Q channel
ϕ_v	Velocity-defect function
$\boldsymbol{\rho}$	Spatial lag in 2D space
ρ	Spatial separation
ρ_f	Density of the fluid
ρ_{mn}	Spatial seperation between wave probe m and wave probe n
σ_a	Standard deviation of acceleration fluctuation
σ_{DIC}	Mean surface roughness height from DIC
σ_{mDIC}	Mean surface roughness height from DIC at single point
σ_j	Standard deviation of jerk fluctuation
σ_u	Standard deviation of velocity fluctuation
σ_w	Correlation radius
σ_{wp}	Mean surface roughness height from wave probe
σ_{mwp}	Mean surface roughness height from wave probe at single point
τ	Time lag
Θ	Water surface angle, indicated in Fig. 2.1
θ	Phase term in baseband signal
υ_f	Kinematic viscosity of the fluid

Acronyms / Abbreviations

ADV Acoustic Doppler Velocimetry

CNC Compter numerical control

DFT Discrete Fourier transform

DIC Digital Image Correlation

DRS Doppler radar sensor

EA Environment Agency

ECM Electromagnetic current meters

EVM Error Vector Magnitude

FIR Finite Impulse Response

FMCW Frequency-Modulated Continuous-Wave

GS Gramm-Schmidt

HDD hard disk drivers

HWA Hot wire anemometry

LDA Laser Doppler anemometry

LDS Laser displacement sensor

LM Levenberg-Marquardt

LSPIV large-scale Particle Image Velocimetry

NI National Instruments

Ofwat Water Services Regulation Authority

PDF Probability density function

PID Proportional-integral-derivative

PIV Particle Image Velocimetry

PTV Particle Tracking Vlocimetry

S-PIV Stereoscopic Particle Image Velocimetry

SNR Signal to noise ratio

SSD solid-state drive

std Standard deviation

TiO_2 Titanium dioxide

TKE Turbulent Kinetic Energy

TPAV Short-time temporary average

UGS Universal Gcode Sender

UFH ultra high frequency

VITA Variable interval time averaging

WAG Window average gradient

WP Wave probe

Chapter 1

Introduction

1.1 Background and motivation

The UK has the most complex and oldest sewerage system in the world (Clegg et al., 1989). Water sectors are facing severe challenges, such as increased extreme weather events, change of rainfall patterns and increased concentration of assets in urbanised areas. Water is a finite resource and its transportation and treatment is costly. It is of increasing significance for companies to use a range of data to help understand their asset health in order to optimise treatment procedures, and to minimise the instances of sewer flooding, sewer blockages and pollution events. Sewer flooding is one of the most distressing service failures for customers. It is important for companies to mitigate the risk of service failure to benefit the environment and deliver resilient services. In the latest service delivery report by Water Services Regulation Authority (Ofwat), only three out of eleven water companies achieved their internal sewer flooding targets in 2020 - 2021 (Ofwat, 2021). Ofwat suggested that companies can improve response times to incidents as well as improve understanding and monitoring the sewer network to ensure they meet their committed performance levels.

The need to accurately monitor flows within drainage systems is an emerging challenge, driven by the effects of urbanisation, climate change, and population change that alter the hydraulic load on drainage assets. As Bevan (2018) mentioned in a speech in RSA (Royal Society for the encouragement of Arts, Manufactures and Commerce), climate change means more floods, bigger floods at larger scale and more extreme rainfall. Environment Agency (EA) has recently launched a roadmap over the next four years to tackle the growing flooding threat and become more resilient to challenges. One of the key actions is to develop a new national assessment of flood and provide better data, which will benefit informing future risk and investment decisions (EA, 2022). Accurate and widespread monitoring of flow, turbulence, and sedimentation is critical for the timely prediction and mitigation of flood

events. Most existing methods are intrusive and therefore suffer from high maintenance requirements. Existing non-intrusive methods only estimate surface velocity and / or flow depth, while measurements of turbulence, which governs mixing and transport of sediments and pollutants, are too expensive, energy-intensive, or invasive for widespread deployment.

There is hence a demand from the water industry and environmental managers for accurate robust and non-intrusive characterisation of turbulent flow processes. Research studies from Fujita et al. (2007), Savelsberg and Van De Water (2008) have linked these processes to the dynamic free-surface pattern of shallow flows, but so far our ability to measure this pattern is limited, and it has only been examined in detail for flows in rectangular channels. Nichols (2014), Romanova (2013) have implemented non-contact acoustic methods to measure the water surface pattern in open channel flows. Romanova (2013) suggested to develop a more compact field prototype instrument for analysis of live pipes' hydraulic characteristics.

Radar was first developed in the 1930s (Watson-Watt, 1945) and has been widely used in military applications. It is a measurement of distance, inferred from a relative time-delay and a known speed of travel of radio waves. Over recent decades, radar systems have become increasingly compact and have extended application from military to commercial areas (Peng and Li, 2019). For example, radar systems are able to remotely detect and monitor health vital signs (Huang et al., 2016, Lv et al., 2018, Peng and Li, 2019), hand gestures (Fan et al., 2016, Skaria et al., 2019) and air bubbles (Rodrigues et al., 2021). Recently, Alimenti et al. (2020) have implemented a low cost Doppler radar sensor in river surface velocity measurements. It can propagate much better than laser light through foggy or dusty air (Linz et al., 2014) and could make autonomous driving technology possible in a broader range of weather conditions (Peng and Li, 2019). The radar sensing technology has the potential to provide detailed free-surface data that can enable the robust flow characterisation required by the water sector.

1.2 Aims and objectives

The primary aim of this study is to collect a representative set of hydraulic and radar data which show that the microwave signal response above a turbulent flow is related to the flow conditions and that it contains unambiguous information about the flow conditions.

With these aims in mind, the objectives of this study are formulated as follows:

- Establish an experiment setup that is able to measure the instantaneous surface fluctuations and sub-surface velocity field in a partially filled pipe flow.

- Apply the non-contact Digital Image Correlation (DIC) technique to measure the water surface fluctuations in a 2D area and validate its accuracy against intrusive wave probes.
- Propose a quantitative analysis method that is able to objectively detect turbulent events from velocity data.
- Explore the sub-surface hydrodynamics in a partially filled pipe flow.
- Investigate the free surface behaviour of partially filled pipe turbulent flows and identify linkages between free surface and sub-surface.
- Calibrate and characterise a Doppler radar sensor (DRS) that is able to measure motion of the free surface.
- Find linkages between the Doppler radar sensor signals and the flow properties.

1.3 Thesis structure

This thesis is organised as follows: Chapter 2 provides the literature review of previous research on open channel flows and pipe flows. Also, the theory and application of the Doppler radar sensor (DRS) is addressed. In chapter 3, the development of the new experimental facilities and flow conditions are presented. A report of data pre-processing and validation is given in chapter 4 to show that the measurement techniques provide sensible, repeatable and reliable information. The information will then be used in chapter 5 to investigate dependence of free surface dynamics and radar response on the sub-surface flow field. Finally, the conclusions are drawn in chapter 6, and recommendations are made for further studies.

Chapter 2

Literature review

2.1 Hydraulics in pipe

Fluid flow in circular pipes is commonly encountered in practice. Blood is carried away from and toward the heart through arteries and veins. PVC, cast iron and copper plumbing pipes are mainly used at our homes to carry hot and cold water. In industries, large pipelines are used to transport oil and natural gas. This chapter starts with a review on hydraulics in pipes. The pipe geometric parameters are first defined and the key hydraulic parameters are introduced in subsection 2.1.1. Experimental studies in partially filled pipes are then summarised in subsection 2.1.2. Finally, in subsection 2.1.3, the current understanding on hydrodynamics in partially filled pipes are discussed.

2.1.1 Geometric considerations and key parameters for partially filled pipes

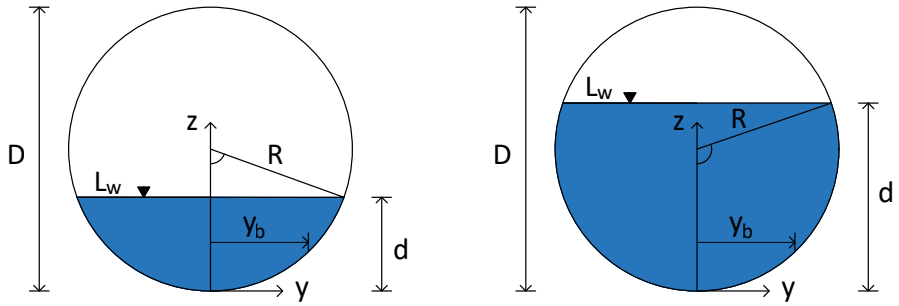

Figure 2.1 Cross-section of pipe showing definitions of depth and free surface width (a) less than half filled (b) more than half filled.

Figure 2.1 shows the cross-section of the pipe with radius R and flow depth d. As illustrated in Fig. 2.1, the lateral and vertical direction are represented by y and z, respectively. The streamwise direction is represented by x. The water surface angle Θ is

$$\cos\Theta = \frac{R-d}{R} \tag{2.1}$$

where Θ is in the range of 0 - 180 °. The occupied flow cross-sectional area A and wetted perimeter P_w are

$$A = R^2\left(\Theta - \sin\Theta\cos\Theta\right), \tag{2.2}$$

$$P_w = 2R\Theta, \tag{2.3}$$

respectively. Therefore the hydraulic radius, the ratio of flow area to wetted perimeter, is

$$R_h = \frac{A}{P_w} = \frac{R\left(\Theta - \sin\Theta\cos\Theta\right)}{2\Theta}. \tag{2.4}$$

The hydraulic diameter is defined as four times the hydraulic radius:

$$D_h = 4R_h. \tag{2.5}$$

The free surface width L_w for partially filled pipe is given by

$$L_w = 2\sqrt{2Rd - d^2}. \tag{2.6}$$

The depth of water increases with the increase of flow rate in the pipe. The flow rate and velocity in the pipe are usually expressed in dimensionless form as (S. K Som and Biswas, 2010)

$$\frac{Q}{Q_f} = \frac{1}{\pi}(\Theta - \frac{\sin 2\Theta}{2})(1 - \frac{\sin 2\Theta}{2\Theta})^{2/3}, \tag{2.7a}$$

$$\frac{U_b}{U_{bf}} = (1 - \frac{\sin 2\Theta}{2\Theta})^{2/3}, \tag{2.7b}$$

$$\frac{d}{D} = \frac{1}{2} - \frac{1}{2}\cos\Theta, \tag{2.7c}$$

where U_{bf} and Q_f are the bulk flow velocity and flow rate for fully filled pipe flow, respectively. Figure 2.2 is a hydraulic-elements graph for sewers of circular cross-section and Manning roughness coefficient throughout the surface area developed by Camp (1946). It shows the change of dimensionless velocity U_b/U_{bf} and flow rate Q/Q_f as functions of

the ratio of depth of flow to pipe diameter d/D. These two properties show different curve geometry. This happens as the wetted perimeter changes more rapidly compared to the area of flow. This graph has been widely used in the calculations of flow velocity and flow rate in partially filled pipes with a known depth and pipe diameter by reading values off the graph.

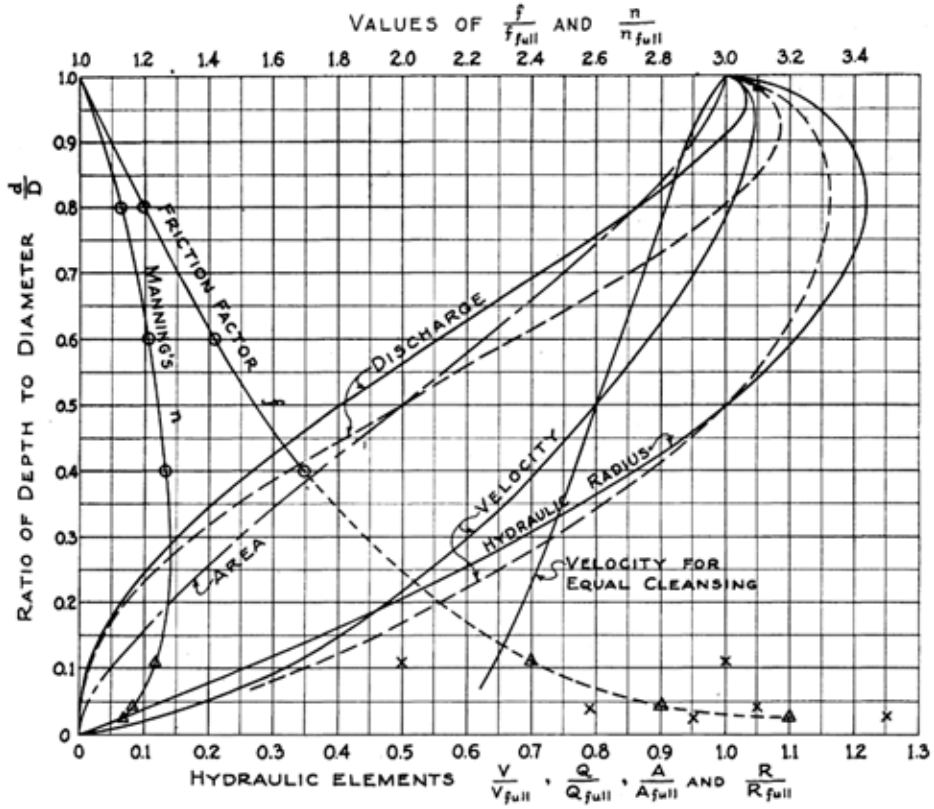

Figure 2.2 Hydraulic-elements graph for circular sewers (Tchobanoglous, 1981).

To characterize the flow type, a Reynolds number Re is used:

$$\mathsf{Re} = \frac{\rho_f U_b R_h}{\mu_f}, \tag{2.8}$$

where ρ_f is the density of the fluid and μ_f is the dynamic viscosity of the fluid. The Froude number Fr is used to define the type of experimental flow:

$$\mathsf{Fr} = \frac{U_b}{\sqrt{\frac{gA}{L_w}}} \tag{2.9}$$

where U_b is the bulk flow velocity, which is calculated by

$$U_b = \frac{Q}{A}. \tag{2.10}$$

Froude number is a dimensionless quantity used to indicate the influence of gravity on fluid motions. The denominator in Eq. 2.11 represents the speed with which gravity waves propagate. For critical flow $\mathsf{Fr} = 1$, the mean bulk velocity of the flow is equal to the mean velocity of surface waves. Supercritical flow is achieved at $\mathsf{Fr} > 1$, at which small surface waves will only be carried downstream. For subcritical flow $\mathsf{Fr} < 1$, small surface waves can move upstream. Weber number Re is a dimensionless quantity used to indicate whether the kinetic energy or surface tension energy dominate:

$$\mathsf{We} = \frac{\rho_f U_b l}{T}, \tag{2.11}$$

where l is the characteristic length. The Darcy-Weisbach friction factor f in partially filled pipes is calculated by

$$f = \frac{8gR_hS_f}{{U_b}^2}, \tag{2.12}$$

where S_f is the slope of the pipe. The hydraulic roughness k_s, also known as equivalent sand-grain roughness, is derived from Colebrook's friction equation

$$\frac{k_s}{D_h} = 3.7e^{-\frac{U_b \ln 10}{\sqrt{8gD_hS_f}}}. \tag{2.13}$$

The shear velocity is determined by

$$U_* = \sqrt{gR_hS_f}. \tag{2.14}$$

2.1.2 Experiments in partially filled pipes

Though the theory of laminar fully filled pipe flow is reasonably well understood, the analytical solutions are still limited. Transition to turbulence in pipe flow, observed by Osborne Reynolds in the late 19th century, is still not completely understood to this day (Osb, 1895). Most fluid flow problems rely on experimental results and empirical relations. The hydrodynamics of pipes running partially full has received far less attention compared to fully filled pipe flow. Fundamentally, the flow in a partially filled pipe is different from the pressure-driven full filled pipe flows due to the presence of a free surface(Ng et al., 2018). In recent decades, several studies have conducted experiments in partially filled pipes. Table

2.1 summarises the studies in partially filled pipes, with pipe size, pipe material, pipe slope, filling ratio, flow rate range, bulk flow velocity range, and the Reynolds number range. The surface and sub-surface measurement techniques are also summarised. It can be seen from Table 2.1 that experiments measuring free surfaces in partially filled pipes are very limited. Turbulent properties at or very close to the free surface are usually estimated from values below the surface as the measurement of surface dynamics is very challenging (Flores et al., 2017).

Table 2.1 Summary of experimental study in partially filled pipe.

Study	Diam -eter	Type	Slope	Filling ratio	Flow rate	Mean veloc- ity	Reynolds number	Surface measurement	Under surface measurement
	D		S_f	d/D	Q	U_b	Re		
(-)	(mm)	(-)	(%)	(%)	(Ls^{-1})	(ms^{-1})	$\times 10^4$ (-)	(-)	(-)
Ead et al. (2000)	622	Corrug -ated steel	0.55-2.55	34-61	30-200	0.67-1.71	19.1-85.9	Water surface profiles measured by a manometer at 14 streamwise positions	Velocity profiles measured by a Prandtl tube
Knight and Sterling (2000)	244	PVC & acry -lic	1	33-83	5.4-22.9	0.39-0.55	6.5-15.0	Normal depth obtained from M1 and M2 water surface profiles	Local streamwise velocities measured by a pitot-static tube and local boundary shear stresses measured by a Preston tube
Clark and Kehler (2011)	800	Corrug -ated metal	0.028-0.27	34-61	86-176	0.26-0.69	N/A	N/A	Velocity profiles measured by an ADV

Table 2.1 Summary of experimental study in partially filled pipe. (continued)

Romanova (2013)	290	Perspex	0.05		18 - 37	0.16-0.26	1.29-5.62	Surface fluctuations at multiple single positions by wave probes and a novel acoustic instrumentation	NA
Jiang et al. (2020)	40	Transp-rant acrylic	0.33	42-79	N/A	N/A	N/A	N/A	Fluid velocity of a single point measured by Particle Image Velocimetry (PIV)
Guala et al. (2021)	127	Plexi-glas	N/A	N/A	N/A	22.8-49.9	19.3-42.3	N/A	Streamwise and wall normal velocity by a dual-sensor hot-film anemometer system
Ng et al. (2021)	100	glass	N/A	44-100	N/A	0.23-0.35	2.9-3.5	N/A	2D velocity field measured by PIV
This study	290	Perspex	0.1	16-66	2-28	0.30-0.60	0.84-5.05	Surface fluctuations over a 2D area by DIC and multiple single positions by wave probe	1D 3C velocity profiles by ADV

2.1.3 Hydrodynamics in partially filled pipe

Velocity distribution in partially filled pipe is of great importance for industries, such as fish passage design, transportation of slurries and prediction of sewer blockage (Cun, 2021, Guo et al., 2015, Ng et al., 2021). There is a relatively complete theory on the velocity distribution in fully filled pipe flows. However, much uncertainty still exists about the velocity distribution in partially filled pipe turbulent flows. The influence of free surface and secondary flow in partially filled pipe make the velocity distribution much more complex (Ng et al., 2018).

Both laminar and turbulent fully filled pipe flow produce velocity profiles that are symmetric about axis of the pipe with a maximum velocity at the centre of the pipe. The empirically based power law functions have been successfully used to describe and model mean turbulent flows for many years (Salama, 2021, Schlichting, 1979, White, 1991). The power law model takes the form:

$$\frac{\bar{u}}{U_{max}} = (1 - \frac{|y-R|}{R})^{1/n} \tag{2.15}$$

where $\bar{u}$ is the local mean streamwise velocity and U_{max} is the maximum streamwise velocity. The exponent n is a constant value that depends on the Reynolds number. The dependency is empirical and the value of n increases with increasing Reynolds number. $n = 7$ is applicable to a wide range of pipe flows and is the one most commonly used (De Chant, 2005, Salama, 2021). The power law with the exponent equal to seven is referred to as the 'one seventh power law'.

Power law solutions are dependent on Reynolds number. The log law (law of the wall) is usually used to approximate the velocity profile as a logarithmic shape, where the velocity increases from the wall towards the free surface (Nezu and Nakagawa, 1993). The constant in this solution does not depend on Reynolds number. The log law is represented by Eq. 2.16:

$$U^+ = \frac{1}{\kappa}\ln(\frac{y}{k_s}) + Ar, \tag{2.16}$$

where U^+ is the normalised depth-local mean streamwise velocity, calculated by the ratio of the depth-local mean streamwise velocity $\bar{u}$ and the shear velocity U_* as

$$U^+ = \bar{u}/U_*, \tag{2.17}$$

$\kappa = 0.41$ is the Von Kármán constant, k_s is the hydraulic roughness coefficient as defined in Eq. 2.13 and Ar is the integration constant. A linear relationship can be found between normalised depth-local mean streamwise velocity, U^+ and normalised depthwise location, y^+, where y^+ is represented by

$$y^+ = zU_*/\upsilon_f. \tag{2.18}$$

υ_f corresponds to the kinematic viscosity of the fluid.

Ead et al. (2000) measured the velocity profile in a 622 mm diameter corrugated pipe by a Prandtl tube and found that the velocity profiles follow the log-law up to a certain height, beyond which the velocity is less than the log-law. He has observed that the deviations occurred closer to the bed and a larger deviation with increase in depth. Clark and Kehler (2011) found that the normalised velocity profile agrees well with the log law in the depthwise position $y/d < 0.36$. A modification factor that varies with perimetric distance and distance from the wall was added to the log law to represent the deviation for depthwise position $y/d \geq 0.36$. A manual calibration is required to obtain the coefficients of the proposed empirical velocity profile model. In 2015, Guo et al. (2015) modified the conventional log-law by introducing a cubic deduction near the water surface to represent the downward deviation. The proposed velocity distribution model is

$$\frac{u(0,z)}{U_{*c}} = \frac{1}{\kappa}\ln\frac{z}{z_0} - (I_1 - \frac{A\ln z_0}{2} - \frac{3A}{8\lambda_s} - \frac{\kappa Q}{2U_{*c}})\frac{z^3}{\kappa I_2} \tag{2.19}$$

where $u(0,z)$ is the centreline velocity at depth z, U_{*c} is the centerline velocity. I_1 and I_2 are integrals for velocity-dip position from bottom:

$$I_1 = \int_0^d y_b \ln z\, dz, \tag{2.20a}$$

$$I_2 = \int_0^d y_b z^3\, dz, \tag{2.20b}$$

which can be easily calculated using Matlab 'integral' function. y_b is boundary coordinate (the half width of the flow at a certain depth-wise position) indicated in Fig. 2.1. It is calculated by

$$y_b = R\sqrt{(2-\frac{z}{R})\frac{z}{R}}. \tag{2.21}$$

The zero-velocity position z_0, the position at which the fluid velocity is zero,is determined by

$$z_0 = \frac{\upsilon_f}{9U_{*c}} + \frac{k_s}{30[1-\exp(-\frac{k_s U_{*c}}{26\upsilon_f})]}. \tag{2.22}$$

It is related with bed roughness. The modified log law velocity distribution equation proposed by Guo et al. (2015) can be applied to all depthwise positions and no fitting

parameter is required. Furthermore, cross-sectional 2D velocity distribution can be derived by

$$u(y,z) = \frac{\lambda_s U_*}{\kappa}[\ln\frac{z}{z_0} - \frac{1}{3}(\frac{z}{\delta})^3] - U_*\phi_v(y,y_b), \tag{2.23a}$$

$$\phi_v(y,y_b) = -\frac{1}{\kappa}\ln(1-|\frac{y}{y_b}|) + \frac{1}{3}[1-1-|\frac{y}{y_b}|^3], \tag{2.23b}$$

$$\frac{1}{\delta^3} = \frac{3}{I_2}(I_1 - \frac{A\ln z_0}{2} - \frac{3A}{8\lambda_s} - \frac{\kappa Q}{2U_{*c}}), \tag{2.23c}$$

where λ_s is the ratio of centreline to average shear velocity, ϕ_v is the velocity-defect function and δ is the velocity dip position from bottom.

Following a series of open channel flow experiments, Nezu and Nakagawa (1993) established a set of universal exponential expressions to describe the variation of turbulence intensities in the streamwise, lateral and vertical directions along the vertical water depth:

$$S_u/U_* = 2.30e^{-z/d}, \tag{2.24a}$$

$$S_v/U_* = 1.27e^{-z/d}, \tag{2.24b}$$

$$S_w/U_* = 1.63e^{-z/d}. \tag{2.24c}$$

S_u, S_v and S_w represent streamwise, lateral and vertical turbulence root-mean square velocities, respectively. Some researchers have reported different coefficients in Eq. 2.24 for their experimental data, such as Carling et al. (2002), Johnson and Cowen (2017), Sukhodolov et al. (2006). The general range for streamwise, lateral and vertical turbulence intensity coefficients are 0.97 - 3.02, 1.39 - 1.89 and 1.04 - 1.67, respectively(Johnson and Cowen, 2020).

Knight and Shiono (1990) explained the discrepancy between their measured turbulent intensity data and Nezu and Nakagawa (1993) turbulent intensity theory by the influence of strong lateral shear and secondary flows in the compound channel. Clark and Kehler (2011) have investigated the turbulence intensities in circular corrugated culverts and found that their experimental data does not fit Nezu and Nakagawa (1993) turbulent intensity theory. The circular geometry has a significant effect on the turbulence intensity distribution. To describe the observation in circular channels, Clark and Kehler (2011) proposed the following expressions:

$$S_u/U_* = 2.93z/d^2 - 3.96z/d + 2.16, \tag{2.25a}$$

$$S_v/U_* = 2.24z/d^2 - 2.87z/d + 1.54, \tag{2.25b}$$

$$S_w/U_* = 0.53z/d^2 - 0.99z/d + 0.97. \tag{2.25c}$$

Previous studies focused on the turbulence intensities on the centerline, so that is where this study focused to, in order to be comparable.

Ng et al. (2021) investigated turbulence in a partially filled 100 mm diameter glass pipe at a nominally constant Reynolds number of 30,000 by using stereoscopic particle image velocimetry (S-PIV). They have summarized the large-scale features in partially filled pipes as shown in Fig. 2.3a. The mean secondary flow (A) occupied the half width of the cross-section area and was mirrored about the pipe bisector, which is also observed by Sterling and Knight (2000). Large-scale motions that are attached to wall (B) are not largely affected by the mean secondary flow. Large-scale motions (C) near the surface are influenced by the mean secondary flow. Bursting motions (D) or second quadrant events close to the free surface are associated with 'upwellings' and 'downdrafts'. Instantaneous roll cells (E) are linked to large scale motions (B) and bursts (D). 'Whirlpools' (F) also appear on the surface and are associated with vortices. Instantaneous roll cells (G) are swept toward the vertical bisector by the mean secondary flow. Liu et al. (2022) have modelled not only the turbulent flow underneath but also the free surface using large eddy simulations (LES). They have proposed another conceptual model as shown in Fig. 2.3b. Comparing Fig. 2.3a and b, both studies found a pair of secondary currents beneath the surface and bust motions. The most evident difference is that Liu et al. (2022) have found the main secondary flows are not equally distributed in one half of the geometry. One instantaneous main secondary flow vortex is stronger and one is weaker. The high speed streaks at the water surface meander due to the meandering of the main secondary currents. Besides, there are surface boils generated due to the bursting motion between the corner vortex and the main secondary flow (Liu et al., 2022).

2.2 Free surface dynamics

As mentioned in subsection 2.1.2, free surface measurements in partially filled pipes are limited. Therefore, the free surface dynamics in rectangular open channels are reviewed in this section. Firstly, the dynamics of turbulence at the free surface is presented in subsection 2.2.1. Subsection 2.2.2 describes the three main mechanisms driving the deformation of the free surface. Finally, the free surface dynamics in rectangular open channels are reviewed in subsection 2.2.3.

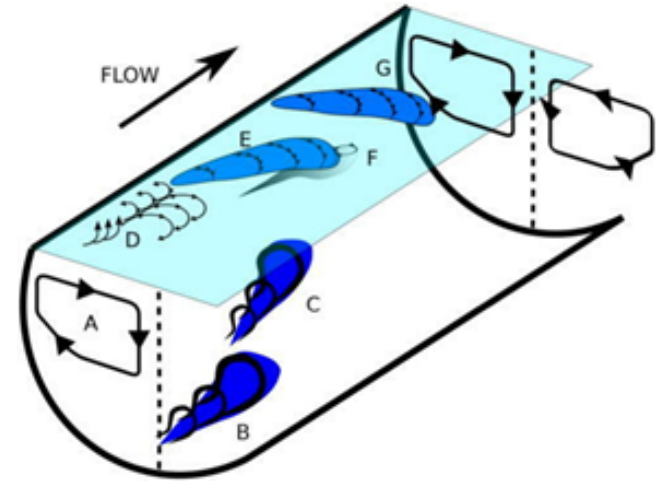

(a)

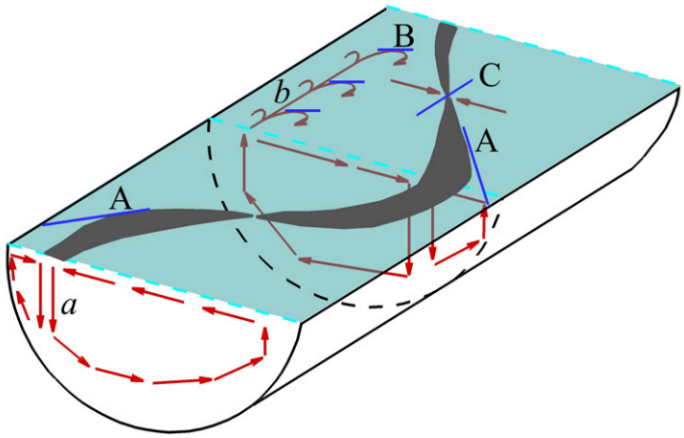

(b)

Figure 2.3 Conceptual sketch showing the large-scale motion in turbulent partially filled pipe flow proposed by (a) Ng et al. (2021) and (b) Liu et al. (2022).

2.2.1 Thy dynamics of turbulence at free surfaces

The dynamics of turbulence at the free surface play a significant role in air-water gas fluxes, with implications for various environmental and geophysical phenomena, such as CO_2 uptake in the oceans (Flores et al., 2017). However, experimental measurements of free surface dynamics have been challenging, leading to limited studies in this area until the influential work by Brocchini and Peregrine (2001). They investigated the behavior of the free surface under the influence of turbulence in different flow scenarios. The authors identified the key physical mechanisms governing free surface deformations, which involve the stabilizing effects of capillary forces and gravity counteracting the disruptive effects caused by turbulence kinetic energy. To analyze and categorize the diverse surface deformations, they introduced a two-dimensional parameter framework known as the "q-L diagram" (Figure 2.4), where "q" represents the turbulent velocity and "L" represents the turbulent length scale. In this framework, the authors introduced the concept of "blobs," moderately coherent and discrete volumes of fluid that interact with the surface, leading to disturbances. The turbulent length scale (L) is approximated as the length of the most energetic turbulent scale or the dominant surface length scale, while the turbulent velocity (q) is defined as the norm of the velocity vector. According to the authors, different combinations of turbulent velocity and turbulent length scale account for different surface deformation patterns. Hence, they propose using these two parameters as a framework to describe and investigate various surface behaviors in future studies.

As the surface behaviour depends on both Froude number Fr and Weber number We, the L-q plan is divided into four regions by specific critical Froude number and Weber numbers obtained from the energy balance for a typical turbulence structure at the free surface

$$q = \sqrt{2{Fr_{BP}}^2 gL} \tag{2.26a}$$

$$q = \sqrt{\frac{2We_{BP}T}{\rho_f L}} \tag{2.26b}$$

where Fr_{BP} is the Froude number defined by Brocchini and Peregrine (2001), We_{BP} is the Weber number defined by Brocchini and Peregrine (2001), g is the gravitational acceleration and T is the surface tension. As is shown in Figure 2.4, two dotted lines (Equation 2.26a and Equation 2.26b) divide the space into four regions labelled 0 to 3. They are region 0: weak turbulence, region 1: turbulence with surface tension dominant and gravity unimportant, region 2: very strong turbulence and region 3: gravity-dominated turbulence.

In region 0, both the Froude number and the Weber number of the turbulence are small (typically $Fr_{BP} \ll 1$, $We_{BP} \ll 1$) and there is little or no surface disturbance due to the

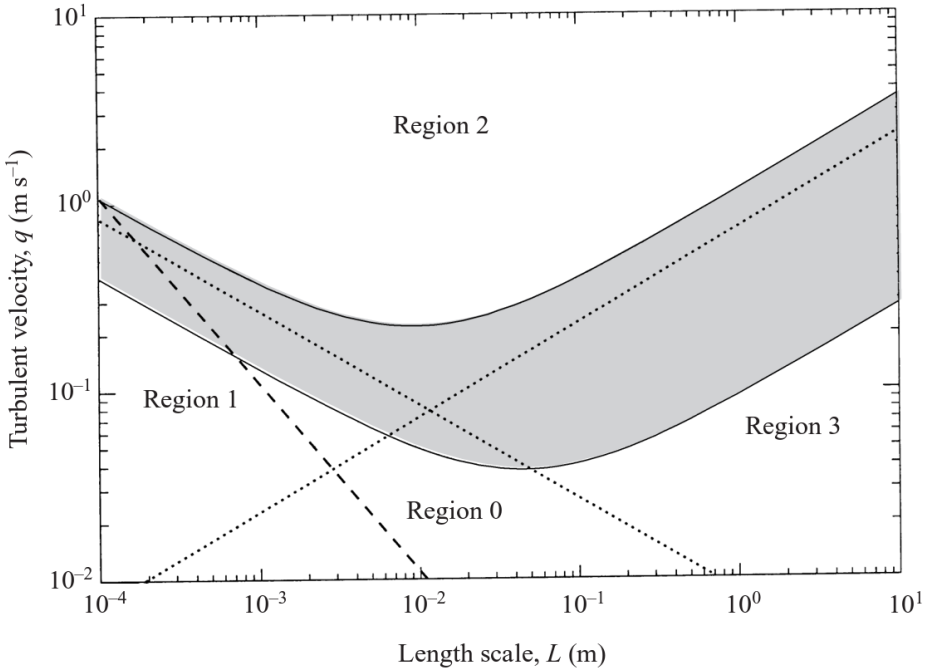

Figure 2.4 Diagram of L-q for water flows. Two dotted lines correspond to Eq. 2.26a and 2.26b and they divide the space into four regions (region 0 – region 3). The dashed line represents Re = 100. The shaded area represents the region of marginal breaking (Brocchini and Peregrine, 2001).

stabilizing effect of the capillary and gravity forces. Region 2 represents a state of intense turbulence where neither gravity nor surface tension can maintain the integrity of the free surface. Drops and bubbles are released, leading to a two-phase flow of air and water. Turbulent eddies become unrestrained by the surface boundary, resulting in violent liquid eruptions due to the lack of significant deceleration of turbulent elements near the surface. In addition to the regions of weak and strong turbulence, the diagram also includes two other distinct regions, in which gravity or surface tension dominate. In region 1, the Froude number is large and the Weber number is small, where surface tension plays a more important role than gravity. The turbulence scale is relatively small with typical scale around 1cm. In region 3, gravity is dominating the turbulence with weak surface tension. It is the most common region observed in nature: rivers, streams, oceans and seas. The dashed line represents Re = 100, below which viscosity plays an important role on the evolution of any turbulence. The shaded area is the region of marginal breaking and the upper and lower bounds of this region are calculated by

$$q^2 = 0.13gL + 1.57\frac{S}{L} \tag{2.27a}$$

and

$$q^2 = 7.7 \times 10^{-4} gL + 0.22\frac{S}{L}, \tag{2.27b}$$

respectively, where S is the ratio of surface tension and fluid density. These two bounds represent a transitional region of marginal breaking. This 'L-q' diagram has become a convenient way for approximate characterization of a free surface regime in comparison with other research, such as in (Freeze et al. (2003),Smolentsev et al. (2004),Smolentsev and Miraghaie (2005) and Muraro et al. (2021)).

Some key studies of the behaviour of free surface pattern in open channel flows are summarised in Fig. 2.5. The aim of this summary is to find the gap in the available dataset from field or laboratory studies in different regions of flow. The vertical axis turbulent velocity component was taken as 7.5 % of the bulk flow velocity, which is an approximate measure of the relative scale between the streamwise turbulent component and the bulk velocity (Muraro et al., 2021, Nezu and Nakagawa, 1993). For the horizontal axis water depth is chosen as most of the past studies did not estimate the turbulence length scale. Roy et al. (2004) suggested that the size of turbulent macrostructures increases with water depth. The definition of solid, dotted and dashed lines in Fig. 2.5 are the same as in Fig. 2.4. Markers represent studies of Cooper et al. (2006), Dolcetti (2016), Freeze et al. (2003), Fujita et al. (2011), Horoshenkov et al. (2013), Jackson (1976), Satoru et al. (1982), Komori et al. (1989), Kumar et al. (1998), Legleiter et al. (2017), Longo (2010), Maddux et al. (2003),

Mandel et al. (2019), Nichols et al. (2016), Noss et al. (2019), Rashidi (1997), Savelsberg et al. (2006), Savelsberg and Van De Water (2008, 2009), Smolentsev and Miraghaie (2005), Tamburrino and Gulliver (2007), Tani and Fujita (2018) and this study (details of this study's flow conditions can be found in Table 3.2 in subsection 3.8). It can be seen from Fig. 2.5 that most of laboratory studies are in region 0 and most field studies are in region 3. There is generally a lack in laboratory study in region 3. This is due to the difficulty in producing high bulk velocity flows for a given flow depth in laboratory conditions (Muraro et al., 2021). Besides, the field measurement accuracy and resolution are usually not as high as in laboratory. Hence, there is a need for study of region 3 flows in the laboratory.

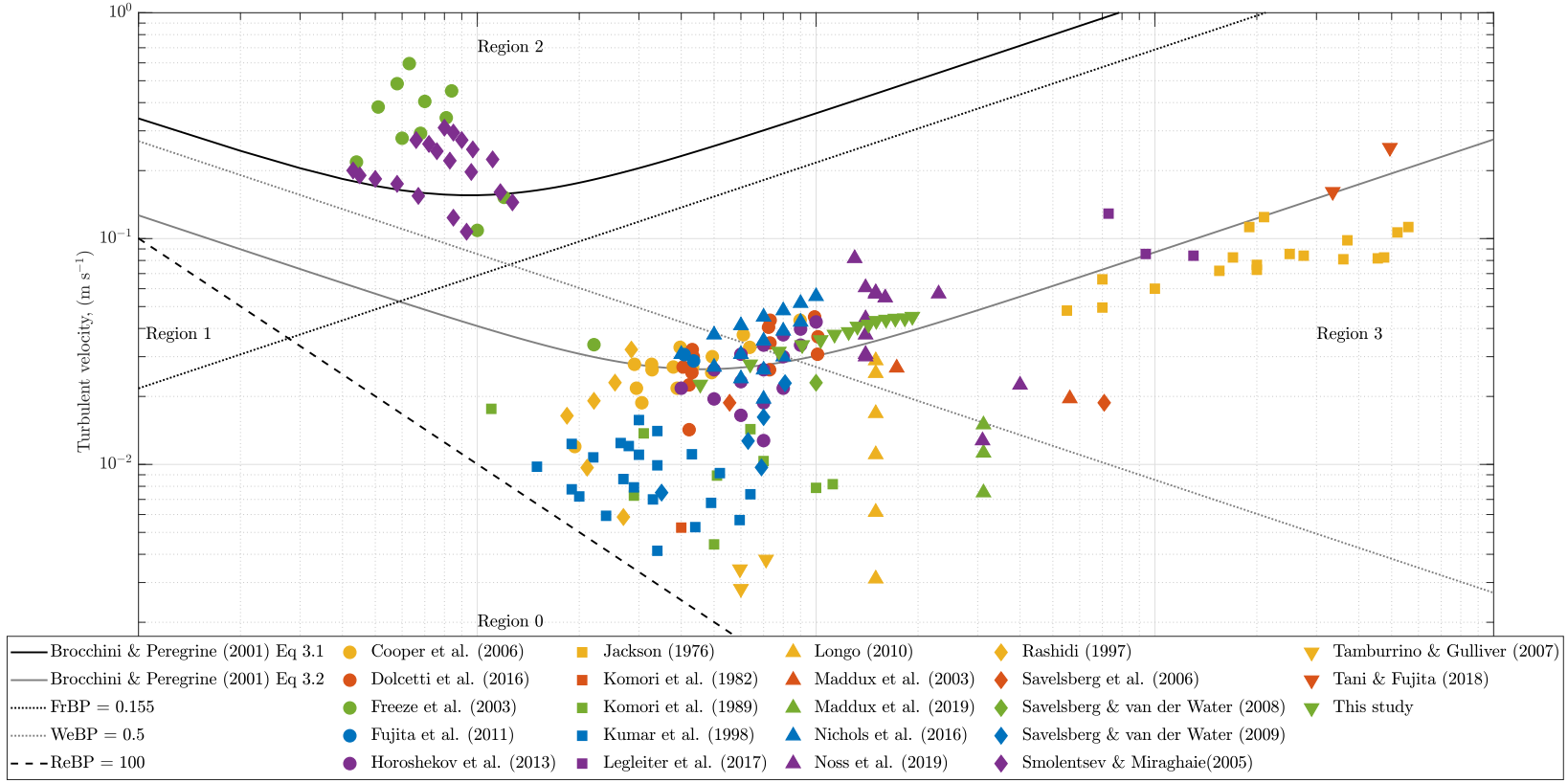

Figure 2.5 A summary of previous studies and this study organised following Brocchini and Peregrine (2001). The streamwise turbulent velocity component was defined through the bulk velocity using the relations given in Nezu and Nakagawa (1993). Water depth scales with the largest size of a coherent structure. Solid lines are obtained from Eq. 2.27a and 2.27b. Dotted lines are the separations between the regions and are obtained from Eq. 2.26a and 2.26b using $Fr_{BP} = 0.155$ and $We_{BP} = 0.5$. Dashed line represents the condition of the Brocchini and Peregrine (2001) defined Reynolds number $\mathrm{Re}_{BP} = 100$. Modified from Muraro et al. (2021) with permission.

2.2.2 Mechanisms driving the deformation of the free surface

The reason for the specific surface deformation is not yet fully understood due to the lack of studies that simultaneously measure both sub-surface and surface properties in sufficient quantities. Muraro et al. (2021) summarized three possible mechanisms that account for the free surface deformation: impact of coherent structures onto the water surface, excitation through resonance and influence of bed topography.

Coherent structures are defined as a connected turbulent fluid mass with instantaneously phase-correlated vorticity over its spatial extent by Hussain (1986). It is a parcel of fluid that has its life cycle organised in space and time. Muraro et al. (2021) summarised coherent structures into two categories: bursting phenomena (Kline et al., 1967, Rashidi, 1997) and large-scale vortical motions (Nezu and Nakagawa, 1993, Zho, 2015). As is shown in Fig. 2.6a, bursting processes start with the periodic lifting of low-speed streaks from the bed (Bogardt and Tiederman, 1986, Tang et al., 2016). Low-speed streaks along with horseshoe shape vortices then oscillate vertically and break down into several ejections. The broken vortices reach to the free surface and form surface patches (Rashidi, 1997). Matthes (1947) defined a new term 'kolk', which is the only large-scale motion related to turbulence. As is shown in Fig. 2.6b, kolk vortices rise towards to the surface, generating a boil and then dissipating (Matthes, 1947).

Several studies have proven that the presence of capillary gravity waves excite the dynamic appearance of the free surface (Dolcetti et al., 2020, Falcon and Mordant, 2022, Savelsberg and Van De Water, 2008, Young and Wolfe, 2014). Linear dispersion relationship describes the dependence of angular frequency with respect to wavenumber. In fluid dynamics, airy wave theory, also known as linear wave theory, provides a linearised description of motion of gravity waves on a fluid surface (Airy, 1845). In turbulent flows, capillary gravity waves travel in different directions at a celerity that is frequency and wavenumber dependent (Dolcetti, 2016). The minimum phase velocity of the gravity capillary waves is 0.23 ms^{-1} (Savelsberg and Van De Water, 2008, Dolcetti, 2016). Resonance only happens when the mean surface velocity is greater than 0.23 ms^{-1} (Dolcetti, 2016, Muraro et al., 2021). When the mean surface surface velocity is smaller than 0.23 ms^{-1}, the free surface is dominated by patterns moving at a velocity close to the mean surface velocity.

Beds with small roughness can excite waves with different wavelengths in different directions, including free resonant waves (Harband, 1976). The resonant waves are fixed in time with 0 Hz frequency. These waves are also known as stationary waves or standing waves (Rayleigh, 1883). Dolcetti (2016) has proven that when the mean surface velocity of the flow is larger than the minimum phase velocity of the gravity-capillary waves (0.23 ms^{-1}), the spatial and temporal scales of the free surface can be predicted based on the wavelength of

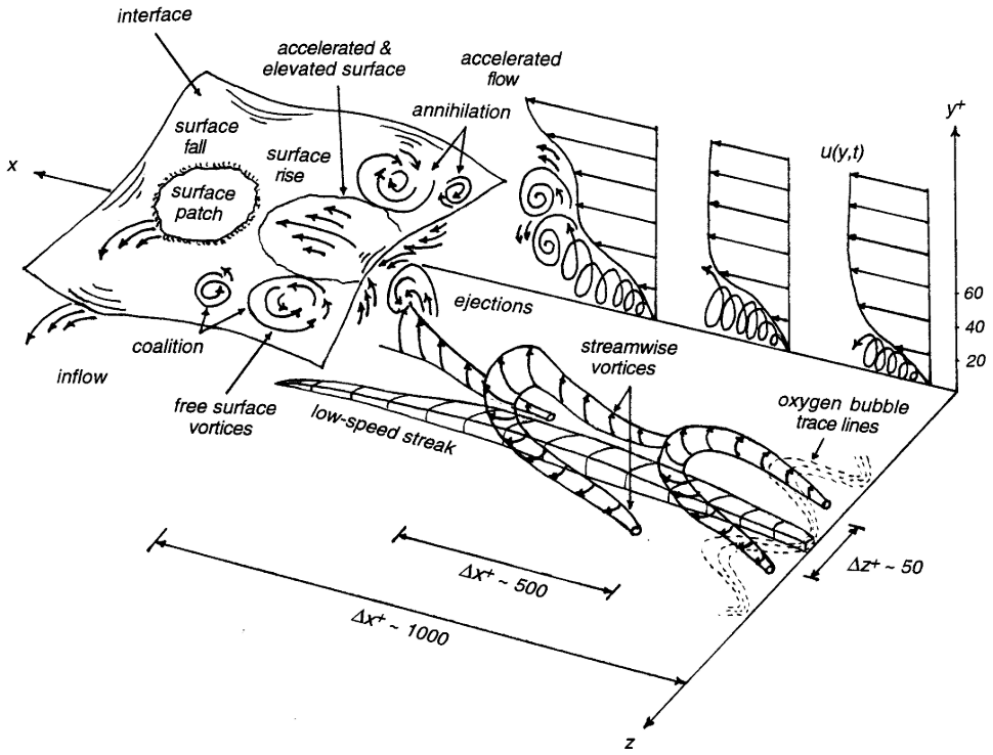

(a)

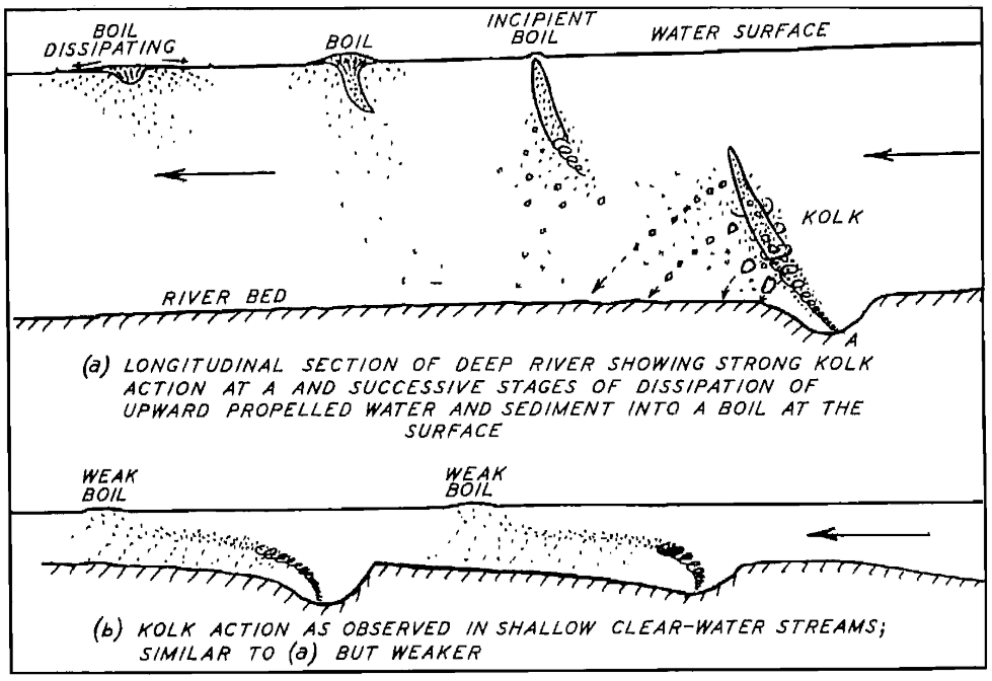

(b)

Figure 2.6 Conceptual sketch showing the development of coherent structures toward to the free surface proposed by (a) Rashidi (1997) and (b) Matthes (1947).

the stationary waves. The wavenumber of the stationary waves k_0 can be solved analytically according to Burns (1953)

$$k_0 \frac{I_{-1/2-n}(k_0 d)}{I_{1/2-n}(k_0 d)} = \frac{g + \frac{T}{\rho_f} {k_0}^2}{{U_s}^2}, \tag{2.28}$$

where I_n is the modified Bessel function of order n. Teixeira (2019) proposed a simplified equation to estimate the stationary wave wavelength λ_0 based on constant-shear, deep-water gravity wave approximation:

$$\frac{\lambda_0}{d} = \frac{2\pi Fr^2}{1 + nFr^2}. \tag{2.29}$$

2.2.3 Open channel flows free surface dynamics

The linkage and potential interdependence between the turbulence field and the free surface deformation is still not fully understood. This is due to the lack of data for simultaneous measurement of the free surface and the sub-surface velocity field, especially the free surface data. One of the earliest experimental data on instantaneous water depth was probably from Freeze et al. (2003). They have measured the instantaneous water depth by an ultrasound transducer at relatively high Froude number flows (supercritical flows) in a very steep flume. This experimental study has shown that the wave amplitude and wave number increase with Froude number. Following an experimental study by Freeze et al. (2003), Smolentsev and Miraghaie (2005) measured the instantaneous 1D surface-normal displacement fluctuation using an ultrasound transducer, and in-plane changes in surface structures using a high-speed camera. They found that a unique feature of the flow is a cell-type structure of the free surface. The cell-type structures have a characteristic size comparable with half the flow depth. From images of the surface plane, long gravity waves, capillary waves and turbulence cells can be observed (Smolentsev and Miraghaie, 2005).

Fujita has utilised PIV and large-scale PIV (LSPIV) techniques for free surface velocity measurement in river flows and laboratory flows (Fujita and Tsubaki, 2002, Fujita et al., 2007, 2011, Fujita, 2017). Fujita et al. (2011) have simultaneously measured the free surface profile and 2D velocity field under the free surface. For rough wall open-channel turbulent flow conditions in the study of Fujita et al. (2011), the advection characteristics of water surface profiles exhibit similarities to those of near-surface flow velocities. Nichols (2014) has observed that the coherent structures travel with an advection velocity close to the mean streamwise velocity. This further confirms the correlation between the surface velocity and sub-surface velocity. By correlating the water surface fluctuation and near surface vertical

velocity component, Fujita et al. (2011) have found the water surface fluctuation is induced by clockwise rotating vortical structures at the intermediate depth, which tend to move upwards to the free surface, interacting with the local water surface together with a counterclockwise vortex. Tani and Fujita (2020) have found that the sub-surface vortex motions do not dominate in turbulence related motions for shallow open-channel sub-critical turbulent flows over rough beds. In these cases, gravity waves contribute more than turbulence waves for higher Froude number, which is similar to smooth wall open-channel turbulence.

Horoshenkov et al. (2013) proposed a new analytical expression to approximate the free surface pattern:

$$W(\rho) = e^{-\frac{\rho^2}{\sigma_w{}^2}} \cos(q_0 \rho) \tag{2.30}$$

where ρ is the spatial lag, σ_w relates to spatial radius of correlation and q_0 relates to the characteristic period in the surface wave pattern. These parameters can define objectively the surface pattern in the developed flow. Similar correlation functions are also true for sea surface waves (G. Bass and I. M. Fuks, 1979):

$$W(x) = e^{-\frac{x^2}{l^2}} \cos(p\rho) \tag{2.31}$$

where p is the wavelength and l is the order of the correlation radius. Dolcetti et al. (2020) further expanded the free surface correlation in 2D space and time by a full spatio-temporal correlation function:

$$\begin{aligned} W(\boldsymbol{\rho}, \tau) = 2\pi e^{-b} I_0(-b) J_0(k_0 |\boldsymbol{\rho} - \boldsymbol{U_s}\tau|) \cos(\omega_0 \tau) + \\ 2\pi e^{-b} \sum_{n=1}^{\infty} I_n(-b)(-1)^{n/2} \cos(n\beta) [J_n(k_0 |\boldsymbol{\rho} - \boldsymbol{U_s}\tau|) e^{-i\omega_0(k_0)\tau} + J_n(-k_0 |\boldsymbol{\rho} - \boldsymbol{U_s}\tau|) e^{i\omega - 0(k_0)\tau}], \end{aligned} \tag{2.32}$$

where $\boldsymbol{\rho}$ is the spatial lag in 2D space, τ is the time lag, $\boldsymbol{U_s}$ is the surface flow velocity vector, ω_0 is the intrinsic frequency of gravity-capillary waves in still water, β is the angle of the vector $\boldsymbol{\rho}$-$\boldsymbol{U_s}\tau$ measured from the direction of U_s, I_n is the modified Bessel function of the first kind of order n and J_n is the Bessel function of the first kind of order n. Dolcetti et al. (2020) used $b = 2$ and $n = 10$ for calculation. This analytic model is comparable with video recording measurement, which proves it is a simple way to estimate the shape of the spatio-temporal correction function.

By comparing the spatial correlation parameters and corresponding hydraulic parameters, Horoshenkov et al. (2013) observed that the spatial correlation pattern of the water surface has a strong non-linear relationship with the underlying turbulent flow features. Nichols (2014) has calculated the spatial correlation function of the free surface from LIF images. The data were obtained from the same flow conditions examined in Horoshenkov et al. (2013). Nichols (2014) found an oscillatory component in the correlation function with a clear spatial period, which influenced the near surface velocity. More recently, Nichols et al. (2016) have developed a model to demonstrate that the frequency of free surface oscillation is a function of the deformation height and the depth of influence factor:

$$f_{shm} \approx \frac{1}{2\pi}\left[\frac{g}{(1.5N+1)\sigma}\right]^{1/2}, \tag{2.33}$$

where f_{shm} is the frequency of simple harmonic motion, N is the number of rms water surface wave heights below the surface affected by the motion (depth of influence factor) and σ is the rms wave height. The depth of influence factor N is almost constant ($N = 28$) for the range of flow conditions in the study of Nichols et al. (2016), which means the free surface dynamics can influence up to 28 surface height standard deviations below the mean water depth.

2.3 Conditional analysis techniques

As mentioned in subsection 2.2.2, coherent structures are one of the main driving mechanisms for free surface deformation. It is important to characterise these 'parcels' of fluid, such as size, occurrence frequency and duration. Flow visualization is the traditional method to extract this information, which is explained in subsection 2.3.1. With the development of probe measurement techniques, some conditional analysis techniques were proposed, which are mentioned in subsection 2.3.2. Among all these conditional analysis techniques, U-level is the most widely used technique, which is explained in detail in subsection 2.3.3.

2.3.1 Flow visualization

Flow visualization is commonly used for studying three-dimensional turbulence and dynamic fluid phenomena, providing valuable insights into coherent flow structures. While various visualization methods (e.g. dye injection or hydrogen bubbles) have been employed in numerous studies (Bogardt and Tiederman, 1986, Roy et al., 2004, Shvidchenko and Pende, 2001), it is important to note that this technique has limitations. Flow visualization relies on manual visual estimation, leading to subjective outputs and limited quantitative information (Boppe and Neu, 1995). In some studies, 1D detection techniques were calibrated against

flow visualizations at relatively low Reynolds numbers. But its reliability diminishes at higher Reynolds numbers (Shah and Antonia, 1989). Moreover, the technique can be laborious to implement, requiring extensive trial and error (Smits, 2012). Therefore, despite its usefulness in providing qualitative descriptions, flow visualization has limited capabilities for quantitative measurements.

2.3.2 Probe measurement with 1D techniques

Considering the limitations of flow visualization, recent studies have been performed using probes to measure the velocity or pressure fields. With a reliable detection algorithm, probe measurements can be used to identify coherent structures in flows at much higher Reynolds number than is possible with flow visualization. Several measurement techniques have been used in laboratory and field studies, such as hot wire anemometry (HWA), laser Doppler anemometry (LDA), electromagnetic current meters (ECM) and acoustic Doppler velocimetry (ADV). These probe measurements can provide a very good temporal resolution of 3D velocity fluctuations at a single position. Taylor's hypothesis can be invoked to turn time-resolved data to spatial data. This has been employed by many researchers in turbulent structure analysis, such as Boppe et al. (1999), Ferraro et al. (2019), Guerra and Thomson (2017), Ng et al. (2021). The turbulence velocity fluctuation is assumed to be an ergodic process so that it is possible to use a sufficiently long time observation to reduce its statistical properties which are usually measured through a set of sufficiently large number of random realisations in multiple spatial locations.

To extract useful information from these velocity data, considerable effort has been given to the study of coherent structure detection techniques. 1D detection techniques (using time series of velocity or pressure recorded at a single spatial location) are the most straightforward, and are relatively simple to apply. They can also be applied not only to 1D data but also to 2D and 3D data by repeating the algorithm at different single points in the 2D plane or 3D volume. The most common 1D techniques for coherent structure detection are U-level (Bogardt and Tiederman, 1986), window average gradient (WAG) (Antonia A N and Bisset, 1990, Krogstad et al., 1998), variable interval time averaging (VITA) (Bogardt and Tiederman (1986)), Quadrant (Lu and Willmarth, 1973, Wallace, 2016) and short-time temporary average (TPAV) (Wallace et al., 1977). These detection algorithms were found to be highly dependent on a user-defined threshold level and window size, which are often determined by a subjective comparison with flow visualisation at low Reynolds number. The U-level algorithm (Lu and Willmarth, 1973) does not require a manually-defined threshold, and is therefore the only existing objective 1D detection method, but it only defines coherent structures according to a limited definition of extreme high or low velocity compared to the

mean. The following subsection 2.3.3 describes the development of the U-level algorithm by several authors.

2.3.3 U-level

U-level is a relatively simple to implement technique for coherent structure detection, and the amount of data required for its use is minimal. It has been used in various previous studies such as Antonia A N and Bisset (1990), Baron and Quadrio (1997), Metzger et al. (2010), Nichols (2014), Tang et al. (2016), Vinuesa et al. (2015). This technique looks at deficits from the mean streamwise velocity component and identifies extreme events as coherent structures. The U-level technique was first proposed by Lu and Willmarth (1973) for detection of burst-related events. An ejection event was assumed to occur whenever the velocity magnitude was below a certain threshold level

$$u^{'} < -k_U S_u, \tag{2.34}$$

where $u^{'}$ is the instantaneous streamwise velocity fluctuation and k_U is the threshold value. Bogardt and Tiederman (1986) evaluated the effectiveness of this technique by comparing with dye flow visualization in a 60 mm by 575 mm rectangular channel at average velocity 0.129 m s^{-1}, depth 60 mm and Reynolds number 8200. When the threshold $k_U = 1$, the U-level technique gives 76 % probability of detecting an ejection and 26 % probability of a false detection. The threshold value k_U was then adjusted so that the number of events detected by U-level corresponded to the number of ejections identified by flow visualization, giving k_U = 1.3. This resulted in a U-level technique that appears to have a reasonably high probability of correctly detecting an ejection (63 %) and a low probability of false detections (23 %). Luchiktand et al. (1987) also analysed the effectiveness of the U-level technique with flow visualization. They confirmed that a higher threshold level leads to a lower probability of false detection, but also a lower probability of correct detection. Luchiktand et al. (1987) modified the U-level technique with an additional lower threshold to eliminate multiple detections of a single ejection or sweep and a sign to distinguish between ejections (α = -1) and sweeps (α = 1). The detector function was turned on and output D was set to 1 when

$$u^{'}\alpha < -k_U S_u \tag{2.35}$$

and was turned off (output D was set to 0) when

$$u^{'}\alpha \geq -0.25 k_U S_u. \tag{2.36}$$

With the modification, Luchiktand et al. (1987) showed that the modified U-level technique had a substantial improvement in the probability of detecting an ejection while the probability of false detection only increased slightly. Besides, it gave a reasonable estimate of the average duration of an ejection at a point in the flow. It is necessary to determine the appropriate threshold for the detection technique. Luchiktand et al. (1987) suggested that the threshold levels should be taken as the ratio between the absolute value of the long time average in the second quadrant $|\overline{u_2}|$ (where streamwise velocity fluctuation $u^{'}$ is negative and vertical velocity fluctuation $v^{'}$ is positive) and the standard deviation of velocity fluctuations S_u, thus:

$$k_U = \frac{|\overline{u_2}|}{S_u} \tag{2.37}$$

Roy et al. (2004) and Nichols (2014) took the absolute value of velocity fluctuation instead of using the sign for detection of large-scale flow structures. The detection function was turned on when

$$|u^{'}| > k_U S_u \tag{2.38}$$

and off when

$$|u^{'}| < 0.25 k_U S_u. \tag{2.39}$$

Taking the absolute value will give similar statistics but cannot distinguish between sweep and ejection events. The U-level method is not applied to each time step individually; the value (on/off) of each time step depends upon the value of the previous time step. Moving through from $t = 0$, the detector function is turned on when Eq. 2.38 condition is met, and remains on for subsequent time steps until Eq. 2.39 condition is met, at which point the detector function is turned off and remains so until Eq. 2.38 condition is met again.

Despite the development of the U-level technique as an objective 1D method, it is still based upon the fundamental assumption that a coherent structure consists only of extreme velocity fluctuations. Coherent structures embody more than just extreme instantaneous velocities, and it can be argued they should be identified by also considering areas of high acceleration and jerk.

2.4 Measurement techniques for free surface dynamics

This section provides an overview of the three main free surface measurement techniques: optical, acoustic, and microwave. The existing optical methods are reviewed, highlighting their working principles and limitations in the context of this study. Additionally, several

studies have applied acoustic methods to investigate free surface dynamics, as referenced (Nichols, 2014, Krynkin et al., 2014, Dolcetti, 2016). While microwave sensing techniques are commonly used for motion detection, their application in free surface dynamics is relatively limited. Subsection 2.4.1 covers the optical methods, subsection 2.4.2 presents the acoustic methods, and section 2.5 provides detailed explanations of the microwave sensing techniques.

2.4.1 Optical methods

The principle of optical techniques to measure dynamics of liquid surfaces may be broadly divided into three categories: refraction-based methods, particle illumination methods and projection-based methods. The refraction-based techniques measure the slope of the free surface based on the intensity of the refracted light (Moisy et al., 2009, Savelsberg et al., 2006, Zhang and Cox, 1994). It is a technique that is relatively easy to set up but not suitable for deep water or waves with strong curvature (Moisy et al., 2009). The particle illumination method was implemented by Douxchamps et al. (2005), Simonini et al. (2021), Turney et al. (2009), and involves seeding the surface with buoyant particles. Significant effort is required for seeding preparation, distribution of seeding and seeding illumination. The accuracy of this technique is also limited by the distribution of particles. Projection-based techniques are seedless methods conducted by projecting a pattern on the water surface. The water is usually tinted to make the water opaque so that the surface appears solid. Nichols et al. (2020) have summarized literature on the use of colourant for surface visualization and suggested an optimum concentration of colourant. Different projection patterns have been implemented, such as a matrix of dots (Gomit et al., 2015), images of fringes (Cobelli et al., 2009) and speckle image patterns (Tsubaki et al., 2005).

2.4.2 Acoustic methods

Acoustic based sensing techniques have been implemented in water level and flow rate measurement. Ultrasonic flow meters measure the flow velocity based on the ultrasonic transit-time difference between a pair of sensors sending and receiving ultrasonic pulses as shown in Fig. 2.7. The key principle is that the sound waves travelling with the flow (a to b) will move faster than those travelling against it (b to a). The time difference is proportional to the bulk flow velocity and hence flow rate can be computed. These sensors can have a robust and reliable flow measurement regardless of the external conditions, such as fouling due to debris and grease (EMS, 2022). The ultrasonic technique is usually affected by other

factors, such as flow profile, type of liquid and pipe material. Therefore a calibration process is required to compensate for these effects.

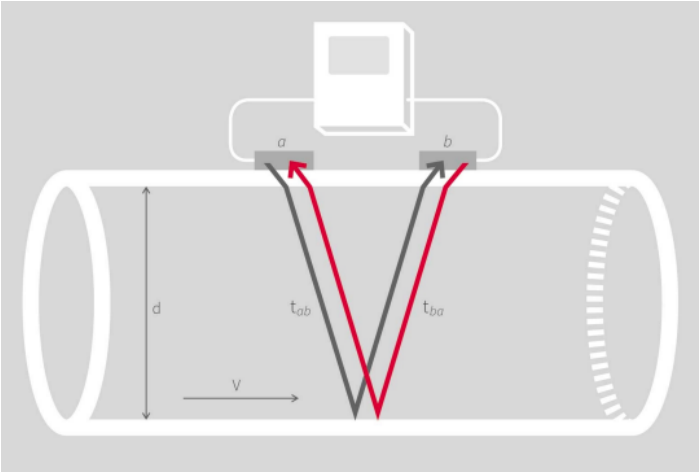

Figure 2.7 Ultrasonic flow transmitter measurement principle (Katronic, 2020).

Another type of velocity sensor known as area velocity sensor (e.g. TIENet 350 velocity sensor) acts within the flow and uses ultrasound based Doppler shift with an accuracy of $\pm$ 2 %. It contains a pair of ultrasonic transducers. One transmits ultrasound which is then reflected back by the bubbles or particles to the receiver (see Fig. 2.8). The sensor determines the frequency shift between the transmitted and received waves. The degree of change in frequency is proportional to the velocity of the flow stream. This sensor can also contain a pressure transducer. The difference between the pressures exerted on outer and inner diaphragms is equal to the hydrostatic pressure, from which the level can be calculated (TELEDYNE, 2016).

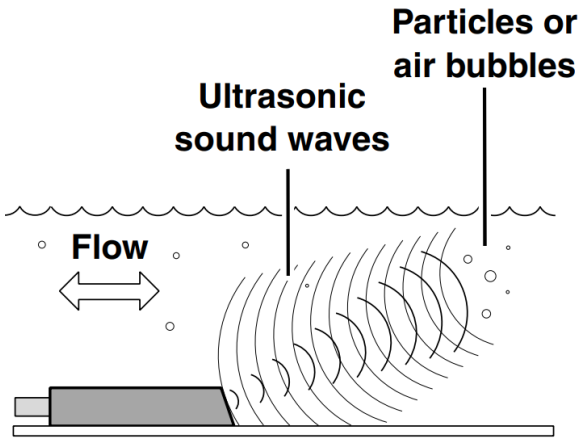

Figure 2.8 TIENet 350 area velocity sensor velocity operation (TELEDYNE, 2016).

Both acoustic sensors mentioned in preceding paragraphs can measure the water surface velocity but not surface fluctuations. Wang et al. (1991) have first designed a simple ultrasound device for flat water surface measurement. The working principle of this device is comparing the phase of a transmitted signal with that reflected from the surface to a detecter, with the assumption that the speed of sound is constant. Nichols et al. (2013) have further extended this technique into water gravity waves and turbulence generated surface waves measurement in a laboratory flume. The instantaneous water surface fluctuation can be recovered from the temporal variation of the phase difference between a sent and received ultrasonic signal reflected form the dynamically rough surface. In order to effectively extract the accurate information, three criteria must be satisfied: (i) the minimum wavelength must satisfy the theory of Fresnel zone ensonification, (ii) the mean magnitude of the instantaneous local surface gradient must not exceed 0.025 (-) and (iii) the rms wave height must be smaller than 1 % of the acoustic wavelength. Krynkin et al. (2014) have successfully determined the water surface roughness using an acoustical technique based on stationary phase method in shallow water flow on open channels. Research from Dolcetti (2016) has shown that the measurement of the acoustic Doppler spectra in the backscattering configuration is related to water surface pattern. Both capillary waves propagating in upstream and downstream directions and mean surface velocity can be observed in the Doppler spectra. Romanova et al. (2018) have recorded the amplitude of an acoustic field over a range of flow regimes in a partially filled pipe. It has been found that the statistical behaviour in sound pressure increases with the water depth and bed roughness.

2.5 Microwave sensing

Doppler radar sensors are increasingly popular for vibration monitoring and motion detection, such as measurement of breathing and heart rate (Costanzo, 2019), human walking (Mercuri et al., 2013), fall events (Karsmakers et al., 2012) and hand gesture recognition (Skaria et al., 2019). It has advantages of good performance in any weather conditions (e.g. darkness, fog and rain). It can perform its function at long and short ranges and can provide measurements with high accuracy.

2.5.1 Continuous wave (CW) Doppler radar

Doppler radar motion sensing usually transmits a continuous wave (CW) signal, which is reflected by a moving target and then demodulated in the receiver. An un-modulated signal

$$T_{mw}(t) = \cos[2\pi f_{LO}t + \phi(t)] \tag{2.40}$$

with carrier frequency f_{LO} is transmitted toward the detecting object and $\phi(t)$ is the phase noise of the transmitter (Gu, 2016, Wang et al., 2014). Neglecting amplitude variation, the reflected signal captured by the radar receiver is represented as

$$R_{mw}(t) = \cos[2\pi f_{LO}t - \frac{4\pi d_0}{\lambda} - \frac{4\pi x_m(t)}{\lambda} + \phi(t - \frac{2d_0}{c})] \tag{2.41}$$

where $x_m(t)$ is the mechanical movement, λ is the wavelength of the wireless signal, c is the speed of electromagnetic wave and d_0 is the nominal distance between the transmitter and the target (Li et al., 2013, Gu, 2016). The received signal is similar to the transmitted signal with a time delay determined by the nominal of the target and with its phase modulated by the motion of the target. The received signal (Eq. 2.41 signal) and local oscillator (LO) signal (Eq. 2.40 signal) that is derived from the same source as the transmitted signal are mixed and down-converted into the baseband signal

$$B(t) = \cos[\theta + \frac{4\pi x_m(t)}{\lambda} + \Delta\phi(t)], \tag{2.42}$$

where $\theta = 4\pi d_0/\lambda + \theta_0$ is determined by the nominal detection distance d_0 and the phase shift θ_0 at the reflection surface. $\Delta\phi(t) = \phi(t) - \phi(t - 2d_0/c)$ is the residual oscillator phase noise (Li et al., 2013, Gu, 2016).

2.5.2 Quadrature receivers

After analog-to-digital conversion (ADC) (convert analog signal to digital signal), the information of the motion can be identified by processing the digitized $B(t)$. When the movement amplitude is much smaller than the wavelength λ and θ in Eq. 2.42 is an odd multiple of $\pi/2$ (i.e. $\theta = (2n+1)\pi/2$, where n is an integer), a linear approximation can be applied to Equation 2.42 and the baseband output is approximated as (Li et al., 2013)

$$\begin{aligned} B(t) &= \cos[(2n+1)\frac{\pi}{2} + \frac{4\pi x_m(t)}{\lambda} + \Delta\phi(t)], \\ &= \sin[\frac{4\pi x_m(t)}{\lambda} + \Delta\phi(t)], \\ &\approx \frac{4\pi x_m(t)}{\lambda} + \Delta\phi(t), \end{aligned} \tag{2.43}$$

However, when θ is an even multiple of $\pi/2$ (i.e. $\theta = (2n)\pi/2$, where n is an integer), the baseband output is approximately (Li et al., 2013)

$$\begin{aligned} B(t) &= \cos[(2n)\frac{\pi}{2} + \frac{4\pi x_m(t)}{\lambda} + \Delta\phi(t)], \\ &= \cos[\frac{4\pi x_m(t)}{\lambda} + \Delta\phi(t)], \\ &\approx 1 - [\frac{4\pi x_m(t)}{\lambda} + \Delta\phi(t)]^2, \end{aligned} \tag{2.44}$$

which is no longer proportional to $x_m(t)$, which is known as a 'null point' (Droitcour et al., 2004). At null points, the baseband output can lead to inaccurate measurement results (Droitcour et al., 2004, Gu, 2016). This null point occurs with a target distance every $\lambda/4$ from the radar. In order to overcome the null point issue, a frequency tuning technique was developed (Gu, 2016). As shown in Fig. 2.9, it uses double sideband transmission, with two different LO frequency and thus two wavelengths λ_1, λ_2. The null points in these two sidebands happen every $\lambda_1/4$ and $\lambda_2/4$, which are indicated as red markers in Fig. 2.9a. In such way, the null points from one sideband and the optimum points from the other sideband can overlap each other. Though the frequency tuning technique implemented by hardward tuning can solve the null point problem, it is not very convenient (Gu, 2016). Another approach, a quadrature receiver is proposed, in which the received signal is mixed with two signals with phases 90 degrees apart as shown in Fig. 2.9b. The output signals of the receiver for these two 90 degrees phase shift signals are called in-phase (I) and quadrature (Q) signal. The quadrature I/Q channels ensure that there is always one channel not in null point and do not require a tuning hardware. The baseband I/Q output can be represented as (Rodriguez and Li, 2019, Wang et al., 2014)

$$I(t) = A_I \cos\left(\frac{4\pi x_m(t)}{\lambda} + \phi_I\right) + DC_I \tag{2.45a}$$

$$Q(t) = A_Q \sin\left(\frac{4\pi x_m(t)}{\lambda} + \phi_Q\right) + DC_Q \tag{2.45b}$$

where A_I and A_Q are the amplitude, DC_I and DC_Q are the DC offsets in two channels, ϕ_I and ϕ_Q are the Q residual phase in two channels.

2.5.3 AC coupling signal distortion

In order to reduce the impact of the noise in ADC, the mixer output I/Q signals are usually further boosted by the baseband amplifier. AC coupling is usually used between the mixer

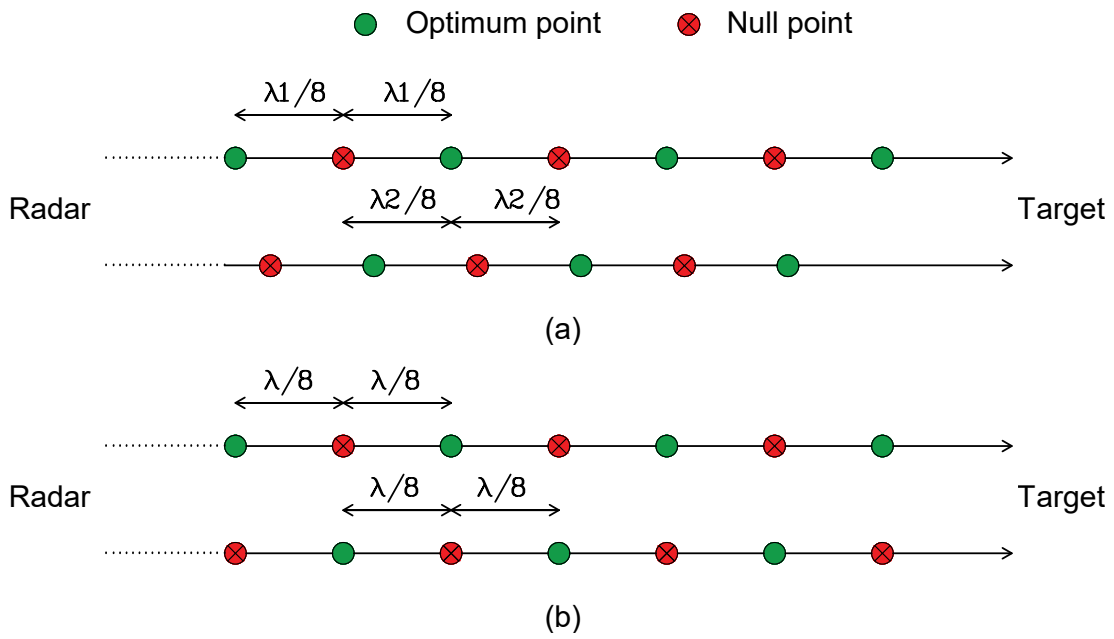

Figure 2.9 Sketch showing the null point issue (a) solved by frequency tunning and (b) solved by I/Q channels.

and the baseband amplifier to avoid the DC offsets saturation. The capacitor and resistor forms a high pass filter with cutoff frequency of $f_{cH} = 1/(2\pi CR)$. The ideal I/Q trajectory should form an arch that fits with the circle centred in (DC_I, DC_Q) and radius A_I. In AC coupled circuit, the I/Q signals are distorted and do not form a perfect arch anymore. The I/Q trajectory is distorted into a ribbon-like shape as indicated in Fig. 2.10 as a blue curve.

The distortion introduced by the AC coupling circuit was discussed and solved by Gu et al. (2016). The baseband transfer function between the mixer output and the baseband amplifier $H_B(z)$ can be represented as

$$H_B(z) = A_s \frac{1 - \sum_1^M b_k \cdot z^{-k}}{1 - \sum_1^N a_k \cdot z^{-k}} \tag{2.46}$$

where A_s is the baseband gain factor and the coefficient b_k/a_k determine the characteristics of the high pass response of the RC filter. Gu et al. (2016) proposed a digital post-distortion technique (DPoD) to compensate the AC coupling distortion by applying an inverse function of the baseband transfer function. The compensation system response is expressed as

$$H_D(z) = \frac{1 - \sum_1^N a_k \cdot z^{-k}}{1 - \sum_1^M b_k \cdot z^{-k}}. \tag{2.47}$$

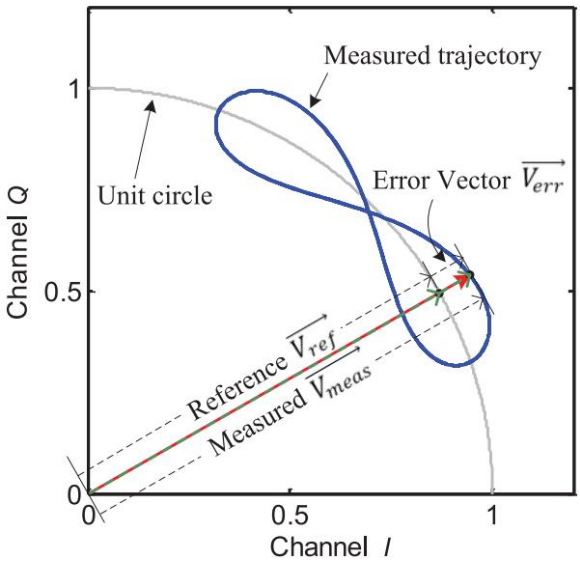

Figure 2.10 Simulated I/Q trajectory showing the error vector that is due to distortion at the AC-coupled baseband (Gu et al., 2016).

To quantify the degree of distortion and the quality of the I/Q trajectory, Gu et al. (2016) proposed to use error vector magnitude (EVM) measurement. Ideally, the I/Q trajectory is expected to fall on the idea unit circle as shown in Fig. 2.10 as grey circle. The distorted signal deviates from the unit circle, with a vector of $\vec{V_{means}}$ as shown in Fig. 2.10 as blue ribbon. The EVM for the whole I/Q trajectory is defined as (Gu et al., 2016)

$$\mathrm{EVM} = \frac{\sum_{k=1}^{N} 10 \cdot \log_{10}\left(\frac{\left|\vec{V_{err}^{k}}\right|}{\left|\vec{V_{ref}^{k}}\right|}\right)}{N}, \tag{2.48a}$$

$$\vec{V_{err}^{k}} = \vec{V_{means}^{k}} - \vec{V_{ref}^{k}}, \tag{2.48b}$$

where N is the number of signal points in the I/Q trajectory, $\vec{V_{means}^{k}}$ is the vector from the circle center to the k$^{\text{th}}$ measured signal point, $\vec{V_{ref}^{k}}$ is the k$^{\text{th}}$ reference vector from the center to the ideal circle and $\vec{V_{err}^{k}}$ is the error vector representing the difference between $\vec{V_{means}^{k}}$ and $\vec{V_{ref}^{k}}$. Larger EVM value means a more distorted ribbon shape and larger signal distortion, thus less accurate signal demodulation. The value of EVM should be minimised to achieve the accurate phase information caused by the target motion rather than the circuit imperfections Gu et al. (2016).

2.5.4 Amplitude and phase imbalances

In addition to the distortion caused by AC coupling, the amplitude and phase imbalance from I/Q channels can also cause signal distortion. The amplitude imbalance is

$$A_e = A_Q / A_I \tag{2.49}$$

and the phase imbalance is

$$\phi_e = \phi_Q - \phi_I. \tag{2.50}$$

These imbalances can corrupt the signal quality and introduce error in measurements (Park et al., 2007c, Singh et al., 2013, Zakrzewski et al., 2014). Park et al. (2007c) has introduced a physical phase shifter at the receiver input to simulate an object moving at a constant velocity. The amplitude and phase imbalance can be determined from the resulted sinusoidal I/Q outputs time series. This imbalance estimation method is call the 'time domain' method and such modification itself is able to change the imbalance values(Zakrzewski et al., 2014). An efficient data based method that does not require circuit modification, called 'ellipse fitting' has been proposed by Singh et al. (2013). As shown in Fig. 2.11a, the I/Q data with imbalances form an arc of an ellipse (or an ellipse if the displacement is larger than half of the radar wavelength) rather than a unit circle. The imbalanced I/Q data needs to be corrected to form a unit circle arc (or a full unit circle) for accurate phase demodulation as shown in Fig. 2.11b. The imbalance parameters are estimated from the ellipse that the data forms in the I/Q plot.

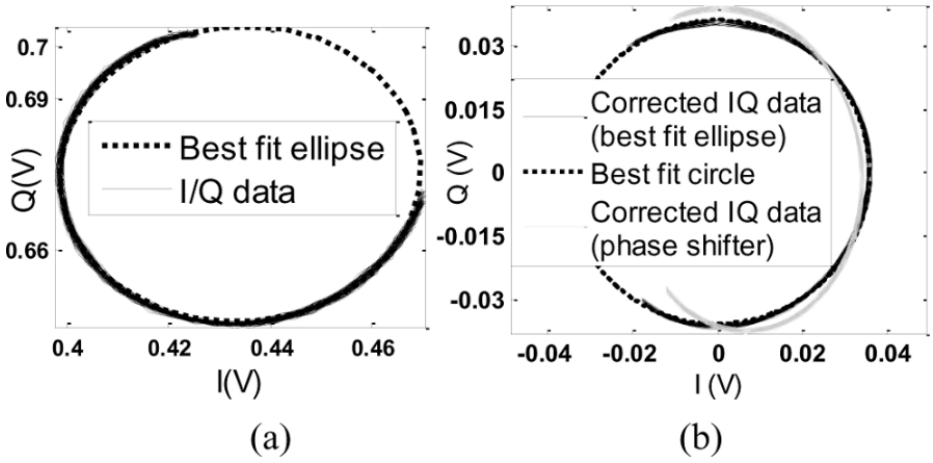

Figure 2.11 (a) I/Q data with imbalances (b) corrected I/Q data (Singh et al., 2013).

By expanding Eq. 2.45a and substituting it with Eq. 2.50 into Eq. 2.45b, gives the following equation

$$\left(\frac{Q}{A_Q}-\frac{DC_Q}{A_Q}\right)^2+\left(\frac{I}{A_I}-\frac{DC_I}{A_I}\right)^2-2\left(\frac{Q}{A_Q}-\frac{DC_Q}{A_Q}\right)\left(\frac{I}{A_I}-\frac{DC_I}{A_I}\right)\sin(\phi_e)-\cos^2(\phi_e)=0 \tag{2.51}$$

This ellipse equation can be normalized to the standard equation as

$$I^2+A\times Q^2+B\times IQ+C\times I+D\times Q+E=0. \tag{2.52}$$

The amplitude and phase imbalance can be determined as

$$A_e=\sqrt{\frac{1}{A}}, \tag{2.53a}$$

$$\phi_e=\arcsin\frac{B}{-2\sqrt{A}}. \tag{2.53b}$$

In general, there are two main methods for ellipse fitting: (i) algebraic method and (ii) geometric method. The method proposed by Singh et al. (2013) is usually used in radar sensing represented as the algebraic method (Sim et al., 2020, Arsalan et al., 2020). Assuming the measured N ($N \gg 5$) samples of data are (I_1, Q_1), (I_2, Q_2), ..., (I_N, Q_N). Ideally, they should satisfy the ellipse, which is rearranged from Eq. 2.52 ,as follows, :

$$A\times {Q_N}^2+B\times I_nQ_N+C\times I_N+D\times Q_n+E=-{I_N}^2. \tag{2.54}$$

The best solution for A, B, C, D and E can be found with linear algebra as (Strang, 2009)

$$\begin{bmatrix}A\\B\\C\\D\\E\end{bmatrix}=(M^TM)^{-1}M^Tb, \tag{2.55}$$

where matrix M and b are

$$M=\begin{bmatrix}{Q_1}^2 & I_1Q_1 & I_1 & Q_1 & 1\\ \vdots & \vdots & \vdots & \vdots & \vdots\\ {Q_N}^2 & I_NQ_N & I_N & Q_N & 1\end{bmatrix} \tag{2.56}$$

and

$$b = \begin{bmatrix} -{I_1}^2 \\ \vdots \\ -{I_N}^2 \end{bmatrix} \tag{2.57}$$

Geometric ellipse-fitting methods are iterative methods applied by minimizing geometric distance from the data points to their projections on the ellipse. The Levenberg-Marquardt (LM) method is usually used in radar sensing as it has been proven to be robust even though the arc length is short (Zakrzewski et al., 2012, 2014). Zakrzewski et al. (2014) has used LM correction of the classical Gauss-Newton method with the initial guess obtained from the Taubin algebraic method (Taubin, 1991).

Zakrzewski et al. (2014) has compared both the algebraic method and geometric method for imbalance estimation. Both methods can correct the signal when the arc length is greater than 60 % and the noise level is below 1.5 %. The geometric method performs more robustly when the noise level is higher.

With the estimated amplitude and phase imbalances, the Gram–Schmidt (GS) method was used to correct the imbalances (Bjorck, 1967). The imbalance corrected signals $I^{'}(t), Q^{'}(t)$ are obtained by

$$\begin{bmatrix} I^{'}(t) \\ Q^{'}(t) \end{bmatrix} = \begin{bmatrix} 1 & 0 \\ -\tan\phi_e & \dfrac{A_I}{A_Q \cos\phi_e} \end{bmatrix} \begin{bmatrix} I(t) \\ Q(t) \end{bmatrix} \tag{2.58}$$

2.5.5 Demodulation techniques

There are two main techniques for demodulating the I/Q channels: linear and nonlinear demodulation techniques. The linear demodulation method approximates the arc of a circle as a line (Zakrzewski et al., 2015a). This method is computationally simple but it has the disadvantage of losing the absolute value of the displacement. Moreover, this method is only valid when the displacement is significantly small compared to the radar wavelength $x_m(t) \ll \lambda$. Besides, as mentioned in subsection 2.5.2, the single channel may face the null point problem (Girbau et al., 2012). Therefore, the demodulation may be inaccurate in certain radar-subject distances (Droitcour, 2006).

Another technique for demodulating I/Q channel outputs is nonlinear demodulation (Par, 2007). There are two most widely used non-linear demodulation techniques for quadrature radar, (i) arctangent demodulation (Par, 2007, Hu et al., 2014, Boric-Lubecke et al., 2009) and (ii) extended differentiate and cross multiply (DACM) (Wang et al., 2015, 2020, Lv et al., 2014). Arctangent demodulation is usually used in recovering the target's movement $x_m(t)$:

$$\Phi(t) = \frac{4\pi x_m(t)}{\lambda} + \theta + \Delta\phi(t) = \arctan\left(\frac{Q(t)}{I(t)}\right) \tag{2.59}$$

Mathematically, the arctangent demodulation only allows a codomain range of (-π/2,+π/2). If the target's movement is large compared to the carrier wavelength (the wavelength of LO), the demodulation may exceed this range and discontinuity will occur. When the displacement is small enough, the discontinuity caused by phase wrapping can easily be calibrated by adding or subtracting π. However, when the displacement is larger than λ/8 (Wang et al., 2014), the calibration gets more complicated so that for some signal segments the discontinuity is resolved by adding π while for other π needs to be subtracted. Wang et al. (2014) proposed and investigated a DACM algorithm. The discrete form of this algorithm is

$$\Phi[n] = \sum_{k=2}^{n} \frac{I[k]\{Q[k]-Q[k-1]\} - \{I[k]-I[k-1]\}Q[k]}{I[k]^2 + Q[k]^2} \tag{2.60}$$

The extended DACM algorithm is capable of resolving issues with with phase unwrapping and accurately demodulating the phase regardless of the magnitude of the target's motion.

2.6 Literature review summary

This chapter provides a comprehensive overview of the key parameters and formulas related to partially filled pipes, which will be utilized in this study. It also reviews previous experimental studies on partially filled pipes, highlighting the limited availability of free surface dynamics measurements and the absence of 2D surface data. Most of these studies have focused on under-surface velocity measurements. The hydrodynamics findings from these studies, including velocity distribution and turbulence quantities, are presented and will be compared to the findings of this study, leading to the modification of empirical equations. The review of free surface dynamics in rectangular channels will help explain the observed phenomena in this study, and similar analysis methods employed in rectangular channel studies can be applied in this study. Additionally, the existing conditional analysis techniques are reviewed, their limitations identified, and a comparison will be made with the proposed conditional analysis technique in this study. The common surface dynamics measurement technique, optical and acoustic technique, are reviewed. The review also highlights the gap in microwave sensing application for free surface dynamics. Finally, the working principles and signal processing techniques of the Doppler radar sensor are explained, which will be employed in this study.

In summary, previous studies in rectangular channels indicate a relationship between sub-surface dynamics and free surface dynamics. However, research on flows in partially filled circular pipes is limited. The use of Doppler radar sensors offers the potential to remotely measure motion dynamics. Investigating these aspects could pave the way for a new non-invasive pipe flow monitoring approach.

Chapter 3

Experimental facilities & flow conditions

A series of experiments were conducted in which the behaviour of the water surface and the changes of turbulence properties in response to different hydraulic conditions could be measured. This chapter will describe the experimental setup, instrumentation and measurement techniques, and the range of flow conditions examined.

3.1 Pipe setup

The work reported in this study was carried out in a 290 mm inner diameter and 300 mm outer diameter perspex pipe (see Fig. 3.1) in the RA08 Hydraulics Laboratory of The University of Sheffield. The pipe is 20 m long and it consists of 10 equal 2 m long sections. The pipe joints were carefully machined to provide little or no disturbance to the free flow, and were sealed with external rubber gaskets. In Fig. 3.2, the labels 'a' to 'c' and 'h' to 'k' represent components of the pipe which allow control of the flow conditions, which will be described later. There are several rectangular or circle entry slots cut into the pipe top to install the measurement equipment. Sections 'd', 'f' and 'g' represent the measurement sections of the pipe, where velocity field and free surface measurement take place. These measurement systems were located 9.1m from the flow inlet ($x/D \approx 30$) and will be described in detail in subsection 3.2 - 3.6.

The slope of the pipe, S_f, was fixed at 1/1000, which corresponds to a 2 cm height difference from the pipe inlet to the pipe outlet. The reason for choosing this specific slope is that it is the minimum slope that could be achieved due to the potential bending of the old pipe supporting frame. To achieve this slope, the pipe upstream and downstream end were blocked by two circle segment shape blockages and sealed as illustrated in Fig. 3.3a and c. Still water was added in between the blockages, with the surface below the top of the blockages. The amount of water did not change over time. The depth of still water at

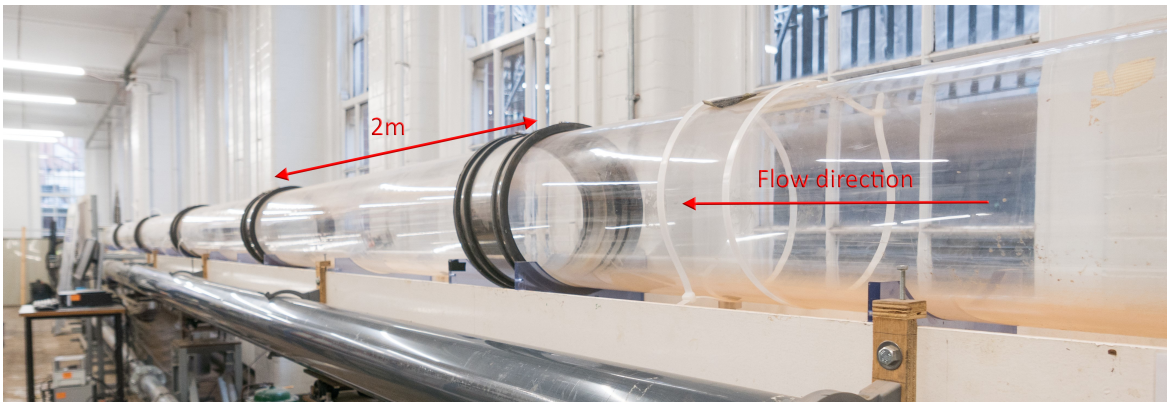

Figure 3.1 Photography of the flume view from upstream.

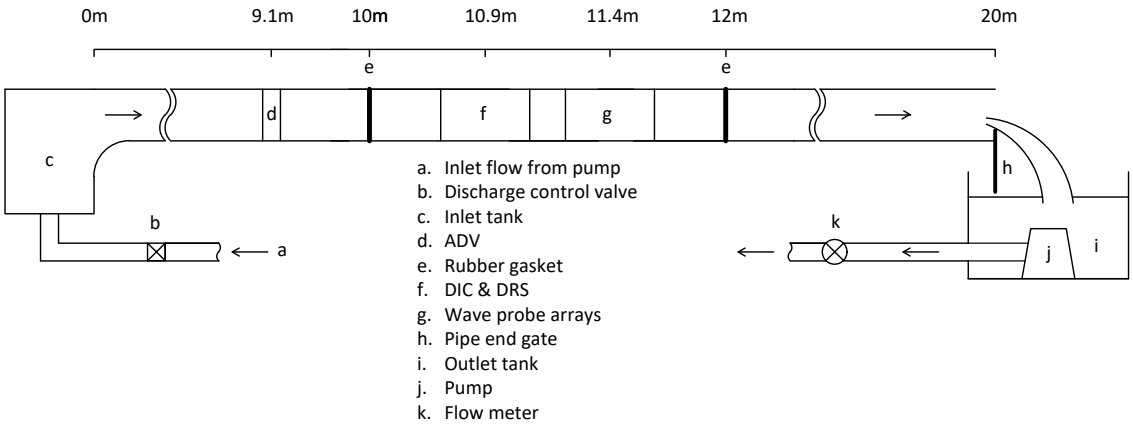

Figure 3.2 Sketch of the experimental setup in this pipe showing the relative position of the measurement section with respect to upstream and downstream sections of the pipe.

different streamwise locations was measured by a point gauge. Then the slope of the pipe was adjusted by inserting shims (thickness ranging from 1 mm to 5 mm) under the supports for the pipe sections. The measurement of water depth and the insertion of shims were iterated until the desired slope was achieved along the full length of the pipe. In an end sealed pipe, the water depth gradient corresponds to the gradient of the pipe. Figure 3.4 shows the water depth measured at 18 different streamwise locations against the longitudinal position. A linear function is fitted to these measurement points with a slope of 1/1000 and a coefficient of determination $R^2 = 0.992$. The coefficient of determination (R^2) is a statistical measure that represents the proportion of the total variation in the dependent variable that is explained by the independent variable in a regression model. It is calculated using the formula: R^2 = 1 - (SSR / SST), where SSR is the sum of squared residuals (or residual sum of squares) and SST is the total sum of squares. A perfect fit of the model to the data results in an R^2 value of 1, indicating that all the variation in the dependent variable is accounted for by the independent variable. On the other hand, an R^2 value of 0 suggests that the model does not explain any of the variation beyond the mean value. R^2 values between 0 and 1 indicate the proportion of the total variation in the dependent variable that is explained by the model. This means the pipe was set to a slope of 1/1000 with relative error of $\pm$ 0.28 %.

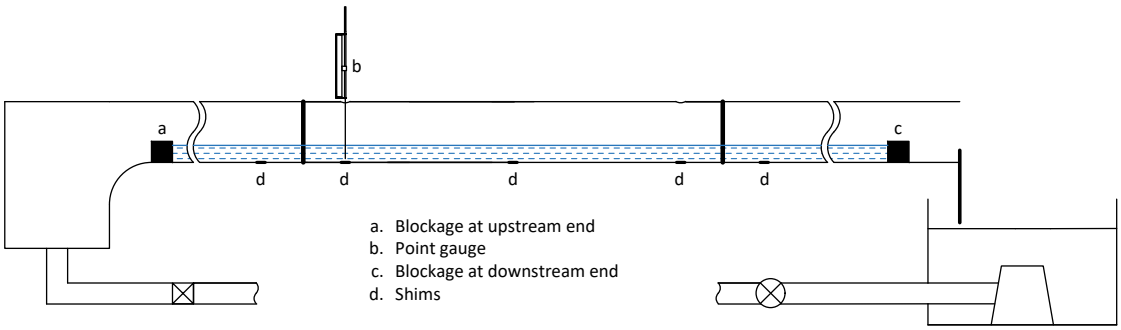

Figure 3.3 Pipe slope adjustment with shims.

A pump was used to recirculate water from the outlet tank (with dimensions 253 $\times$ 181 $\times$ 104 cm, see Fig. 3.5a) to the inlet tank (with dimensions 95.3 $\times$ 81.1 $\times$ 71 cm, see Fig. 3.5b) and then into the pipe. Control of the discharge from the pump was achieved with an adjustable butterfly valve (a Fisher type 8580 valve with a type 2052 actuator) (see Fig. 3.5c) upstream of the inlet tank. The magnitude of the discharge was determined using an electromagnetic flow meter (Arkon MAG 910) (see Fig. 3.5d). The depth of the flow was controlled by an adjustable gate at the downstream end of the pipe to ensure uniform flow conditions throughout (see Fig. 3.5a), verified via point gauge. As is shown in Fig. 3.6a, the end gate was adjusted to 6 different height and the depth of water was measured at 9 different

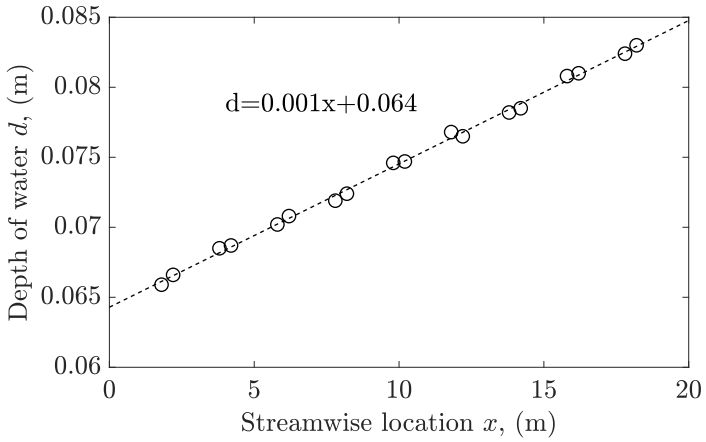

Figure 3.4 Sealed end measured water depth versus streamwise location.

streamwise positions. Linear regression lines are fit to these measurement and the gradient of the regression line is plot against end gate height in Fig. 3.6b. When the end gate height is too high, the water depth would be higher in downstream and vice versa. The end gate height to obtain the uniform condition is the one give the water depth gradient closest to 0. The ruler attached to the end gate is accurate to 1 millimetre. The end gate was adjusted separately for each flow/water depth condition. As shown in Fig. 3.5a, a sieve was placed over the outlet tank to remove any potential large debris in the flow. Temperature was measured before and after each test using a digital thermometer accurate to $\pm$ 0.5 °C, placed 0.5 m upstream of the wave probe measurement area. The regular temperature measurements ensured stable thermal conditions and therefore constant viscosity and surface tension.

3.2 Point gauge

The measurement of water depth was frequently needed for this study. A point gauge (see Fig. 3.7) is an accurate and straightforward method for water depth measurement, and is accurate to 0.1 mm. A point gauge was mounted to a sliding frame above the lateral center of the pipe, and water depth was measured at seven stream-wise locations with an average spacing of 1.14 m both before and after the measurement area. At the start of the depth measurement, the datum of the gauge was zeroed when the tip of the gauge was touching the bottom of the pipe. It was then lifted until its tip was observed to be in contract with the water surface approximately half of the time (to account for surface waves). A depth reading was thus taken from the vertical movement on a Vernier scale.

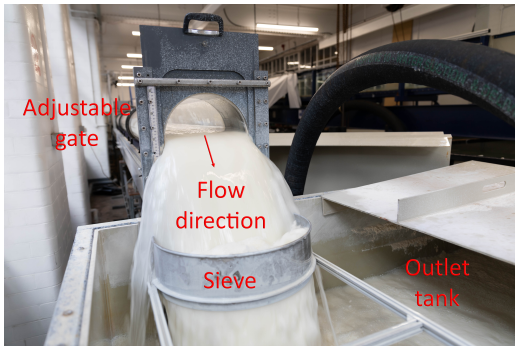

(a)

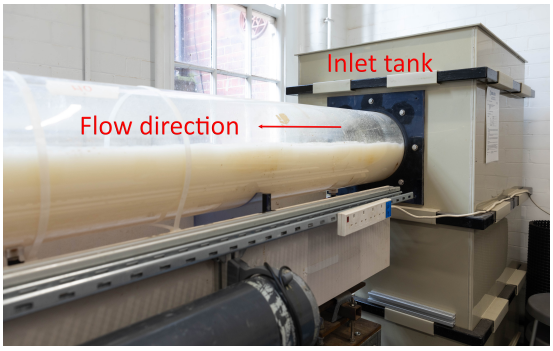

(b)

(c)

(d)

Figure 3.5 Photography of the pipe rig elements (a) outlet adjustable end gate and outlet tank, (b) inlet tank, (c) butterfly valve and (d) flow meter.

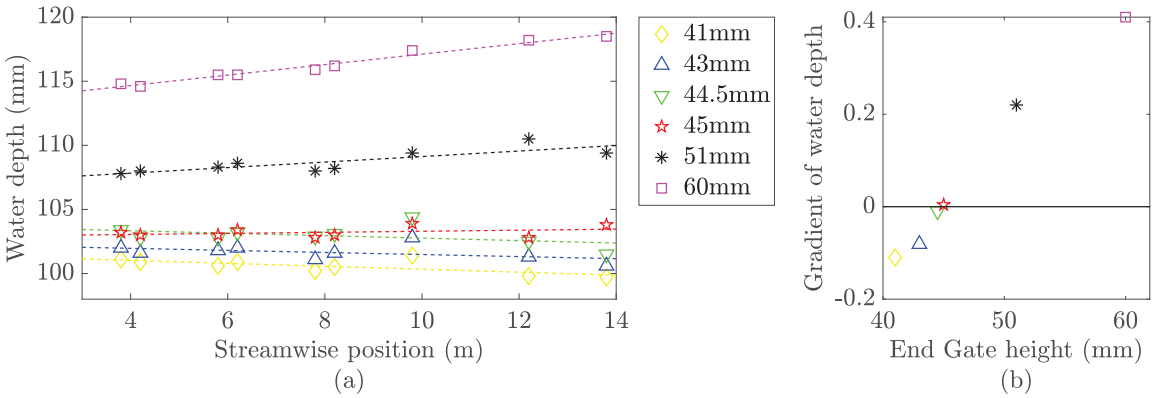

Figure 3.6 End gate adjustment for flow condition 5 (a) water depth versus streamwsie positions for different end gate height and (b) Gradient of water depth versus end gate height.

Figure 3.7 Photography of the point gauge.

3.3 Wave probes

A wave probe is an intrusive electric device that consists of two thin wires, capable of measuring 1D surface fluctuations over time. An electric current is generated, and the resulting voltage between these wires is proportional to the water level. The operation of a wave probe is based on the principle of capacitance. When an electric current is passed through the wires, an electric field is established between them. As water waves pass over the wires, the capacitance of the system changes due to the varying distance between the wires and the water surface. The change in capacitance results in a voltage difference between the wires, which is proportional to the water level. By measuring this voltage over time, the wave probe can provide information about the surface fluctuations of the water waves. Wave probes are typically calibrated before deployment to ensure accurate measurements. The calibration process involves relating the voltage output of the probe to the actual water level. This calibration allows for the conversion of voltage readings into meaningful units, such as millimeters, for quantifying wave characteristics accurately. Overall, wave probes provide a convenient and reliable method for monitoring surface fluctuations of water waves, enabling researchers and engineers to study and analyze wave behavior in different water surface fluctuations.

3.3.1 Wave probes array positions

There were 7 wave probes placed in the centre of the flume, with two wires in each pair separated 10 mm apart in the lateral direction (see Fig. 3.8). The distances between each pair were set to be non-uniform (see Fig. 3.9 and 3.10), which results in more possible distance combinations when correlating two pairs of probes, and thus higher resolution spatial correlation data. To minimize potential interference between adjacent probes, the shortest separation of 20 mm (between wave probes 6 and 7) was placed at the downstream end of the array. This configuration was chosen because the wake generated by upstream probes can potentially affect the measurements of downstream probes, leading to potential interference. All 22 possible wave probe pairs and their separations are summarised in Table 3.1. The separations range from the self paired probes at 0 mm to the furthest paired probes at 500 mm (between wave probes 1 and 7).

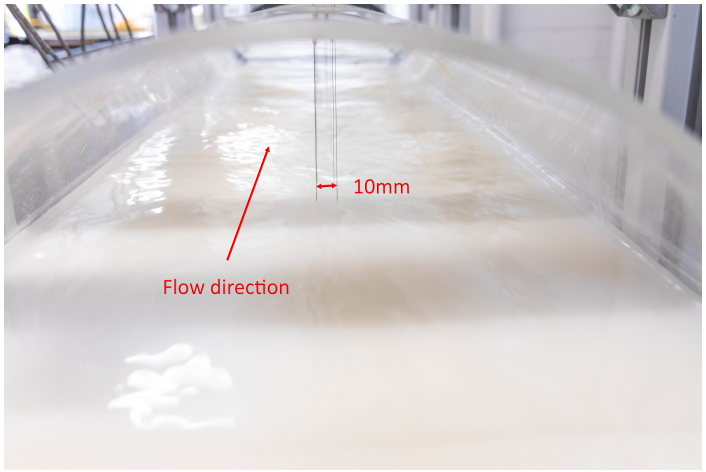

Figure 3.8 Photograph of wave probes showing the distance between two wires.

The probe wires were glued to the pipe bottom using acrylic blockages, as illustrated in Fig. 3.11. The wires were inserted through the acrylic blockages and wound around them. Subsequently, the acrylic blockages were glued and sealed to the bottom of the pipe. Throughout the experiment, no water leakage was observed. They were tensioned by adjustable guitar pegs and connected to a standard wave probe control module (see Fig. 3.12) provided by Churchill Controls. External RC filters were connected between wave probe BNC cable and control module to eliminate aliasing of high frequency noise. The filter was a low pass symmetrical unbalanced 'T' network, with the Z1 (transmission line impedance) component comprising two 16 kω (series) resistors, and the Z2 component (shunt line impedance) being a 33 nF capacitor. The details of this filter can be found in Nichols (2014). The electric signals generated by the wave probe module were digitised and stored using a

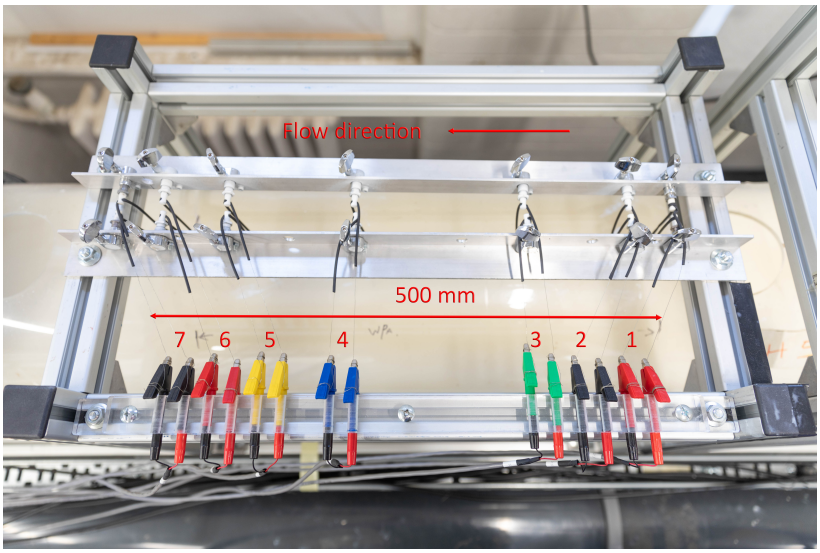

Figure 3.9 Photograph of wave probes showing the streamwise positions.

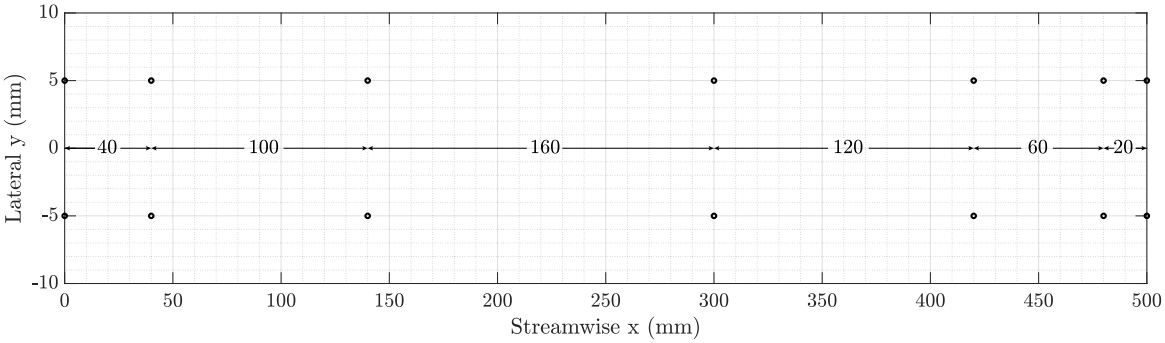

Figure 3.10 Arrangement of wave probe arrays. Flow direction is from left to right.

Table 3.1 Wave probe pairs and spatial lags. The first column is the number of possible wave probe pairs. The second column shows the pairing of two wave probes, with the first digit representing the index of the first probe and the second digit representing the index of the second probe. The third column displays the separation between the two wave probes in the second column, measured in millimeters.

No. of pairs	**Probe pairs**	**Lag (mm)**
1	11	0
2	67	20
3	12	40
4	56	60
5	57	80
6	23	100
7	45	120
8	13	140
9	34	160
10	46	180
11	47	200
12	24	260
13	35	280
14	14	300
15	36	340
16	37	360
17	25	380
18	15	420
19	26	440
20	27	460
21	16	480
22	17	500

National Instrument (NI6211 with 16 bits resolution), which is part of the DIC system. As is shown in Fig. 3.13, the box is able to record analog signals up to 8 channels. For this study, channel A0 to A6 were used for wave probe 1 to 7.

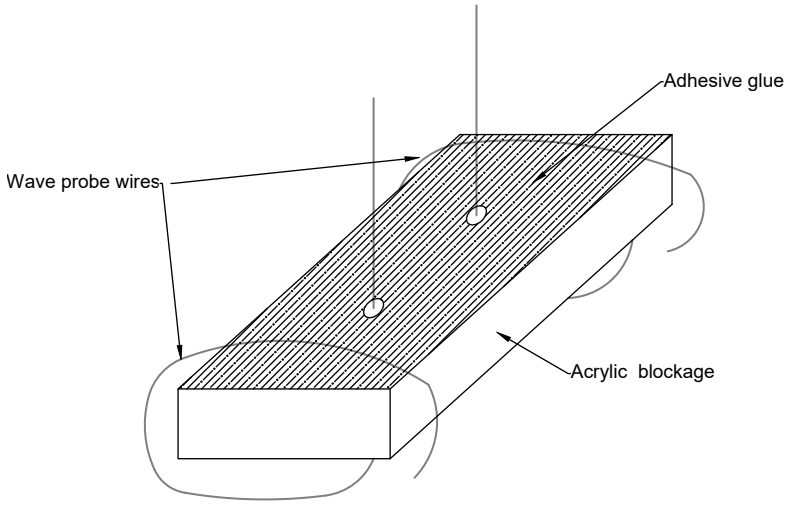

Figure 3.11 Sketch depicting the attachment of wave probes at the bottom of the pipe.

Figure 3.12 Photography of front pannel of wave monitor modules.

3.3.2 Wave probes calibration

The wave probes were cleaned regularly to maintain their performance and accuracy in measuring water surface elevation for all flow conditions. In addition, a calibration process was carried out to establish the relationship between the voltage output of each wave probe

Figure 3.13 Photography of front pannel of Dantec timing box, including a DAQ timing and analog data recording board.

and the corresponding water depth. To calibrate the wave probes, the water depth measured using a point gauge was plotted against the mean output of each wave probe, denoted as M (depicted as markers in Fig.3.14). Through this empirical analysis, linear regression lines were derived (represented by dashed lines in Fig.3.14), allowing for the conversion of the recorded instantaneous voltage on a specific probe into the corresponding instantaneous water fluctuation. The calibration procedure was performed at all 14 different flow conditions to ensure accurate measurements across a range of water depths. By conducting calibration for each wave probe separately, any variations or differences in their performance characteristics could be accounted for and accounted during the data analysis process. The calibration process played a crucial role in obtaining reliable and precise measurements of water surface fluctuations using the wave probes. It allowed for the conversion of voltage readings into meaningful units of water depth or elevation, enabling accurate quantification and analysis of wave characteristics under different flow conditions.

3.4 Digital Image Correlation

Digital Image Correlation (DIC) is an optical measurement method and has been used for two- or three-dimensional displacement measurement in a wide field of applications in experimental mechanics, such as fracture mechanics, high-speed deformation measurements and surfaces with restricted access (Pan et al., 2009, Reu and Miller, 2008, Wang et al., 2015). It is able to observe different deformation phenomena. The image correlation technique

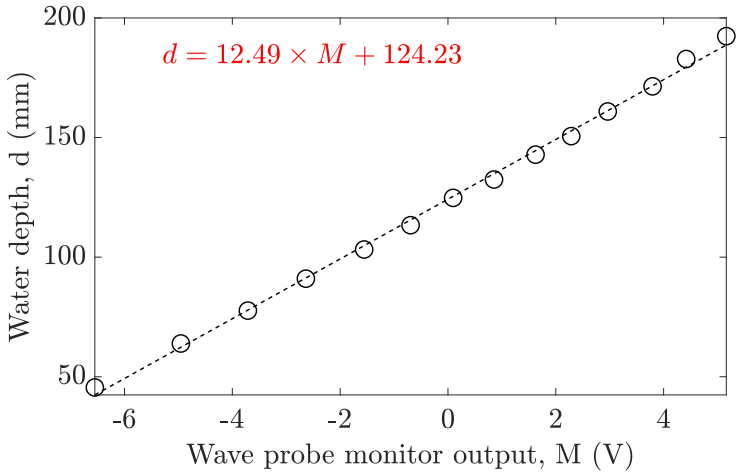

Figure 3.14 Example of wave probe calibration.

based on the Q400 measuring system developed by Dantec Dynamics has been proven to be a useful tool for deformation analysis. This system has been implemented in many studies for solid material deformation measurement (Mrówka et al., 2021, Gschwandl et al., 2019, Techens et al., 2020, Yan et al., 2019). In this study, it was used to measure fluid surface deformation.

3.4.1 DIC hardware setup

The DIC system, being a non-intrusive technique, was positioned upstream of the wave probe array to avoid potential interference from the joint of two pipe sections (refer to Fig. 3.15). They were both placed in the same pipe section. As is shown in Fig. 3.15, a high-definition (HD) projector (NEC109 M403H with 1080p native resolution) was placed above the pipe, projecting a 5 megapixel speckle pattern onto the water surface. This speckle pattern consisted of a random distribution of black and white dots or marks (as depicted in Fig. 3.16), which created a unique and identifiable pattern for tracking and analyzing the deformation or motion of the water surface. Two high-speed CMOS cameras (Mikrotron EOSENSE 4CXP, 4 megapixels in resolution, 2336 x 1728 pixels at 563 fps frame rate, 8-bit, black-and-white) were placed just below the projector with a separation between them, resulting in an angular displacement of approximately 40 degrees. The HD projector remained fixed in the same position throughout all the tests and was focused on the water surface for each flow condition. The cameras were mounted on a round bar, allowing for adjustment of the distance and angle between them. The round bar was attached to vertical struts, enabling vertical adjustment of the cameras. The apertures of both cameras were

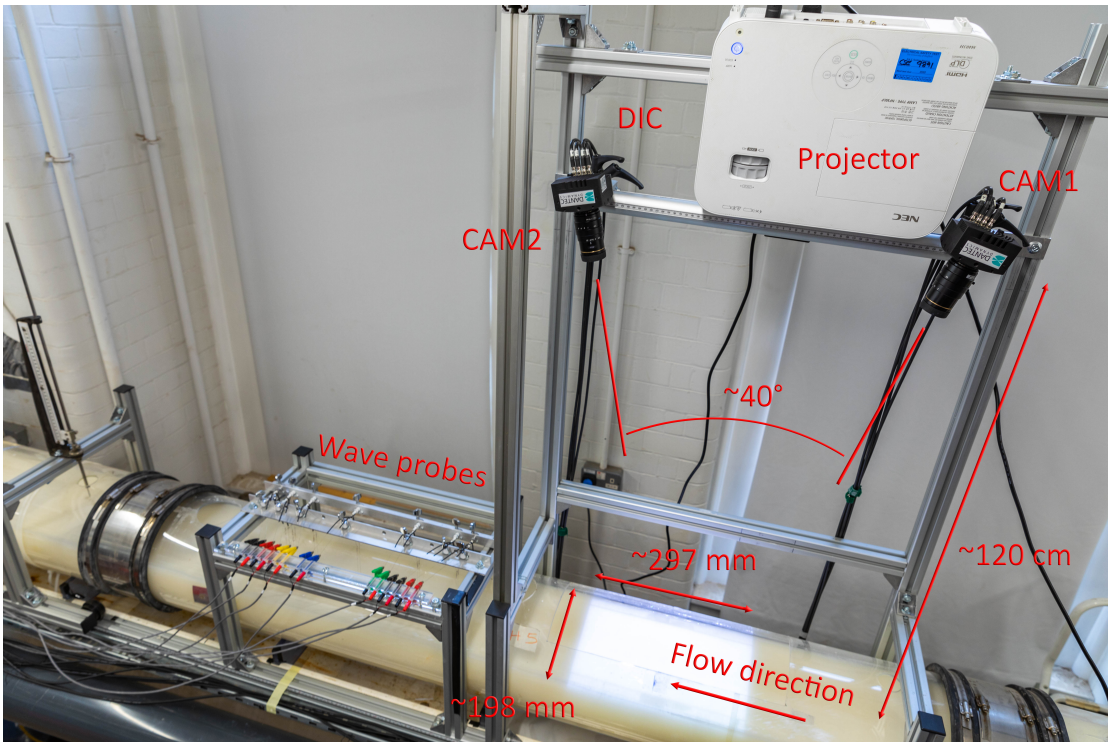

Figure 3.15 Photograph of DIC and wave probes setup.

consistently set to f/8, and they were independently focused on the same patch of the water surface.

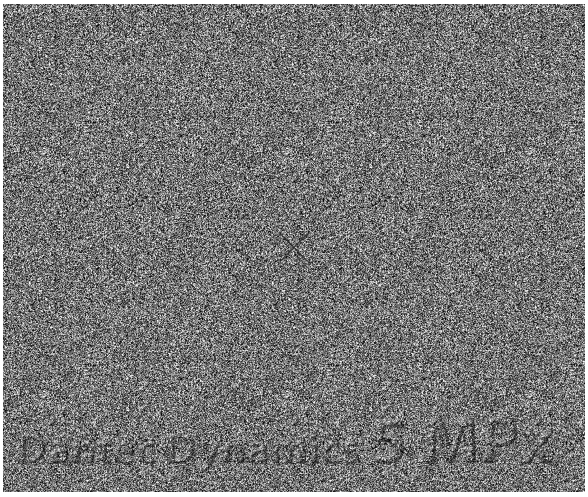

Figure 3.16 5-megapixel speckle pattern applied to the water surface for the DIC system. The pattern consists of a random distribution of black and white dots or marks, enabling the tracking and analysis of water surface deformation or motion.

To compare the water surface fluctuation that was measured by wave probes and DIC simultaneously, a Dantec timing box (see Fig. 3.13) was used. It is an interface between the control computer and the sensors. It consists of a DAQ timing and analog data recording board. The timing functions can be used to synchronize multiple sensors and ensure that the DIC images are recorded at the same time. The sampling frequency of the DIC cameras is set to 120 Hz in order to synchronize with the HD projector pulse with 60 Hz. The overlapping field of view of the two cameras covered an area of water surface of approximately 297 mm in streamwise and 198 mm in lateral.

3.4.2 DIC calibration

The system calibration is an important step performed prior to any measurement. Since different flow conditions can have varying flow depths, which affect the distance from the water surface to the cameras, camera calibration was conducted for each new flow condition. For calibration, a Dantec Dynamics calibration target (AI-11–BMB-9×9) was utilized, as shown in Fig. 3.17. This target consists of a patterned board with a regular grid of black and white squares, specifically designed for camera calibration in DIC systems. The calibration target was positioned within the pipe measurement area. In the Istra4D software, the appropriate calibration target type was selected, and the new calibration setup was initiated. The calibration target was systematically moved across the measurement area, covering different sides, orientations, and positions. To enable a 3D calibration, 10 images of the target were captured in various positions and angles. It was ensured that the calibration plate remained fixed in the same position (with the same streamwise, lateral, and vertical coordinates) for the first image of the calibration, as illustrated in Fig. 3.18. This approach provided a consistent datum and coordinate system for all flow conditions.

Appendix A provides a detailed presentation of the DIC calibration process using the Istra4D software. In Figure A.1, the calibration board is illustrated, with the center corresponding to the DIC coordinate system $(0,0,0)$. The red and green arrows represent the streamwise and lateral directions, respectively. This means that the center of the calibration board positioned as shown in Fig. 3.18 corresponds to $(0,0,0)$ in the DIC coordinate system for all flow conditions. The calibration parameters were saved after the cameras registered their positions. It is important to note that uncertainties in the calibration parameters can introduce measurement errors. If the calibration residuum value was not within the acceptable range (below 0.3) (DantecDynamics, 2018), the calibration process was repeated. By recording the calibration plate in various positions, the software automatically identifies the nodal points of the calibration plate (green markers in Fig.A.1) and calculates the intrinsic parameters (focal length, principal point, and lens distortions) as well as the extrinsic param-

Figure 3.17 Photography of DIC calibration target Dantec Dynamics 11mm.

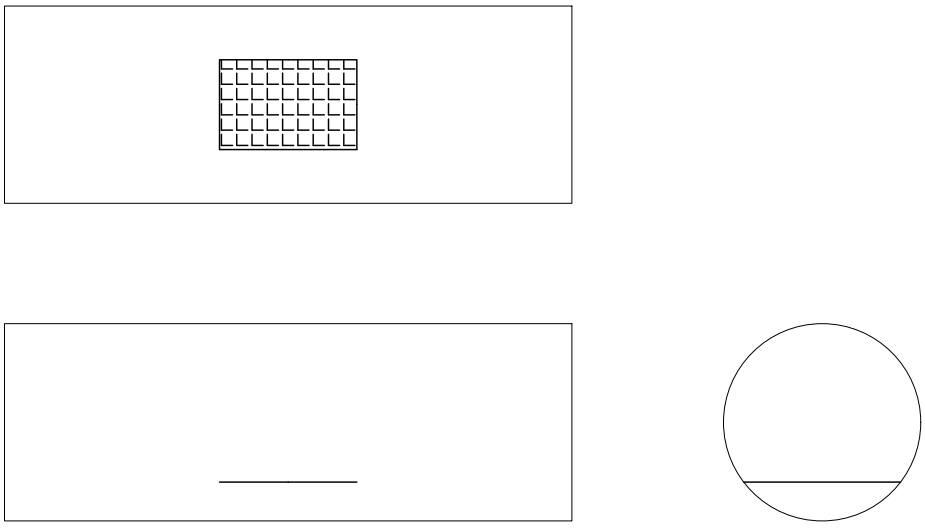

Figure 3.18 The position of the calibration board during the first calibration image, illustrating the DIC coordinate system. Top left - top view, bottom left - front view, bottom right - side view. The center of the calibration board corresponds to the origin $(0, 0, 0)$ in DIC coordinates.

eters (translation vector and rotation matrix). With these known parameters for each camera and the orientations of the cameras relative to each other, the positions of each facet of an object can be accurately calculated.

3.4.3 DIC software

The Istra4D software was used to calibrate cameras, capture images, evaluate images and visualize images. After the calibration procedure, a series of images were captured by these calibrated cameras. The upper limit of measurement time was controleld by the size of RAM and size of solid-state drive/ hard disk drivers (SSD/ HDD), and depends on the frame rate and the image resolution. In this study, the PC had 128GB RAM size and 1TB SSD/HDD, and was capable of a measurement of 66 s DIC in synchronised with 7 wave probes. After the measurement, the evaluation was performed in the Istra4D software. The area of interest was first defined as is depicted in Fig. 3.19 with a blue polygon and a cross marker inside. The images were processed and divided into multiple facets, as illustrated in Fig. 3.20, using a facet size of 25 pixels. This facet size corresponds to an approximate spatial resolution of 2 mm in this study, with a grid spacing of 17 pixels. The correlation algorithm can determine the shift, rotation and distortion of these facet elements (Martin and Miroslav, 2021). This correlation algorithm was performed for each individual facet in the measured surface. With the known intrinsic and extrinsic parameters obtained from the calibration, the 3D displacement of each facet of the water surface can thus be determined.

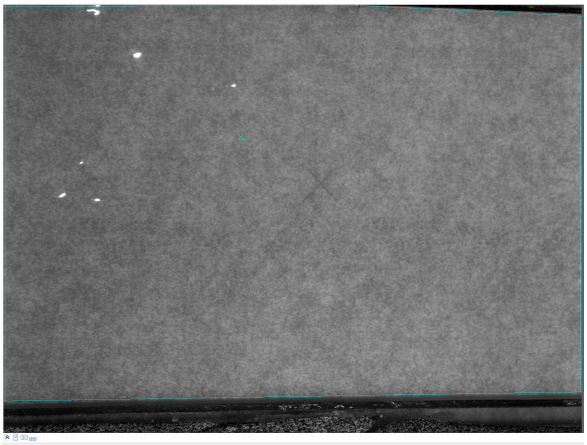

Figure 3.19 Define the area of interest in DIC evaluation.

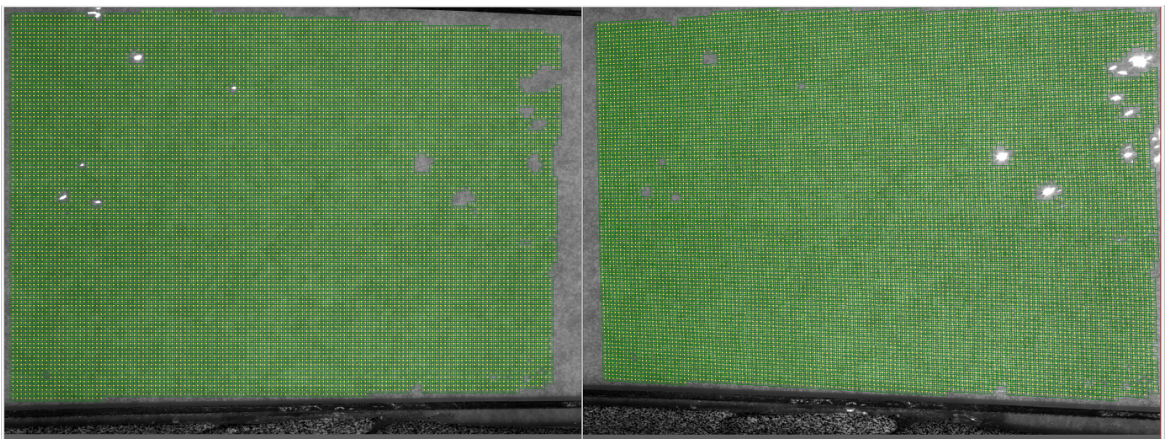

Figure 3.20 Mesh the recorded images into several facets, with more than 90% detectable area and less than 10% grey non detectable area.

3.5 Acoustic Doppler Velocimetry

The Acoustic Doppler Velocimeter (ADV) is a widely used instrument in field and laboratory studies for measuring instantaneous velocity components with reliability and robustness (Cea et al., 2007, Clark and Kehler, 2011, Novo and Kyozuka, 2019). It is capable of measuring all three velocity components (streamwise, lateral, and vertical velocities) at a single spatial point, referred to as 1D 3C (one dimension in space and three dimensions of velocity components) in this study.

The ADV operates based on the principle of Doppler shift, utilizing sound waves to measure the velocity of particles within a fluid. The ADV probe head consists of one transmitter and multiple receivers. The transmitter emits short pulses of acoustic waves into the fluid, which propagate through the medium and interact with the suspended particles. When the sound waves encounter moving particles, such as water droplets or sediment grains, the motion of these particles causes a change in the frequency of the sound waves, known as the Doppler shift. The ADV detects this frequency difference between the transmitted and received signals at the receivers, allowing for the determination of particle velocity along the acoustic beam.

In this study, the ADV probe head consists of one transmitter and four receivers. The measurement volume of the ADV is depicted as a cylinder in Fig. 3.21, located 5 cm away from the transmitter. It has a vertical coverage of 7 mm and a diameter of 6 mm. In this study, two types of ADV developed by Nortek were utilized: a side-looking ADV and a downward-looking ADV. Both ADVs were positioned at the lateral center of the measurement area and moved vertically up and down to capture velocity profiles at different depths. For each ADV measurement, a minimum of 8 depth-wise positions were sampled. The side-looking ADV

is specifically designed for near free-surface measurements, allowing for accurate velocity measurements in the vicinity of the water surface. On the other hand, the downward-looking ADV is focused on near-bed measurements, providing detailed velocity information close to the bed surface. By employing both ADVs, comprehensive velocity profiles were obtained throughout the water column. To ensure the reliability and validate the performance of the ADVs, there were overlapping regions where measurements were captured by both ADVs. These overlapping regions allowed for a direct comparison of the velocity data obtained from the side-looking ADV and the downward-looking ADV, enabling the assessment of consistency and agreement between the two instruments. To ensure accurate depth-wise positioning, the side-looking ADV was attached to a modified point gauge with an accuracy of 0.1 mm, and the downward-looking ADV was attached to a linear stage gauge with an accuracy of 0.01 mm, as depicted in Fig.3.22. The depth-wise measurement positions for each flow condition are summarized in AppendixB, where cross markers represent discarded data points. The criteria for selecting good quality data are discussed in subsection 4.4.1.

In addition to providing velocity components, the ADV also offers two important parameters for assessing data quality: the signal-to-noise ratio (SNR) and the correlation (COR). The correlation value represents the similarity between the two pulse echoes being measured and ranges from 0 to 100%. Higher correlation values indicate a stronger similarity between the echoes, reflecting accurate phase shift measurements by the system. Typically, an SNR above 15 dB and a correlation above approximately 70% are considered indicative of good quality data (Nortek, 2021). These parameters were used to evaluate and ensure the reliability of the ADV measurements in this study.

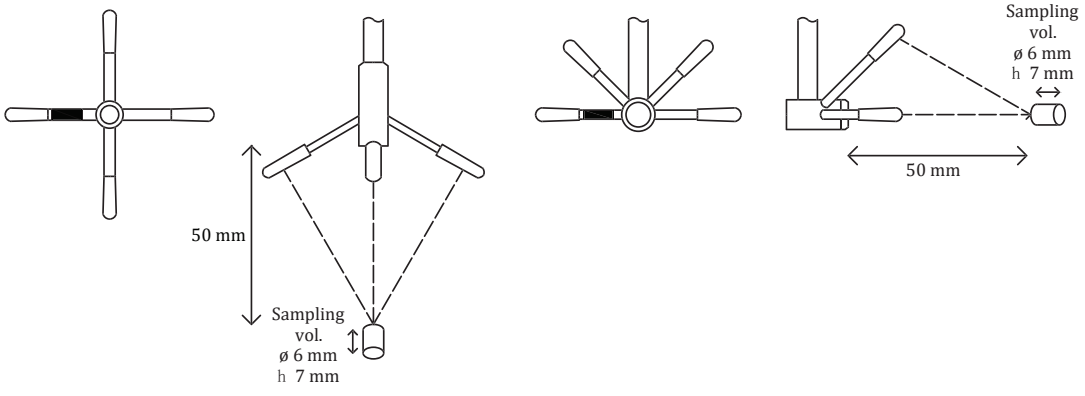

Figure 3.21 Sketch of (a) side-looking ADV and (b) downward-looking ADV showing the probe arrangement.

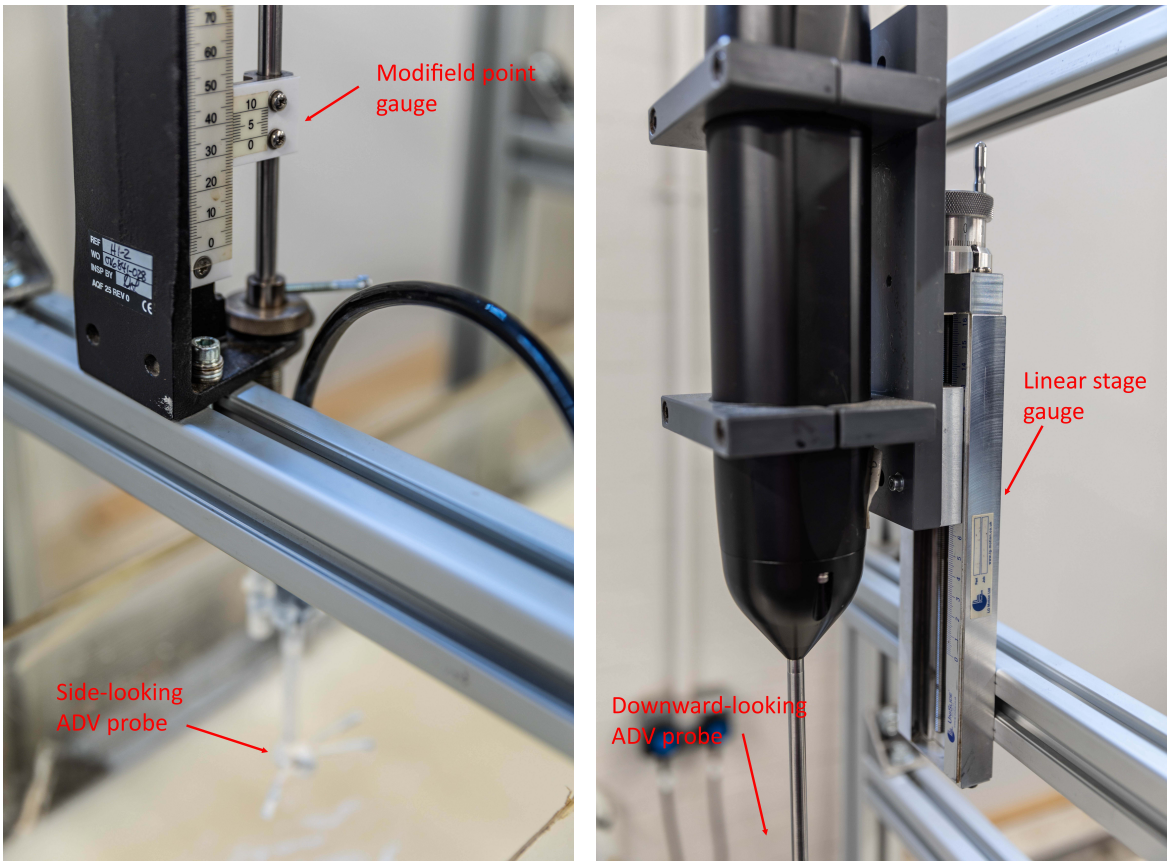

(a) (b)

Figure 3.22 Photography of attachment frame for ADV (a) side-looking ADV (b) downward-looking ADV.

3.6 Doppler radar sensor

The choice of carrier frequency is very important. Various carrier frequency bands ranging from milimeter band (40 - 100 GHz) to ultra high frequency (UHF)(0.3 - 1 GHz) have been tested for non-contact detection (Wang et al., 2015). Shorter wavelengths (higher frequencies) provide a greater sensitivity to small displacement. One of the widely used electromagnetic microwave sensors in industrial applications is the quadrature Frequency-Modulated Continuous-Wave (FMCW) Doppler radar. In this study, a 24 GHz (12.5 mm wavelength) quadrature Doppler radar sensor (DRS) from RFbeam has been used for non-contact measurement of free surface. The minimum antenna size is proportional to wavelength and inversely proportional to frequency. The 24 GHz K band radar compromise between antenna size and the measurement resolution, which is suitable for airborne water surface measurement.

3.6.1 Doppler radar architecture

The entire structure of the prototype radar system is shown in Fig. 3.23. The transceiver unit K-LC7 is shown in Fig. C.1, which is fabricated with one transmitter and two receivers. The operational transmitter frequency is centered at 24.125 GHz frequency, with frequency range 24 $\sim$ 24.25 GHz. The transceiver includes a voltage-controlled oscillator (VCO) pin that allows for the frequency modulation of the radar setup. The transceiver was powered by a 10 V power generator (5 V for each sensor) as is shown in Fig. C.2. An amplifier (see Fig. C.3) was connected to the transceiver so that the amplified Doppler signals could be properly observed. A data acquisition system by National Instruments (NI USB-6001) was used for data logging as shown in Fig. C.4. The data acquisition unit was connected to a laptop and the data acquired were then analysed in MATLAB.

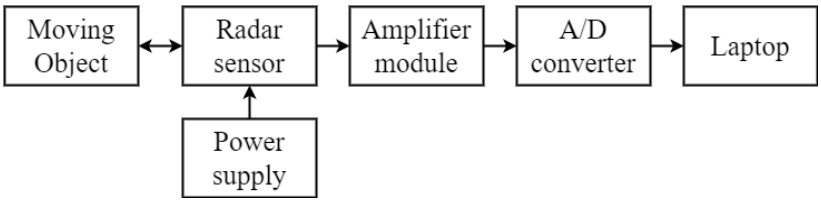

Figure 3.23 Schematic representation of the prototype radar system.

Fig. 3.24 shows a block diagram of the amplifier module. The filters are the same for the I/Q channels, and each consist of a cascade of two active band pass filters. Each active band pass filter is the cascade of a passive high pass filter and a passive low pass filter. The high pass filter is formed by resistor R1 ($3.9\times10^{3}\Omega$) and capacitor C1 (10×10^{-6} F) with the cutoff frequency f_{cH} of 4.1 Hz ($1/2\pi R_1 C_1$) and the low pass filter is formed by resistor

R2 ($150\times10^3\Omega$) and capacitor C2 (1×10^{-9}F) with the cutoff frequency f_{cL} of 1.1 kHz ($1/2\pi R_2C_2$). Together this forms a band pass filter between 4.1 Hz and 1.1 kHz. There is also approximately 64 dB of voltage gain. The gain value $20\log10(V_{out}/V_{in})$ is calculated by solving the following system of linear equations

$$V_{out1} = V_{in2}, \tag{3.1a}$$

$$\frac{V_{out1} - 2.5}{R_2} = \frac{2.5 - V_{in1}}{R_1}, \tag{3.1b}$$

$$\frac{V_{out2} - 2.5}{R_2} = \frac{2.5 - V_{in2}}{R_1}, \tag{3.1c}$$

where 2.5 means the 2.5 V DC input, V_{in1} and V_{out1} represent the input and output for the first stage band pass filter and V_{in2} and V_{out2} represent the input and output for the second stage band pass filter.

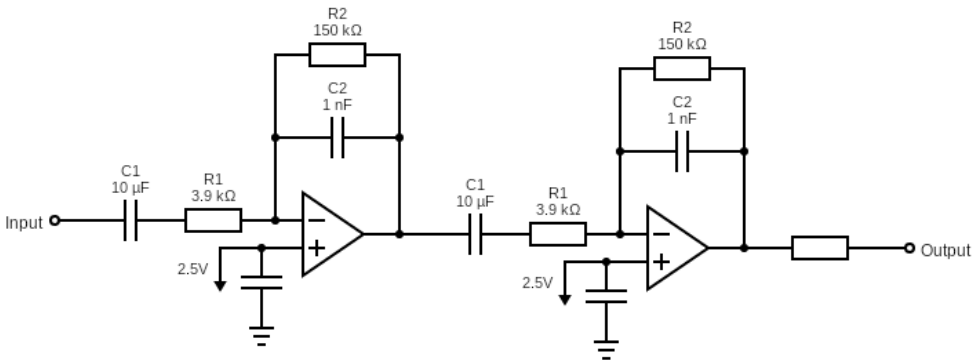

Figure 3.24 The circuit diagram of the amplifier board.

3.6.2 Doppler radar sensor setup

For radar sensing measurement in the partially filled pipe, a Doppler radar sensor was placed at in the lateral center and 425 mm above the bottom of the pipe as illustrated in Fig. 3.25. It was 585 mm upstream of wave probe 1, which was in the DIC measurement area.

3.7 Temperature and Concentration of TiO_2

The measurement of water temperature and the concentration of TiO2 serve important purposes in this study. Both of these parameters have the potential to influence water

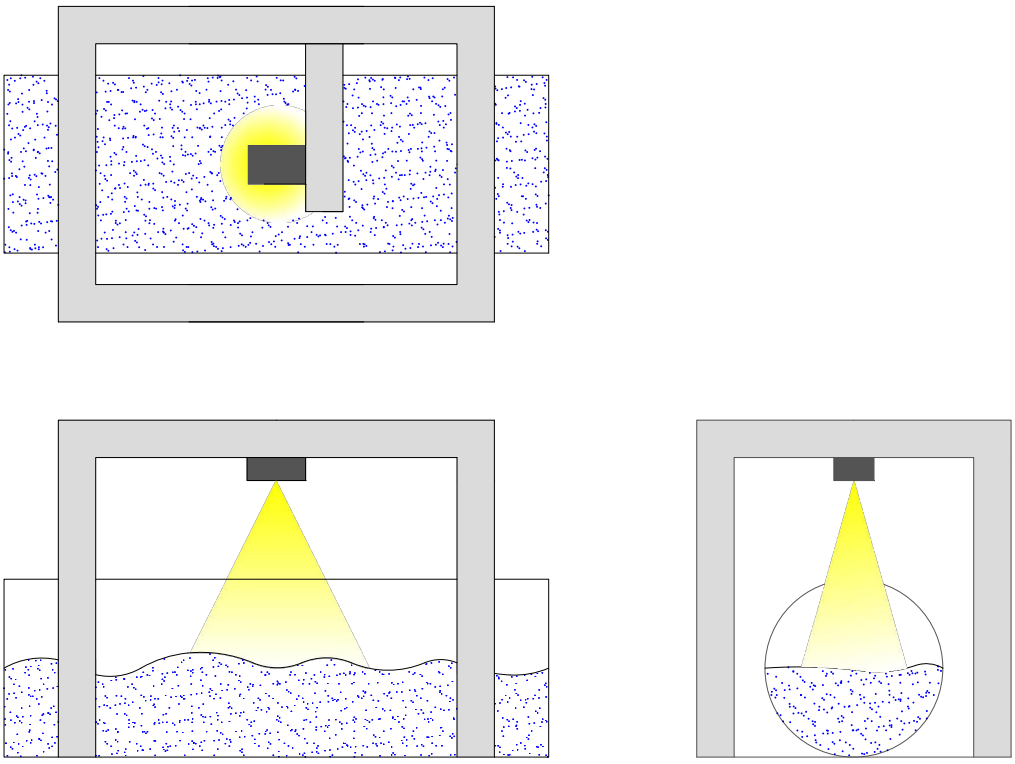

Figure 3.25 Sketch of DRS setup over the pipe: top left - top view, bottom left - front view, bottom right - side view.

properties such as density, viscosity, and conductivity. Additionally, the concentration of TiO2 can affect the transparency of the water, which in turn impacts the clarity of the DIC images obtained during the experiment. To ensure the accuracy and reliability of the experimental results, it is necessary to record the water temperature and the concentration of TiO_2 throughout the duration of the measurements. The water temperature, although difficult to maintain at a fixed value in a laboratory setting, was regularly monitored using a probe thermometer with an accuracy of 0.1°C. These measurements were conducted at intervals of approximately 30 minutes, allowing any potential variations caused by temperature changes to be monitored and taken into account during the data analysis. In addition to temperature, an appropriate concentration of TiO2 needed to be determined and maintained consistently throughout the experiment. The concentration of TiO2 plays a crucial role in controlling the water's optical properties, and it directly impacts the clarity and quality of the DIC images. By establishing and maintaining a specific TiO2 concentration for all experimental conditions, any variations or differences observed can be attributed to the specific flow conditions rather than changes in TiO2 concentration. By recording and monitoring the water temperature and the concentration of TiO_2, this study ensures that any potential effects caused by these factors are considered and accounted for in the analysis of the experimental data.

In this study, various measurements were performed to evaluate the influence of temperature variation on surface fluctuations and to identify the optimal concentration of TiO2 to be used. Pure water was gradually supplemented with a specific mass of TiO2, resulting in TiO2 concentrations ranging from 0% to 0.06%. To capture the water surface conditions at different TiO2 concentrations, snapshots were taken using DIC. These raw DIC images provide a visual representation of the clarity and contrast achieved with varying TiO_2 concentrations. The DIC setup is illustrated in Figure 3.15, and it involved the use of two cameras, namely the upstream camera (CAM1) and the downstream camera (CAM2). Figure 3.26 shows snapshots of the water surface captured by the upstream camera (CAM1) with different concentrations of TiO2. The position marked as 'X' in these snapshots corresponds to the position of the projected pattern shown in Fig. 3.16. In the pure water condition (Figure 3.26a), no marker is visible. However, as the concentration of TiO2 increases (Figures 3.26b and c), the marker becomes faintly visible and appears blurry. The contrast and clarity of the marker improve with higher concentrations of TiO_2 (Figures 3.26d, e, and f). To determine the appropriate concentration of TiO2 for this study, it was important to strike a balance between achieving good data quality and minimizing the impact on the surface dynamics. Previous studies (Nichols et al., 2020) have found that a minimum TiO2 concentration of 0.01% mass concentration is required for reliable time and space-averaged water depth measurements using Kinect infrared optical sensors. However, for accurate water surface fluctuations in

this study, a higher concentration of TiO2 was necessary. After careful consideration of the factors mentioned, a mass concentration of 0.06% TiO2, utilizing titanium dioxide from Fisher Scientific, was selected for this study. This concentration was chosen to maintain a close approximation to the pure water condition while still providing sufficient visibility of the projected pattern on the water surface. The goal was to simulate the properties of pure water as closely as possible. It is important to note that adding excessive amounts of TiO2 can potentially alter the water properties. Moreover, since pure water is transparent, DIC techniques cannot effectively analyze transparent surfaces. Therefore, an optimal concentration of TiO2 was determined, which represents the minimum amount necessary for DIC to function reliably. Figure 3.27 presents a snapshot of synchronized views from the two cameras (CAM1 and CAM2) using the selected 0.06% TiO2 concentration. Both camera views clearly depict the stochastic pattern, indicating good visibility of the speckle pattern. Some white spots at the edges of the images correspond to points of direct reflection of the projector lamp. It is worth mentioning that the TiO2 powder was mixed in the downstream tank and continuously recirculated using a pump. Regular agitation of the downstream tank was performed to prevent the deposition of TiO_2 powder. The effect of temperature and concentration of TiO_2 on the measurement of surface properties will be further evaluated and discussed in Section 4.6.

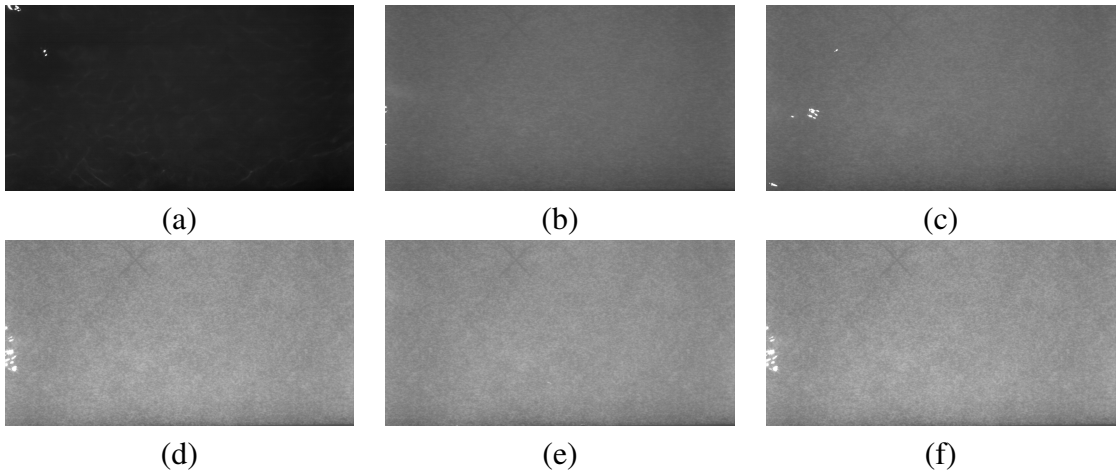

Figure 3.26 Snapshots of surface with different mass concentrations of TiO_2 (a) 0.000 %, (b) 0.006 % , (c) 0.012 %, (d) 0.018 %, (e) 0.030 % and (f) 0.040 %, dotted lines means power proportional to f^{-5}.

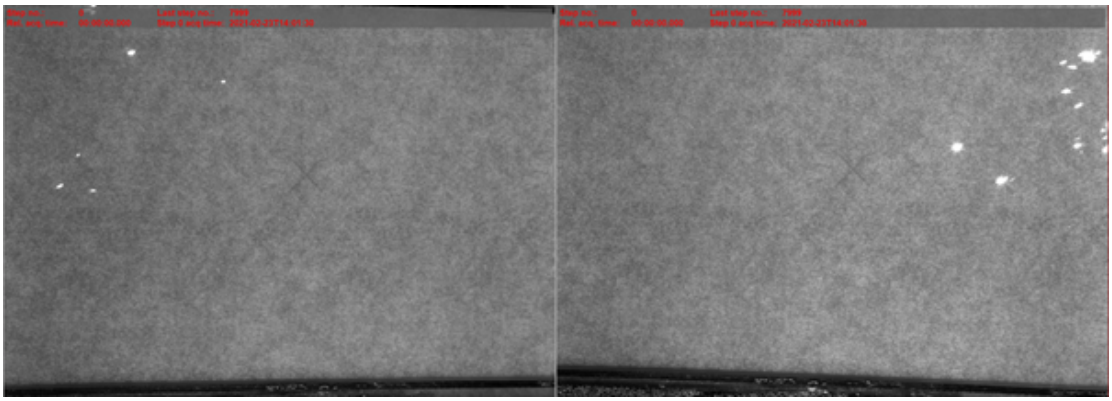

Figure 3.27 Synchronized views from two cameras showing a snapshot of the water surface for a specific time step. The views are captured simultaneously by the upstream camera (CAM1) and the downstream camera (CAM2).

3.8 Bulk flow conditions

The uniform flow conditions were examined in the order given in Table 3.2. The gradient of the pipe is fixed at 1/1000 with smooth roughness (Manning's roughness coefficient 0.0099 estimated in section 4.1). The flow conditions were designed to have a uniform flow rate increment (2 Ls^{-1}) in between and cover ranges of both flow depths below half the pipe diameter and over half the pipe diameter. The pump has the ability to generate flows up to $\sim 30\ \mathrm{Ls}^{-1}$ and therefore the maximum flow rate (flow condition 14) was set to 28 Ls^{-1} to ensure reliable uniform flow rate. For each flow condition, the desired flow rate was set by adjusting the inlet valve controlled by Labview. The downstream gate was carefully adjusted in order to give uniform flow depth at the desired flow rates. The corresponding uniform flow depth is the mean of the water depth measured by point gauge at the 7 streamwise locations with average spacing 1.14 m. 14 flow conditions were examined for this study, with water depth d ranging from 45.5 mm to 192.4 mm and flow rate Q ranging from 2 Ls^{-1} to 28 Ls^{-1}.

In Table 3.2, the following parameters were recorded directly from instruments: end gate height, h_g, from the end gate ruler, flow rate, Q, from the flow meter and the water depth, d, from the point gauge. The rest of the parameters were calculated from the directly measured parameters: mean velocity, U_b, from Equation 2.10, free surface width, L_w, from Equation 2.6, hydraulic radius, R_h, from Equation 2.4, Reynolds number, Re, from Equation 2.8, Froude number, Fr, from Equation 2.11, friction factor, f, from Equation 2.12 and shear velocity, U_*, from Equation 2.14.

Table 3.2 Bulk flow conditions.

Flow condition	End Gate height	Flow rate	Depth	Relative depth	Mean velocity	Free surface width	Hydraulic radius	Reynolds number	Froude number	Friction factor	Shear velocity
(1)	(2)	(3)	(4)	(5)	(6)	(7)	(8)	(9)	(10)	(11)	(12)
	h_g	Q	d	d/D	U_b	L_w	R_h	Re	Fr	f	U_*
(-)	(mm)	(L/s)	(mm)	(%)	(ms^{-1})	(m)	(m)	$\times 10^4$	(-)	(-)	(ms^{-1})
1	24	2	45.5	15.7	0.30	0.21	0.028	0.84	0.543	0.024	0.017
2	30	4	63.9	22.0	0.37	0.24	0.038	1.41	0.558	0.022	0.019
3	35	6	77.7	26.8	0.42	0.26	0.045	1.89	0.572	0.020	0.021
4	40	8	91.0	31.4	0.45	0.27	0.051	2.31	0.561	0.020	0.022
5	45	10	103.2	35.6	0.47	0.28	0.057	2.69	0.550	0.020	0.024
6	48	12	113.4	39.1	0.50	0.28	0.061	3.05	0.551	0.019	0.024
7	51	14	124.8	43.0	0.52	0.29	0.066	3.36	0.534	0.019	0.025
8	55	16	132.5	45.7	0.54	0.29	0.068	3.70	0.545	0.018	0.026
9	59	18	142.9	49.3	0.56	0.29	0.072	3.97	0.531	0.018	0.027
10	62	20	151.3	51.9	0.57	0.290	0.074	4.27	0.533	0.017	0.027
11	65	22	160.9	55.5	0.59	0.288	0.077	4.50	0.517	0.018	0.028
12	70	24	171.4	59.1	0.59	0.285	0.080	4.70	0.499	0.018	0.028
13	74	26	181.8	63.0	0.60	0.280	0.083	4.87	0.478	0.018	0.028
14	78	28	192.4	66.3	0.60	0.274	0.084	5.05	0.466	0.018	0.029

3.9 Experimental protocol

The gradient of the pipe was fixed to 1/1000 as described in section 3.1. The water was tinted with 0.06 % TiO_2 and treated with 135 ml Rodolite H every two weeks to disinfect water. The measurement procedure was the same for all 14 flow conditions. The flow was established by adjusting the valve controlled by Labview. There was a proportional-integral-derivative (PID) feedback system used to adjust the valve to maintain the desired flow rate, by comparing the actual flow rate from the flow meter and the applied input flow rate. All measurements were taken at least an hour after the required uniform flow was achieved to ensure the steady state of the flow.

Firstly, the water depth was measured by point gauge and the flow rate was read from Labview based on the flow meter. Secondly, synchronised DIC and wave probe data were recorded for a duration of 66 s 5 times at the sampling frequency of 120 Hz. The choice of 66 s measurement duration was limited by the PC capacity as mentioned in subsection 3.4.3. Thirdly, a long continuous 300 s wave probes data recording was made. After that, Doppler radar sensor was installed in the DIC measurement area and a measurement of 300 s was taken with 3 repeats. Following this, the ADV was installed inside the pipe for sub-surface velocity measurement. The ADV was fixed in the same streamwise position (9.1 m downstream to the inlet tank as indicated in Fig. 3.2d) and moved to different depth-wise positions with approximate 10 mm depth increment in between. A 300 s ADV recording was made for each depth-wise position. Additionally, the temperature of the fluid was measured regularly by a probe thermometer during the experiment. It was found that the change of temperature was generally less than 5% over the measurement period of each flow condition.

The measurement duration was 300 s because this was the time required for the standard deviation of the surface fluctuation signals to comfortably settle to within $\pm$ 1 %. Figure 3.28 shows the standard deviation of water surface fluctuations measured by the wave probe in time series with an increase in measurement time duration in relative to the standard deviation of 300 s recording duration. Data shown in Fig. 3.28 is for wave probe 1 and for 4 flow conditions (flow condition 1, 5, 9 and 13) representative of all hydraulic flow conditions examined in this study. The y-axis is normalised cumulative standard deviation, calculated by

$$\frac{\mathrm{std}(\eta(\tau))}{\mathrm{std}(\eta(T))} \times 100, \tag{3.2}$$

where $\mathrm{std}(\eta(\tau))$ is the standard deviation of surface fluctuation over a time period of τ, $\mathrm{std}(\eta(T))$ is the standard deviation of surface fluctuation over a time period of T, τ is in

the range of 0-300 s and T is 300 s. Similar settling times were observed in the standard deviation of the ADV velocity data and Doppler radar sensor channel output.

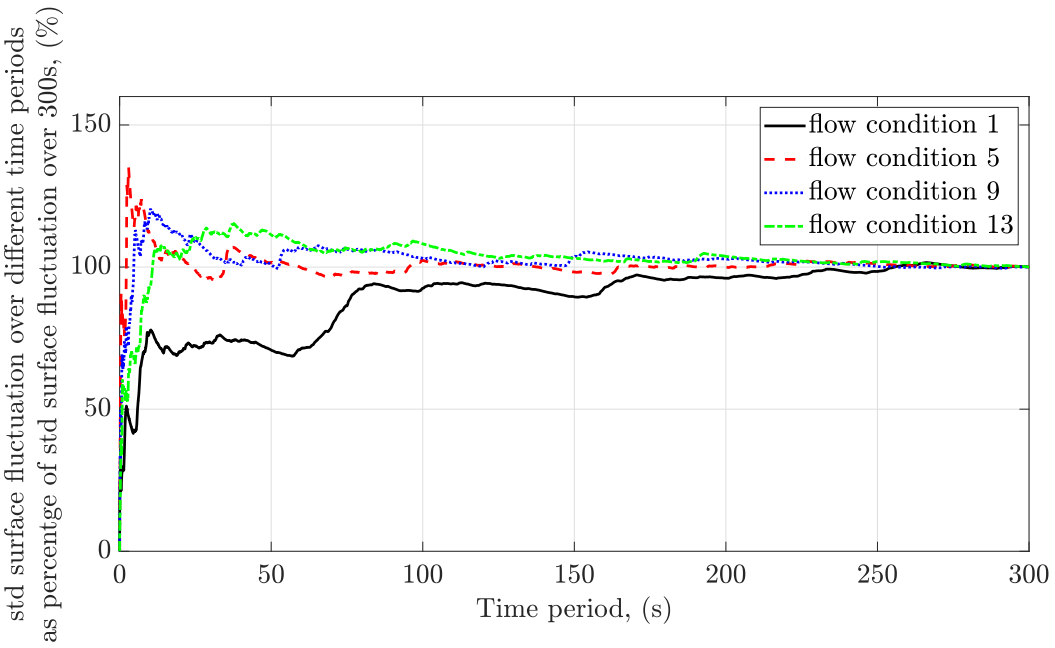

Figure 3.28 Settling time of std of surface fluctuation for increasing recording time duration measured by wave probe no. 1.

3.10 Experimental setup conclusions

An extensive experimental setup has been carefully designed and constructed to allow detailed and accurate measurement of multiple properties of partially filled pipe flows. A 20 m long, 290 mm internal diameter smooth pipe fixed at 1/1000 gradient was employed for this study as described in subsection 3.1. A range of flow conditions mentioned in subsection 3.8 were selected in order to generate a range of turbulent flow fields giving rise to a range of free surface patterns. These flow conditions were chosen in order to study both less than half and more than half filled pipe flows and do not exceed the pump's maximum ability. The instruments employed and their usage are illustrated in Fig. 3.29 and summarized in Table 3.3. Surface properties were assessed using a synchronized DIC/wave probe system, floating tracers, a point gauge, and a Doppler radar sensor. The wave probe system primarily targeted lateral center surface fluctuations over an extended streamwise distance, while DIC focused on surface fluctuations across a two-dimensional area with a shorter streamwise distance. To measure sub-surface properties, three instruments were utilized: a side-looking ADV, a down-looking ADV, and a flow meter. The side-looking ADV primarily focused

on near-surface measurements, while the down-looking ADV emphasized near pipe bottom measurements. This differentiation in focus was due to the geometry limitations of the ADVs and the principle of a 5 cm measurement volume at a distance. The point gauge and ADVs were equipped with sliding frames designed to fit along the pipe and enable vertical movement. Wave probes were inserted through the pipe and tensioned using a newly designed guitar peg system. The DIC system and DRS were mounted on a frame positioned above the pipe, allowing for vertical adjustments. The sequence of the experiment is illustrated in Fig. 3.30. The flow chart depicts the order in which equipment was used, identifies the equipment used simultaneously, indicates the measurement duration for each equipment, and highlights the number of times the experiment was repeated. The sampling frequency, measurement duration and number of repeats of measurements are summarized in Table 3.4. The choice of sampling frequencies, 100 Hz and 120 Hz, in this study can be justified by several reasons. Firstly, the dominant free surface features and fluctuations of interest are typically below 10 Hz (Nichols, 2014). Therefore, a sampling frequency of 100 Hz is considered sufficient to capture the relevant dynamics accurately. Previous studies on free surface dynamics have also successfully utilized a sampling frequency of 100 Hz (Nichols, 2014), demonstrating its effectiveness in capturing the key characteristics and variations of the free surface. In addition, Romanova (2013) used a sampling rate of 22.1 kHz and downsampled it to 20 Hz for studying turbulence surface dynamics in a partially filled pipe. This suggests that lower sampling frequencies can still provide valuable insights into surface dynamics. Furthermore, the sampling frequency of 120 Hz was specifically chosen for the Digital Image Correlation (DIC) technique in this study. This frequency allows for the alignment of the cameras' shuttle with the projector frequency, ensuring synchronization and accurate measurement of the surface fluctuations. Overall, the selected sampling frequencies were carefully considered to capture the relevant dynamics of the free surface, align with previous studies, and enable accurate measurement techniques. The unique experimental setup described in this chapter will allow the study of hydrodynamics in a partially filled pipe and the radar sensing of the free water surface.

Table 3.3 Summary of instrument and type of measurement.

Instrument	Type of measurement and limitation
Flow meter	Instantaneous flow rate.
Point gauge	Water depth of different streamwise locations. It provides straightforward readings, but it needs to be manually moved to different streamwise locations for each reading.
Wave probes	Instantaneous surface fluctuations at multiple streamwise locations. Seven wave probes were deployed, spanning a streamwise distance of 500 mm at the lateral center. Wave probes solely capture measurements of lateral center surface fluctuations in this study.
DIC	Instantaneous surface fluctuations for a specific area, approximately 297 mm by 198 mm in this study. It enables the acquisition of 2D surface data, but with a shorter streamwise span compared to the wave probes."
DRS	Instantaneous radar signal response with respect to water surface fluctuations. It captures the response from a patch of dynamic water, but directly recovering the actual surface fluctuation is challenging. Additional signal processing is required to extract meaningful information.
ADV	Instantaneous 1D 3C velocity fluctuations at different positions along the depth. However, in this study, only 1D data at the lateral center can be obtained. It is not possible to obtain a planar or volumetric velocity field.
Floating tracers	Mean surface velocity. Ensuring that the tracers float precisely over the lateral center can be challenging. However, repeating the measurement 10 times helps reduce uncertainty and improve accuracy.
Probe thermometer	Fluid temperature. It provides one time reading but does not provide instantaneous temperature measurements.

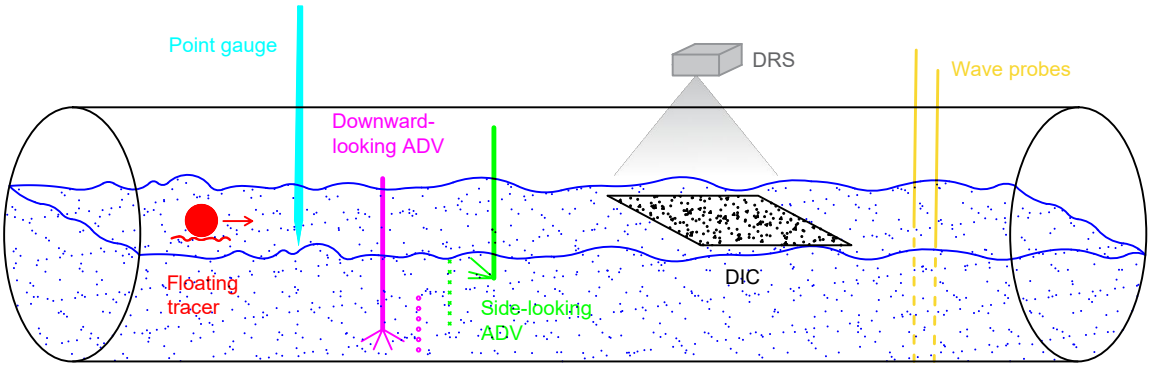

Figure 3.29 Sketch of instrument summary.

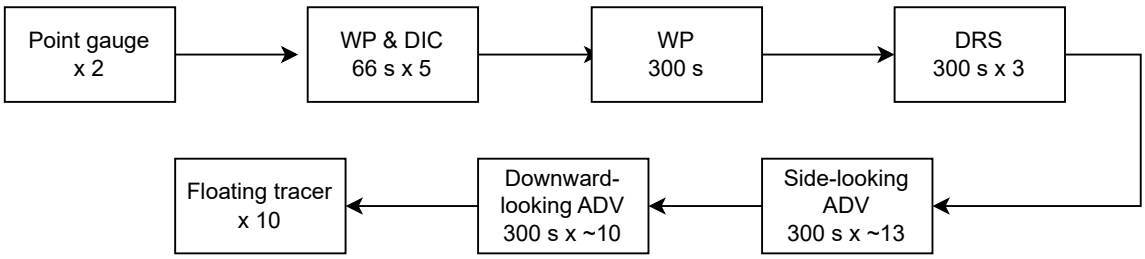

Figure 3.30 Flow chart of experiment sequence.

Table 3.4 Summary of instrument measurement sampling frequency, duration and number of repeats.

	Sampling frequency fs, (Hz)	**Measurement Duration** T, (s)	**Number of repeats,** (-)
Wave probes	120 100	66 300	5 1
DIC	120	66	5
ADV	100	300	1
DRS	100	300	3
Floating tracers	-	-	10

Chapter 4

Data pre-processing and validation

4.1 Uniform flow conditions

As the surface fluctuations measured by DIC and wave probes were at different locations, it is important to ensure the flow is uniform in the measurement area. The method of adjusting the end gate height to find the uniform flow is discussed in section 3.1. In theory, to achieve uniform flow for a certain flow rate, a specific end gate height is required. This end gate height ensures a uniform water depth and a consistent velocity profile along the streamwise direction. Figure 4.1a illustrates the validation of uniform flow conditions by comparing the dimensionless quantities U_b/U_bf and Q/Qf derived from experimental measurements with the theoretical graph proposed by Camp (1946) (as mentioned in subsection2.1.1). The experimental values show a good overlap with the theoretical graph, indicating uniform flow. Additionally, in Fig. 4.1b, the flow rates are plotted against $AR_h{}^{2/3}S_f{}^{1/2}$ from Manning's equation, with a best-fit line. The line represents a Manning's roughness value of 0.0099, which closely approximates the roughness value of perspex (Capart et al., 1997, Tullis et al., 1990) (the material the pipe is made from). This further confirms the uniform flow conditions in the measurement area.

The dimensionless quantity analysis and the Manning's equation analysis have verified the uniform flow conditions in terms of water depth. A downward-looking ADV and a side-looking ADV were implemented to validate the uniform flow conditions in terms of velocity profile. ADVs were sampled at 100 Hz and recorded by the software Vectrino Plus for a 300 s measurement duration. The velocity profiles were measured at several depth-wise positions for the highest flow, flow condition 14. The depth-wise positions z/d and streamwise positions for the ADV measurement are indicated in Fig. 4.2. The highest flow was selected as this is the flow that needs the longest distance from the inlet before it reaches uniform conditions. Figure 4.2a shows the sub-surface velocity fluctuations measured by the

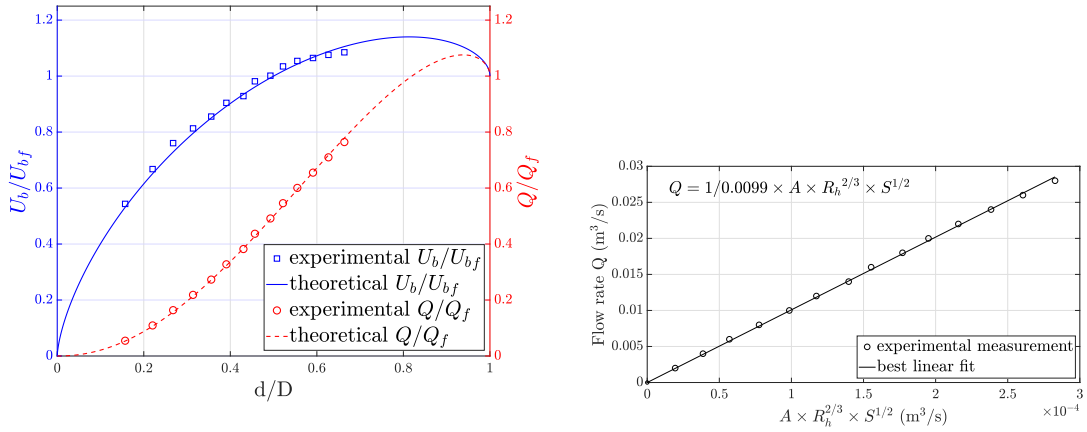

(a) (b)

Figure 4.1 Comparison of experimental measurements to theory for the validation of uniform flow conditions: (a) Dimensionless quantities over relative depth, and (b) Manning's equation.

downward-looking ADV at eight different streamwise positions and 13 different depth-wise positions. It is clear that the flow was not well developed in the position near the pipe entry x = 2.38 m, showing velocity magnitude $\sim$ 7.7 % smaller than the other positions as indicated by the black square markers in Fig. 4.2a. The streamwise position x = 12.61 m is the place just after the intrusive wave probes. The velocity profile at this position, indicated by yellow star markers in Fig. 4.2a, shows velocity magnitude $\sim$ 4.6% smaller than the other positions. This is likely due to the disturbance by the intrusive wave probes. In general, the magnitude of the velocity profile difference at different streamwise positions is within 1.5 %. The side-looking ADV was placed 0.9 m upstream of DIC measurement area and 2.7 m downstream of the wave probes measurement area to validate the downward-looking probe and collect data closer to the free surface. The sub-surface velocity fluctuations were measured by the side-looking ADV at two different streamwise positions and 15 different depth-wise positions. The velocity profiles measured at these two positions for the highest flow, flow condition 14, are compared in Fig. 4.2b. Markers represent the mean streamwise velocity and error bars correspond to the standard deviation of velocity time history, calculated by taking the standard deviation of ADV measured 300 s long streamwise velocity (std(u)). As is shown in Fig. 4.2b, the mean streamwise velocity profile and standard deviation of velocity fluctuations are comparable upstream and downstream of the measurement area. The downstream mean streamwise velocity is slightly smaller in magnitude compared to the upstream one, with a small mean streamwise velocity difference within 3.95%. The difference is to be caused by the intrusive wave probes between these two ADV measurement positions. The difference is

larger in the depth-wise positions $0.3 < z/d < 0.65$ and relatively smaller in the near surface and bottom positions. Overall, the velocity profile difference before and after the surface measurement area for depth-wise position $0.06 < z/d < 0.86$ is within 4 %, which verifies the uniform flow conditions.

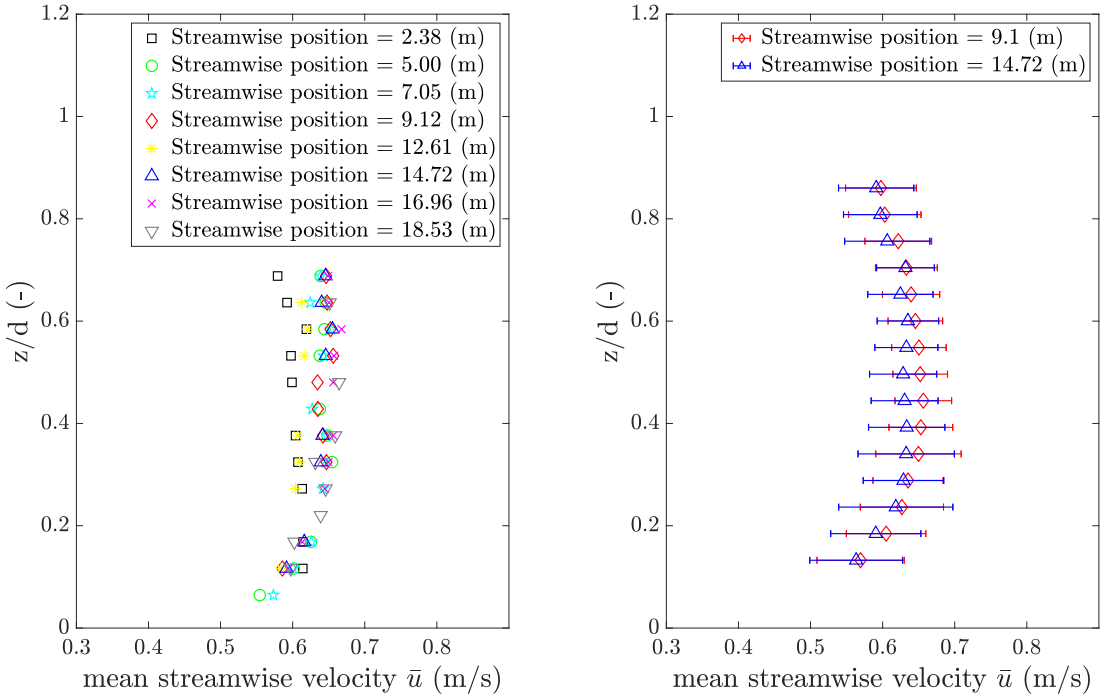

(a) (b)

Figure 4.2 Velocity profile measurements obtained by ADV for flow condition 14: (a) before and after the surface measurement area, as measured by a side-looking ADV; (b) at multiple streamwise positions, as measured by a downward-looking ADV.

The measurement location of this study is positioned 9.1 m downstream from the inlet pipe and 12 m upstream from the outlet pipe. In pipe flow, the stabilization zone is known to occur approximately 10 pipe diameters downstream from the entrance, which corresponds to 2.9 m downstream from the inlet pipe in this study. Therefore, the measurement section is located within the stabilization zone. However, it is important to note that the velocity profile analysis, as discussed in the preceding paragraph, demonstrates a uniform distribution both before and after the measurement section. This validates that the measurement section is indeed within the stabilisation zone and ensures that it is not affected by the inlet and outlet regions.

4.2 Wave probe data

As mentioned in subsection , a physical low pass filter was connected to the wave monitor output to remove any high frequency noise. The filter was connected and then removed to check the effect of the filter and the wave probe voltage was recorded for flow conditions 1 and 14. Fig. 4.3 shows the power spectra of the voltage fluctuations from wave probes with and without filter for the lowest and highest flow conditions, with frequency shown up to 50 Hz. It can be seen that the power spectra generally overlay each other in the frequency range below 10 Hz and the filter is capable of removing some spikes in the higher frequency ranges. Therefore, the filter implemented is able to reduce random noise and aliasing effects, while not affecting the wave probe reading.

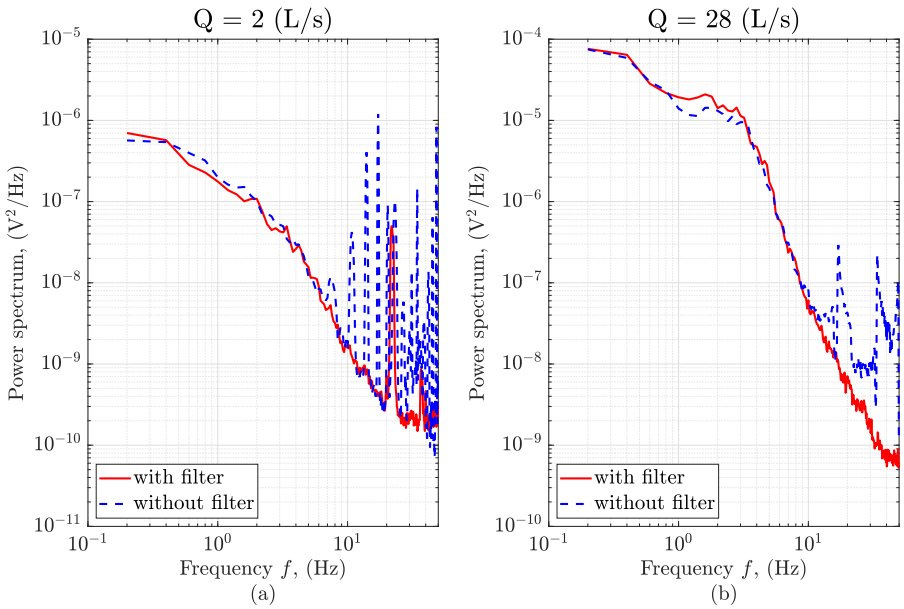

Figure 4.3 Power spectra of voltage fluctuation from wave probe with and without filter (a) flow condition 1 and (b) flow condition 14.

The wave probe voltage fluctuation was first converted into surface fluctuation by the calibration coefficient as described in subsection 3.3.2. The surface fluctuation was then filtered with a 10 Hz low pass filter and detrended to remove any small linear drift over the course of the measurement. The 10 Hz frequency was selected as the wave probe module Churchill itself includes an internal 10 Hz low pass hardware filter, so that any signal component above this frequency range could be considered as noise. This cutoff frequency was also implemented by Nichols (2014) as the frequency content of surface fluctuation time series is well below 10 Hz. Figure 4.4 shows an example of a wave probe measured surface fluctuation time series for a duration of 20 s with and without a 10 Hz low pass filter.

The 10 Hz low pass filter is able to remove some outliers in the signal without changing the turbulence information. After that the signal is subtracted by its time averaged mean to obtain surface fluctuation. This pre-processing procedure was applied to all 7 wave probes and for all flow conditions.

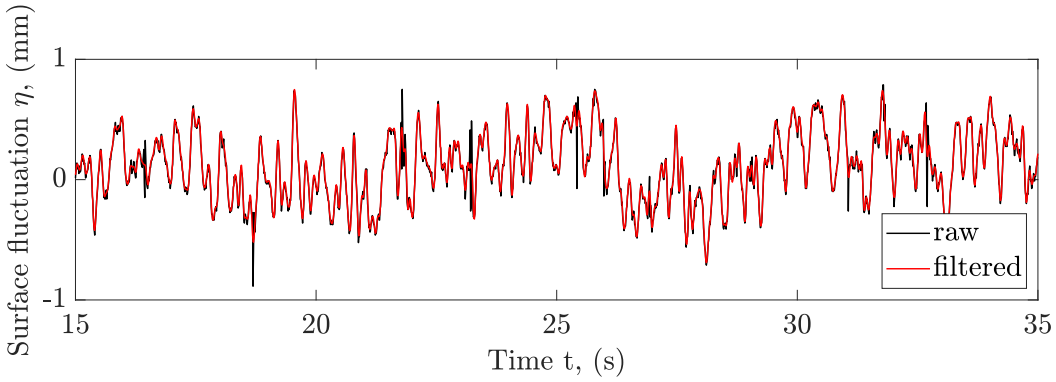

Figure 4.4 Surface fluctuation time series of 20 s segment measured by wave probe 1 for flow condition 4 with and without filter.

Figure 4.5 shows an example of the power spectra measured by the wave probe 1 to 7 for condition 1, 6 and 11. Data is shown up to 10 Hz as the signal above 10 Hz are rolled off. The dominant spectral content is below 5 Hz and the amplitude of the water surface fluctuation spectrum above 5 Hz is at least an order magnitude lower than the maximum amplitude. A 20 s section of the corresponding water surface fluctuation time series data recorded on probe 1 is shown for the same three flow conditions on the right. Larger surface fluctuation can be observed in higher flow rate flows.

4.3 DIC data

4.3.1 DIC data pre-processing

To process the raw DIC data for later post-processing analysis, several steps are involved to address any distortions or inaccuracies encountered by the DIC setup. Firstly, the raw data is initially non-uniformly distributed over space. To rectify this, a scatter interpolation technique is employed to convert the raw data into a spatially uniformly distributed format. Secondly, the raw data may contain certain anomalies such as missing points or spikes caused by factors like light reflection or floating air bubbles. To address these issues, a combination of a 2D median filter and a 10 Hz low pass filter is applied to remove these outliers, ensuring a more accurate dataset. Lastly, the coordinate system used by the DIC system needs to be converted to the coordinate system specific to the pipe being analysed.

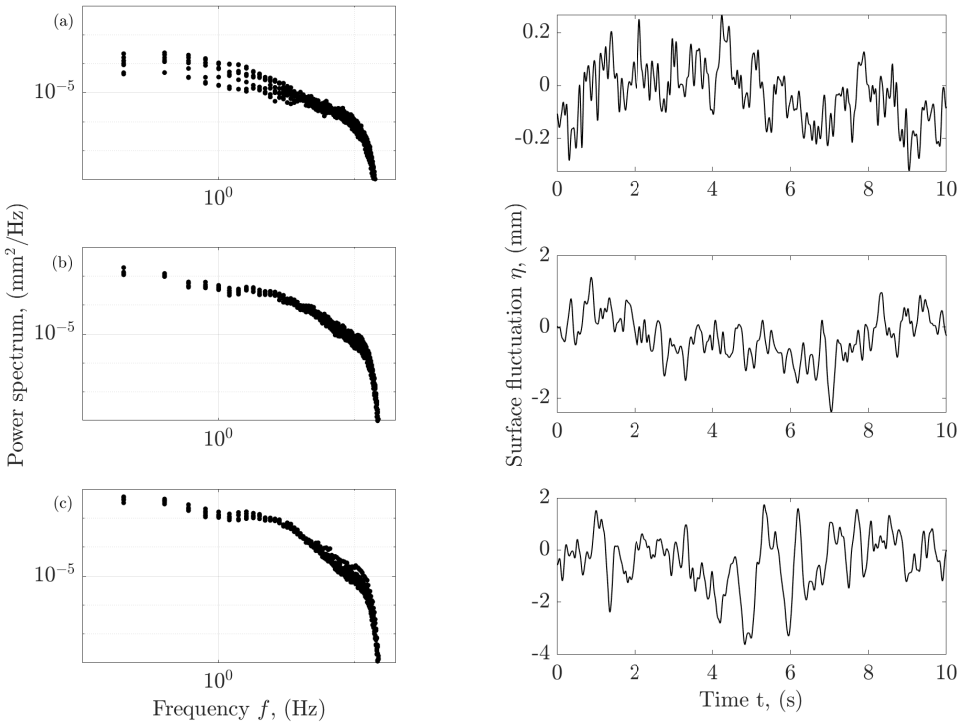

Figure 4.5 The power spectrum of water surface fluctuation for flow conditions 1, 6 and 11, (a) Q =2 (L/s), (b) Q =12 (L/s) and (c) Q =22 (L/s) measured by 7 wave probes (left) and example segment of time series recorded on wave probe 1 (right). The power spectrum show data from all 7 wave probes and the time history only show data from wave probe 1.

This conversion enables proper alignment and comparison of the DIC data with wave probes data. By implementing these processing steps, the raw DIC data is enhanced, making it more suitable for subsequent analysis and interpretation. Detailed information regarding the pre-processing steps is provided in the following paragraphs.

The raw DIC export from the Istra 4D software for each time step is the (x, y, z) coordinate of each facet relative to the initial position of the calibration plate as described in subsection 3.4.2. The centre of the calibration plate is 500 mm upstream of wave probe 1. Therefore the DIC xy coordinate $(0, 0)$ means the point in the lateral centre of the flow and 500 mm upstream of wave probe 1. The raw DIC data points are non-equidistantly spaced, with some missing points in the areas with reflections or air bubbles. The first step of the DIC data pre-processing is to interpolate the raw DIC data with the MATLAB function 'scatteredInterpolant' (MATLAB, 2019) into orthogonal equidistantly spaced data as is shown in Fig. 4.6a and b. The scatter interpolation usually does not function well in areas with missing data and leads to spikes in the interpolated surface. Tsubaki et al. (2005) observed similar protrusions in their measurement of a fluctuating free surface using a projection-based technique, which are caused by the matching error of local surface images. They suggested to eliminated by a statistical procedure. In this study, to eliminate the spikes in the data caused by reflections and air bubbles, a 2D median filter and a 10 Hz low pass filter were applied to the interpolated data (see Fig. 4.6c). Figure 4.7 shows the difference of the filtered data and the interpolated data over 2D space for flow condition 12, repeat 1 at frame 55. It shows high differences at positions such as $(88, -6)$, $(100, -38)$ and $(156, 0)$, where the interpolation function failed to interpolate the missing data points. Despite these areas, the filter procedure does not change the value of the z coordinate by more than 0.2 mm. The time series of z coordinate fluctuations at the xy coordinates $(100, -38)$ before and after filtration is demonstrated in Fig. 4.8. The differences before and after filtering are generally below 0.2 mm, showing that spike points can be removed robustly while not losing flow turbulence information.

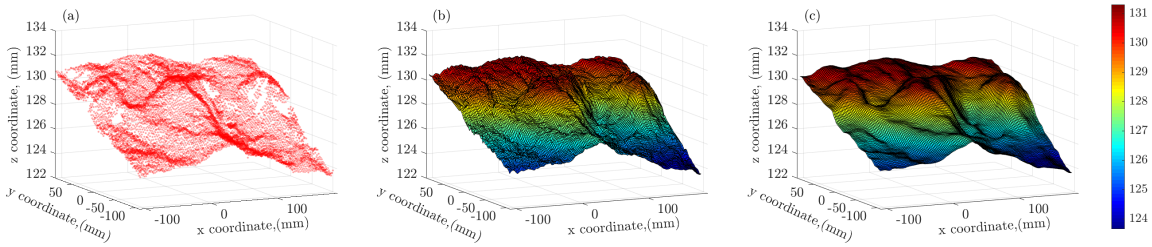

Figure 4.6 The free surface measured by DIC system for flow condition 12 repeat 1 frame 55 (a) raw, (b) interpolated and (c) filtered.

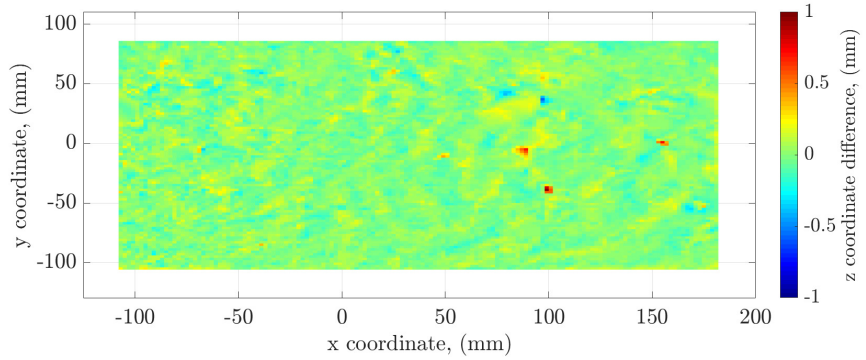

Figure 4.7 The difference between interpolated and filtered data over 2D space for flow condition 12 from first 66 s measurement repeat at the 55 time frame.

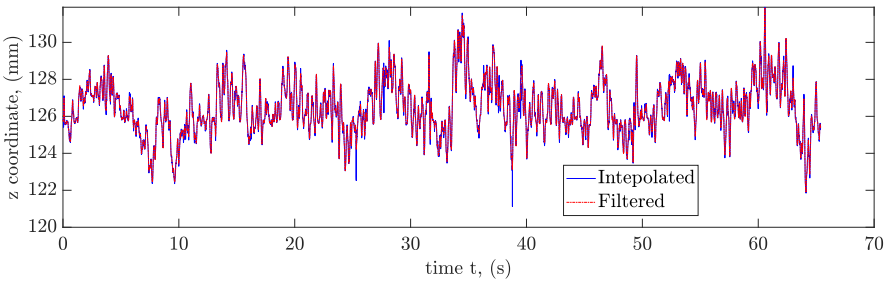

Figure 4.8 The difference between interpolated and filtered data over time for flow condition 12 repeat 1 at spatial point (100,-38).

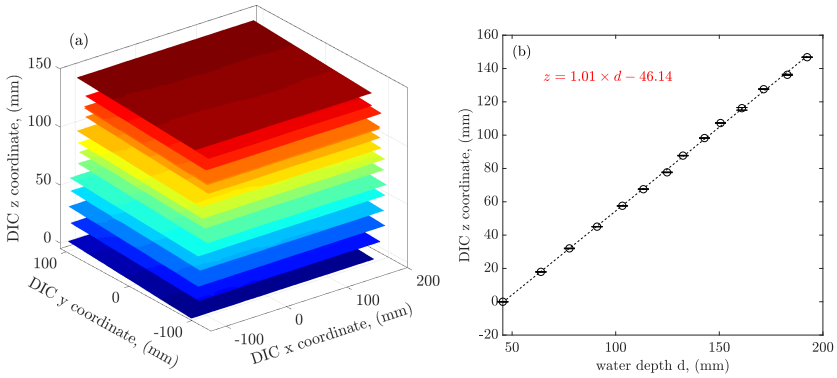

Figure 4.9 (a) DIC measured mean 2D z coordinate for 14 flows (b) DIC measured mean z coordinate versus water depth measured by point gauge.

The mean surface of the z coordinate fluctuations for 14 different flows is shown in Fig. 4.9a. The DIC technique measures the surface deformation over a 2D area relative to the position of the calibration board in the first image. The figure illustrates 14 2D layers with different colors, representing the mean surface deformation for each of the 14 different flows. Each 2D layer is averaged over five sets of 66 s DIC measurements. In Fig. 4.9b, the mean of these surfaces over the 2D space is compared to the water depth measured by the point gauge. The x-coordinate values correspond to the 14 water depth measurements obtained by the point gauges, while the y-coordinate values correspond to the mean values of the 14 layers in Fig. 4.9a. The vertical error bars in the plot represent the estimated maximum difference between the results obtained from five reproducibility experiments, indicating the variability in the measurements. The maximum difference for the 14 flows is found to be 0.41 mm, which demonstrates the repeatability of the measurement technique and the consistency of the results. The dashed line in Fig. 4.9b represents the best-fit line between the mean z coordinate obtained from DIC and the water depth measured by the point gauge. This line exhibits a linear relationship with a gradient close to 1, indicating a strong agreement between the DIC measurement and the point gauge measurement. The mean relative difference between the two measurements is below 6.64%, further confirming the consistency and reliability of the two methods. It is important to note that the surface fluctuation is derived from the z coordinate fluctuations by subtracting the mean value over time. This allows for the characterization of the dynamic changes in the water surface over the course of the experiment, providing valuable insights into the surface dynamics and behavior.

4.3.2 DIC data validation

In this subsection, the comparison of DIC and wave probes measurement are made in terms of probability density, roughness height and power spectrum. Then the ability of the DIC system to recover the instantaneous free surface is examined.

Figure 4.10 shows examples of probability density function (PDF) of the surface fluctuation measured by DIC and wave probes for flow conditions 1, 3, 5, 8, 11 and 14. These conditions were representative of the full range of flows. It is evident that all PDFs show an approximately Gaussian distribution with the width of the PDF (related to water surface wave height) increasing with the increase of flow. The width of the PDF is smaller from DIC in low flows (see Fig. 4.10a and b) while wider in high flows (see Fig. 4.10e and f). Except for flow conditions 13 and 14 (Fig. 4.10f), the DIC tends to show higher density in small fluctuations in low flow rates, suggesting DIC is usually able to detect more small surface fluctuations than wave probes. This can be explained by the 10mm distance between two wires of the wave probe. This separation distance is likely to average the surface features between two wires Krynkin et al. (2014) and thus they are unable to detect features much smaller than the separation between wires.

The surface roughness height (standard deviation) of surface fluctuations for all flow conditions obtained by DIC against wave probes is shown in Fig. 4.11 with a 1:1 line for reference. The surface roughness height was calculated from

$$\sigma_m = \sqrt{\frac{1}{T}\int_0^T \eta^2(t)dt}, \tag{4.1}$$

where $\eta(t)$ is the time-dependent water surface fluctuation over the period T. The mean DIC surface roughness height σ_{DIC} is averaged over 50 streamwise locations with 2mm spacing on average at the lateral centerline as Eq. 4.2 and mean wave probe surface roughness height σ_{wp} is averaged over all 7 probes as Eq. 4.3.

$$\sigma_{DIC} = \frac{1}{50}\sum_{m=1}^{50}\sigma_{mDIC} \tag{4.2}$$

$$\sigma_{wp} = \frac{1}{7}\sum_{m=1}^{7}\sigma_{mwp} \tag{4.3}$$

The error bars in Fig. 4.11 represent the maximum and minimum values obtained by DIC at different streamwise locations or different wave probes. It is evident that these two techniques show the most comparable results for medium flows. DIC shows higher surface roughness in high flows than wave probes and vice versa for low flows. Figure 4.12 shows the plot of

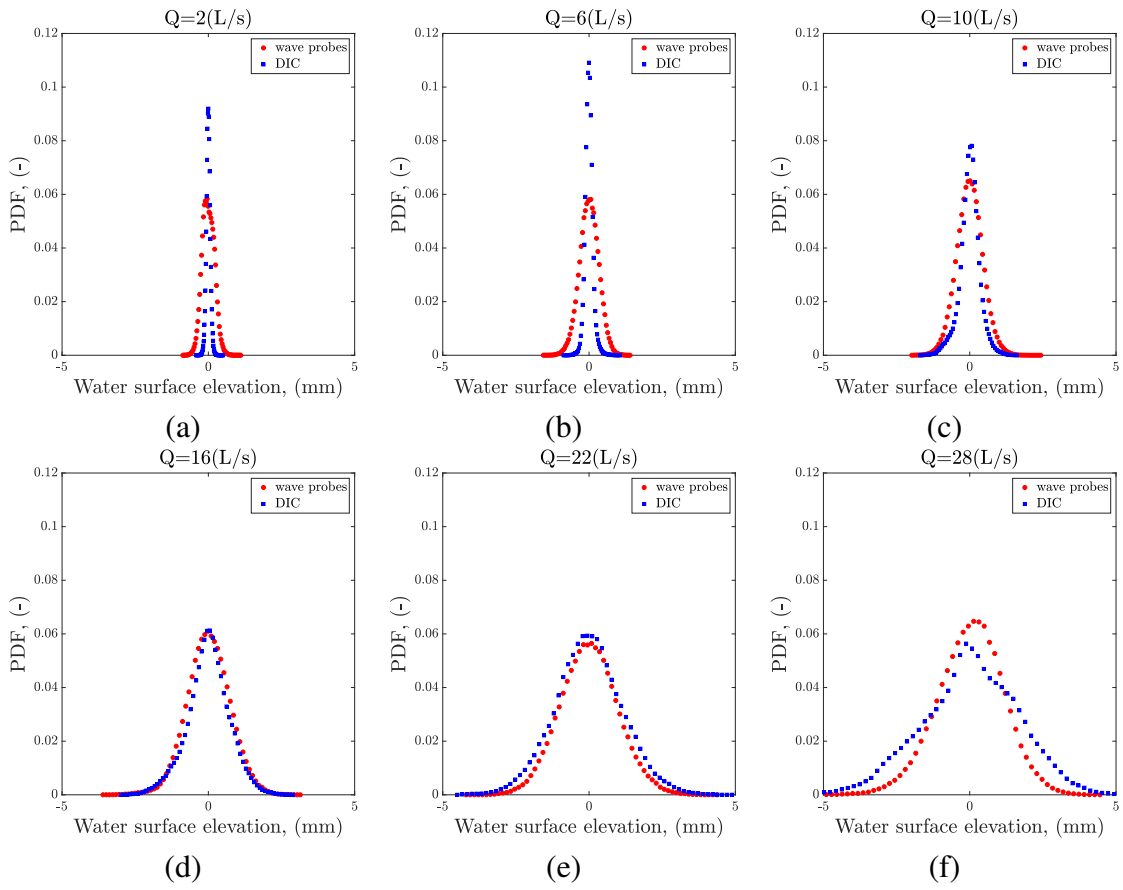

Figure 4.10 Probability density functions of surface fluctuations for flow conditions (a) Q =2 (L/s), (b) Q = 6 (L/s), (c) Q = 10 (L/s), (d) Q = 16 (L/s), (e) Q = 22 (L/s) and (f) Q = 28 (L/s). The PDF is averaged over 7 wave probes and 50 DIC streamwise locations.

the standard deviation of the surface fluctuations measured by both techniques against the ratio of water depth and pipe inner diameter. Both techniques reveal a parabolic trend of the relationship between the surface roughness and the water depth. The standard deviation measured by wave probes for the highest flow is somewhat offset from the parabolic trend. This is likely due to strong lateral motions in this flow affecting the wave probe measurement. It is also possible that there are wake effects from upstream wave probes on downstream probes for this high flow condition. Figure 4.13 illustrates the variability of surface roughness calculated from different streamwise locations for DIC and wave probes. The values for both DIC and wave probes are consistently below 0.05 mm, indicating minimal variation among streamwise locations. However, it is worth noting that significant variance is observed among different wave probes at the highest two flow conditions, suggesting potential interference issues with the wave probes under high flow conditions. This figure provides insights into the spatial variability of surface fluctuations and highlights the need to consider probe performance in accurately capturing turbulence characteristics under high flows. Furthermore, wave probes show bigger surface roughness when the pipe is less than half filled while relatively smaller surface roughness when more than half filled. The difference between results from DIC and wave probes is not surprising as the DIC measures in small areas while the wave probes measure between two separated points (as discussed in the last paragraph). In addition, the standard deviation over a 2D space measured by DIC (see Fig. 4.14) shows that there is some variance in both streamwise and lateral directions. It can be observed that strong lateral variations occur in the highest flow condition ($Q = 28$ Ls^{-1}). This is likely due to secondary currents at this depth ratio and further study is required. There were only a limited number of wave probes available at different streamwise positions and only one lateral position. They do not provide representative data collection points to investigate the variation of surface fluctuation in both directions.

Figure 4.15 shows three example snapshots of free surface fluctuations measured by DIC at time intervals of 0.25 s. It is evident that the surface is rougher and changes more rapidly for higher flows, which agrees with Fig. 4.12. Figure 4.16 shows a detailed surface contour plot with surface gradient vectors in a 100 $\times$ 100 mm area at a time interval of 0.04 s. The surface gradient vectors represent the spatial variation of the surface elevation. They provide information about the steepness and direction of the surface slope at each point. By analyzing the surface gradient vectors, we can observe the advection of the water surface pattern from upstream to downstream (left to right) in all three examples. The advection of the surface pattern in the lateral direction can also be observed in moderate (Fig. 4.16b) and high flow regimes (Fig. 4.16c). It also shows that the size of the surface pattern is larger and advection speed is faster in higher flows.

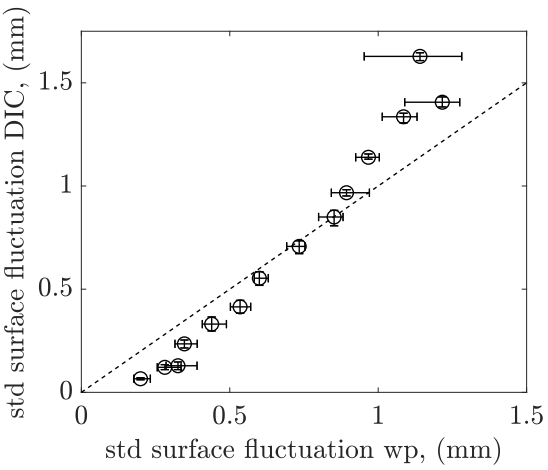

Figure 4.11 Surface fluctuation std measured by DIC compared against wave probes. The error bars represent the variations among 50 DIC probes and 7 wave probes. The dashed line represents the 1:1 reference line.

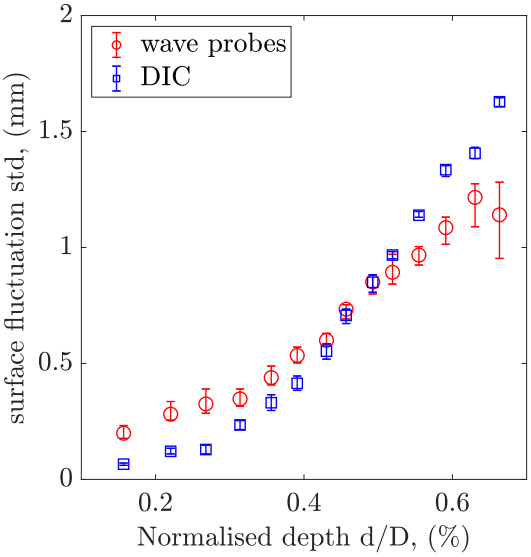

Figure 4.12 The relationship between surface roughness and the ratio of water depth and pipe inner diameter.

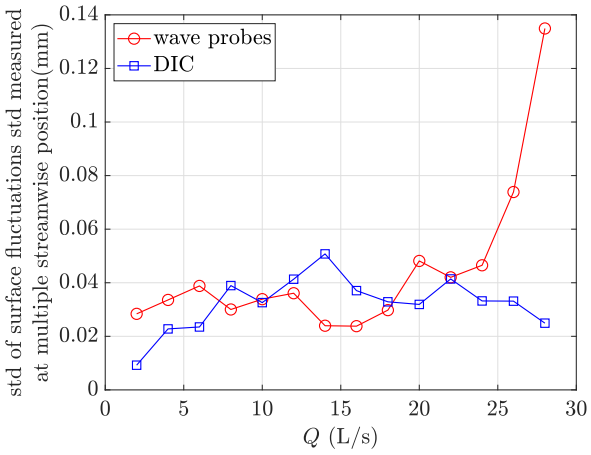

Figure 4.13 Standard deviation of surface roughness measured at multiple streamwise positions.

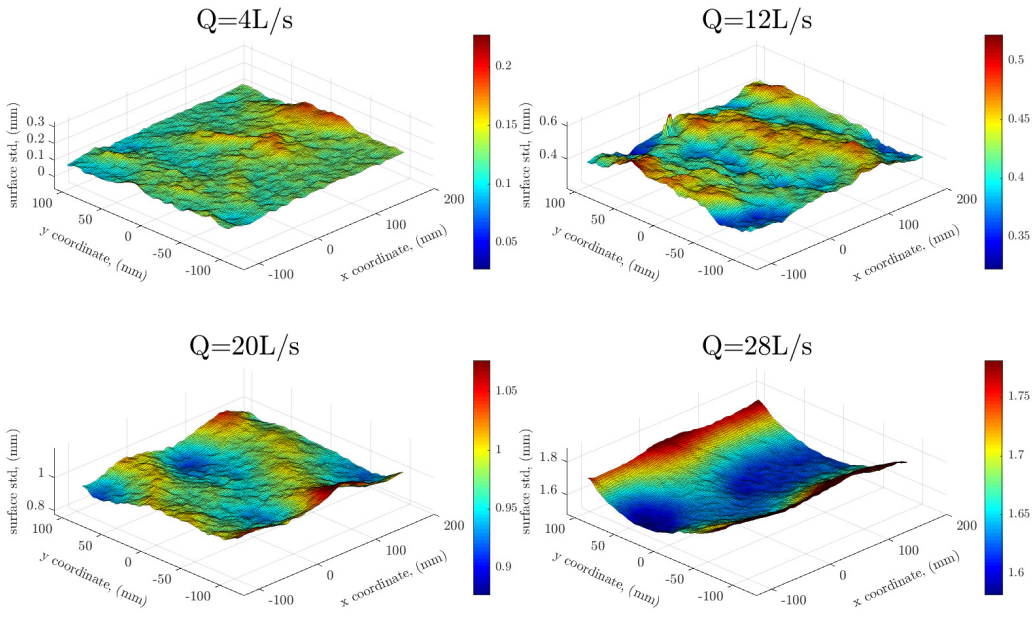

Figure 4.14 The std surface measured by DIC for flow conditions 2, 6, 10 and 14.

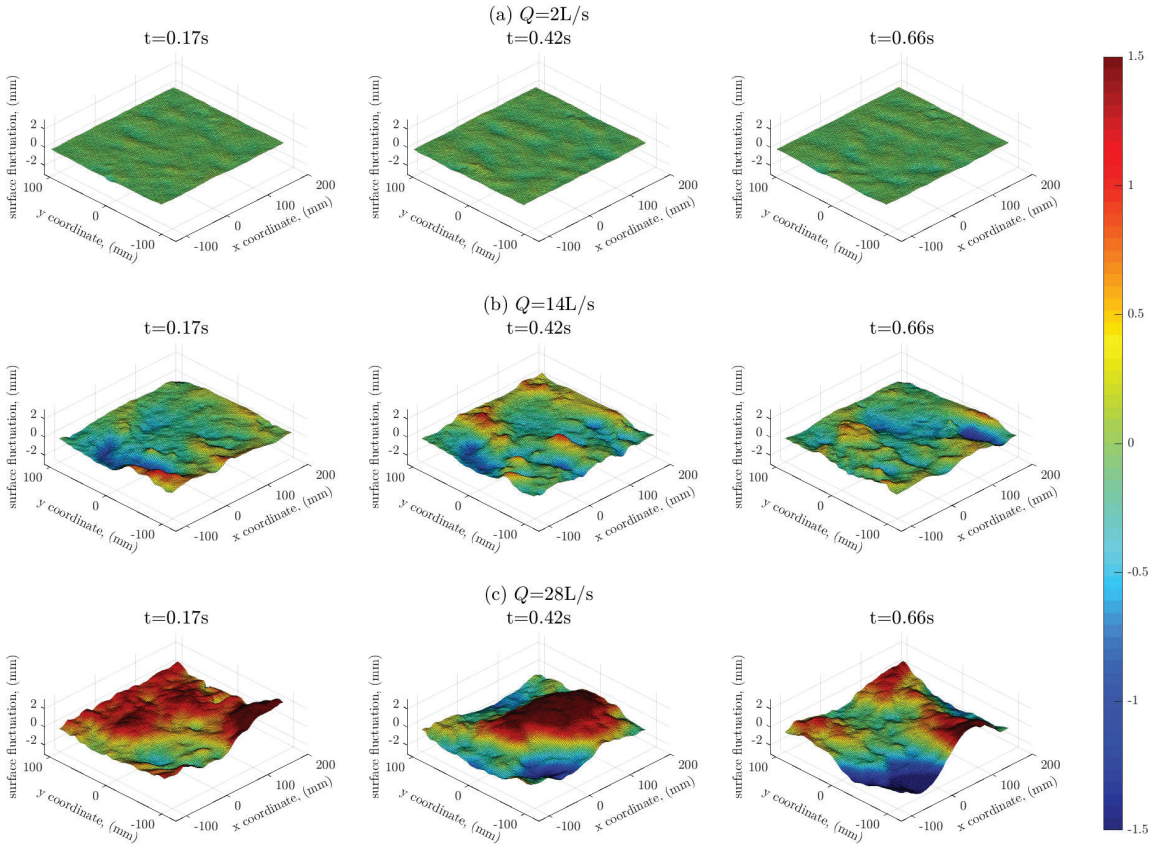

Figure 4.15 Snapshots of instantaneous free-surface profile.

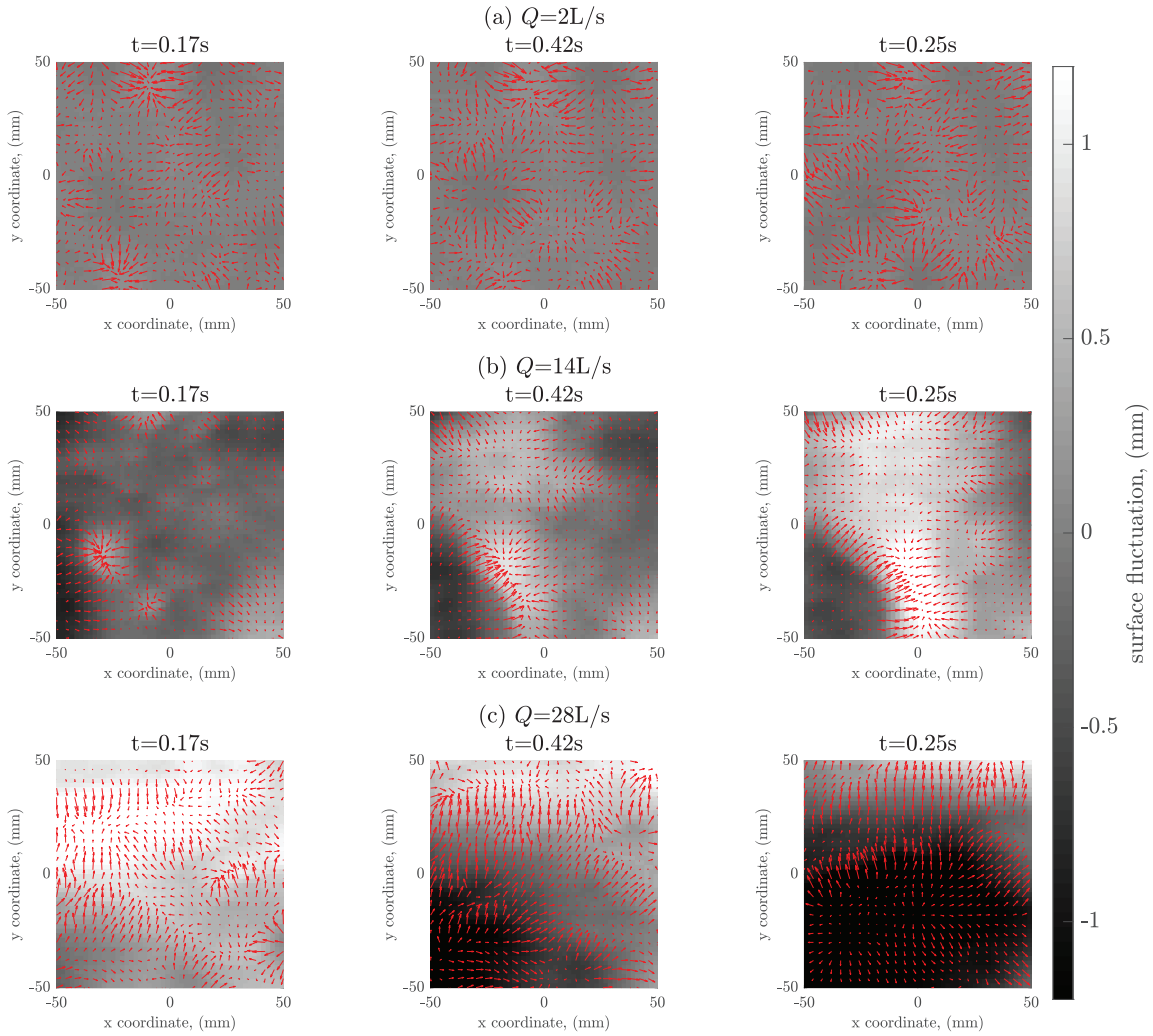

Figure 4.16 Instantaneous surface fluctuation with surface gradient vectors.

4.4 ADV data

4.4.1 ADV data pre-processing

ADV data are often contaminated by spikes (erroneous data points) as shown by the black line in Fig. 4.17b and it is essential to despike ADV data to ensure validity of data. A number of despiking methods are available in the literature (Hu and Kim, 2013, Cea et al., 2007) where the two most widely used methods are the phase-space method proposed by Goring and Nikora (2002) and the Kernel Density-based method proposed by Islam et al. (2013). This study has divided all ADV measured data into 4 categories : (i) High correlation no contamination data, (ii) High correlation low contamination data, (iii) High correlation high contamination data and (iv) Low correlation high contamination data as summarised in Table 4.1. The correlation value from the ADV is a measure of the similarity between the two pulse echoes that are being measured. High ADV correlation values indicate accurate and reliable velocity measurements, while low correlation values suggest decreased confidence in the data quality. Contamination refers to unwanted spikes in the signal. High contamination refers to a significant presence of unwanted spikes in the signal, while low contamination indicates a minimal presence of such disturbances. According to the Nortek ADV manual (Nortek, 2021), 70 % is chosen to be the correlation threshold. Correlation values above 70 % are regarded as highly correlated data and below 70 % is low correlated data, which is discarded for this study. Figure 4.17 shows examples of raw and despiked velocity time series by phase-space and Kernel density method for these four categories. The ADV type, measurement depth-wise position and velocity type of these four examples are shown in Table 4.1. The two despiking methods perform almost equally when the contamination is low (see Fig. 4.17b). The Kernel density method is able to remove spikes in all four situations while the phase-space method is not able to remove all spikes in the highly contaminated situation (see Fig. 4.17c) and the low correlation situation (see Fig. 4.17d). However, in the clean data situation (see Fig. 4.17a), the Kernel density method performs over efficiently, the standard deviation of surface fluctuation is unavoidably reduced compared to raw data and phase-space despiked data.

Figure 4.18 presents the raw and dispiked probability density distribution of the velocity time series for these four situations. It can be seen from Fig. 4.18a that the Kernel density despiked PDF is narrower than the raw and the phase-space despiked one for the clean data. The standard deviation of the velocity time series is 0.03 ms^{-1}, 0.03 ms^{-1} and 0.024 ms^{-1} for the raw, phase-space despiked and Kernel density despiked, respectively. These results suggest that the phase-space despike method does not affect the variance of the velocity while the Kernel density method reduces the standard deviation by 20 % compared with the data

Table 4.1 ADV data quality categories with examples from measurements taken under flow condition 8

Category	Correlation	Contamination	ADV type	Depthwise position z/d	Velocity dimension
I	High	No	Side	0.77	Streamwise
II	High	Low	Downward	0.06	Vertical
III	High	High	Downward	0.09	Lateral
IV	Low	High	Downward	0.13	Streamwise

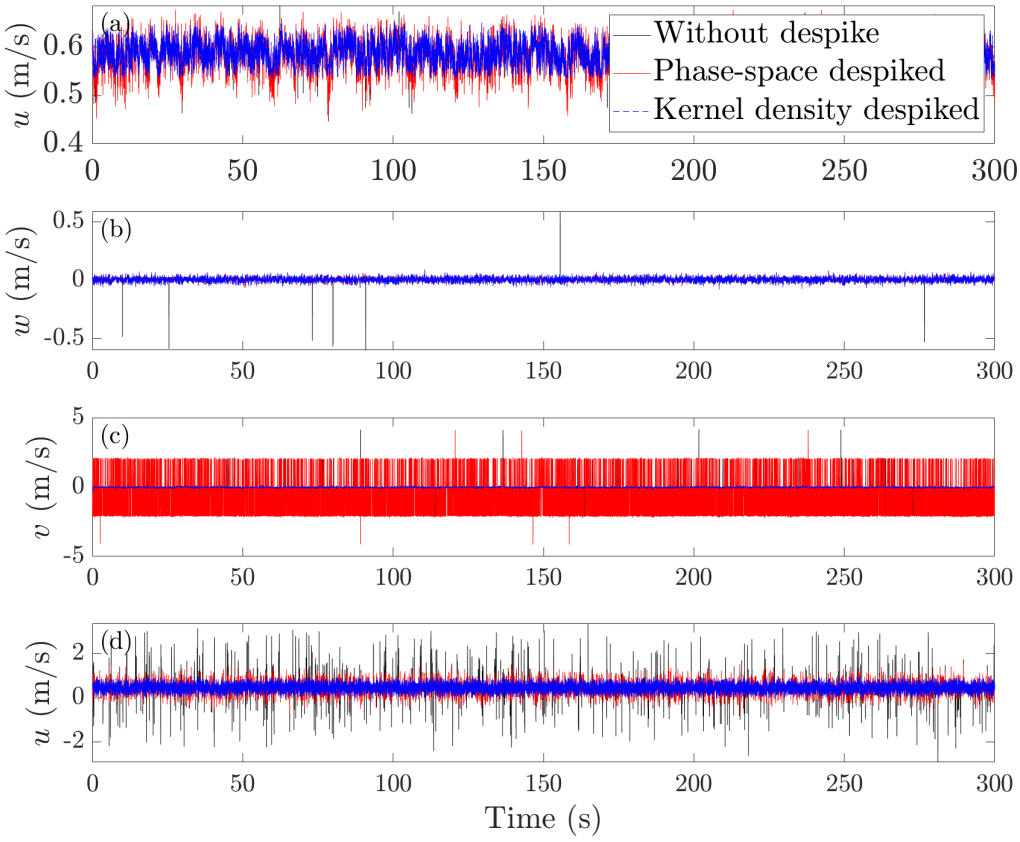

Figure 4.17 Raw and despiked velocity time series by phase-space method and Kernel Density-based method for (a) category I data with high correlation and no contamination, (b) category II data with high correlation and low contamination, (c) category III data with high correlation and high contamination and (d) category IV data with low correlation and high contamination.

without despike. For the high correlation with few contamination data (see Fig. 4.18b), the probability density distribution from phase-space and Kernel density method are similar and result in the same standard deviation of velocity. There are two apparent spikes in Fig. 4.18 even though the correlation of this data is high (97.8 %), which correspond to the positive and negative spikes in Fig. 4.17c. Phase-space method failed to remove these spikes as the spike density is over 25 % while the Kernel density method is still able to remove them. The low correlation data (see Fig. 4.18d) shows some probability density in high velocity magnitudes (>2 %), which corresponds to noise. Both methods can remove these outliers but this data is not reliable as it has a low correlation value (only 17.6 %).

Based on the time sereis and PDF analysis in the last paragraphs, as Kernel density despiking method is likely to alter the raw data, all the ADV data in this study are despiked by the phase-space method. As is shown in Fig. 4.19, spikes are efficiently removed by phase-space method and replaced by cubic interpolation without altering the clean data. It is known from Nichols (2014) that the frequency content of velocity time series in this type of flow is well below 10 Hz. For this data, the power spectrum calculated in MATLAB version R2019a with function 'fft' showed that the dominant components of the signal are well below 10 Hz. Therefore, the despiked velocity fluctuation data was low pass filtered using a third order Butterworth filter with a cut-off frequency at 10 Hz to remove any risk of remaining high frequency noise. The filter would not affect the results apart from removing erroneous data points. Besides, the surface data (wave probes and DIC) are 10 Hz low pass filtered. That means the filteration for both surface data and under surface data are consistent.

Figure 4.20a show the streamwise, lateral and vertical mean velocity profiles with all measured data, with standard deviations represented as error bars. It is evident that some markers are out of the velocity profile trend and show very high standard deviation. The undesirable low correlated data (Type IV data in Table 4.1) like the one in Fig. 4.17d are discarded in this study as suggested by Nortek (2021). After discarding all the data with correlation value below 70 %, the velocity profile is illustrated in Fig. 4.20b. There are still two lateral velocity markers showing large error bars, which are the category III data. This type of data is highly contaminated and is not used in this study. A PDF fitting method is proposed to discard this type of bad quality data. Figure 4.21 shows the probability density distribution of phase-space dispiked velocity time series with a best fit normal distribution curve, obtained by MATLAB function 'fitdist'. The coefficients of determination R^2 for category I, II and IV are all above 0.9 while only 0.16 for category III due to the two additional spikes (see Fig. 4.21). Therefore, for all the highly correlated data, the best fit normal distribution is examined. If the value of R^2 is below 0.9, this set of data is discarded for this study. Figure 4.20c shows the velocity profile after the 70 % correlation threshold

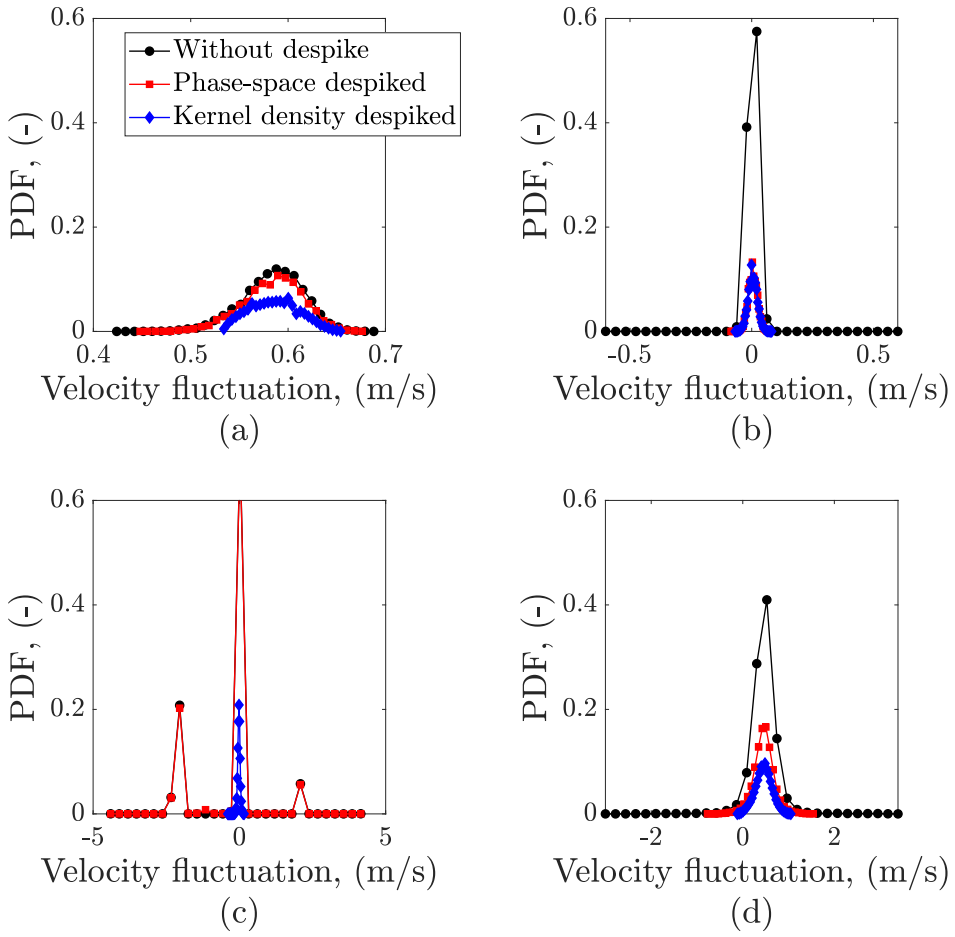

Figure 4.18 Raw and despiked velocity time series probability density distribution by phase-space methods and Kernel Density-based method for (a) category I data with high correlation and no contamination, (b) category II data with high correlation and low contamination, (c) category III data with high correlation and high contamination and (d) category IV data with low correlation and high contamination.

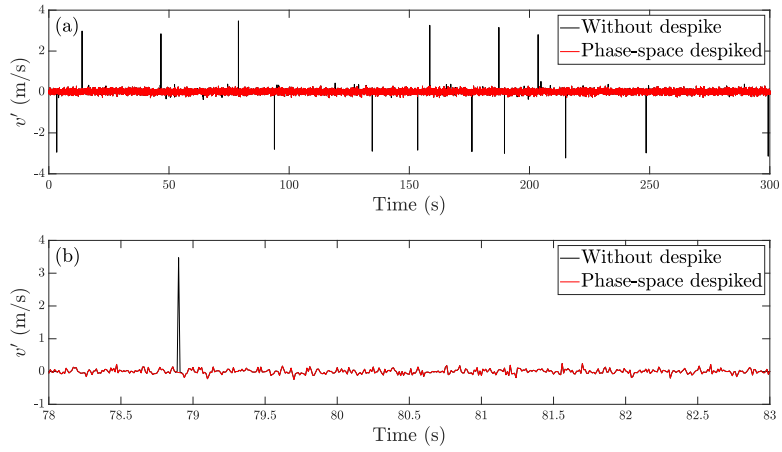

Figure 4.19 Time series for raw and despiked vertical velocity for flow condition 10 at depth-wise position $z/d = 0.64$ (a) full 300 s (b) portion of 5 s

and 0.9 R^2 threshold were applied. The best fit normal distribution method is able to discard all the unwanted data and keep the good quality data. After the two threshold selection, the objectively selected good quality data are summarised in Appendix B.

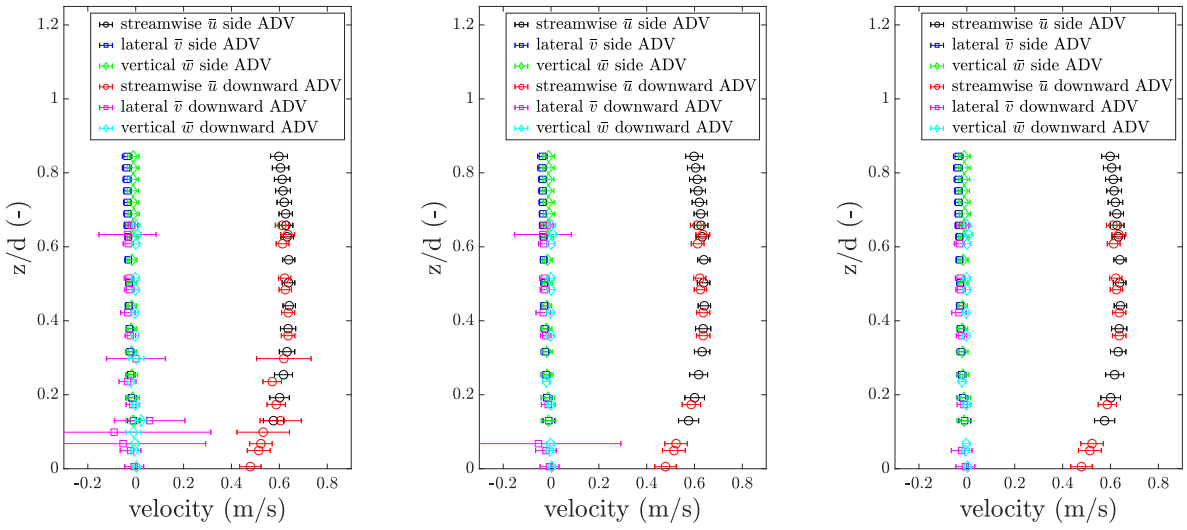

Figure 4.20 ADV data selection: (a) all measurement data, (b) after discarding based on correlation threshold, and (c) after discarding based on correlation and PDF fit R^2 threshold. Error bars represent the standard deviation of velocity time history.

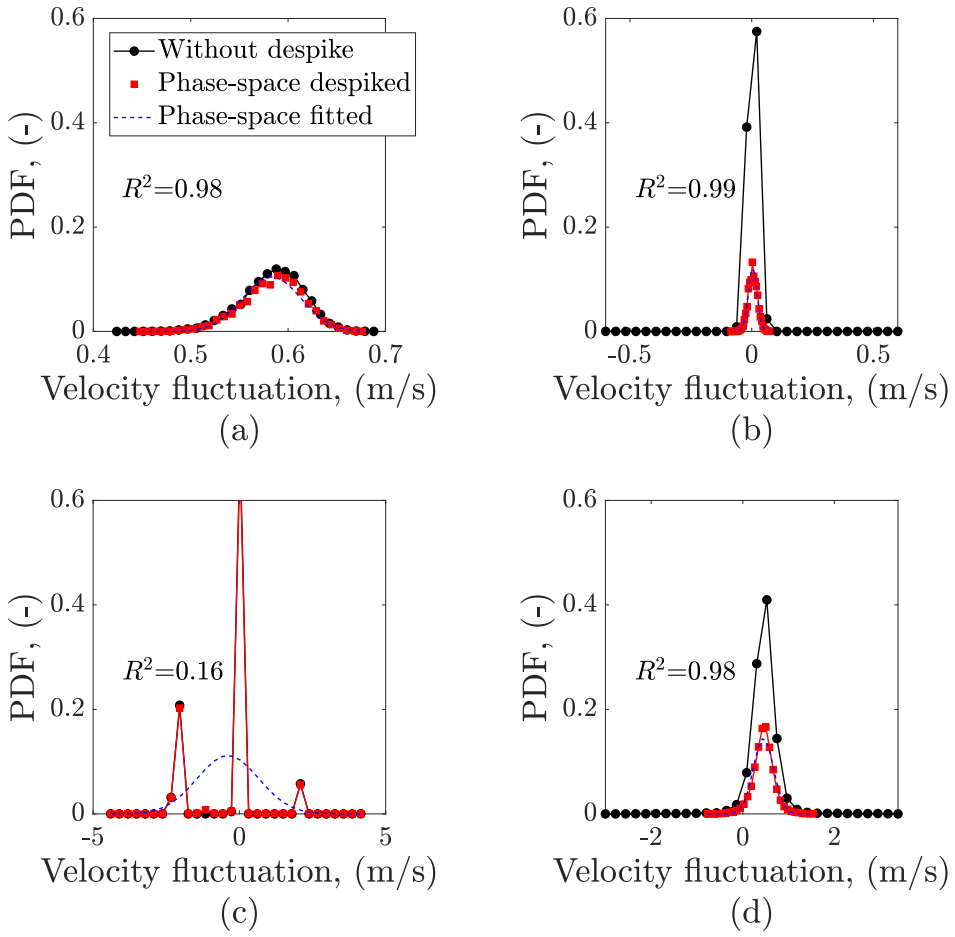

Figure 4.21 Raw and phase-space despiked velocity time series probability density distribution with best fit normal distributionn for (a) category I data with high correlation and no contamination, (b) category II data with high correlation and low contamination, (c) category III data with high correlation and high contamination and (d) category IV data with low correlation and high contamination.

4.4.2 ADV data validation

The shape of the mean velocity profile is first visualised as this is the most straight forward way to check the velocity measurement quality. Figure 4.22 shows the mean streamwise, lateral and vertical velocity profiles for flow conditions 4 and 10, measured by both ADVs. Markers are the mean velocities calculated by time average of velocity and error bars are the standard deviation of the velocity. The same direction velocity measured by the side-looking and downward-looking ADV are in the same marker type with different colors. The markers on the free surface (z/d = 1) represent the mean surface velocity measured by floating tracer and the error bars represent the maximum and minimum values in 10 repeated measurements. The dashed vertical line corresponds to the mean bulk flow velocity calculated from Eq. 2.10. This figure illustrates the lateral and vertical mean velocities being close to zero and the mean streamwise velocity profile resembling a parabolic shape. The surface velocity is in the trend of the streamwise velocity profile and the mean bulk flow velocity passes through the streamwise velocity profile. The side-looking and downward-looking ADV measured results overlap at the same depth-wise position and follow the same trend for the other positions.

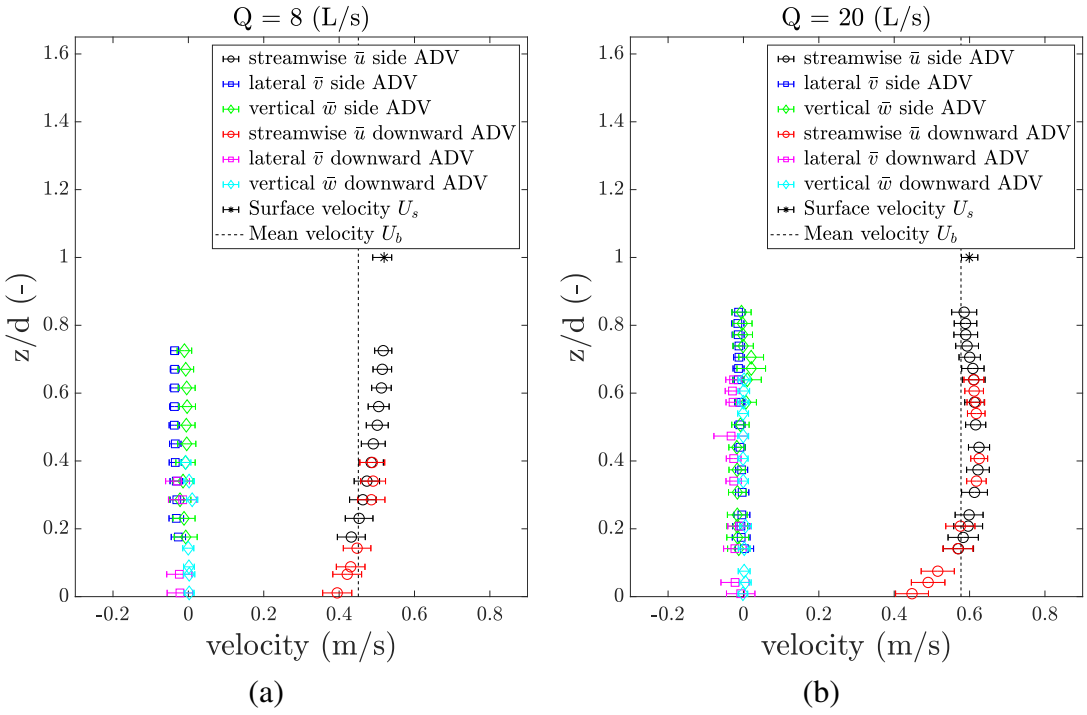

Figure 4.22 Mean velocity profile ($\bar{u}$, $\bar{v}$ and $\bar{w}$) for flow conditions (a) 4 and (b) 10.

It can be seen from Fig. 4.22 that side-looking and downward-looking ADV have some velocities measured at the same depth-wise positions. To quantify the similarity between the measurements of the two instruments, these same depth-wise positions were found

and velocities measured at these positions are compared. In Table 4.2, the number of the overlapping depth-wise positions in each velocity direction are shown in the number columns. There are no overlap positions for flow conditions 1, 2 and 14. For the other flows, the relative difference between mean velocity and standard deviation of the velocity are calculated by $(\bar{u}_B - \bar{u}_s)/\bar{u}_s \times 100$ and $(\sigma_{uB} - \sigma_{uS})/\sigma_{uS} \times 100$, respectively, where $\bar{u}_B$ is mean velocity from downward-looking ADV, $\bar{u}_s$ is the mean velocity from side-looking ADV, σ_{uB} is the standard deviation of velocity from downward-looking ADV and σ_{uS} is the standard deviation of velocity from side-looking ADV. In general, the relative differences of mean velocity in all three directions are below 2.04 % and the relative differences of velocity standard deviation are 5.45 % on average as summarised in Table 4.2.

Table 4.2 The mean and standard deviation of velocity difference between side-looking and downward-looking ADVs

Flow Condition	Streamwise difference			Lateral difference			Vertical difference		
	no.	mean	std	no.	mean	std	no.	mean	std
	(-)	(%)	(%)	(-)	(%)	(%)	(-)	(%)	(%)
1	0	N/A	N/A	0	N/A	N/A	0	N/A	N/A
2	0	N/A	N/A	0	N/A	N/A	0	N/A	N/A
3	2	3.62	4.90	1	4.24	9.06	2	3.62	4.90
4	3	3.00	1.87	2	4.18	1.97	3	3.00	1.87
5	2	2.75	7.27	2	2.75	7.27	2	2.75	7.27
6	2	1.64	5.26	2	1.64	5.26	2	1.64	5.26
7	4	2.02	7.57	4	2.02	7.57	4	2.02	7.57
8	4	0.94	2.98	4	0.94	2.98	4	0.94	2.98
9	2	0.60	3.73	1	0.70	5.37	2	0.60	3.73
10	4	1.08	6.30	4	1.08	6.30	4	1.08	6.30
11	1	2.71	2.56	1	2.71	2.56	1	2.71	2.56
12	3	1.25	11.02	2	0.80	7.91	3	1.25	11.02
13	7	1.02	5.39	5	1.32	4.12	8	1.52	7.25
14	0	N/A	N/A	0	N/A	N/A	0	N/A	N/A
Mean		1.88	5.35		2.04	5.49		1.92	5.52

In summary, the results obtained from the two types of ADVs demonstrate a high degree of consistency and agreement. Furthermore, the ADV results exhibit a strong correlation with the mean velocity calculated based on the flow rate and water depth measurements. Additionally, the ADV measurements align with the observed trend in the surface velocity measurements obtained using floating tracers. These collective findings serve as compelling

evidence for the reliability and consistency of the ADV measurements. Further analysis and evaluation of the ADV measurement results will be conducted in section 5.1, where they will be compared to relevant literature and established hydrodynamic principles. This detailed comparison will provide a more comprehensive understanding of the ADV data and its accuracy in capturing the sub-surface hydrodynamics.

4.5 Radar data

Some preliminary tests, including sensing mechanical motions of a metal plate and water surface motions in a wave tank, have been carried out to check the performance of the Doppler radar sensor (DRS). Subsection. 4.5.1 describes the setup and experiment procedure for tests with a metal plate. The preliminary water surface measurements in a wave tank are described in subsection 4.5.2. Preliminary analysis of these results are presented and discussed in subsection. 4.5.3. More in depth analysis of the DRS data is given in section. 5.5.

4.5.1 DRS preliminary metal plate tests

To characterise the performance of the DRS, a series of calibration tests was carried out on a calibration table. Similar calibration tests were performed by Gao and Boric-Lubecke (2015), Guan et al. (2014), Hu et al. (2014), Zakrzewski et al. (2015a). As shown in Fig. 4.23, the DRS was placed 300 mm away from a 30 $\times$ 30 cm thin metal plate. The metal plate was attached to a linear stage driven by a motor. The motor was connected via an Arduino and controlled by the CNC (Computer numerical control) controller software UGS (Universal GCode Sender). A laser displacement sensor (LDS) ILD1320-10 from Micro-Epsilon was attached 5 mm away from the metal plate to provide a reference measurement. The LDS measuring range is 10 mm, with a resolution of 1 μm (Micro-Epsilon, 2010). The advantage of LDS is that it is able to measure the displacement remotely with high resolution. However, the measuring distance is only 10 mm, which means it must be placed very close to the object. Beside, the LDS is approximate 20 times more expensive than the DRS. Therefore, the LDS is a good reference measuring tool for DRS metal plate calibration analysis but not suitable for water surface measurement. All of the DRS calibration apparatus were fixed on a rigid heavy metallic table to reduce unwanted extra vibrations to a minimum level. Different sinusoidal motions were designed, generated and measured, with amplitude varying from 0.5 mm to 5 mm with 0.5 mm increment and frequency varying from 1 Hz to 10 Hz with 1 Hz increment, resulting in 100 different monochromatic motions in total. These motion amplitudes and frequencies were selected as these include the dominant amplitudes and frequencies of free surface motion in partially filled pipes (see Fig. 4.5) and are in the measurement range of the LDS. The actual 100 mechanical motions of the metal plate measured by LDS are summarised in Table. 4.3. The actual amplitude is calculated by square root two times the standard deviation of the surface fluctuation and the dominant frequency is found by the MATLAB 'pwelch' function. LDS is able to measure mechanical motions for most of the cases, except motion 91 whose amplitude slightly exceeds 5 mm, out of the LDS measurement range. It can be noted that the actual metal plate mechanical motion amplitude

range is 0.5 - 5 mm and frequency range is 1 - 7.8 Hz. The difference in the actual frequency (1 - 7.8 Hz) and the input frequency (1 - 10 Hz) is because the input motion exceeds the velocity limit of the motor. The DRS and LDS were sampled at 1000 Hz and 2000 Hz, respectively for a time duration of 30 s asynchronously.

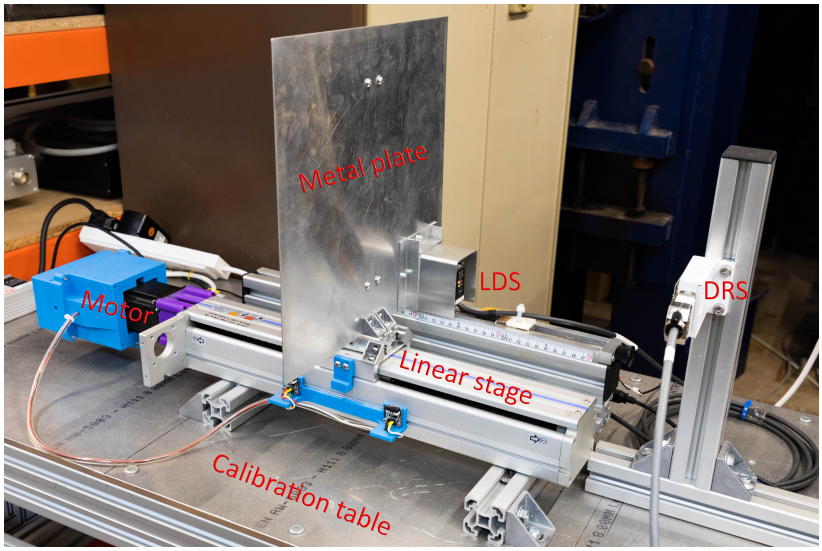

(a)

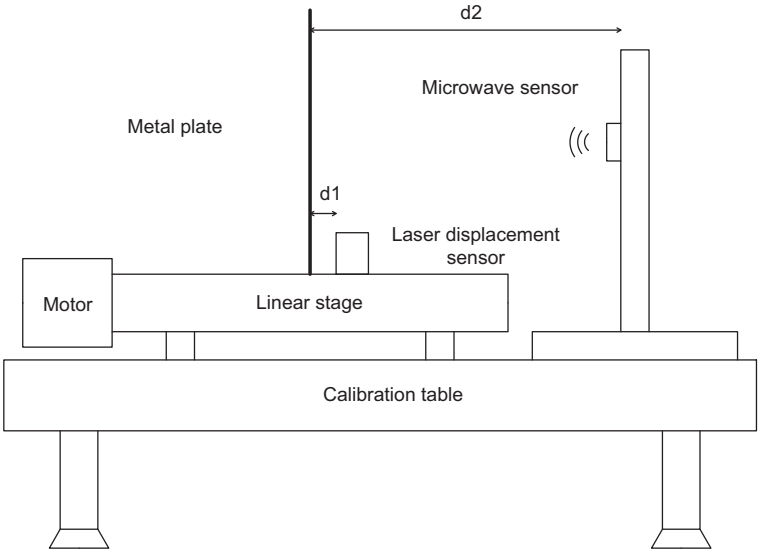

(b)

Figure 4.23 Experiment setup for microwave sensor calibration, (a) Photography and (b) Sketch

Table 4.3 Metal plate mechanical motion conditions

Motion (-)	**1**	**2**	**3**	**4**	**5**	**6**	**7**	**8**	**9**	**10**
LDS A (mm)	0.50	0.49	0.49	0.49	0.46	0.46	0.46	0.45	0.46	0.43
LDS f (Hz)	1.00	2.00	3.00	3.60	4.80	5.60	6.00	6.60	7.00	7.80
Motion (-)	**11**	**12**	**13**	**14**	**15**	**16**	**17**	**18**	**19**	**20**
LDS A (mm)	1.00	0.98	0.99	0.97	0.95	0.94	0.94	0.93	0.93	0.88
LDS f (Hz)	1.00	2.00	2.80	3.60	4.40	5.00	5.20	5.20	5.20	5.80
Motion (-)	**21**	**22**	**23**	**24**	**25**	**26**	**27**	**28**	**29**	**30**
LDS A (mm)	1.48	1.45	1.47	1.45	1.43	1.41	1.41	1.40	1.39	1.34
LDS f (Hz)	1.00	2.00	2.80	3.40	4.00	4.40	4.40	4.40	4.40	4.60
Motion (-)	**31**	**32**	**33**	**34**	**35**	**36**	**37**	**38**	**39**	**40**
LDS A (mm)	1.96	1.93	1.96	1.95	1.92	1.89	1.87	1.76	1.59	1.59
LDS f (Hz)	1.00	2.00	2.60	3.40	3.60	3.80	4.00	4.00	4.20	4.20
Motion (-)	**41**	**42**	**43**	**44**	**45**	**46**	**47**	**48**	**49**	**50**
LDS A (mm)	2.44	2.41	2.45	2.45	2.41	2.35	2.10	1.84	1.60	1.37
LDS f (Hz)	1.00	2.00	2.60	3.20	3.40	3.60	3.80	4.00	4.20	4.60
Motion (-)	**51**	**52**	**53**	**54**	**55**	**56**	**57**	**58**	**59**	**60**
LDS A (mm)	3.03	2.89	2.92	2.93	2.84	2.51	2.16	1.87	1.63	1.56
LDS f (Hz)	1.00	2.00	2.80	3.00	3.20	3.40	3.60	4.00	4.20	4.40
Motion (-)	**61**	**62**	**63**	**64**	**65**	**66**	**67**	**68**	**69**	**70**
LDS A (mm)	3.54	3.39	3.47	3.40	3.06	2.54	2.18	1.89	1.64	1.56
LDS f (Hz)	1.00	2.00	2.60	2.80	3.00	3.40	3.60	4.00	4.20	4.40
Motion (-)	**71**	**72**	**73**	**74**	**75**	**76**	**77**	**78**	**79**	**80**
LDS A (mm)	4.03	3.89	3.96	3.74	3.13	2.58	2.20	1.90	1.66	1.56
LDS f (Hz)	1.00	2.00	2.60	2.80	3.00	3.40	3.60	3.80	4.20	4.40
Motion (-)	**81**	**82**	**83**	**84**	**85**	**86**	**87**	**88**	**89**	**90**
LDS A (mm)	4.51	4.38	4.41	3.87	3.23	2.55	2.21	1.89	1.69	1.56
LDS f (Hz)	1.00	2.00	2.40	2.60	3.00	3.40	3.60	4.00	4.20	4.40
Motion (-)	**91**	**92**	**93**	**94**	**95**	**96**	**97**	**98**	**99**	**100**
LDS A (mm)	~ 5	4.90	4.78	3.87	2.97	2.63	2.21	1.89	1.73	1.56
LDS f (Hz)	1.00	2.00	2.20	2.60	3.00	3.40	3.60	4.00	4.20	4.40

4.5.2 DRS preliminary wave tank tests

The implemented DRS is usually used in vital signs sensing (Droitcour et al., 2004, Mercuri et al., 2013, Lee et al., 2014, Lee, 2017). Vital signs and water gravity waves are both periodic motions Park et al. (2007b). Nichols et al. (2013) have measured gravity wave surface fluctuation with wave amplitude range 0.03 - 14.83 mm and frequency range 0.7 - 2.2 Hz in a rectangular channel by a non-invasive acoustic method. In their study, the acoustic technique is able to estimate the standard deviation of gravity waves with relative errors generally below 10 %. Reduced wavelength or increased wave height of gravity waves may increase error in displacement measurement. Inspired by past studies on vital sign DRS sensing and gravity wave acoustic sensing, this study presents a novel application of the DRS sensor for gravity wave surface fluctuation measurement. The experiment was carried out in an 11 m long and 0.5 m wide flume with 0 gradient in University of Sheffield Laboratory for Verification and Validation as shown in Fig. 4.24. The flume contained water of 990 mm in depth, with both flume ends sealed. The flume included a flap wave generator at each end enabling simulation of gravity waves. The generated gravity waves were homogeneous in the measurement area. The DRS was placed 35 cm above the water surface and 5.66 m away from the generating flap. Wave probes 1, 2 and 3 were placed 1.5, 1.3 and 1 m away from the DRS to avoid potential wake effects caused by intrusive wave probes. The DRS and wave probes were sampled at 1000 Hz and 128 Hz, respectively for a time duration of 30 s, asynchronously.

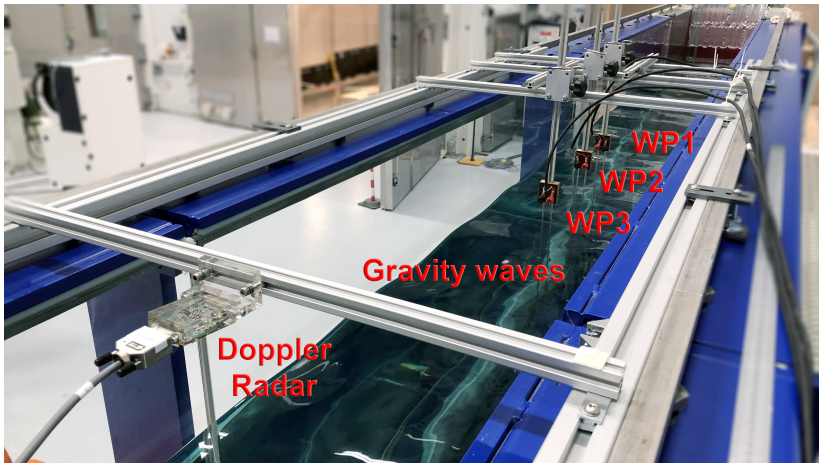

Figure 4.24 Photograph of experimental setup in a rectangular channel with high amplitude low frequency gravity waves, measured by the DRS and 3 wave probes.

All 20 gravity wave conditions are summarised in Table 4.4. The input motion amplitude and frequency are given in columns 2 and 3. The measured amplitudes averaged from the 3

wave probes, and from each individual wave probe, are given in column $4 \sim 7$. The measured dominant frequency is shown in column 8 and is exactly the same with 0.125 Hz precision for all three wave probes. The amplitude from each wave probe is calculated by square root two times the standard deviation of the surface fluctuation, and the dominant frequency is found by the MATLAB 'pwelch' function. The actual motion has the same frequency but a smaller amplitude compared with the input, which is because the input exceeds the system limit.

Table 4.4 Large gravity wave conditions

Wave Condition	Input A_m	Input f_m	WP mean A_m	WP1 A_m	WP2 A_m	WP3 A_m	WP f_m
(1)	(2)	(3)	(4)	(5)	(6)	(7)	(8)
(-)	(mm)	(Hz)	(mm)	(mm)	(mm)	(mm)	(Hz)
1	5	0.3	4.71	4.72	4.62	4.80	0.25
2	7	0.3	6.79	6.80	6.64	6.92	0.25
3	10	0.3	9.93	9.96	9.69	10.14	0.25
4	15	0.3	15.19	15.24	14.84	15.48	0.25
5	5	0.5	4.52	4.49	4.56	4.50	0.5
6	7	0.5	6.48	6.45	6.60	6.39	0.5
7	10	0.5	9.43	9.38	9.67	9.23	0.5
8	15	0.5	14.33	14.27	14.78	13.95	0.5
9	5	1	4.41	3.74	4.75	4.75	1
10	7	1	6.29	5.40	6.74	6.73	1
11	10	1	9.13	8.10	9.66	9.62	1
12	11	1	10.12	9.02	10.69	10.66	1
13	5	1.5	3.54	2.91	3.78	3.92	1.5
14	7	1.5	5.06	4.39	5.47	5.33	1.5
15	9	1.5	6.59	6.00	7.24	6.53	1.5
16	10	1.5	7.29	6.70	8.06	7.09	1.5
17	5	2	2.25	1.62	3.26	1.88	2
18	7	2	3.58	3.19	4.06	3.48	2
19	8	2	4.09	3.73	4.46	4.08	2
20	9	2	4.92	4.50	5.14	5.11	2

The experiment described in the last paragraph examined the DRS performance on large amplitude low frequency gravity waves. Experiments focusing on small amplitude waves were also carried out in the same rectangular open channel. As shown in Fig. 4.25, some small amplitude sinusoidal gravity waves (Fig. 4.25a) and random waves (broad spectrum waves) (Fig. 4.25) were generated by a plunger controlled by the same CNC controlled system described in the metal plate calibration experiment in subsection 4.5.1. The DRS was

placed 1.290 m away from the plunger and three wave probes were placed 1.138, 1.150 and 1.968 m away from the plunger, respectively for reference measurement.

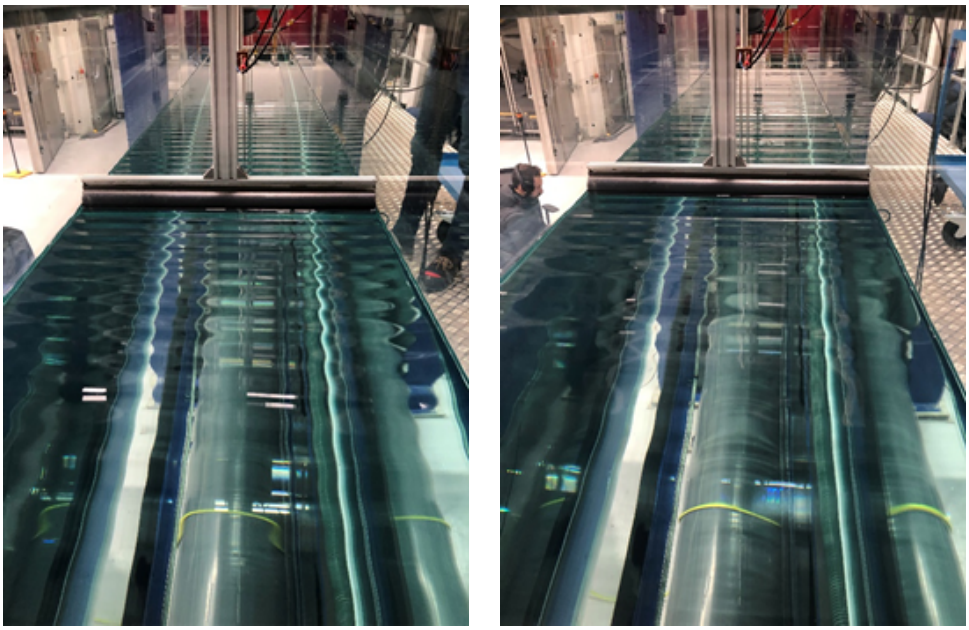

(a) (b)

Figure 4.25 Photography of generated small waves by the plunger in a rectangular open channel (a) small amplitude high frequency gravity waves and (b) small random waves.

There were four sinusoidal wave conditions and four random wave conditions being tested. The wave conditions are summarised in Table 4.5 below. The standard deviation of surface fluctuation is calculated from wave probe measurement.

Table 4.5 Small sinusoidal gravity wave and broad spectrum small random wave conditions

	Wave Condition	Std of surface fluctuation	Frequency
	(-)	(mm)	(Hz)
Random	1	0.39	broad
	2	0.40	broad
	3	0.92	broad
	4	1.33	broad
Sinusoidal	5	0.48	3.4
	6	0.05	6.1
	7	0.07	5.9
	8	0.23	2.3

4.5.3 DRS preliminary results and discussion

According to Eq. 2.45, the received I/Q signals carry the information of target motion. Some example time series of raw I/Q channel outputs for metal plate mechanical motions, water gravity wave motions and water random motions are demonstrated in Fig. 4.26, with period intervals calculated from a reference tool (LDS or wave probes) illustrated as dashed vertical lines for reference. For sinusoidal motions, it is apparent that both I/Q channel outputs show periodic patterns, which match the dominant frequency of the mechanical motion or gravity wave. The time series show how the DRS responds to a wave approaching and then leaving, resulting in areas of symmetry in the signal. In general, the I channel output has higher voltage magnitude compared with the Q channel, indicating potential amplitude imbalance in the channels. The I/Q channel outputs become noisy when the motion amplitude and frequency are small, such as examples in Fig. 4.26a and f.

Measurement results with I/Q constellations for different experiments are shown in Fig. 4.27. None of these examples form an arc or a circle, indicating the existence of signal distortion. The ribbon like trajectory in Fig. 4.27a is also observed by Gu et al. (2016), Rodriguez and Li (2019), Gao and Boric-Lubecke (2015), Yavari et al. (2012). The distortion in Fig. 4.27c and d look more complex compared to Fig. 4.27a and b. This is because motions in Fig. 4.27a and b have amplitudes less than half the radar wavelength (6 mm) while in Fig. 4.27c and d the motions are more than half a radar wavelength in amplitude. Motion with amplitude more than half the radar wavelength should form a complete circle. Therefore Fig. 4.27a, b and Fig. 4.27c, d are the result of distortion of an arc and a circle, respectively. Besides, the frequency of motion in Fig. 4.27c and d is less than the low pass filter cut off frequency (4.1 Hz), meaning more significant signal distortion. Amplitude and phase imbalances, and signal distortion are all evidently observed in Fig. 4.27d, which means amplitude, phase imbalances and distortion compensation are all required in post processing to accurately extract the displacement information. Random motion response as shown in Fig. 4.27f is the most complicated case and demodulation may fail in such cases (Lv et al., 2018, Zakrzewski et al., 2012, 2015b).

Since signal distortion can be evidently seen in Fig. 4.27, a post processing signal distortion compensation is required for more accurate signal demodulation. As mentioned in subsection 3.6.1, the amplifier module is formed by two cascaded (in series) band pass filters with high pass cutoff frequency 4.08 Hz and low pass cutoff frequency 1.06 kHz. As the frequency range of interest in this study (< 10 Hz) is much lower than the low pass cutoff frequency (1.06 kHz), the low pass filter effect can be neglected and only the effects of two first-order high pass filters require compensation. One first-order high pass RC filter

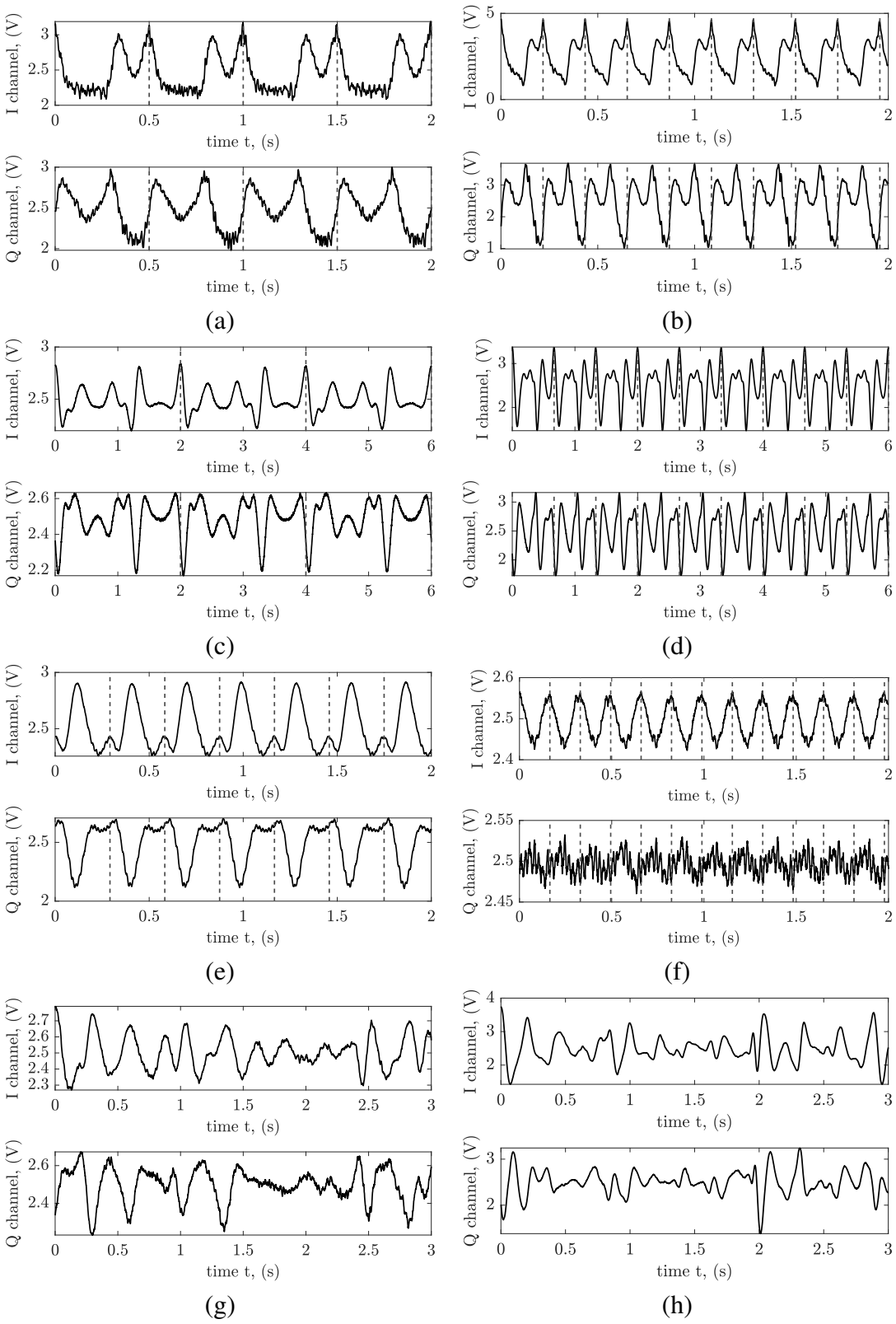

Figure 4.26 Time series of I/Q channels for sensing (a) 1.45 mm amplitude 2 Hz metal plate motion, (b) 1.37 mm 4.6 Hz metal plate motion, (c) 4.52 mm amplitude 0.5 Hz gravity wave No.5, (d) 3.54 mm amplitude 1.5 Hz gravity wave No.13, (e) 0.72 mm amplitude 3.4 Hz gravity wave, (f) 0.06 amplitude 6.1 Hz gravity wave, (g) water random motion smaller amplitude (wave condition 2 in Table 4.5) and (h) water random motion larger amplitude (wave condition 4 in Table 4.5).

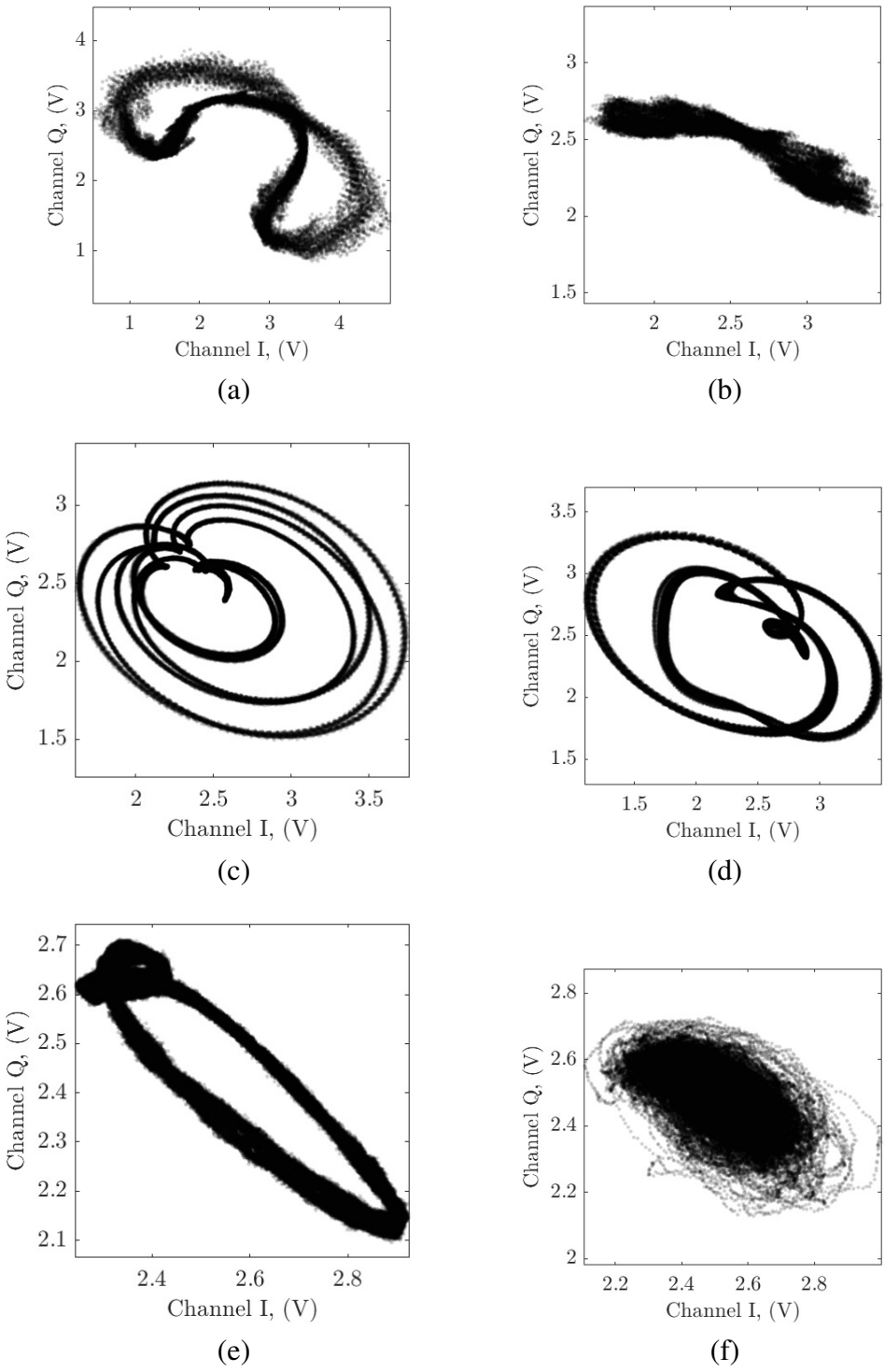

Figure 4.27 Measurements with the I/Q constellations for sensing motions with different amplitude and frequency (a) 1.39 mm amplitude 4.4 Hz metal plate motion, (b) 0.46 mm 5.6 Hz metal plate motion, (c) 9.43 mm amplitude 0.5 Hz gravity wave No.7, (d) 3.58 mm amplitude 2.0 Hz gravity wave N0. 18, (e) 0.72 mm amplitude 3.4 Hz gravity wave and (f) water random motion smaller amplitude (wave condition 2 in Table 4.5).

transform function can be represented as (Gu et al., 2016, Rodriguez and Li, 2019, Tan and Jiang, 2018)

$$H_{B1}(z) = A_s \cdot \frac{1 - z^{-1}}{1 - a_1 z^{-1}} \tag{4.4}$$

where A_s is the gain factor and a_1 is the characteristic coefficient of the system response. This is the first-order form of Eq. 2.46. The value of gain and coefficient a_1 is calculated from the RC electric circuit according to equations (Tan and Jiang, 2018)

$$\text{when } f_c < f_s/4, a_1 \approx 1 - 2 \times (f_c/f_s) \tag{4.5a}$$

$$\text{when } f_c > f_s/4, a_1 \approx -(1 - \pi + 2 \times (f_c/f_s)) \tag{4.5b}$$

$$A_s = \frac{1 + a_1}{2} \tag{4.5c}$$

By substituting the high pass cutoff frequency f_{cH} 4.08 Hz and sampling frequency f_s 1 kHz into equations 4.4 and 4.5, the transfer function of the high pass filter used in this study can be obtained as $H_{B1}(z) = A_s \cdot [(1 - z^{-1})/(1 - 0.974z^{-1})]$. The magnitude response of a single high pass filter and the two cascaded high pass filters are illustrated in Fig. 4.28 as blue and red lines, respectively. Signals below 4 Hz are rolled off and signals below 23 Hz are potentially affected. To compensate the potential signal distortion caused by the high pass filters, a compensation filter proposed by Gu et al. (2016) is applied. The transfer function of the compensation function H_D is the inverse function of $H_{B1}(z)$, which is the first-order form of Eq. 2.47

$$H_{D1}(z) = \frac{1 - a_1 z^{-1}}{1 - z^{-1}}. \tag{4.6}$$

The magnitude response of the compensation function H_{D1} is shown in Fig. 4.28 in a magenta line and the response of two compensation function is in green line. The compensation function $H_{D1}(z) = [(1 - 0.974z^{-1})/(1 - z^{-1})]$ has high gain in the < 4 Hz region. Gu et al. (2016), Rodriguez and Li (2019) have applied the compensation function H_D once to correct the signal distortion caused by one high pass filter. Ideally, the effect of the high pass filters can be compensated by applying the compensation function H_{D1} twice as indicated in Fig. 4.28 by the pink line.

To verify the theory discussed above, simulations were performed for the 24 GHz (12.43 mm wavelength) DRS to detect a 2 mm amplitude 2 Hz sinusoidal displacement ($x_m = A_m \sin(2\pi f_m t)$, $A_m = 2$ mm, $f_m = 2$ Hz). Assuming the I/Q channels have no imbalances or noise, the input signal before the high pass filter can be expressed by $C_{in}(t) = I(t) + j \cdot Q(t)$,

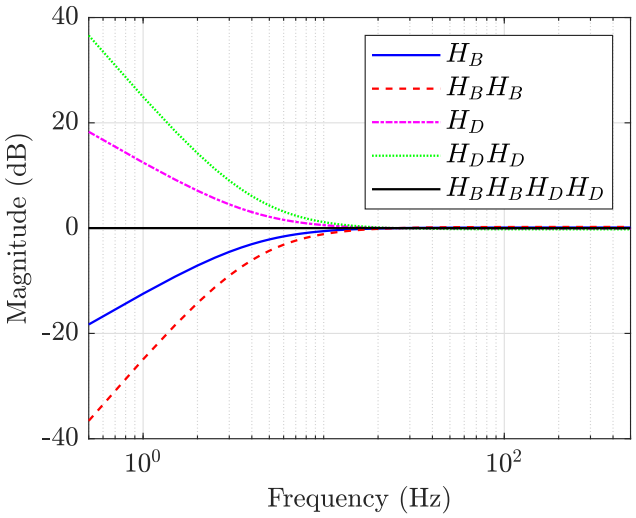

Figure 4.28 Magnitude response of the electric circuit calculated filter transfer function and compensation transfer function.

with $I(t), Q(t)$ calculated according to Equation. 2.45. The time series of I/Q channels are shown in Fig. 4.29 on the left with the corresponding I/Q constellation on the right. From Fig. 4.29a, b and c, it can be seen that the signal can be corrected successfully when distorted by a single high pass filter. After the signal is distorted by the high pass filter twice as shown in Fig. 4.29d, only one stage distortion can be corrected (Fig. 4.29e) while an unstable result is obtained if the distorted signal is corrected twice (Fig. 4.29f). This happens because the gain of $H_{D1} \cdot H_{D1}$ is too high in frequencies close to 0 Hz as indicated by the green line in Fig. 4.28, making the system unstable.

A high pass filter is proposed to be included in the compensation transfer function to reduce the high gain near 0 Hz and make the total system stable. The finite impulse high pass filter is designed by the MATLAB function 'designfilt' with stop band frequency 0.1 Hz and pass band frequency 0.2 Hz. The magnitude response of the designed high pass filter is shown in Fig. 4.30a with a red line. It can be noted that the high gain near 0 Hz is reduced with the addition of the high pass filter while not affecting the magnitude response for other frequencies. The proposed new compensation transfer function $H_{D1} \cdot H_{D1} \cdot H_{HP}$ is applied to the signal distorted by the two high pass filters in Fig. 4.29d and the distorted signal can be effectively corrected as shown in Fig. 4.30b. The proposed compensation transfer function has been shown to be valid for mechanical motion with frequency above $\sim$ 0.5 Hz.

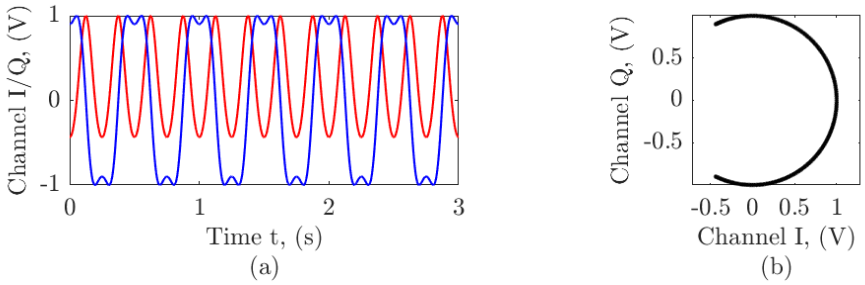
Channel I/Q, (V)
Time t, (s)
(a)
Channel Q, (V)
Channel I, (V)
(b)

(a)

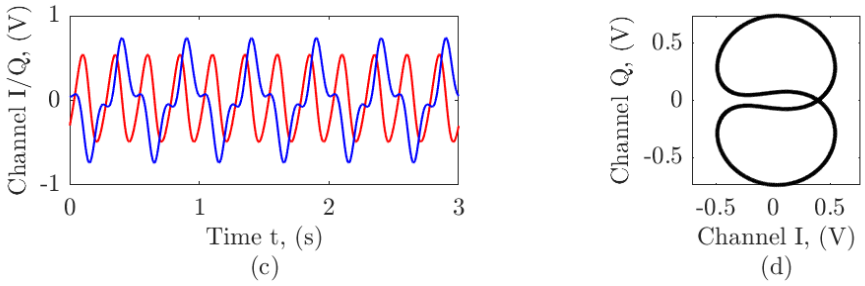
Channel I/Q, (V)
Time t, (s)
(c)
Channel Q, (V)
Channel I, (V)
(d)

(b)

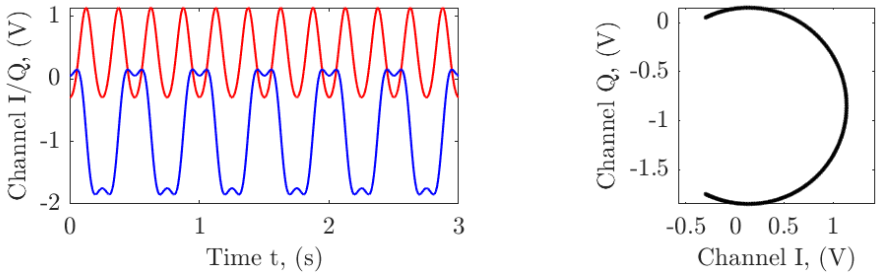
Channel I/Q, (V)
Time t, (s)
Channel Q, (V)
Channel I, (V)

(c)

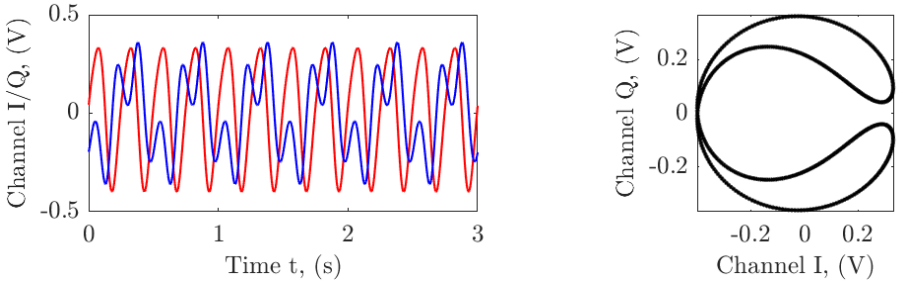
Channel I/Q, (V)
Time t, (s)
Channel Q, (V)
Channel I, (V)

(d)

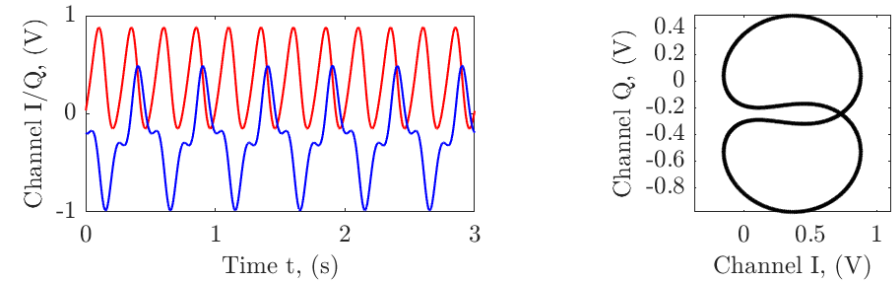

(e)

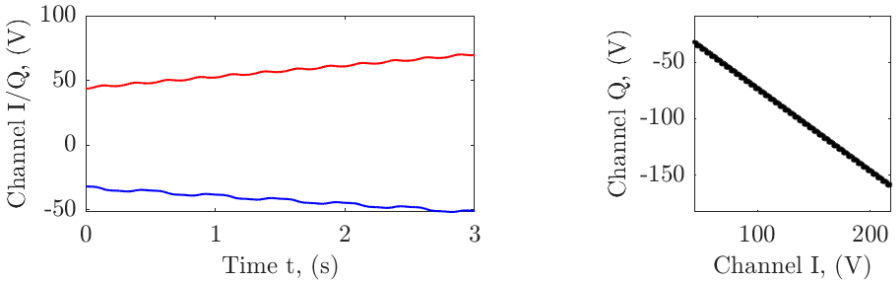

(f)

Figure 4.29 Simulation results of idea, distorted and compensated I/Q signals in time domain and in the I/Q plane: (a) C_{in}, (b) $C_{in} \cdot H_{B1}$, (c) $C_{in} \cdot H_{B1} \cdot H_{D1}$, (d) $C_{in} \cdot H_{B1} \cdot H_{B1}$, (e) $C_{in} \cdot H_{B1} \cdot H_{B1} \cdot H_{D1}$ and (f) $C_{in} \cdot H_{B1} \cdot H_{B1} \cdot H_{D1} \cdot H_{D1}$. (a) and (c) represent signals in the shape of a perfect arc, which correspond to the original signal and the successfully compensated signal, respectively. (b) and (d) show signals distorted into ribbon shapes. (e) represents a signal with a linear trend line, indicating unsuccessful compensation.

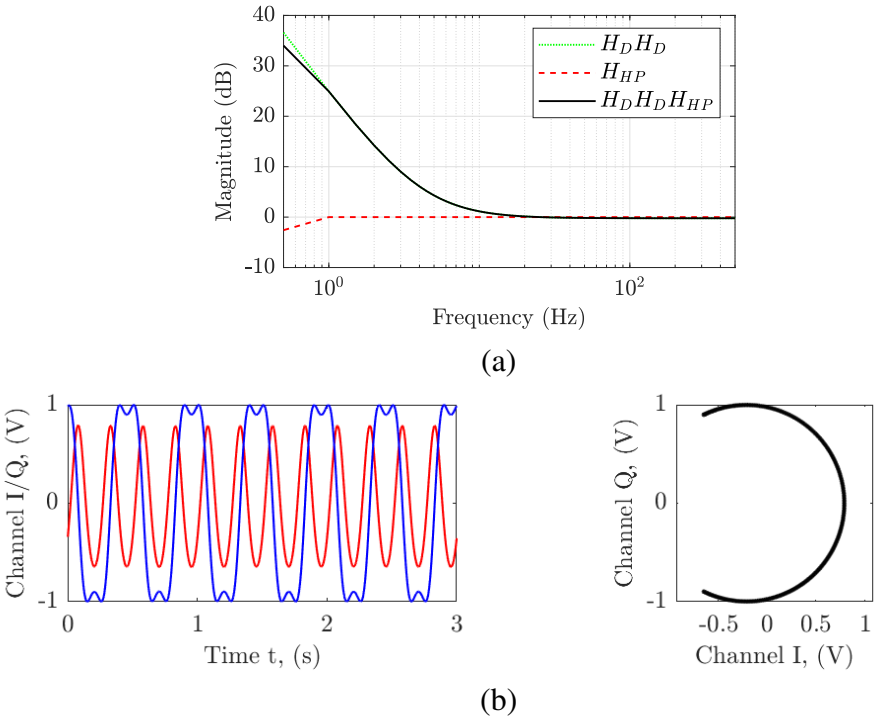

Figure 4.30 (a) Magnitude response of the compensation transfer function with additional FIR high pass filter. (b) Simulation results of the proposed transfer function $H_D \cdot H_D \cdot H_{HP}$.

The proposed modified compensation function $H_{D1} \cdot H_{D1} \cdot H_{HP}$ is then applied to experimental results to verify the performance in reality. The experiment results for two metal plate sinusoidal motions are illustrated in Fig. 4.31a, c and compensated results in b, d. It can be noted that the signal does improve with the compensation while still exhibiting a ribbon like shape. The compensation transfer function coefficients a_1 in Eq. 4.6 are calculated from the electric circuit according to Eq. 4.5. However, the coefficient may change due to the tolerance of the RC components in a practical circuit, causing under or over compensation. The coefficient a_1 calculated from the electric circuit can be used as an initial start. An optimisation procedure is further required to find the optimum coefficient a_1 to match reality. The optimisation procedure and calibration will be presented in subsection 5.5.1.

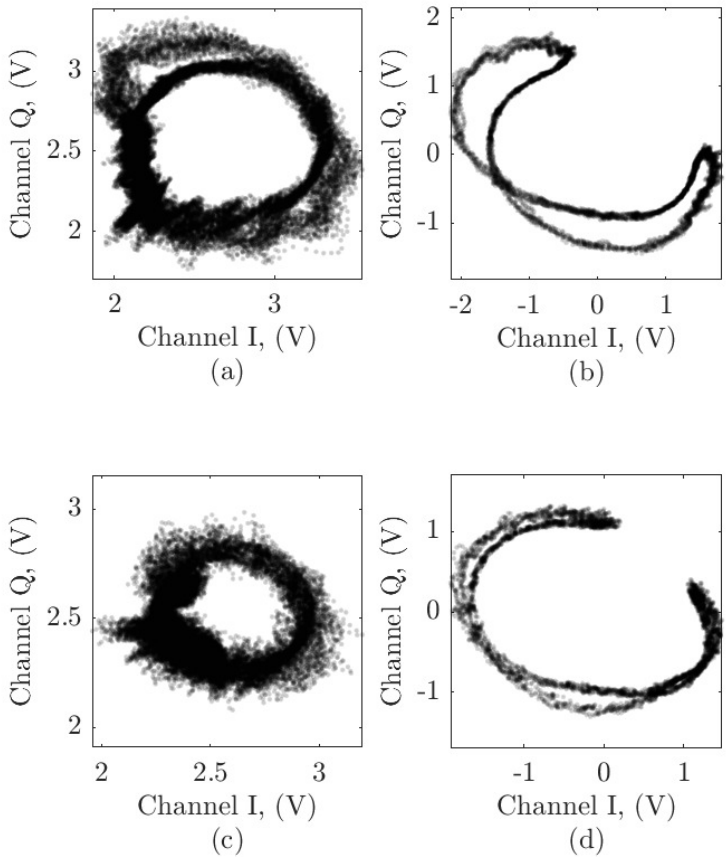

Figure 4.31 Metal plate motion experiment I/Q constellation (left) and compensated I/Q constellation (right). (a)(b) motion 32 ($x_m = A_m \sin(2\pi f_m t)$, $A_m = 1.93$ mm, $f_m = 2$ Hz) and (c)(d) motion 41 ($x_m = A_m \sin(2\pi f_m t)$, $A_m = 2.44$ mm, $f_m = 1$ Hz) in Table. 4.3.

4.6 Effect of temperature and concentration of TiO_2

As mentioned in section 3.7, the water temperature was regularly measured and 0.06 % mass concentration of TiO_2 was added to the water for the flow tests. The effects of temperature and concentration of TiO_2 on surface dynamics are explored in this section. The flow condition 14 (the highest flow with $Q = 28$ Ls^{-1}) was running continuously and the temperature of the water was naturally rising continuously during this period. The voltage of 7 wave probes were recorded at 100 Hz and 180 s for 11 different temperatures (from 19.7 °C to 20.7 °C). Fig. 4.32a and b show the effect of temperature on the wave probe voltage mean and standard deviation, respectively. Diamond markers represent the mean value of 7 wave probes and error bars represent the maximum and minimum values of 7 wave probes. As shown in Fig. 4.32a, the mean voltage increases with the temperature linearly and a degree Celsius in temperature rise results in 0.48 V increase in mean voltage. This result may be explained by the fact that the conductivity of water increases as the water temperature increases. Figure 4.32b shows some fluctuations and a general trend of increase in voltage standard deviation with increase of temperature. This may also be explained by the increase of water conductivity. Two measurements were taken successively at temperature 20.7 °C, which are illustrated by the two rightmost markers and error bars in Fig. 4.32a and b. It can be observed that, with the same temperature, the wave probe mean changes within 0.8 % and the standard deviation varies by 3.8 %. This could also explain the fluctuation of the trend in Fig. 4.32b. Fig. 4.33 demonstrates the power spectrum of wave probe 1 at different temperatures, with a dashed line representing the power decay $\propto f^{-5}$. These results indicate that temperature does not affect the general shape or the slope of the power spectrum significantly.

It is thought that high concentrations of TiO_2 can have a significant effect on the hydrodynamics (Nichols et al., 2020), because a 1 % concentration of TiO_2 is reported to reduce the surface tension by almost 30 % and increase the fluid viscosity by over 10 % (Przadka et al., 2012). Viscosity proportionally affects the flow Reynolds number, which is crucial for understanding turbulence processes and also drag and energy losses resulting from flow around obstacles. Laiadi and Merzougui (2019) showed that changes in surface tension can affect the free-surface profile in shallow flows, while Balabel and Alzaed (2018) showed that changes in surface tension and viscosity can affect the propagation of the wave front in dam break scenarios. This may explain why Martínez-Aranda et al. (2018) found that their experimental TiO_2–Kinect data did not match the established model data, particularly in the vicinity of obstacles, where surface tension and viscosity effects would be more apparent. These experimental uncertainties are also apparent in comparison with other models (Martínez-Aranda et al., 2018). Przadka et al. (2012) found anatase TiO_2 to marginally

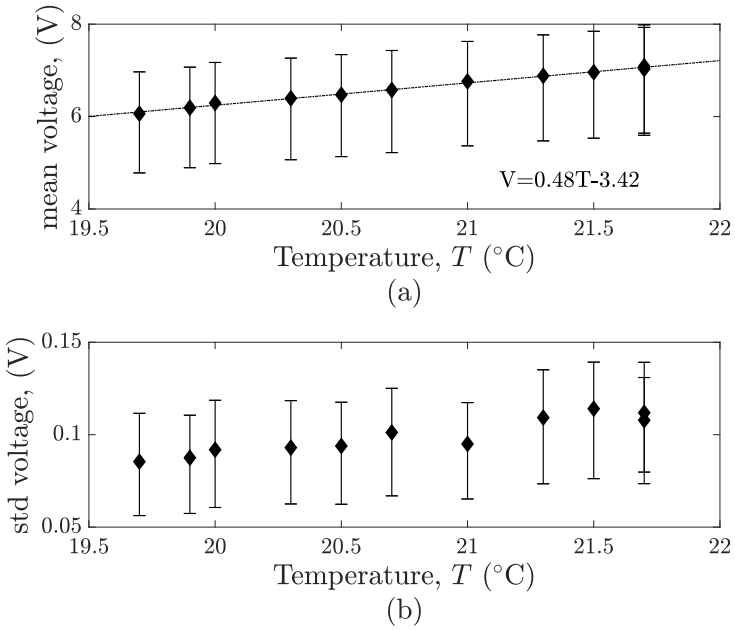

Figure 4.32 The effect of temperature on the wave probe (a) mean of voltage and (b) standard deviation of voltage.

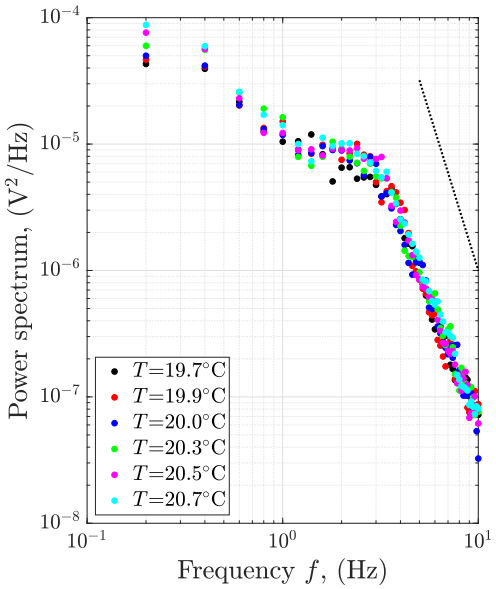

Figure 4.33 The effect of temperature on the wave probe power spectrum.

affect wave properties, but this was for a transient wave of larger magnitude than the waves often of interest in turbulent flows. Hence, the effect of anatase TiO_2 concentration on surface tension and gravity wave behaviour for small-scale, continuously generated waves were systematically explored. The relevance of this is that the effect of TiO_2 may then be inferred for a given concentration. It can therefore be used to elucidate the potential impact on previous studies that used TiO_2 indiscriminately, and to inform experimental design of future TiO_2 tinted water surface optical measurements.

The liquid surface tension was measured using a KRUSS tensiometer (model no. K11MK4) (Fig. 4.34) with the plate method (KRUSS, 2022). Samples of water with different concentrations of TiO_2 (0 - 2 %) were prepared and well mixed before the measurement. A plate was lifted up from the surface of the sample in the container and the force required to raise the plate from the liquid surface was measured to determine the surface tension. Each measurement was repeated five times and averaged.

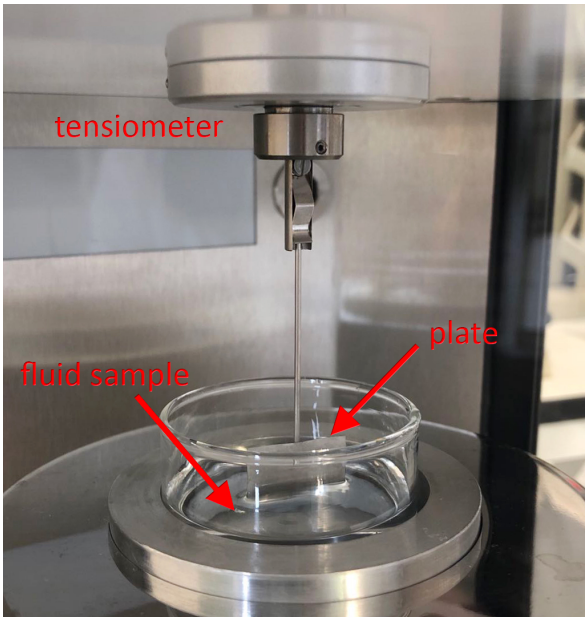

Figure 4.34 Surface tension measurement by KRUSS tensiometer with plate method.

Figure 4.35 shows the surface tension as a function of TiO_2 concentration. It can be seen that even small concentrations cause a change in surface tension, with concentrations above 1 % reducing the surface tension by over 0.5 %. This difference may be enough to substantially affect fluid behaviour in the capillary wave regime or where a fluid is in contact with a solid obstacle.

A preliminary test was carried out in a water tank with horizontal dimensions 355 mm × 210 mm. The purpose of this test was to investigate the effect of anatase TiO_2 concentration

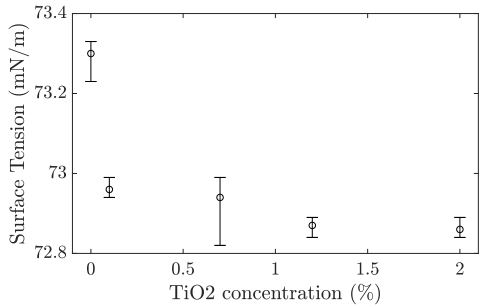

Figure 4.35 Surface tension measurement by KRUSS tensiometer with plate method.

on the behaviour of gravity–capillary waves on a still-water surface. The water surface was characterised using the DIC system, which required the background to be broadly white, with some darker floating tracers (ground black pepper) at the free surface. 5 L of tap water with different concentrations of TiO_2 (0.01 - 1.2 % by mass) was added to the tank. (Fig. 4.36). A continuous wave was excited by a 25 mm diameter sphere moving up and down sinusoidally, connected to a servo motor controlled by an Arduino Uno microprocessor (Arduino AG, Italy) at a frequency of 2.5 Hz and amplitude of 0.25 mm. Tests were repeated 10 times for each concentration and a 10 s period was recorded for every measurement.

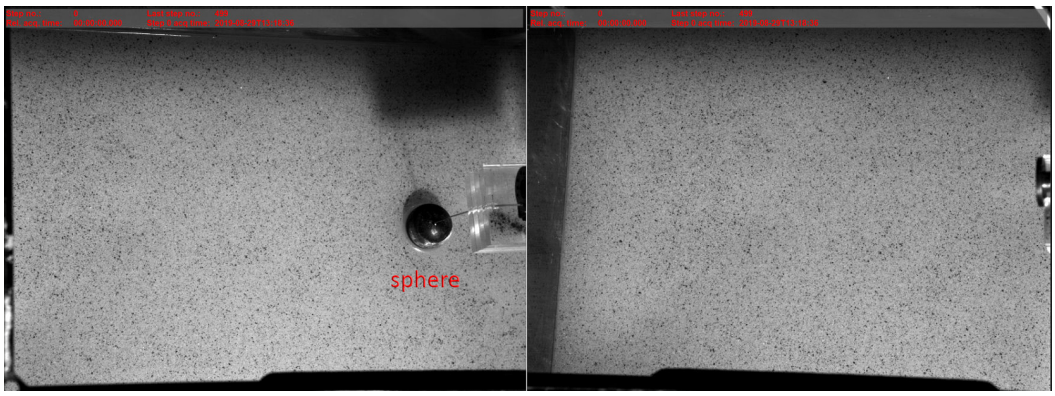

Figure 4.36 Two views of two DIC cameras from two directions.

The displacement of the wave in the vertical direction was evaluated from the videos of the two DIC cameras. Eight gauge points were chosen along the direction of the travelling wave, with different distances from the centre of the sphere generating the waves as illustrated in Fig. 4.37.

The vertical displacement of the eight chosen gauge points was computed by the Dantec dynamics software Istra-4D version 4.4.7.507 (the control software of the system Q-400). The exported data from ISTRA 4D in HDF5 format were imported into MATLAB R2019a and then processed. The wave height decreases as the gauge point moves further away from

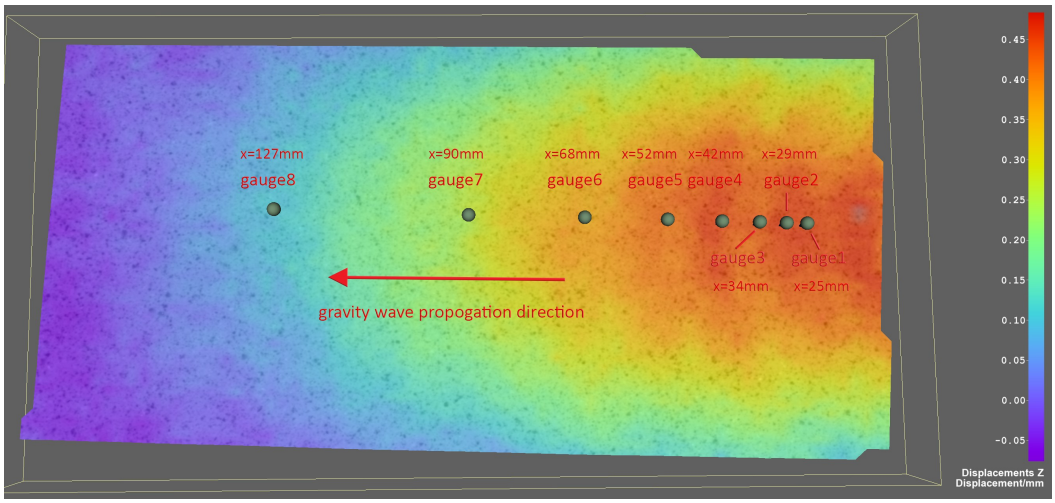

Figure 4.37 A section of evaluated displacement in z-direction by ISTRA 4D (x is the distance between the gauge point and centre of the sphere).

the sphere (centre of the wave), as shown in Fig. 4.38. A phase shift is also recognisable, illustrating the translation and celerity of the wave.

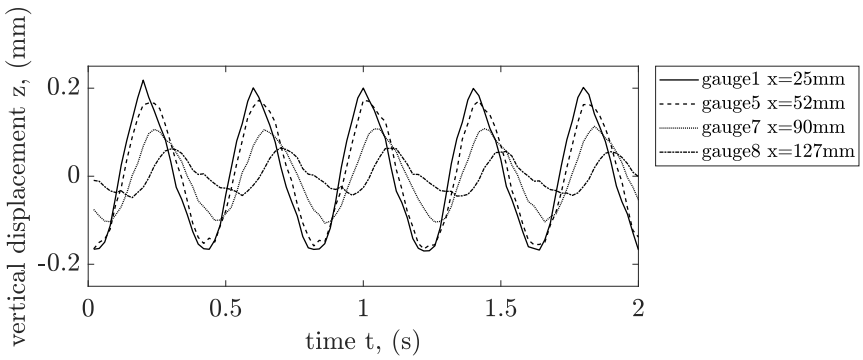

Figure 4.38 Time series of vertical displacement of four gauge points for concentration 1.2 %.

Figure 4.39 shows the standard deviation of the recorded wave signal in mm for gauge point 1, for 10 repeated measurements at each concentration. The cross markers show the mean value for each concentration. It is apparent that the wave height is substantially affected by the TiO_2 concentration. For a TiO_2 concentration of 1 %, the wave height is reduced by more than 25% compared with a 0.01 % concentration. Figure 4.40 shows the mean value of standard deviation for each concentration as a function of distance from the wave centre. It is clear that at all distances the impact of TiO_2 concentration on wave height is apparent.

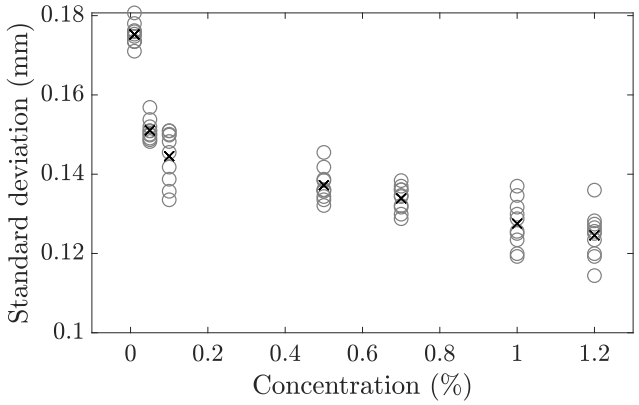

Figure 4.39 Standard deviation of wave fluctuation at gauge point 1 for different concentrations. Circles represent 10 repeats for each concentration, crosses represent the mean.

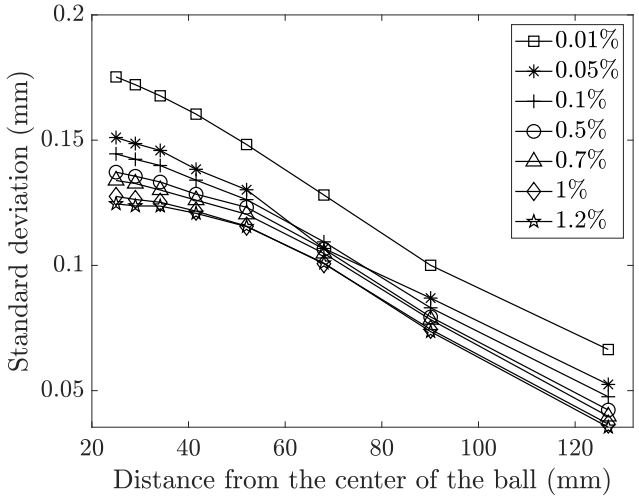

Figure 4.40 Standard deviation of wave fluctuations over distance for a range of concentrations.

Figure 4.41 shows the phase velocity of the wave, measured between gauge points 1 and 8, for each concentration. The wave speed was calculated by the ratio of separation of gauges (1 and 8) and the time lag. The time lag (phase shift) was determined from analytical signal theory (Hilbert transform). There is a clear trend in TiO_2 concentration reducing the phase speed of the wave, with a 1 % concentration reducing the phase speed by as much as 13.91 % compared to 0.01 % concentration. This again indicates that the behaviour of water surfaces with high TiO_2 concentrations (> 0.01 %) may be different to that of water alone.

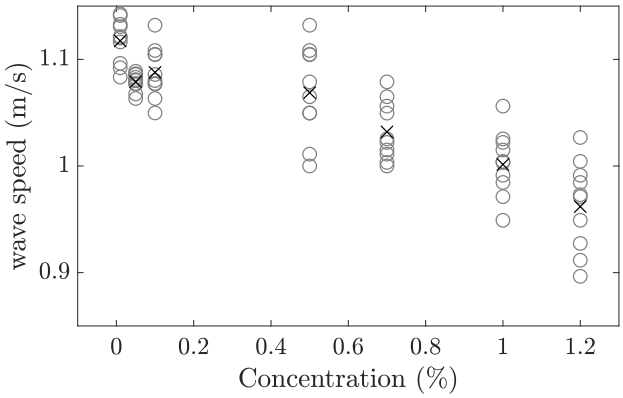

Figure 4.41 Averaged wave speed from 10 repeats versus different concentrations. Circles represent 10 repeats for each concentration, crosses represent the mean.

The preliminary test was carried out in a water tank with gravity waves using particle based optical technique. Results have shown that the gravity wave height and phase speed are affected by the adding of TiO_2. For the turbulent flow in a pipe, the particle based technique was found not to be practical as particles are less controlled on the water surface in turbulent flow. Instead, the projection based technique was implemented as described in 3.4 and 0.06 % of TiO_2 was added. The effect of using TiO_2 in turbulent flow is evaluated here. The flow condition 14 was running continuously and TiO_2 was incrementally added into the water (from 0 % to 0.04 %). The concentration of the TiO_2 is a mass concentration and calculated by the mass ratio of the TiO_2 powder and the mass of water. The temperature of the water was also measured during these measurements, ranging from 19.6 °C to 21.4 °C. As the temperature of the water also changed during this measurement, the wave monitor output is not only affected by concentration of TiO_2. The raw output of the wave probe is a fluctuating voltage. Table 4.6 compares the voltage mean and standard deviation with various temperatures and concentrations of TiO_2. With the same temperature, the mean and standard deviation of voltage always show higher values with higher concentrations of TiO_2. Figure . 4.42 demonstrates the power spectrum of wave probe 1 at different concentrations of TiO_2.

No significant change of the shape and gradient of the power spectrum can be observed due to the increase of TiO_2 concentration.

Table 4.6 The effect of temperature and concentration of TiO_2 on the wave probe mean and standard deviation of voltage for flow condition 14.

Temperature	Concentration of TiO_2	Voltage mean	Voltage std
(°C)	(%)	(V)	(V)
19.7	0	6.06	0.085
	0.002	6.21	0.092
	0.004	6.27	0.102
20	0	6.29	0.092
	0.008	6.44	0.103
20.3	0	6.39	0.093
	0.012	6.56	0.103
20.5	0	6.47	0.094
	0.016	6.66	0.108
20.7	0	6.57	0.101
	0.02	6.77	0.118

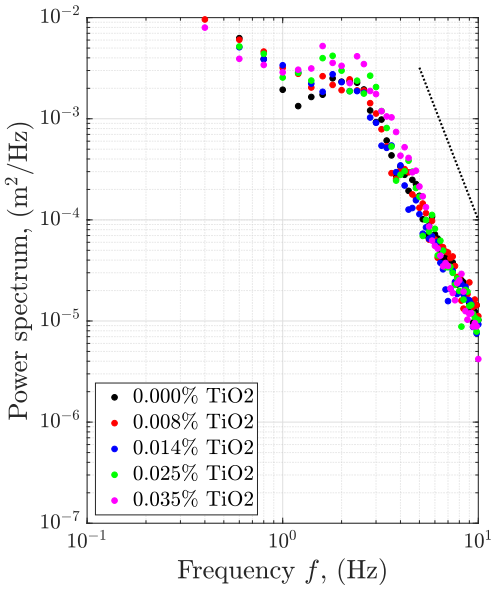

Figure 4.42 The effect of concentration of TiO_2 on the wave probe power spectrum.

4.7 Pre-processing and validation conclusions

In summary, this chapter presents the pre-processing and validation of wave probe data, DIC data, ADV data and radar data. Careful pre-processing of these data will enable a reliable assessment of the aims of this study. The uniform flow conditions were first examined to ensure the hydrodynamics were consistent in the measurement area. The wave probe data were converted from voltage fluctuation to surface fluctuation and then 10 Hz low pass filtered. The raw DIC data, x, y, z coordinate fluctuations of each facet in the image, were turned into surface fluctuations by subtracting their mean. DIC surface data were 2D median filtered to smooth the gap caused by reflection and air bubbles and 10 Hz low pass filtered to be consistent with wave probe data. The surface fluctuation from DIC is validated against wave probes. Good quality ADV data are objectively selected according to correlation value and velocity PDF distribution. ADV data are despiked with a phase-space despiking method and then 10 Hz low pass filtered. The mean velocity profile presented a reasonable parabolic shape and was validated against surface velocity. ADV data from two types of ADV instrument are comparable. The raw I/Q radar signal time series show the same period as the dominant frequency of motion. A modified compensation transfer function is proposed to improve the I/Q signal. The effect of temperature change in the free surface dynamics and the effect of concentration of TiO_2 on surface tension is examined. The effect of concentration of TiO_2 for gravity waves in a confined volume and turbulent flows in a continuously flowing pipe is characterised. With the confidence in the experiment data, more in depth analysis is shown in the next chapter.

Chapter 5

Results and Discussion

5.1 Sub-surface hydrodynamics

The hydrodynamics below the free surface of flows in a partially filled pipe are discussed in this section. First order sub-surface data from ADV (mean velocity profiles) is firstly produced, followed by second order analysis (turbulent quantities).

5.1.1 Velocity distributions

Guo et al. (2015) presented the theoretical centreline velocity profile (Eq. 2.19), which can be rearranged as

$$Y = U_{*c}X, \tag{5.1a}$$

$$Y = \kappa[\bar{u}(0,z) - \frac{Qz^3}{2I_2}], \tag{5.1b}$$

$$X = \ln\frac{z}{z_0} - (I_1 - \frac{A\ln z_0}{2} - \frac{3A}{8\lambda_s})\frac{z^3}{I_2}, \tag{5.1c}$$

where I_1, and I_2 are determined according to Eq. 2.20. According to the centreline velocity distribution theory (Guo et al. (2015)), the value of Y obtained from centerline streamwise velocity data should fall into a single straight line when plotted against X, with the slope representing the centerline shear velocity U_{*c} (see Eq. 5.1a). The rearranged terms X and Y are plotted against each other in Fig. 5.1, with a linear best fit forced through the origin. It can be noted that the velocity data does fall into a straight line and the slope of the straight line is comparable to the centreline shear velocity calculated from

$$U_{*c} = \lambda_s U_* = 1.1\sqrt{gR_hS}. \tag{5.2}$$

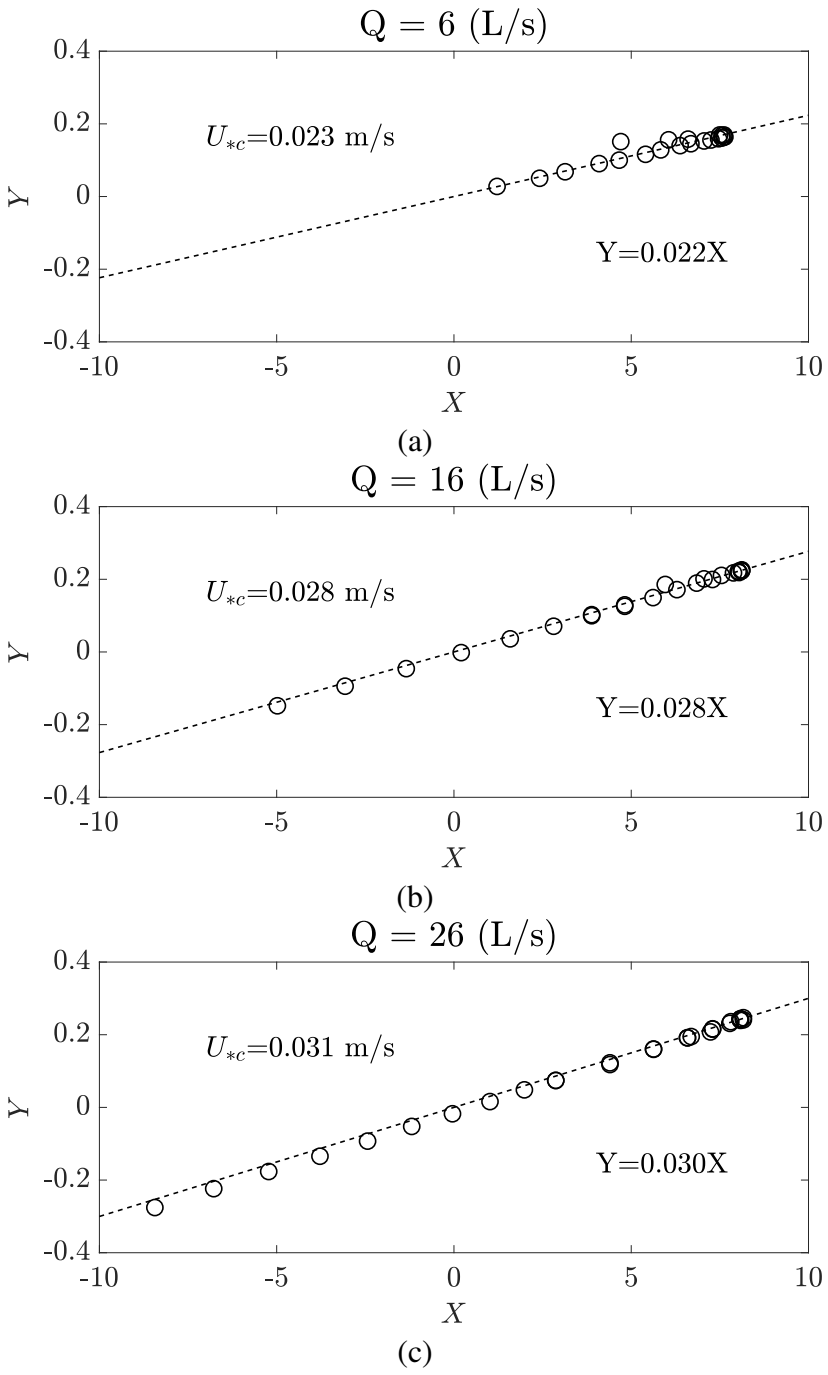

Figure 5.1 Determination of centreline shear velocity from theory of Guo et al. (2015) for flow condition (a) 3, (b) 8 and (c) 13.

The centreline shear velocity determined from the slope of the straight line in Fig. 5.1 is plotted against the centreline shear velocity determined from Eq. 5.2 in Fig. 5.2, with an approximate 1:1 linear relationship. The relative difference of centreline shear velocity determined from ADV streamwise velocity data and from Hydraulic radius and pipe slope

(Eq. 5.2) is within 3.22 %, showing good agreement. It confirms that the turbulent velocity distribution theory with dip phenomenon in conic open channels, which refers to a decrease or dip in the measured velocity profile, proposed by Guo et al. (2015) is also validated by this study. Additionally, this implies that with a known centreline velocity profile, the centreline shear velocity and U_{*c} the shear velocity of the full cross-section U_* can be estimated with 3.22 % relative error.

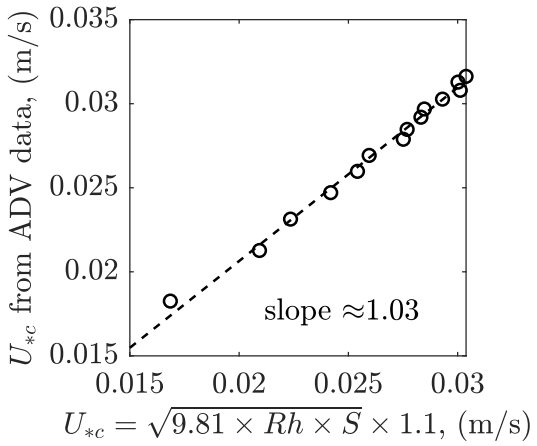

Figure 5.2 Centreline shear velocity from ADV data and from Equation. 5.2 for all flow conditions, with a best fit line through the origin.

Figure 5.3 and 5.4 compare the ADV measured data with the conventional log-law theory and the Guo et al. (2015) modified pipe velocity distribution theory, respectively. The non-dimensionalised mean velocity, U^+ is plotted against the non-dimensionalised depth-wise location, y^+ in accordance with Nezu and Nakagawa (1993), in Fig. 5.3. U^+ and y^+ are calculated according to Equations 2.17 and 2.18, respectively. 5 flow condition results are plotted in the same figure with offsets applied for clarity. It can be noted that normalised velocity follows the conventional log-law up to a certain distance and then deviates downward from the log-law, indicating a dip in velocity close to the free surface. This phenomenon is also observed by several previous studies (Clark and Kehler, 2011, Ead et al., 2000, Guo et al., 2015, Wu et al., 2018). Profiles of centreline streamwise velocity $\bar{u}$ normalised by the centreline shear velocity U_{*c} are shown in rectangular coordinates in Fig. 5.4 and offset by 10 units of normalised velocity between each profile for ease of visualisation. It is evident that the velocity gradient at the wall increases with the increase of flow (higher Re flows), which agrees with the traditional theory of velocity profiles in fullly filled pipes (Michell, 1970). Interestingly, when the pipe is $d/D = 22.04$ % filled, the ADV data overlap with both log-law and the theory of Guo et al. (2015) well. However, the data no longer fit the log-law in high depth-wise positions for flows with $d/D > 35$ %. This makes sense as when the pipe

is shallow filled, the pipe curvature plays a less significant role. From left to right in Fig.5.4, the difference between the log-law and Guo et al. (2015) model is larger with increasing depth d/D and the profile shape tends to be more similar with the velocity profile seen in fully filled pipe flow. The dip phenomenon can be observed for flow with relative depth more than 35 % in this study, whereas Wu et al. (2018) and Yoon et al. (2012) only observe it for over half filled turbulent flow and Guo and Meroney (2013) for $d/D > 0.875$ partially laminar flow. Ng et al. (2021) did observe this phenomenon for both less than half filled and more than half filled (where 44 % < d/D <80 % in their study) turbulent pipe flows and Guo et al. (2015) found the velocity dip for all the flows examined in their study (where 34 % < d/D <65 % in their study). The results presented here are consistent with Guo et al. (2015) and Ng et al. (2021), confirming the occurrence of a velocity dip even when the pipe is less than half filled.

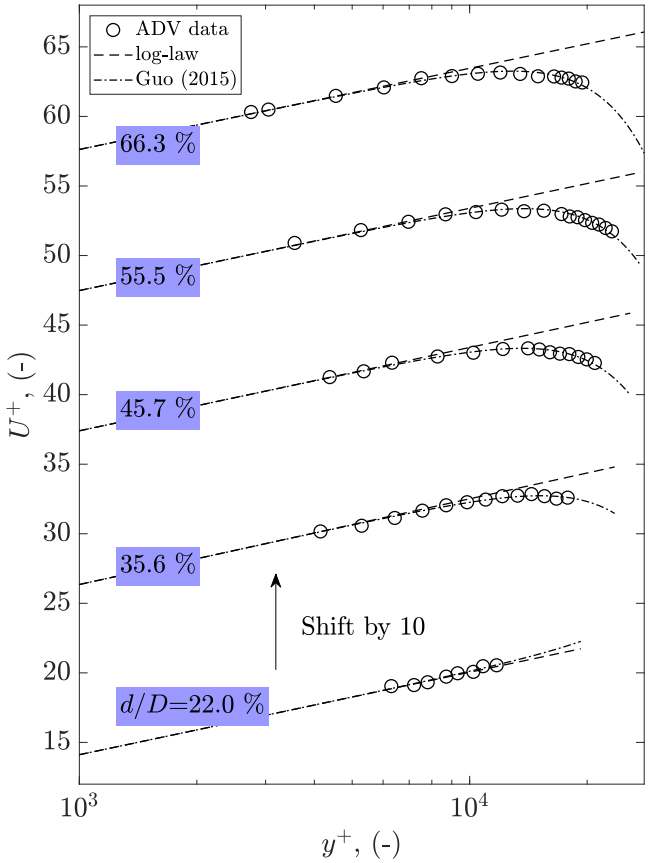

Figure 5.3 Comparison of normalised streamwise centreline velocity distribution from ADV measurement data and Guo et al. (2015) model in semi-log scale, flow condition 2, 5, 8, 11 and 14 (flow bottom to top). d/D represents the depth filling ratio of the pipe. The x values is normalised depthwise location, calculated according to Eq. 2.18.

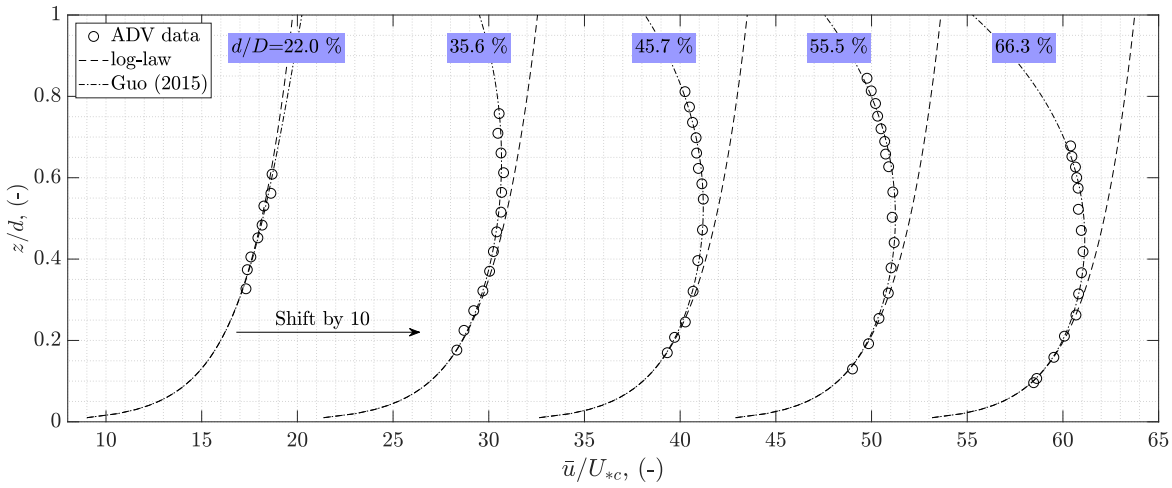

Figure 5.4 Comparison of streamwise centreline velocity distribution from ADV data with convention log-law and modified pipe velocity distribution Equation. 2.19, flow condition 2, 5, 8, 11 and 14 (flow left to right).

The 2D velocity field below the free surface is not obtained experimentally due to the limitation of 2D velocity methods such as PIV or Particle Tracking Vlocimetry (PTV) not working in tinted water. As no 2D sub-surface velocity data was obtained from this study experimentally, and a strong agreement was observed between 1D velocity data and the 1D velocity model of Guo et al. (2015), the 2D velocity field has been estimated using the 2D model of Guo et al. (2015) (Eq. 2.23). Low velocity can be observed near the pipe wall in all flow conditions and in the edge near the free surface in Fig. 5.5b, c and d. The maximum velocity occurs at the free surface as shown in Fig. 5.5a and at approximately 1/4 - 1/3 of the pipe diameter position for other flows (see Fig. 5.5b, c and d). Interestingly, the cross-sectional velocity distribution becomes very similar to that of full pipe flow in Fig. 5.5d, indicating that the free surface plays a role similar to the pipe wall to the under surface velocity field. It is likely that the energy is extracted from the nearby flow due to the roughness or the dynamic motion of free surface.

The velocity dip position from the bottom δ can be obtained from ADV fitted velocity profiles (see Fig. 5.4). To explore how the dip changes with the relative depth, the ratio of velocity dip position and water depth and the ratio of velocity dip position and pipe diameter is plotted against relative filled depth in Fig. 5.6 along with data from other studies. The difference between different studies is not surprising as they are obtained with a different pipe material, diameter and Reynolds number. The first square marker data point in Fig. 5.6a does not occur at the free surface ($\delta/d = 1$) because the equivalent sand-grain roughness k_s is extremely small (~ 0.25 mm) for this shallowest flow condition in a smooth pipe and strictly speaking the Colebrook-White Equation is accurate only for fully filled pipe flows (Guo et al.,

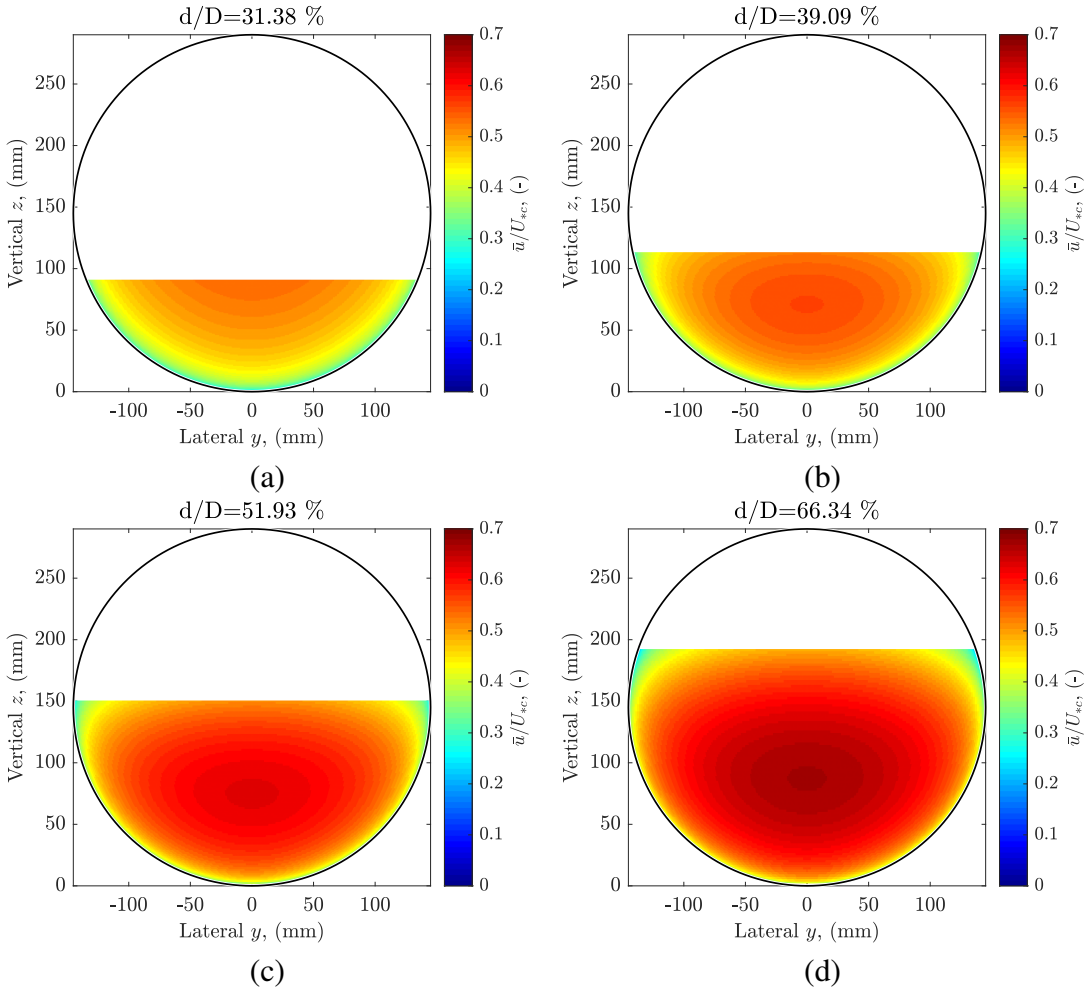

Figure 5.5 Predicted streamwise velocity profile over the cross-sectional area for flow conditions (a) 4, (b) 6, (c) 10 and (d) 14.

2015). The uncertainty in estimation of k_s makes the dip position for the shallowest flow less accurate. As is shown in Fig. 5.6a, the maximum velocity occurs at the free surface for d/D < 32 % and the position gradually decreases with the increase of the relative depth d/D. A similar decrease in δ/d for d/D > 32 % is also observed by Wu et al. (2018) and Yoon et al. (2012) and the magnitude is most similar to Guo et al. (2015). The dip position relative to pipe diameter gradually increases when d/D < 32 % and does not vary much after that. In flow conditions with a velocity dip, the dip always occurs at approximately 0.2 - 0.3 D no matter the increase of flow depth and approximately 0.35 - 0.4 D for Wu et al. (2018), Yoon et al. (2012). Ng et al. (2021) have used a 100 mm diameter pipe to examine both laminar and turbulent flow velocity profiles. Their study suggests that the velocity dip can only be observed for d/D > 85 % laminar flows while for even less than half filled turbulent flows. The dip position for laminar flows is at approximately z/D = 0.5 while at approximately z/D = 0.3 for turbulent flows. Therefore, the difference of the dip position in this study and other studies can be explained by different turbulent flow conditions, especially different Reynolds number. The Reynolds numbers for Guo et al. (2015), Wu et al. (2018), Yoon et al. (2012) and this study are 0.23 - 0.42, 6 - 14, 0.14 - 0.47 and 0.84 - 5.05 $\times 10^4$, respectively. The higher dip position from Wu et al. (2018) and Yoon et al. (2012) can be explained by their lower Reynolds number compared to this study.

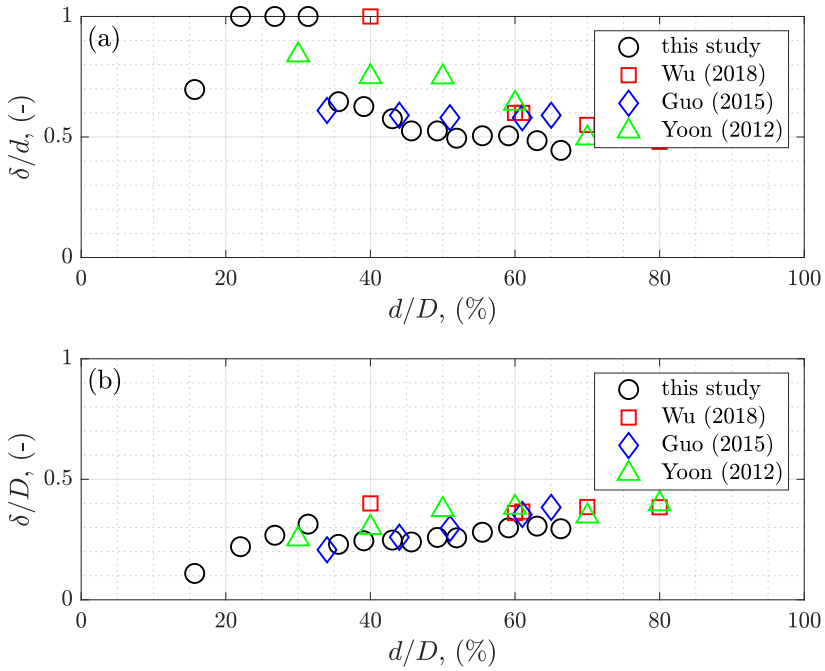

Figure 5.6 Velocity dip position δ relative to (a) water depth d and (b) pipe diameter D for all flow conditions in this study and study of Wu et al. (2018), Guo et al. (2015), Yoon et al. (2012).

The mean streamwise velocity profiles measured at the pipe vertical bisector for flow conditions 2, 5, 8, 11, 14 and fully filled pipe flow according to the one-seventh power-law (Eq. 2.15 with $n = 7$) are shown together in Fig. 5.7. The mean streamwise velocity is normalised by the maximum streamwise velocity in Fig. 5.7 (a)(b)(c) and by the bulk flow velocity in Fig. 5.7(d)(e)(f). The depth-wise position is normalised by water depth, pipe diameter and hydraulic diameter in Fig. 5.7 (a)(d), (b)(e) and (c)(f), respectively. Not surprisingly, all partially filled flows show different behaviour to fully filled pipe flow. The fully filled pipe flow velocity profile is symmetrical vertically while partially filled pipe flows are not. The $d/D = 22.0$ % profile is quite different with other partially filled conditions shown in Fig. 5.7a, c, d, e and f but similar to Fig. 5.7b. This is not observed in study of Ng et al. (2021) as the minimum filling ratio is 44 % in their study. In Fig. 5.7a, the highest flow condition profile shows a similar pattern to the fully filled pipe flow profile. From all sub-figures, it can be seen that flow conditions over $d/D > 35$ % follow the one-seventh power-law up to $z/d \approx 0.5$, $z/D \approx 0.26$ and $z/D_h \approx 0.25$ and deviate beyond that. This overlap and deviation pattern was also observed in the study of Ng et al. (2021) and the deviation positions share similarities. As shown in Fig. 5.7d, the maximum $\bar{u}/U_b$ ratio remains almost constant for flows over $d/D = 45$ %. Ng et al. (2021) claimed that no appreciable trend is found in the z/D_h versus $\bar{u}/U_b$ plot. However, in this study, as shown in Fig. 5.7f, velocity profiles for flows $d/D > 45$ % overlap each other and appear to be symmetrical about $z/D_h = 0.25$. In the study of Ng et al. (2021), this overlap only appears when the pipe is more than 62 % filled. This is likely because the dip phenomenon start to appear in a lower filling ratio compared to the study of Ng et al. (2021).

The relationship between bulk velocity, maximum streamwise velocity and the ratio of between bulk velocity and maximum streamwise velocity is plotted against relative depth in Fig. 5.8. It can be seen that both bulk velocity and maximum streamwise velocity increase with the relative flow depth and the rate of increase gradually decreases. The ratio of bulk velocity to maximum streamwise velocity increases with the relative depth until $d/D = 27$ % and remains almost constant beyond that. The bulk velocity is approximately 0.9 times the maximum streamwise velocity for flows $d/D > 32.4$ %. Yoon et al. (2012) observed a similar constant $\bar{u}/U_{max}$ phenomenon in a study using a 50mm diameter acrylic pipe. However, they found the constant $\bar{u}/U_{max}$ appears for over half filled pipe flows and the constant ratio was approximately 0.71, which is smaller than found in this study.

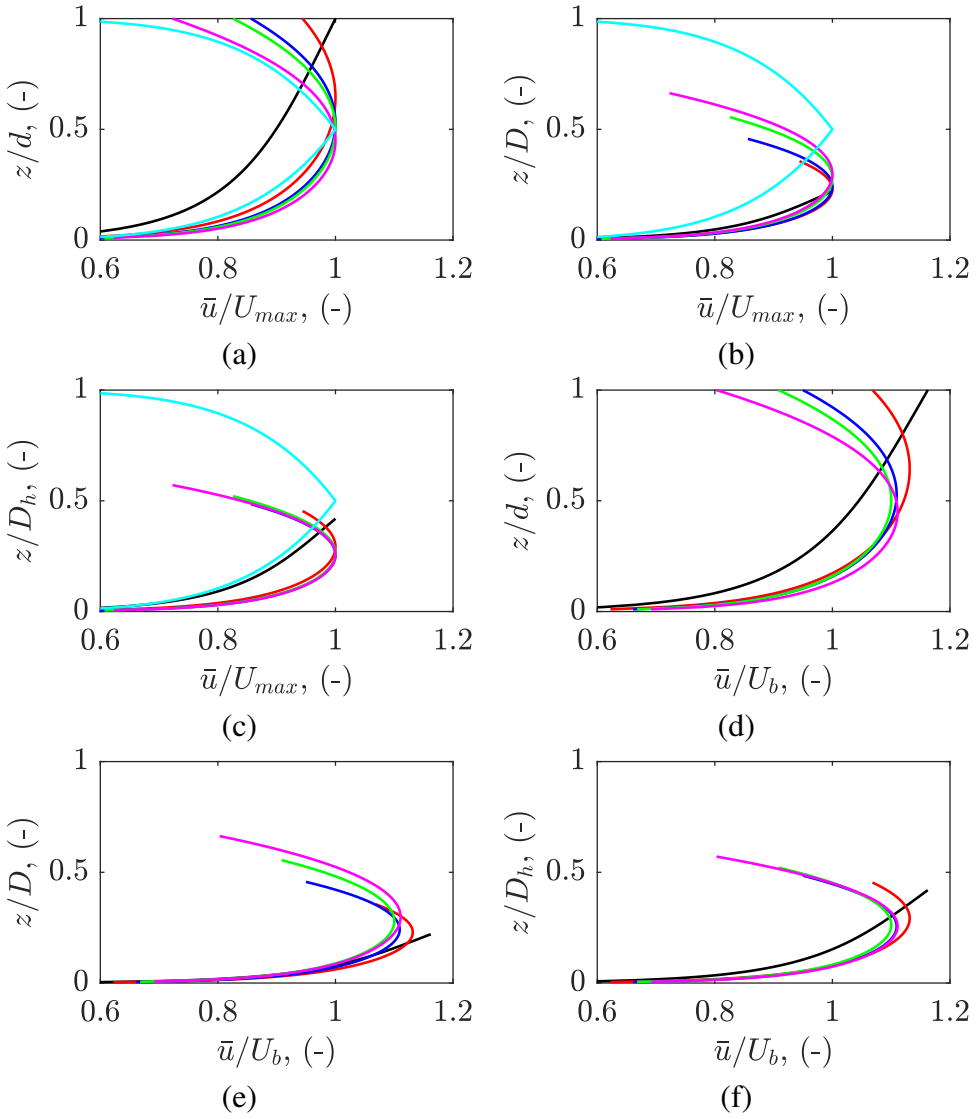

Figure 5.7 (a-c) Mean streamwise velocity $\bar{u}$ along the vertical bisector scaled with maximum streamwise velocity U_{max} and (a) flow depth d; (b) pipe diameter D and (c) hydraulic diameter D_h, respectively. (d-f) (a-c) Mean streamwise velocity $\bar{u}$ along the vertical bisector scaled with bulk flow velocity U_b and (a) flow depth d; (b) pipe diameter D and (c) hydraulic diameter D_h, respectively. (—): flow condition 2, d/D = 22.0 %; (—): flow condition 5, d/D = 35.6 %; (—) flow condition 8, d/D = 45.7 % ; (—) flow condition 11, d/D = 55.5 %, (—) flow condition 14, d/D = 66.3 % and (—) full pipe, d/D = 100.0 %.

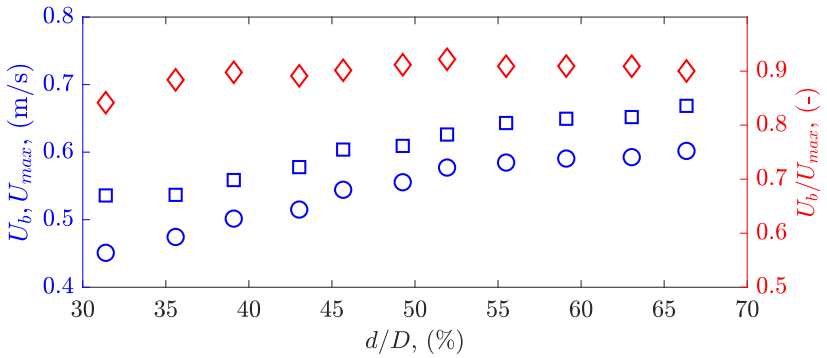

Figure 5.8 The relationship between U_b, U_{max} and U_b/U_{max} with d/D. (**o**): bulk flow velocity; (□): maximum streamwise velocity and (◊): ratio of bulk flow velocity and maximum streamwise velocity.

5.1.2 Turbulence quantities

Subsection 5.1.1 discusses the mean sub-surface velocity field. Higher order sub-surface velocity field analysis, and analysis of turbulence quantities will be presented in this subsection. An example of turbulence intensity profiles (standard deviation of velocity normalized by shear velocity) is shown in Fig. 5.9. Markers in black circles indicate measurement results calculated from side-looking ADV and markers in red squares are from downward-looking ADV. Both types of ADV follow the same trend for streamwise turbulence intensity profiles as shown in Fig. 5.9a while there is some disparity for lateral and vertical intensity profiles as shown in Fig. 5.9b and c. Additionally, side-looking ADV measurement show more consistent results in Fig. 5.9b. As mentioned in subsection 4.4.2, the relative difference of mean value for the two types of ADV is less than 2 % and approximately 5.4 % for standard deviation of velocity. The relative difference in standard deviation of streamwise, lateral and vertical velocities are 5.3 %, 5.5 % and 5.5 %, respectively. Standard deviation of lateral and vertical velocities from downward-looking ADV deviate more from side-looking ADV compared with streamwise velocity. This explains the relative larger discrepancy in the lateral and vertical turbulence intensity profiles in Fig. 5.9b and c. Higher order statistics, such as standard deviation, are more likely to be affected by measurement noise. Side-looking ADV is intended to be used near solid boundaries while downward-looking ADV has strong echoes when it is placed close to the bed, which can affect signal quality. Therefore, only side-looking ADV data and streamwise downward-looking ADV data are used for higher order analysis, such as turbulence intensities, Reynolds normal stress and turbulent kinetic energy (TKE), in this study.

Wu et al. (2005) have found that the turbulence intensity distribution is different for less than half filled and more than half filled pipe flows. This study found the turbulence

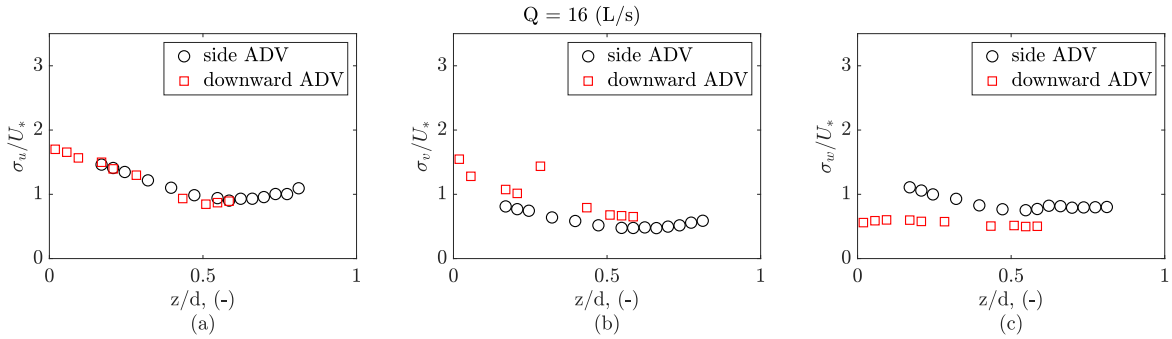

Figure 5.9 Turbulence intensities for flow condition 8 from side-looking ADV and downward-looking ADV, (a) streamwise, (b) lateral and (c) vertical.

intensity distribution is different for $z/d < 35$ and $z/d > 35$. The different threshold is likely due to the dip phenomenon as Wu et al. (2018) only observed the dip phenomenon for the more than half filled pipe conditions. 3C turbulence intensity (three turbulence intensity components) profiles are illustrated in Fig. 5.10, with a theoretical curve proposed by Nezu and Nakagawa (1993) in rectangular open channels and an empirically derived curve for corrugated pipes proposed by Clark and Kehler (2011). Left column sub-figures are overlapped from flow conditions 1 - 4 ($z/d < 35$ %) and right column sub-figures are overlapped from flow conditions 5 - 14 ($z/d > 35$ %).

In general, the turbulence intensities of all three components decrease with depth-wise position for low flow rate flows, as shown in Fig.5.10a, c, and e. The streamwise turbulence intensity profile, depicted in Fig.5.10a, generally follows the trend proposed by Nezu and Nakagawa (1993) and agrees well with Wu et al. (2018). However, the magnitude of streamwise turbulence intensity decreases with increasing depth-wise position, exhibiting a slightly smaller gradient of decay compared to the theory proposed by Nezu and Nakagawa (1993). Regarding lateral turbulence intensity profiles, low flow rate flow turbulence intensity follows the trend from Clark and Kehler (2011) as shown in Fig. 5.10c, although the dip is not as pronounced as observed in the study by Clark and Kehler (2011). Interestingly, the vertical turbulence intensity profile for low flow rate flow does not conform to either of these studies, as higher vertical turbulence intensities were observed.

In the right column of Fig. 5.10, all 3C turbulence intensity decrease and then increase with an increase of the depth-wise position, which agrees with the observation in corrugated pipes (Clark and Kehler, 2011). To describe the variation of turbulence intensity at the lateral center of a smooth perspex pipe for higher flows, the following turbulence intensity equations modified from Eq. 2.25 by Clark and Kehler (2011) are proposed:

$$S_u/U_* = 3.25z/d^2 - 3.73z/d + 2.06, \tag{5.3a}$$

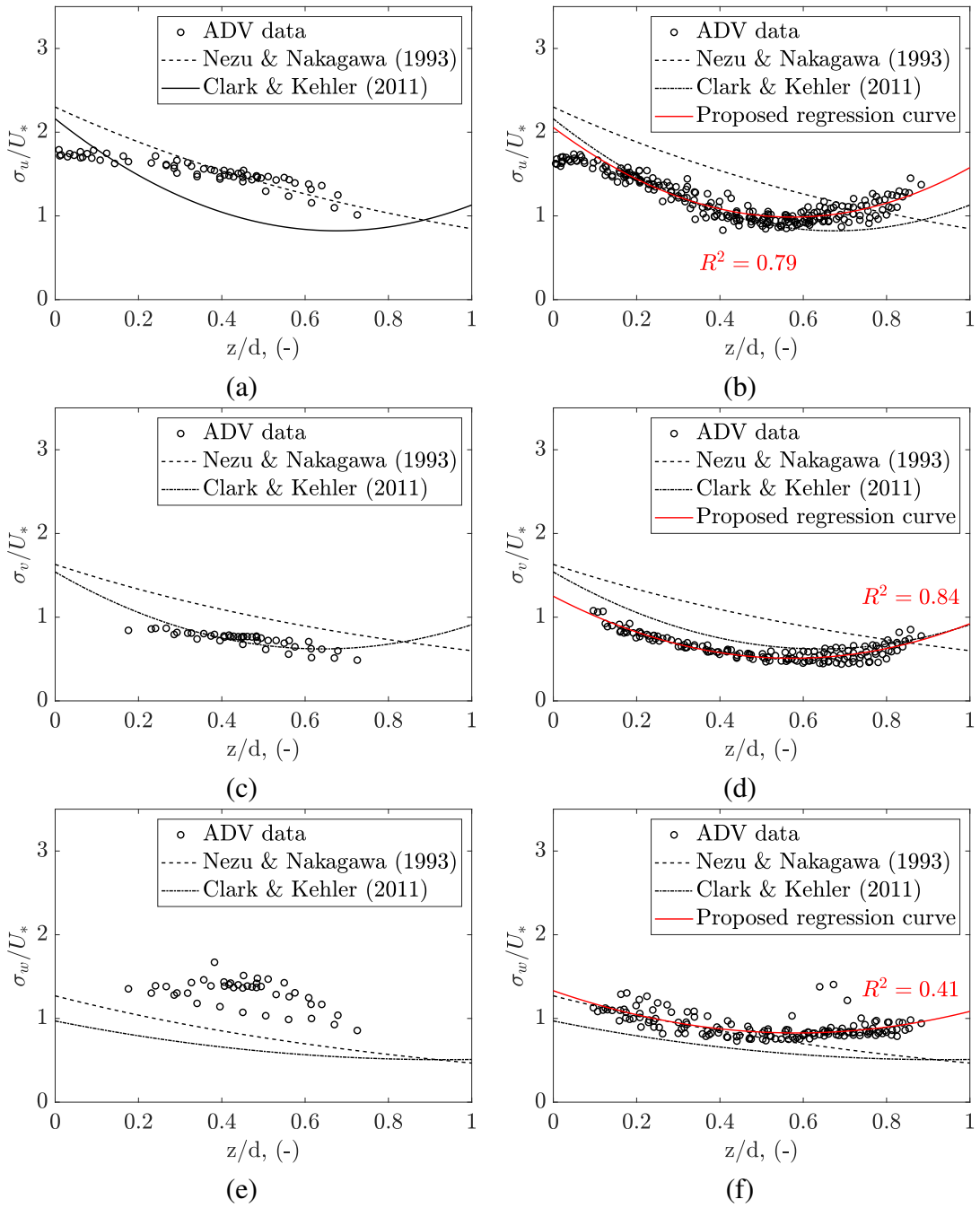

Figure 5.10 Turbulence intensities for flow condition 1 - 4 on the left column and 5 - 14 on the right, (a)(b) streamwise, (c)(d) lateral and (e)(f) vertical. The dashed line represent theory proposed by Nezu and Nakagawa (1993) for a rectangular channel and dotted dashed line represent theory proposed by Clark and Kehler (2011) for a partially filled corrugated pipe.

$$S_v/U_* = 2.26z/d^2 - 2.59z/d + 1.25, \tag{5.3b}$$

$$S_w/U_* = 1.48z/d^2 - 1.73z/d + 1.33. \tag{5.3c}$$

The modified turbulence intensity equations share the same terms with Eq. 2.25, but with different coefficients. The best fit coefficients are determined by the MATLAB 'fit' function with start points using coefficients in Eq. 2.25. Equations 5.3 provide a satisfactory data representation for streamwise and lateral turbulence intensities, with R^2 = 0.79, 0.84, respectively. Wu et al. (2018) have found the streamwise and lateral turbulence intensity starts to increase at a position around $0.5D$. A similar increase in streamwise and lateral turbulence intensity can also be observed in Fig. 5.10b, d but occurs at approximately z/d = 0.5. The vertical turbulence intensity regression curve has fits less well than the other two. This is likely because of: (i) Some outlier points in Fig. 5.10f (from flow condition 10), which could be measurement errors; (ii) The vertical velocity from ADV being generally more noisy compared to streamwise and lateral velocity; (iii) Some turbulence structures from the bed moving upwards affecingt the vertical velocity measurement and causing larger relative deviation in vertical turbulence intensity in $z/d < 0.4$. In theory, the turbulence intensity should be 0 when $z/d = 0$, so these equations are not valid in regions close to the bed.

Figure 5.11, 5.12 and 5.13 present profiles of 3C Reynolds normal stress (streamwise, lateral and vertical), TKE and Reynolds shear stress normalised by bulk flow velocity, respectively. The Reynolds normal stress refers to the components of the total stress tensor that are perpendicular to the mean flow direction. The Reynolds normal stresses can be decomposed into streamwise, lateral, and vertical components. They can can be calculated by taking the time average of the product of the fluctuating velocities in the respective directions ($\overline{u'^2}$, $\overline{v'^2}$ and $\overline{w'^2}$). TKE is a measure of the energy associated with turbulent fluid motion, it is calculated by taking the average of the squared velocities of the turbulent fluctuations in each direction (TKE = $(u'^2 + v'^2 + w'^2)/2$). TKE represents the fluctuating component of kinetic energy in a turbulent flow, and it quantifies the intensity of the turbulent motion. Reynolds shear stress is a component of the total stress tensor in fluid dynamics that accounts for the turbulent fluctuations in fluid momentum. It represents the transfer of momentum between different layers of fluid due to turbulent eddies. It is obtained by taking the average of the product of streamwise and vertical fluctuating velocities ($-\overline{u'w'}$).

Measurement results from flow conditions 2, 5, 8, 11 and 14, corresponding to filled ratio d/D = 22.04 %, 35.59 %, 45.68 %, 55.49 % and 66.34 %, respectively, are superimposed in these figures for better comparison. The results from these 5 flow conditions, are representative of all other flow conditions. As shown in Fig. 5.11 and 5.12, each of Reynolds normal stresses as well as TKE profiles show similar pattern. Streamwise normal stress show

the highest magnitude and lateral normal stress show the lowest magnitude, which means streamwise velocity contributes the most in TKE. Ng et al. (2021) observed 3C Reynolds normal stresses, TKE and shear stress all peak at $z/d \approx 0.2$ for all flow conditions measured by PIV in a $D = 100$ mm glass pipe. In Clark and Kehler (2011) study, similar peak is not observed in a $D = 800$ mm corrugated pipe with ADV measurement. In Fig. 5.11a $d/D = 55.49$ % condition (green markers) and Fig. 5.12 $d/D = 35.59$ %, 55.49 % condition (red and green markers), a peak can be observed at $z/d \approx 0.05$. However, this peak is not observed for other flows in Reynolds normal stress profiles and TKE profiles. The $z/d \approx 0.2$ peak is not obvious in this study is likely because of the resolution of the depth-wise measurement positions and not enough data points near bed. Besides, ADV becomes less robust approaching to the bed, thus has potential to lose some turbulent information close to the bed. The difference in $0 < z/d < 0.2$ region between the observation in Ng et al. (2021) and this study is not surprising as the pipe material, diameter, flow conditions and measurement technique are all different. In general, streamwise Reynolds normal stress, lateral Reynolds normal stress and TKE decrease linearly with the increase of depth-wise position up to $z/d \approx 0.5$, which agrees with study of Clark and Kehler (2011), Ng et al. (2021). Vertical Reynolds normal stress decrease non-linearly with the increase of depth-wise position up to $z/d \approx 0.5$, which is also observed by Clark and Kehler (2011). Beyond $z/d \approx 0.5$, for flow conditions with filled water $d/D < 36$ %, as indicated in Fig. 5.11 and 5.12 red markers, Reynolds normal stress and TKE remain constant until free surface. Similar constant Reynolds normal shear and TKE region is also observed by Ng et al. (2021) when the flow depth is less than $d/D = 52$ %. For flow depth greater than $d/D = 45$ %, 3C Reynolds normal stress and TKE increase non-linear with the increase of depth-wise position, which agrees with study of Clark and Kehler (2011), Ng et al. (2021). In addition, the rate of increase increases with the flow depth. Two types of Reynolds normal stress and TKE profiles pattern in $0.5 < z/d < 1$ region suggest that turbulent energy is affected by the free surface more when the pipe is filled over $d/D = 52$ %. Nichols (2014) has found both streamwise and vertical Reynolds normal stress continuously decrease with the increase of z/d from his PIV measurement in a rectangular open channel and a peak similar to Clark and Kehler (2011) at $z/d \approx 0.1$ from LES model. This suggests that free surface has a larger impact to the underneath turbulence in pipe compared with rectangular channel. As shown in Fig.5.13, Reynolds shear stress continuously decreases with the increase of depth-wise position. Clark and Kehler (2011), Ng et al. (2021) observed an 'S' shape in Reynolds shear stress profile, which is not observed in this study. This is because the data points close to surface $0.75 < z/d < 1$ and bed $0 < z/d < 0.2$ are not enough. Clark and Kehler (2011) have found that the Reynolds shear stress decrease with increasing z/d up to $z/d \approx 0.5$ and become negative value beyond that. Beside,

the sign of Reynolds shear stress changes between $0.4 < z/d < 0.6$ in the study of Ng et al. (2021). The change sign of Reynolds shear stress at $z/d \approx 0.5$ is also observed in this study, which is different from rectangular channel flows (Nichols, 2014).

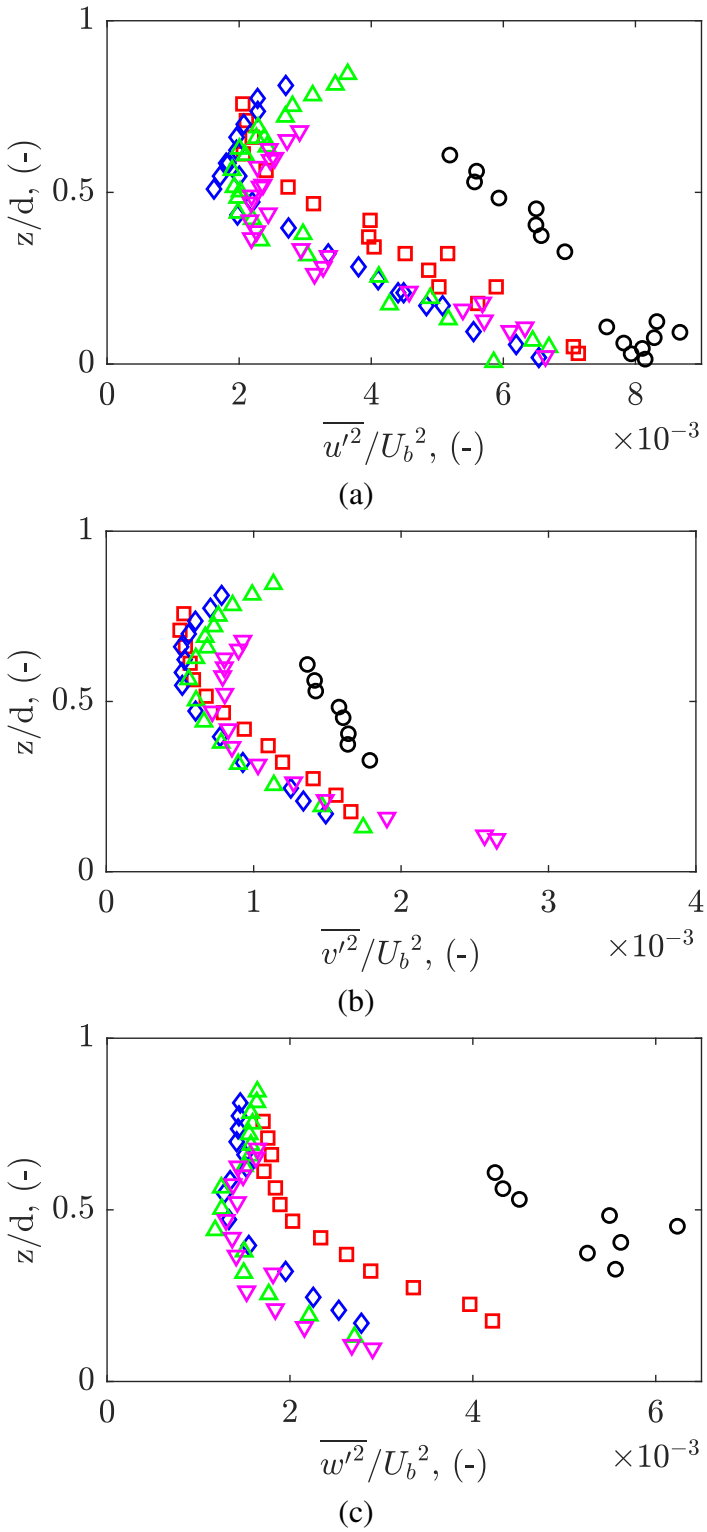

Figure 5.11 Reynolds normal stress (normalised with bulk flow velocity) profiles (a) streamwise, (b) lateral and (c) vertical. (**o**): flow condition 2, d/D = 22.0 %; (□): flow condition 5, d/D = 35.6 %; (◇) flow condition 8, d/D = 45.7 % ; (△) flow condition 11, d/D = 55.5 % and (▽) flow condition 14, d/D = 66.3 %.

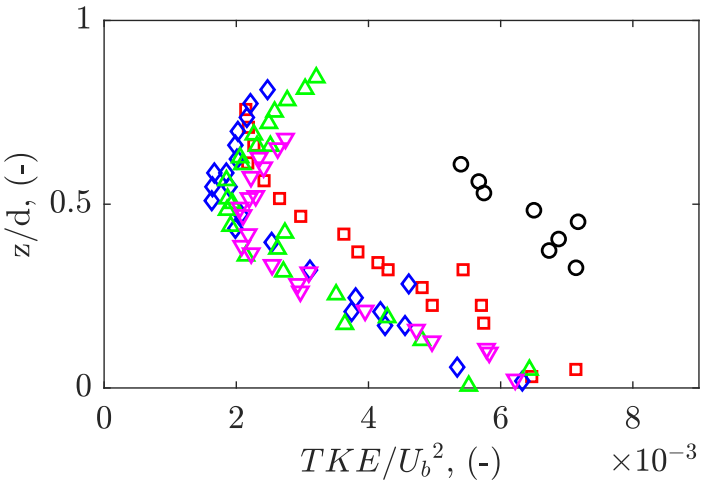

Figure 5.12 TKE profiles. (**o**): flow condition 2, d/D = 22.0 %; (□): flow condition 5, d/D = 35.6 %; (◇) flow condition 8, d/D = 45.7 % ; (△) flow condition 11, d/D = 55.5 % and (▽) flow condition 14, d/D = 66.3 %.

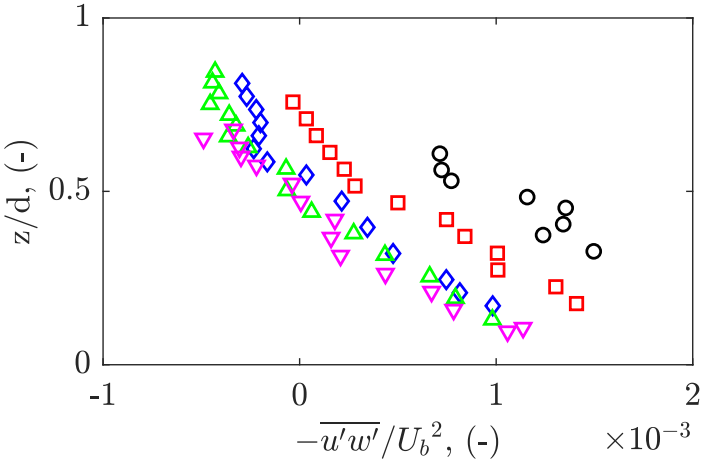

Figure 5.13 Reynolds shear stress (normalised with bulk flow velocity) profiles. (**o**): flow condition 2, d/D = 22.0 %; (□): flow condition 5, d/D = 35.6 %; (◇) flow condition 8, d/D = 45.7 % ; (△) flow condition 11, d/D = 55.5 % and (▽) flow condition 14, d/D = 66.3 %.

5.2 Phase-space quantitative analysis

5.2.1 Proposed phase-space algorithm

Phase-space is a filtering technique commonly used in removing spikes from 1D data, proposed by Goring and Nikora (2002). This method plots the fluctuating component of velocity, its first order derivative with respect to time (acceleration) and its second order derivative with respect to time (jerk) in three-dimensional so-called phase-space axes. It assumes that all points lying outside an ellipsoid in the phase-space are outliers (spikes), while points within the ellipsoid are valid data points. The size of the ellipsoid is determined by the universal threshold λ_{UN}:

$$\lambda_{UN} = \sqrt{2 \ln N} \tag{5.4}$$

where N is the number of data points. This method was shown to have better performance than various other methods and it has the advantage that it requires no external parameters that could otherwise introduce subjectivity.

As the phase-space method has no ambiguity in what threshold to choose, the present work has modified the method to enable detection of turbulent (extreme) events, events with extreme velocity, acceleration and/or jerk, rather than outliers. The steps of this new proposed technique, based on a measured steamwise velocity time series, $u^{'}$, are:

Step 1: Perform the standard phase-space despiking proposed by Goring and Nikora (2002) to remove erroneous data.

Step 2: Calculate the acceleration a_i and jerk j_i using the central difference method (Wu et al., 2005)

$$\triangle t = 1/f_s, \tag{5.5a}$$

$$a_i = \frac{u_{i+1} - u_{i-1}}{2 \triangle t}, \; i = 2,3,...N-1, \tag{5.5b}$$

$$j_i = \frac{u_{i+1} - 2u_i + u_{i-1}}{\triangle t^2}, \; i = 2,3,...N-1. \tag{5.5c}$$

Step 3: Calculate the standard deviations of all three variables σ_u, σ_a and σ_j.

Step 4: Calculate the Universal threshold according to Eq. 5.4.

Step 5: Transform the point cloud to be centred at the origin with no trend in any direction.

Step 6: Calculate the major, median and minor axes for the detection ellipsoid as:

$$e_u = k \lambda_{UN} \sigma_u \tag{5.6a}$$

$$e_a = k\lambda_{UN}\sigma_a \tag{5.6b}$$

$$e_j = k\lambda_{UN}\sigma_j, \tag{5.6c}$$

where k is the phase-space scaling factor.
Step 7: Define the detection ellipsoid based on Eq. 5.7,

$$\frac{u'^2}{e_u{}^2} + \frac{a'^2}{e_a{}^2} + \frac{j'^2}{e_j{}^2} = 1 \tag{5.7}$$

Step 8: Construct a binary series to signify the detection (or not) of turbulent events. Data points outside the defined ellipsoid (that satisfy Eq. 5.8) are recognised as 1 (detection of extreme event, termed as a 'coherent structure data point' in this study), in the binary time series and data points inside the ellipsoid (that satisfy Eq. 5.9) are 0.

$$\frac{u'^2}{e_u{}^2} + \frac{a'^2}{e_a{}^2} + \frac{j'^2}{e_j{}^2} \geq 1 \tag{5.8}$$

$$\frac{u'^2}{e_u{}^2} + \frac{a'^2}{e_a{}^2} + \frac{j'^2}{e_j{}^2} < 1 \tag{5.9}$$

A sustained value of 1 in the binary series is defined as an individual turbulent event (coherent structure). Determine the number of individual turbulent events from the binary series. Roy et al. (2004) only considered events lasting more than 1 s from a modified U-level method while Nichols (2014) considered events of any time duration. Luchiktand et al. (1987) grouped two adjacent ejections, where the time between them was less than a threshold time value, into a single event. Shah and Antonia (1989) noted that the determination of the threshold time value is not totally free of ambiguity. To reduce the ambiguity of the proposed objective method, detected events of any time duration are all considered in this study.
Step 9: Use a value of scaling factor k ranging from 0 to 1 for step 6 to adjust the size of the ellipsoid.
Step 10: The value of k is chosen which gives the maximum number of turbulent events.

An example of these steps being applied to real laboratory data is given in subsection 5.2.2 below.

5.2.2 Phase-space validation

The data points for (u_i,a_i,j_i) were placed in the phase-space axes for values of i (i = 3 to N-2). In order to fit the detection ellipsoid to a cloud of points with no bulk trend in any direction, the data points were first reduced to the j = 0 plane by subtracting the best fit plane from the

jerk values and then reduced to the j = 0, a = 0 line by subtracting the best fit line from the acceleration. The equation of the best fit plane was obtained by the MATLAB 'mldivide' function and the equation of the best fit line was obtained by the MATLAB 'polyfit' function. Since the velocity values are already fluctuations about the mean, the centre of mass of the point cloud is now at (0,0,0) with no trend in any direction. After this detrend procedure, a detection ellipsoid centered at (0,0,0) without rotation can be defined. The sizes of principle axes of the detection ellipsoid were calculated from Eq. 5.6 and the ellipsoid constructed using Eq. 5.7. Then the data points outside the ellipsoid were thus identified as coherent structure data points.

Next, the phase-space scaling parameter, k, was varied from 0 to 1 as described in subsection 5.2.1, enlarging the ellipsoid from a single point to encompassing the full point cloud. As shown in Fig. 5.14a, the number of coherent structure data points detected as being turbulent begins with all data points when $k = 0$, and reduces to zero data points when $k = 1$. But the number of discrete events (continuous periods of positive detection) increases from 1 when $k = 0$ (one continuous event consisting of the entire time series), reaches a peak at some k value, and then decrease to zero when $k = 1$ (all data points within the ellipsoid, so no events detected). Similar plots are obtained for the other flow conditions and measurement positions. For the U-level method, the number of events detected increases with increasing threshold. U-level has a low probability of making a false detection as well as a low probability of a true detection when high thresholds are used (Bogardt and Tiederman, 1986). Therefore, a compromise needed to be made in between the probability of making a false detection and the probability that an event will be detected, and an empirical threshold was settled upon subjectively. In case of the phase-space method, an appropriate threshold must also be determined. For this purpose, the value of the phase-space scale parameter k is chosen when it gives the maximum number of events (see Fig. 5.14b where the maximum number of events is indicated with the red marker). This represents the optimal sensitivity to detect extreme behaviour without merging discrete events. This provides an objective method for selecting the threshold, which yields turbulence statistics comparable with the accepted U-level method. This method was chosen because it provides a completely objective way of setting the threshold, which can be easily automated, and provides turbulence statistics comparable with U-level results.

The resulting phase-space detection using the optimal scaling parameter then enables construction of the optimal ellipsoid so that each point on the time series can be binarised as either (i) a coherent structure is present or (ii) a coherent structure is not present. The average value and standard deviation of the optimal scaling parameter for different flow conditions are calculated at all depth-wise positions. The average scaling factor ranges from 0.294 to

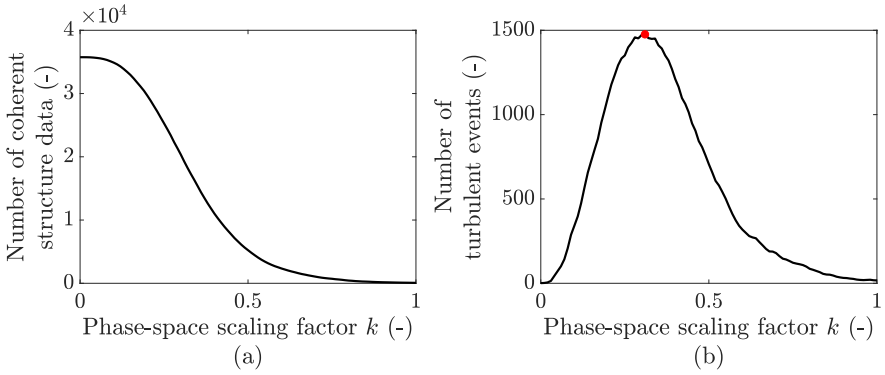

Figure 5.14 (a) Number of detected coherent structure data points versus the scaling factor (b) Number of detected discrete events versus the phase-space threshold, the red dot represents the maximum number of events. Time series analysis for flow condition 4 at depth-wise position y/d=0.62

0.308 for all flow conditions and the standard deviation is within 0.016. This small variation suggests a fixed value of the scaling factor (k = 0.3) may be appropriate for this particular flow system, but it is expected that different flow systems and application areas will exhibit different optimised scaling factors.

Figure 5.15 shows the streamwise velocity, acceleration and jerk time series for a random 8s segment of data. The red markers show where the U-level method detects an event and blue markers show where the phase-space method detects an event. U-level detected events of any time duration are considered, which is consistent with phase-space method as mentioned in step 8 in subsection 5.2.1. Both methods can detect extreme velocity fluctuations (with U-level being more sensitive) while only phase-space can detect the extreme acceleration and jerk. At some time intervals, such as 5.83 - 5.93 s and 8.16 - 8.29 s, U-level does not detect an event because the velocity is not particularly extreme, but the phase-space method detects a high acceleration and/or jerk and identifies this as an event. Conversely, at some time intervals, such as 5 - 5.57 s and 10.27 - 10.37 s, U-level detects an event because the velocity magnitude is moderately high, but phase-space determines that the combined conditions of velocity, acceleration and jerk are not sufficiently unusual to be deemed a coherent structure event. In general, these two methods detect many of the same periods of events (for example 6 - 7 s, 7.5 - 9.8 s and 10.5 - 12.2 s) while the individual event durations differ. This is also observed by Krogstad and Kaspersen (1992), Boppe and Neu (1995) when comparing different detection techniques. Similar plots are obtained for the other flow conditions, measurement positions and time sections. This occurs because U-level is more sensitive in order to produce event statistics similar to manual visualisation, while phase-space can be

more refined, reflecting the physical reality that a coherent structure does not embody just extreme velocities.

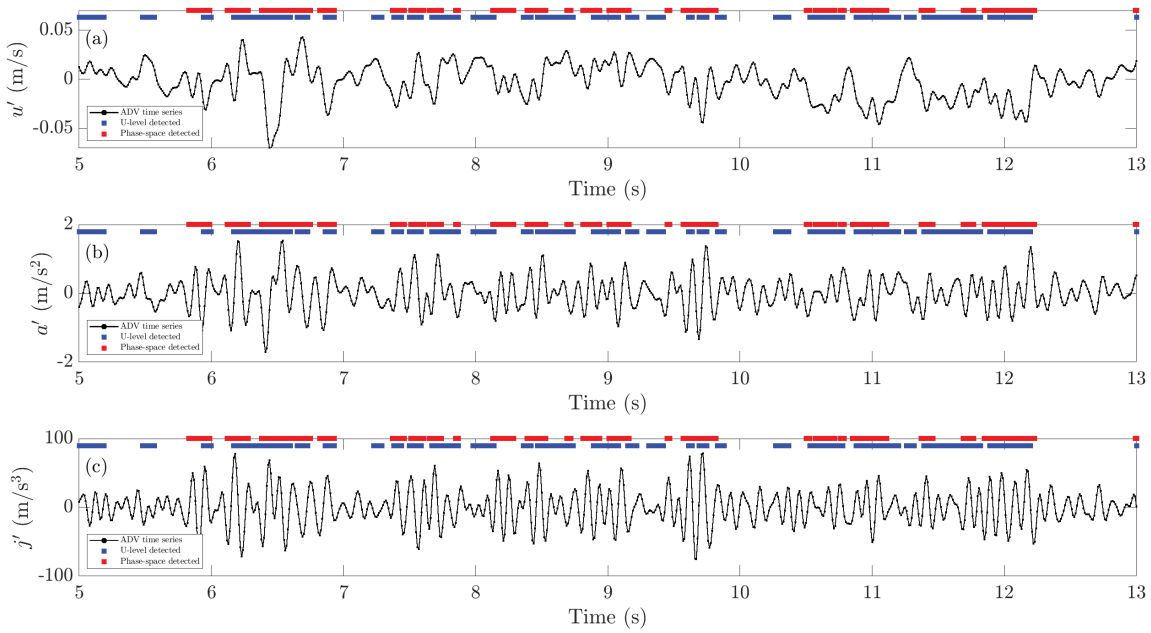

Figure 5.15 Time series of (a) velocity fluctuations (b) acceleration fluctuations (c) jerk fluctuations for flow condition 5 at depth-wise position y/d=0.71 (black lines represent velocity, acceleration and jerk time series, respectively, blue markers are data points detected by U-level and red markers are data points detected by phase-space)

Figure 5.16 shows all the data points (u_i,a_i,j_i) on the phase-space axes. The data points not detected as part of coherent structure events are in black and the data points recognised as events are highlighted in colour (blue for U-level and red for phase-space). It is evident that the black points cluster in the centre of all data points for both methods. The points detected by the U-level algorithm are clearly delineated from the black points at two planes along the u axis, while the points detected by the phase-space algorithm are outside the centre ellipsoid. Similar plots are obtained for the other flow conditions and measurement positions. The abrupt threshold imposed by U-level appears rather aggressive and indiscriminate.

Figure 5.17 presents the phase-space projections of the data points detected by the U-level and phase-space algorithms (the point cloud viewed from three orthogonal directions). Data points highlighted in blue are points detected by U-level and points outside the ellipsoid (whose largest dimension is indicated by the ellipse) are points detected by phase-space. In the plot of number of coherent structure data points versus velocity u distribution plot in Fig. 5.17a, the two algorithms align well in the extreme velocity region. However, no event data points are detected by the U-level algorithm when the velocity fluctuation is

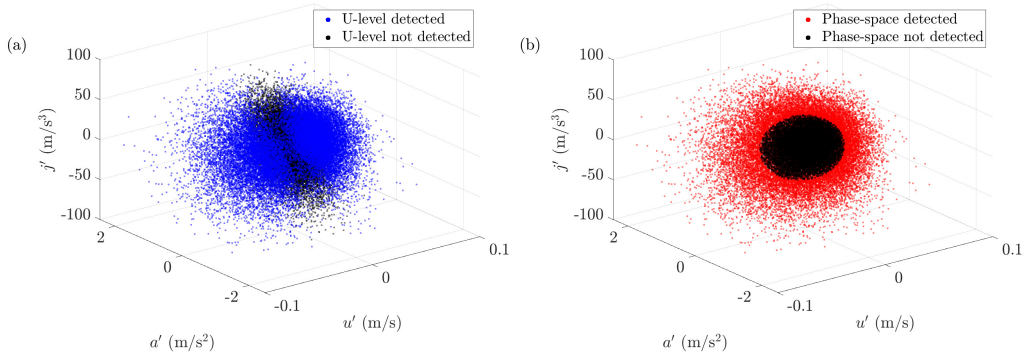

Figure 5.16 Data cluster in phase-space axes, coherent structure data points are in red/blue for flow condition 8 at depth-wise position y/d=0.74

small in magnitude. In the plot of number of coherent structure data points versus a and j (Fig. 5.17d, e, f and h), the U-level algorithm shows a spike when the acceleration and jerk is small. Phase-space gives a more uniform detection towards the middle of the ellipsoid in all three directions, with detection appropriately reducing towards the edges. Similar plots are obtained for the other flow conditions and measurement positions.

Figure 5.18 shows the histogram of the individual event duration $\triangle T$ and individual event period T_e from U-level and phase-space. Event duration is defined as the time between the leading and trailing edges of any continuous event, and event period is defined as the time interval of successive leading edges (Metzger et al., 2010, Tang et al., 2016). The two algorithms result in comparable histograms for both quantities. Exponential decay curves are fitted to the individual event duration plot as is shown in Fig. 5.18a since Bogardt and Tiederman (1986) showed that a histogram of time between ejections from flow visualization analysis fits an exponential distribution. The probability density function of exponential fit is

$$y_e = f(\triangle T|\mu) = \frac{1}{\mu} e^{\frac{-\triangle T}{\mu}} \tag{5.10}$$

where μ is the fitting parameter for exponential distribution. Gamma distribution curves are fitted to the individual event period plot as this more closely represents the histogram shape as is shown in Fig. 5.18b. The probability density function of gamma distribution is

$$y_g = f(T_e|a,b) = \frac{1}{b^a \Gamma(a)} T_e^{a-1} e^{\frac{-T_e}{b}} \tag{5.11}$$

where a and b are fitting parameters for the gamma distribution. The exponential and gamma fit is calculated using the MATLAB function 'fitdist' with distribution name 'Exponential' and 'Normal', respectively. The average values of goodness of fit calculated by MATLAB

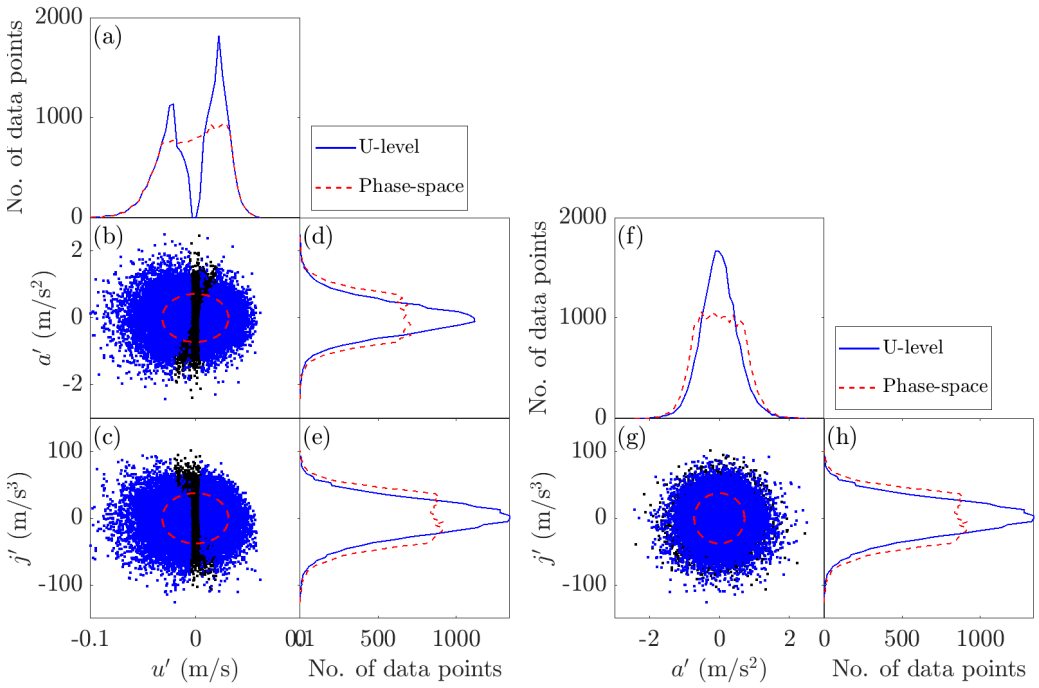

Figure 5.17 Coherent structure data point distribution for flow condition 5 at depth-wise position y/d=0.66

function 'goodnessOfFit' with cost function 'NMSE' (Normalized mean squared error) for all flow conditions and depth-wise positions are approximately 0.93 for individual event duration and approximately 0.81 for individual event period, which means good fittings of histograms. The percentage difference of best fit probability density function parameters from U-level and phase-space is calculated by the value obtained from phase-space minus the value obtained from U-level and then divided by the value obtained from U-level. The best fit probability density function parameters μ, a and b from phase-space shows lower values than U-level. The difference of these parameters from U-level and phase-space are generally less than 20 %. The phase-space method histogram for individual event duration $\triangle T$ shows a skewness towards smaller values of $\triangle T$, which is also observed by Bogardt and Tiederman (1986), Metzger et al. (2010), who found that the histogram of individual event period T_e follows a Poisson- like distribution at any fixed normal location in the boundary layer, demonstrating similarities with the histogram presented here. Similar plots are obtained for the other flow conditions and measurement positions.

Event duration and event period are significant in fluid dynamics analysis as event duration is associated with the structure length and the event period is associated with the frequency of turbulent structure occurrence. The agreement between the two methods shows that phase-space is able to accurately detect the statistics of coherent events while being physically more justifiable in the detection criteria. The percentage difference in the number of events, event duration, mean individual event duration and mean individual event period are calculated by the value obtained from phase-space minus the value obtained from U-level and then divided by the value obtained from U-level. The number of events, i.e. the number of periods of successive values of 1 in the binary time series, from phase-space are usually more than from U-level by 39.66 % on average. The percentage of total event duration is the ratio of the total number of 1 values in the binary time series to the length of the binary time series. On average, the percentage difference in total event duration is less than 1.03 %. In terms of the time scale of events, both mean individual event duration and mean individual event period are lower from phase-space and the differences are 20.50 % and 21.54 %, respectively. It corresponds to more structures being detected by the phase-space method, which are smaller in size than those detected by U-level.

Figure 5.19 shows a quadrant plot (streamwise velocity fluctuation vs vertical velocity fluctuation). As shown in Fig. 5.19, it is evident that there are no coherent structure data points detected by U-level in the middle of the quadrant plot while phase-space detected points are more uniformly distributed, representing the physical reality that a coherent structure does not just depend on velocity in one direction. Similar plots are obtained for the other flow conditions and measurement positions. The distribution of coherent structure data

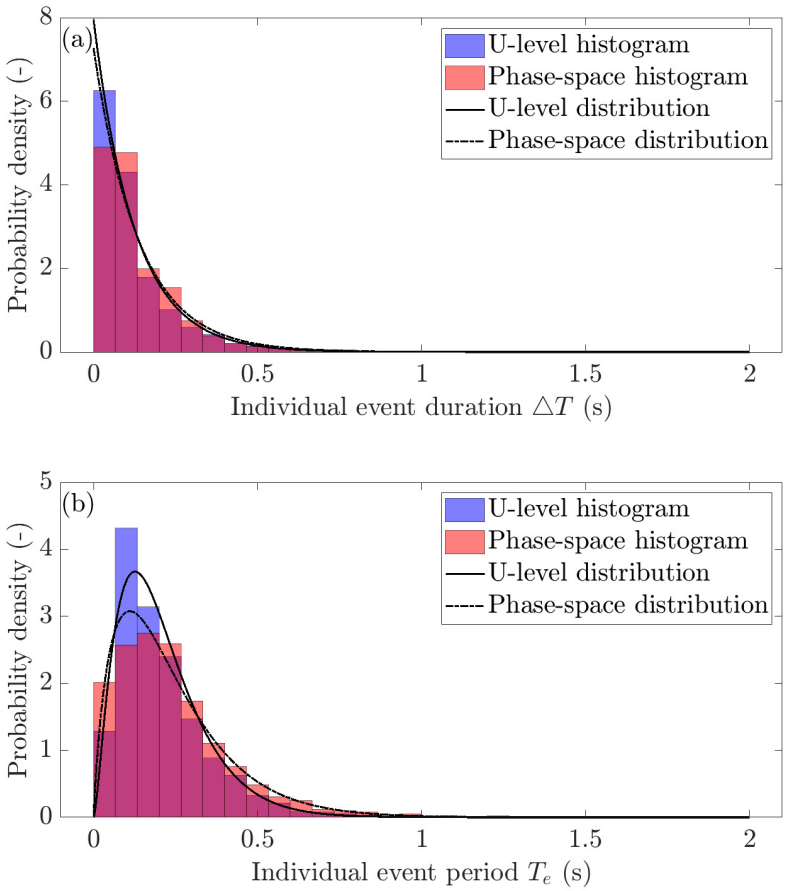

Figure 5.18 Normalised histogram of (a) individual event duration (b) individual event period for flow condition 10 at depth-wise position y/d=0.64

points detected by the two methods over vertical velocity direction show comparable results. The percentage difference of the proportion of detected coherent structure data points in each quadrant is calculated by the value obtained from phase-space minus the value obtained from U-level and then divided by the value obtained from U-level. In general, phase-space shows 8.50% and 11.56% higher percentage of points in quadrants 2 and 3 while U-level shows 5.52% and 10.04% higher percentage of points in quadrants 1 and 4. That means more ejection (Q2) and inward interaction (Q3) events are detected by phase-space while more outward interaction (Q1) and sweep (Q4) events are detected by U-level.

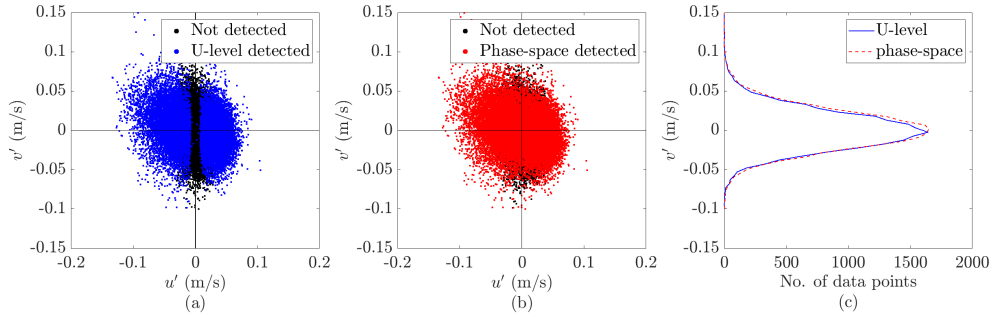

Figure 5.19 Detected coherent structure data points quadrant distribution for flow condition 6 at depth-wise position y/d=0.339 (a) U-level detection, (b) phase-space detection and (c) Number of detected data points over vertical velocity direction

Table5.1 shows the percentage of coherent structure data points being detected by each method, by both methods, and by neither method. It also shows the agreement of the two algorithms (proportion of points detected by both methods or neither) and the disagreement of the two algorithms (proportion of points detected exclusively by each method only). The percentages are averaged over all the depth-wise positions and the average and standard deviation for all flow conditions are summarized in Table5.1. All standard deviation values are less than 0.93 %, which means the performance of these two methods are consistent for all flow conditions. There are 15.92 % and 16.49 % data points that are only detected by U-level and phase-space, respectively. The points detected by one algorithm but not the other are not surprising, since the proposed method uses an entirely different detection criterion to the established U-level method. There are 40.85 % of coherent structure data points detected by both algorithms and 26.74 % of data points are not detected as coherent structures by either algorithm. That together means these two algorithms show 67.59 % agreement and 32.41 % disagreement. Again, this is not surprising, since the phase-space method employs a more physically realistic definition of a coherent structure, where the U-level method only detects based upon extremes in velocity.

Table 5.1 Percentage of a coherent structure data points being detected for all flow conditions

	Average (%)	Standard deviation (%)
U-level only (%)	15.92	0.65
Phase-space only (%)	16.49	0.50
Both methods (%)	40.85	0.91
Neither methods (%)	26.74	0.93
Agreement (%)	67.59	0.57
Disagreement (%)	32.41	0.57

The proposed phase-space method in this study is a technique that can be applied to analyse 1D velocity fluctuation data. While it has the advantage of being applicable to various datasets, it is relatively more sensitive to noise. To assess its performance in the presence of noise, artificial noise of varying levels was added to ADV velocity data measured at flow condition 4 at depth-wise position $y/d = 0.51$. Figure 5.20 presents the results comparing the performance of the U-level method and the phase-space method at different signal-to-noise ratios (SNR). The SNR ranged from 0 to 100, indicating the ratio of the signal strength to the noise level. The figure illustrates the number of detected events and the number of detected coherent structure data points for each method at different SNR levels. It is observed that the U-level method starts to converge at 20 dB SNR, while the phase-space method requires a higher SNR of 50 dB to achieve convergence. The phase-space method involves calculations of acceleration and jerk, as indicated in Eq.5.5, which are sensitive to noise in the velocity data. Consequently, the computation of ellipsoid axes (Eq.5.6) and the detection ellipsoid function (Eq.5.7) are also affected by the noise. Based on these findings, it is recommended to use the phase-space detection method for data with an SNR greater than 50 dB to ensure reliable results. This graph is presented to determine the appropriateness of using the phase-space method with a signal having a certain SNR, thus highlighting its importance in assessing the method's performance under varying noise conditions.

5.2.3 Coherent structure analysis

The proposed phase-space method is applied to the ADV data for all depth-wise positions and flow conditions. The relation between properties of coherent structures measured via the proposed method and the bulk flow conditions and measurement depth-wise positions are presented in this section. Two turbulent event profiles are analysed: size of turbulent structure verse depth-wise position (see Fig. 5.21) and number of turbulent structures per meter (see Fig. 5.22). The size of turbulent structure is the product of mean event duration and mean depth-wise streamwise velocity. The number of turbulent structures per meter is

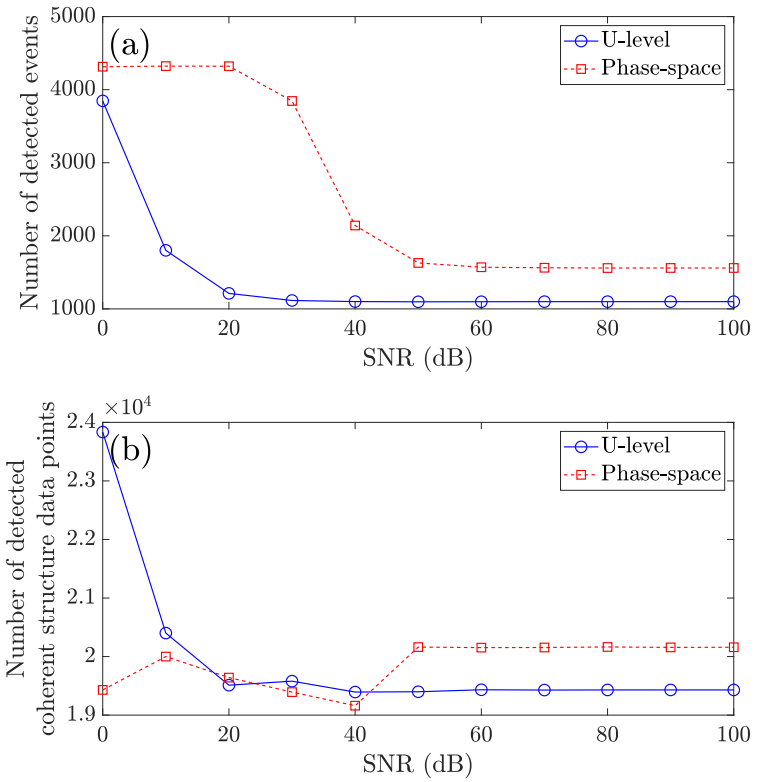

Figure 5.20 The performance of U-level and phase-space with different SNR (a) Number of detected events (b) Number of detected coherent structure data points

calculated from the reciprocal of the product of the mean event period and mean depth-wise streamwise velocity. As shown in Fig. 5.21, both methods show larger turbulent structures with the increase of flow, which agrees with observations of Nichols (2014). This also accords with observations from Roy et al. (2004), which showed that the size of large-scale turbulent flow structure scale with depth of flow. Figure 5.22 shows that with increasing flow, fewer turbulent structures are apparent per meter, with a slight increase in number of turbulent structures per meter near the bed for high flows. This is in agreement with Ng et al. (2021) findings which observe more large scale motions and very large scale motions at the bottom of the pipe compared to lower flow rate flows. Profiles by the two detection methods show similar trends while phase-space shows generally smaller size of turbulent structures and a larger number of structures per meter. This can be explained by the mean event duration and event period measured by phase-space being lower than U-level, as discussed in subsection 5.2.2.

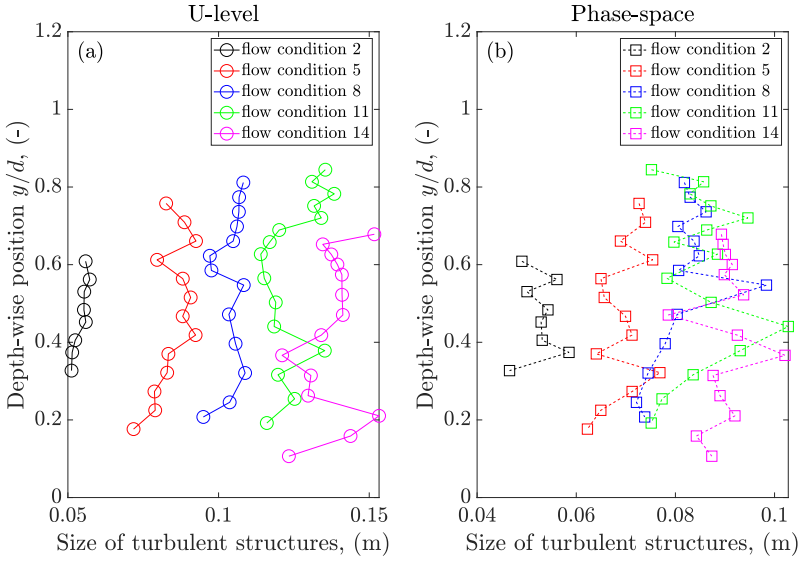

Figure 5.21 Size of turbulent structure profile by (a) U-level, (b) phase-space

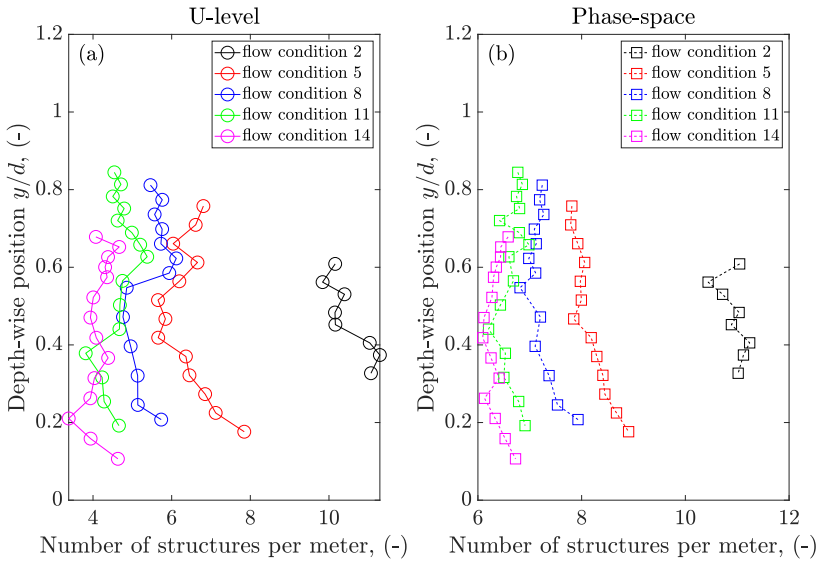

Figure 5.22 Number of structures per meter by (a) U-level, (b) phase-space

5.3 Free surface behaviour of partially filled pipe turbulent flows

5.3.1 Surface ST Matrix

A space time matrix is usually used in investigation, extraction of features and visualisation of free surface fluctuations over space and time (Fujita et al., 2011, Nichols, 2014, Roy et al., 2004, Smolentsev and Miraghaie, 2005). Figure 5.23 shows the space time matrices of instantaneous water surface elevation at the lateral centre-line obtained by DIC system for flow conditions 1, 6 and 14. The greyscale represents the instantaneous deviation from zero. It allows a visual assessment of the behaviour of the dominant features. The dashed lines correspond to the surface velocity measured by timing a floating tracer over a 3.83 m distance downstream of the surface measurement area. The surface velocity is plotted for every 2 s duration for better visualisation with the greyscale streaks. There are three types of motion that can be seen from the space time matrices in Fig. 5.23: turbulence features travelling at the speed of the mean surface flow velocity (corresponding to the red dashed lines in Fig. 5.23), and travelling and receding waves (corresponding to the zig-zag patterns in Fig. 5.23a and b). In the same spatial area, about 4 periods of oscillation can be observed for flow condition 1 (Fig. 5.23a), about 2 periods for flow condition 6 (Fig. 5.23b) and an oscillation is hard to observe in flow condition 14 (Fig. 5.23c). Similar space time matrix patterns were observed by Nichols (2014), Tani and Fujita (2020), Fujita et al. (2011), Fujita

(2017). Moreover, Guo and Shen (2010) have found the free surface deformations consist of both turbulence-induced roughness and propagating waves. The trains of features fluctuating over space and time can be explained by the oscillation theory proposed by Nichols et al. (2016). The spatial frequency of the oscillation was shown to decrease with the increase of flow depth and increase of surface roughness, agreeing with the results here.

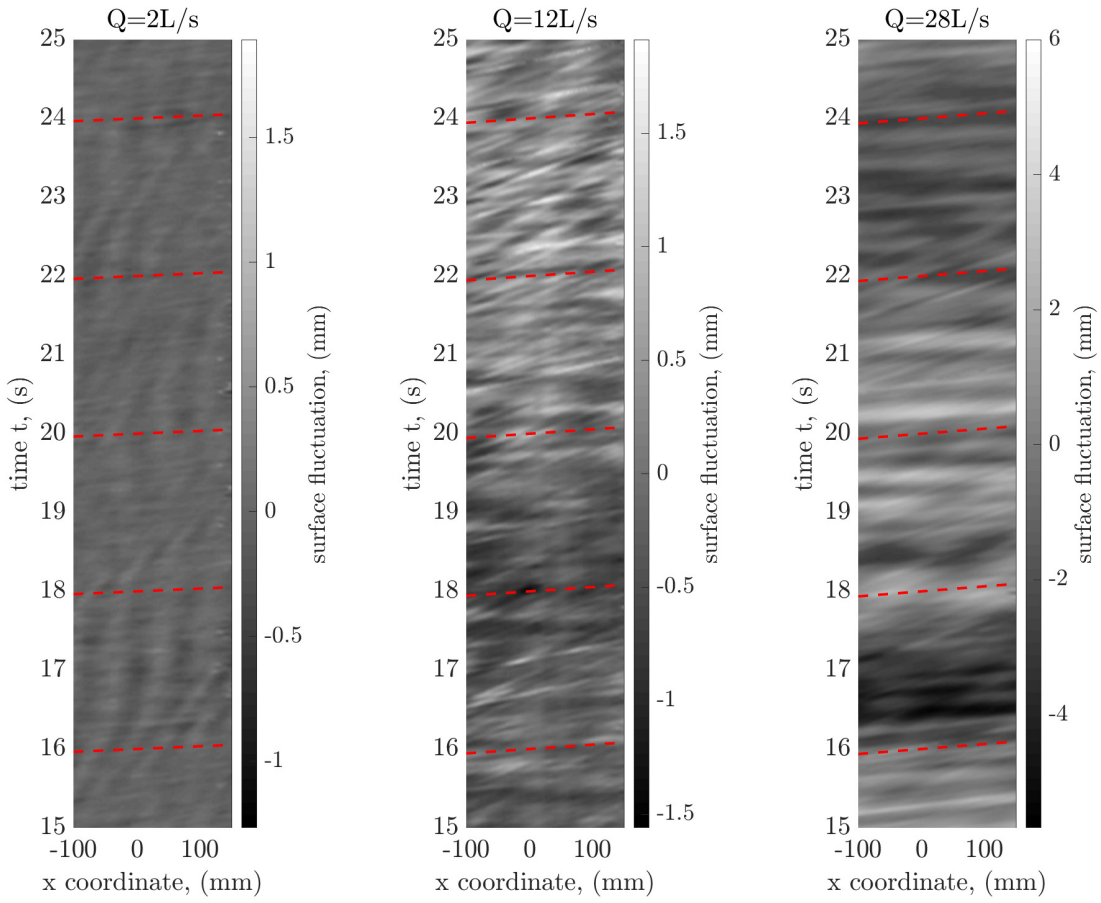

Figure 5.23 Space time matrix for flow conditions (a) 1, (b) 6 and (c) 14 for a duration of 10s, red dashed lines correspond to surface velocity measured by floating tracers.

As different types of motion can be observed in the space-time matrix in Fig. 5.23, a decomposition was performed to evaluate the role of these motions in surface fluctuations Tani and Fujita (2020). The procedure of the decomposition is applying a 2D discrete Fourier transform (DFT) to the space-time matrix first, then applying a binary mask to the DFT transformed data. Finally, the inverse DFT is applied to the masked data (Tani and Fujita, 2020). The mask's function threshold criteria is

$$m_t(k_x,\omega) = \begin{cases} 1 & \text{if } |\omega - U_s k_x| < \sqrt{(gk_x + Tk_x/\rho)\tanh(k_x d)} \\ 0 & otherwise \end{cases} \tag{5.12a}$$

$$m_w(k_x,\omega) = |1 - m_t(k_x,\omega)| \tag{5.12b}$$

where m_t and m_w are mask functions used to extract the turbulence component and wave components, respectively. The decomposed space time matrices for flow conditions 1, 6 and 14 measured at the centerline are shown in Fig. 5.24. Both turbulence and wave components of surface fluctuations (colorbar scale) increase with the flow rate. Comparing the magnitude of surface fluctuations for three columns, it is evident that the surface fluctuations for turbulence component is approximate 1/5 - 1/6 times of wave components. As shown in Fig. 5.24, the oscillation frequency of the turbulence component is higher than that of the wave components for all three examples. This is particularly evident in Fig. 5.24a and c. Tani and Fujita (2020) have observed linear slope patterns with a slope equal to the surface velocity for the turbulence component and steeper or gentler slope patterns for wave components. This is only observed for flow condition 14 among all three examples here as shown in Fig. 5.24c. It can be observed from the middle column of Fig. 5.24a that the gradient of the turbulence component pattern is higher than the surface velocity gradient. For flow condition 6 as shown in Fig. 5.24b middle column, some streaks are parallel to the surface velocity line and some are steeper than it.

The preceding paragraph investigated the lateral center ST matrix, but the laterally offset ST matrix is also worth investigation. The ST matrices at the lateral center, and at 30mm and 60 mm away from the lateral center for flow conditions 2 and 13 are illustrated in Fig. 5.25. In general, the magnitude of surface fluctuation appears quite similar in the ST matrices. The ST matrices at different lateral positions all show some gradient corresponding to the surface velocity. From the flow condition 2 ($Q = 4$ Ls^{-1}) example, it can be observed that some areas of elevated flow surface that appears persistent over time, which corresponds to stationary waves. These stationary patterns are more obvious in the lateral center and the strength decays as the plane moves toward the pipe wall. As shown in the $Q = 26$ Ls^{-1} example, there are some strikes with a gradient larger than the surface velocity, representing travelling waves. These higher than surface velocity strikes are more evident in the lateral center and weaker towards the pipe wall. This indicates that the gravity capillary waves are stronger at the lateral center and become weaker towards the pipe wall. This is likely because the flow nearer the wall is experiencing lower local depth and lower local velocity (comparable with

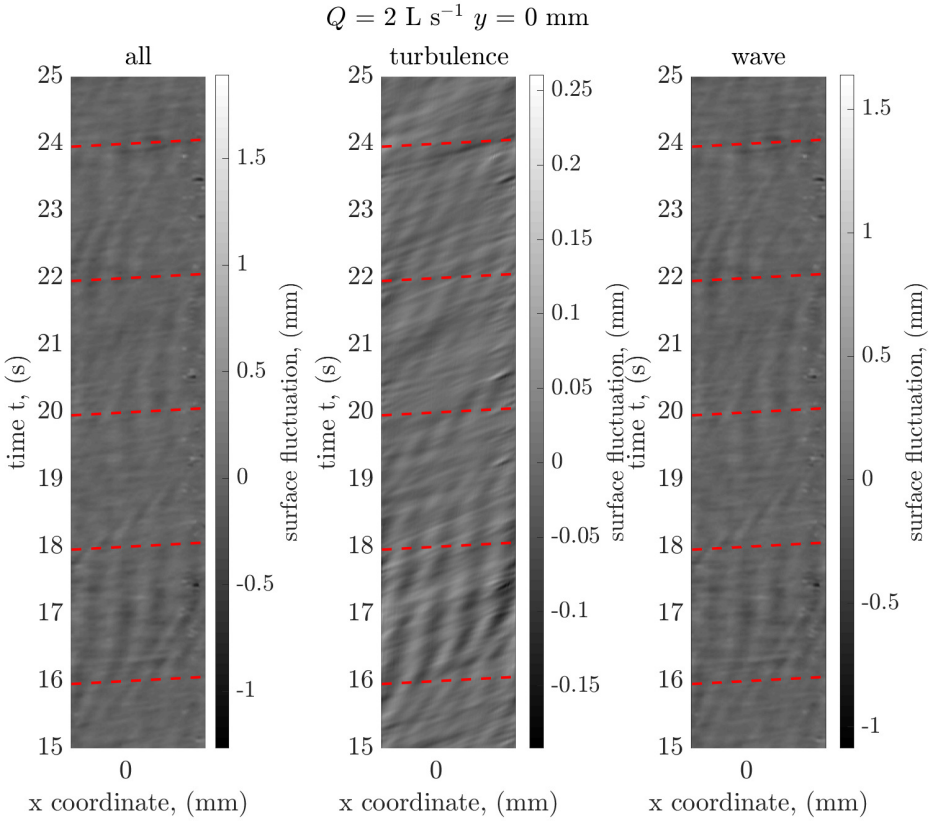
$Q = 2$ L s^{-1} $y = 0$ mm
all
turbulence
wave
time t, (s)
surface fluctuation, (mm)
x coordinate, (mm)

(a)

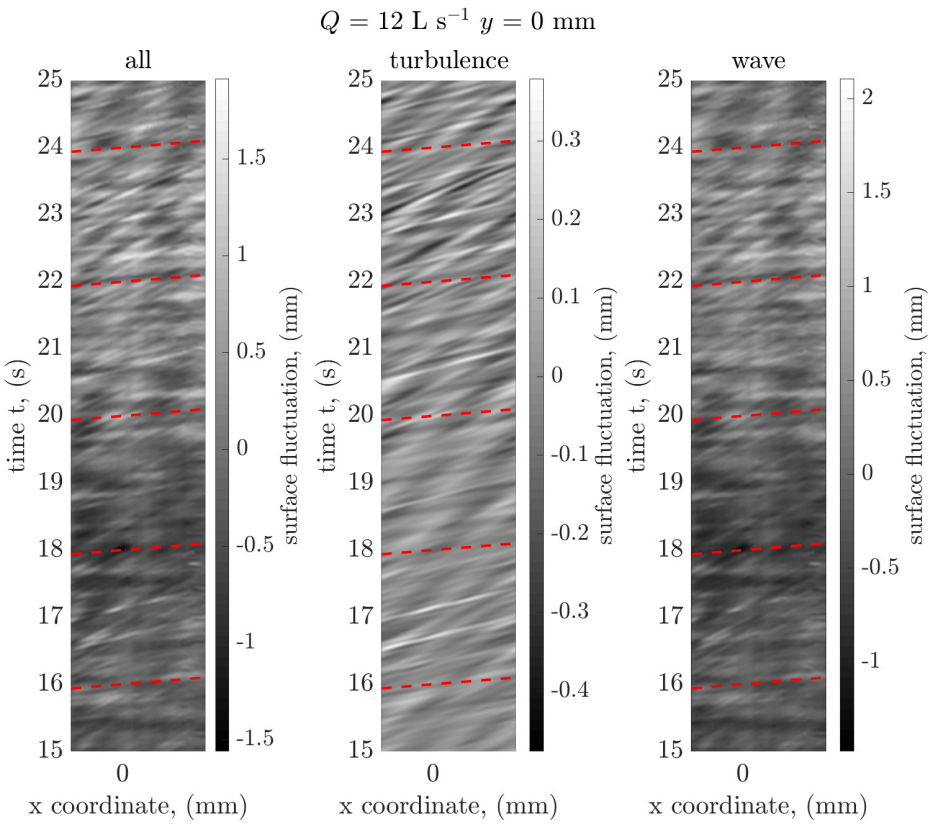
$Q = 12$ L s^{-1} $y = 0$ mm
all
turbulence
wave
time t, (s)
surface fluctuation, (mm)
x coordinate, (mm)

(b)

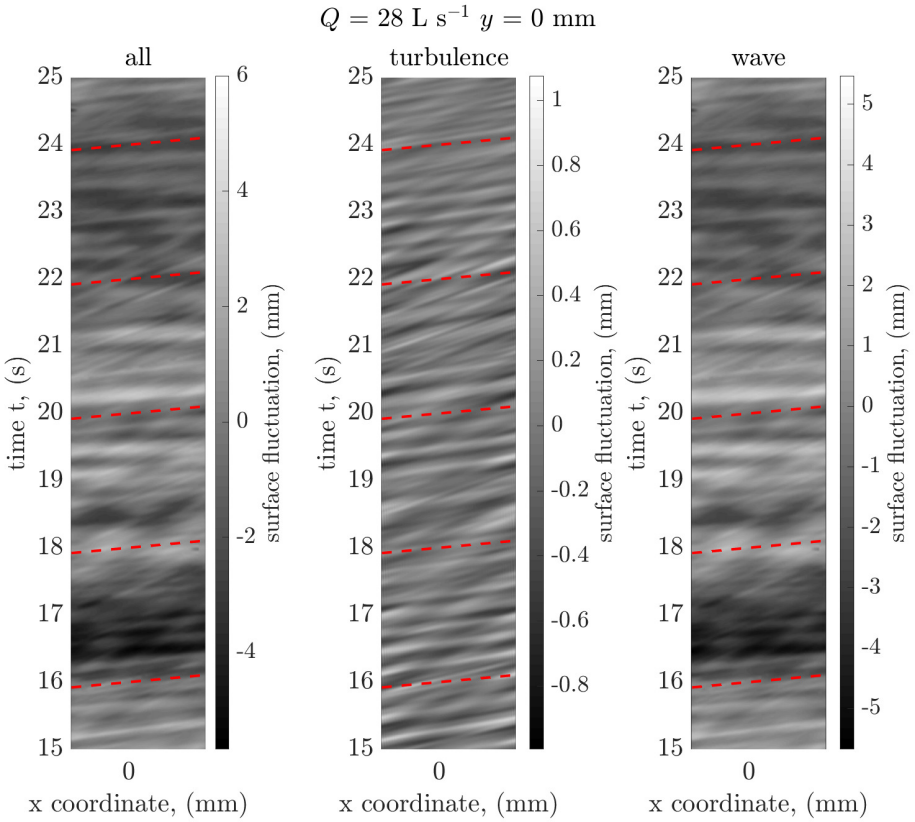

(c)

Figure 5.24 Decomposed Space time matrix for flow conditions (a) 1, (b) 6 and (c) 14 for a duration of 10s, red dashed lines corresponds to surface velocity measured by floating tracers. The left column results are all components ST matrix, middle column results are turbulence component ST matrix and right column results are wave component ST matrix.

rectangular channel theory (Nichols, 2014) where these conditions are shown to generate weaker surface waves); though this has never been shown before in a pipe flow.

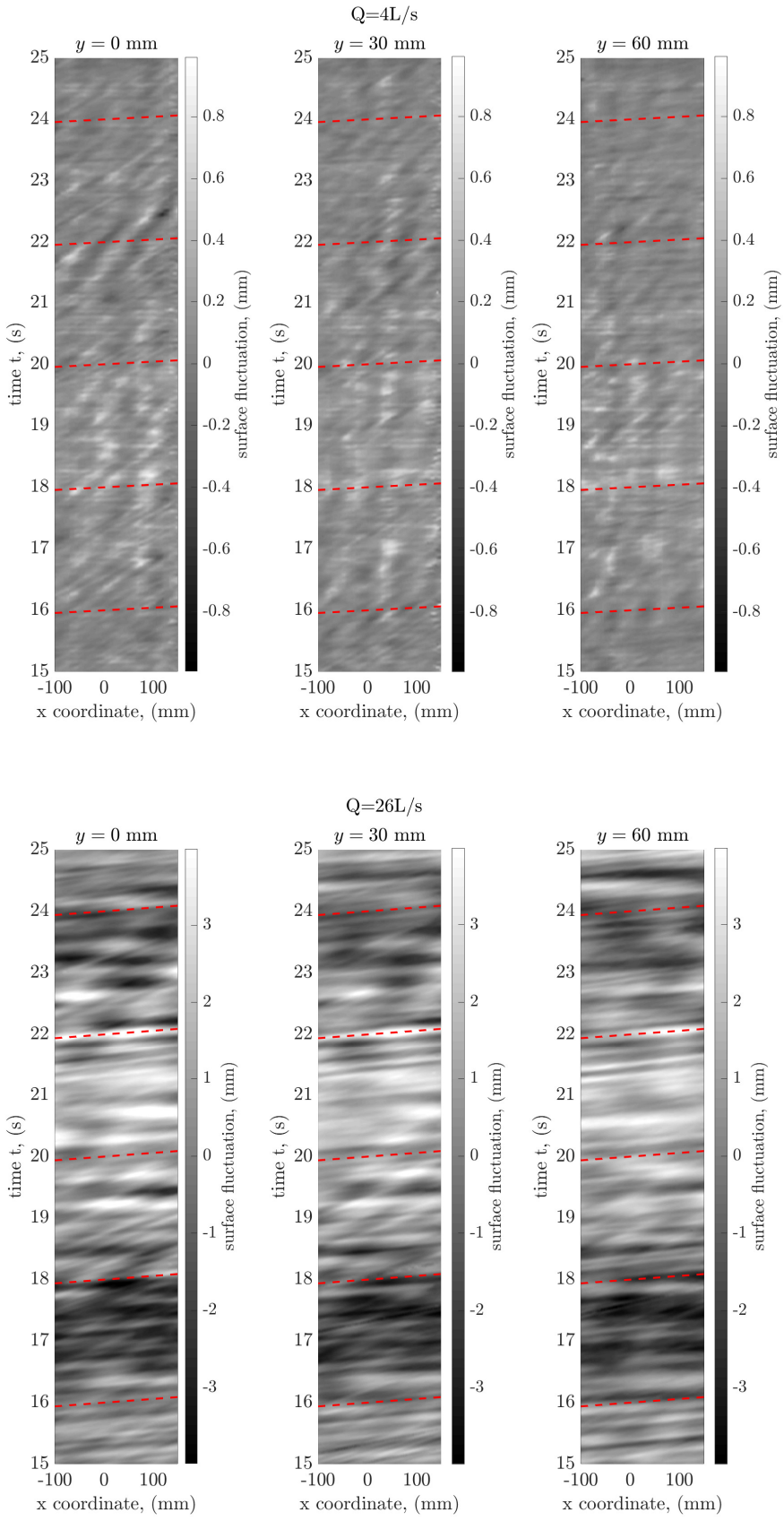

Figure 5.25 Space time matrix at different lateral positions for flow conditions 2 and 13.

5.3.2 Dispersion relationship

Figure 5.26 illustrates the relationship between frequency and the velocity at which turbulence-generated flow structures propagate. The figure specifically shows this relationship for flow conditions 1, 8, and 14. The x-axis represents the center frequency of the waveband, indicating the range of frequencies that the surface fluctuation signal has been bandpass filtered to. For instance, a frequency of 3.5 Hz implies that the surface fluctuation signal has been filtered within the frequency range of 3 to 4 Hz. The analysis involves correlating the bandpass-filtered surface fluctuation signals measured at two different positions. By determining the time lag at which the maximum correlation occurs, the phase velocity of the flow structures can be obtained. The y-axis of the figure represents these phase velocities, which are calculated by dividing the separation distance between the wave probes or DIC points by the corresponding time lag at maximum correlation. In summary, Figure 5.26 provides insights into the advection velocity of surface features across different frequency bands of waves. It demonstrates the relationship between frequency and phase velocity, highlighting how turbulence-generated flow structures propagate at varying speeds depending on the frequency content of the surface fluctuations.

The left column results are obtained from 2 wave probes with 20 mm separation and the right column results are obtained from 2 spatial points in the DIC data with 20 mm separation. The solid line is bulk flow velocity calculated according to Eq. 2.10 and the dashed line is surface velocity measured by timing a floating tracer over a 3.83 m. It can be noted that results from wave probes and DIC are generally comparable. Nichols (2014) has found the phase velocity (the velocity at which flow surface roughness patterns propagate) is relatively independent of frequency and is approximately equal to the surface velocity. However, this is not observed for all frequencies and flow conditions. This is likely because the equivalent roughness k_s is 11.8 - 40.3 mm in the study of Nichols (2014) and below 0.26 mm in this study. Turbulence waves were dominant in the study of Nichols (2014), who used both sphere and gravel beds, while gravity-capillary waves are comparable with turbulence waves in this study with a smooth bed. As discussed in subsection 5.3.1, turbulent waves, travelling waves and receding waves can be observed from the surface fluctuations. When correlating two signals containing all these types of waves, the highest correlation may not represent the turbulence wave for all cases. Smolentsev and Miraghaie (2005) have found the celerity of turbulence structures is slightly above the mean flow velocity while the celerity of gravity capillary waves is different from the mean velocity. Most markers show a phase velocity slightly smaller than the bulk flow velocity for low flow condition as shown in Fig. 5.26a and b. Some markers show phase velocity higher than surface velocity in the frequency range 7 - 10 Hz, which means travelling waves dominate at this frequency range for low flow

conditions. For medium flows (see Fig. 5.26c and d), some markers show phase velocity in between bulk flow and surface velocities in the frequency range 7 - 10 Hz. Most markers are higher than the surface velocity in frequency range 1 - 6 Hz and some are lower than the bulk flow velocity in the frequency range 5 - 10 Hz. Therefore, travelling waves dominate the 1 - 6 Hz components and all three components can be observed for higher frequencies for medium flows. Only a few markers show phase velocity in between bulk flow and surface velocities in the frequency range 8 - 10 Hz for high flows, and most markers show phase velocity higher than surface velocity, which means travelling waves dominate for this flow condition.

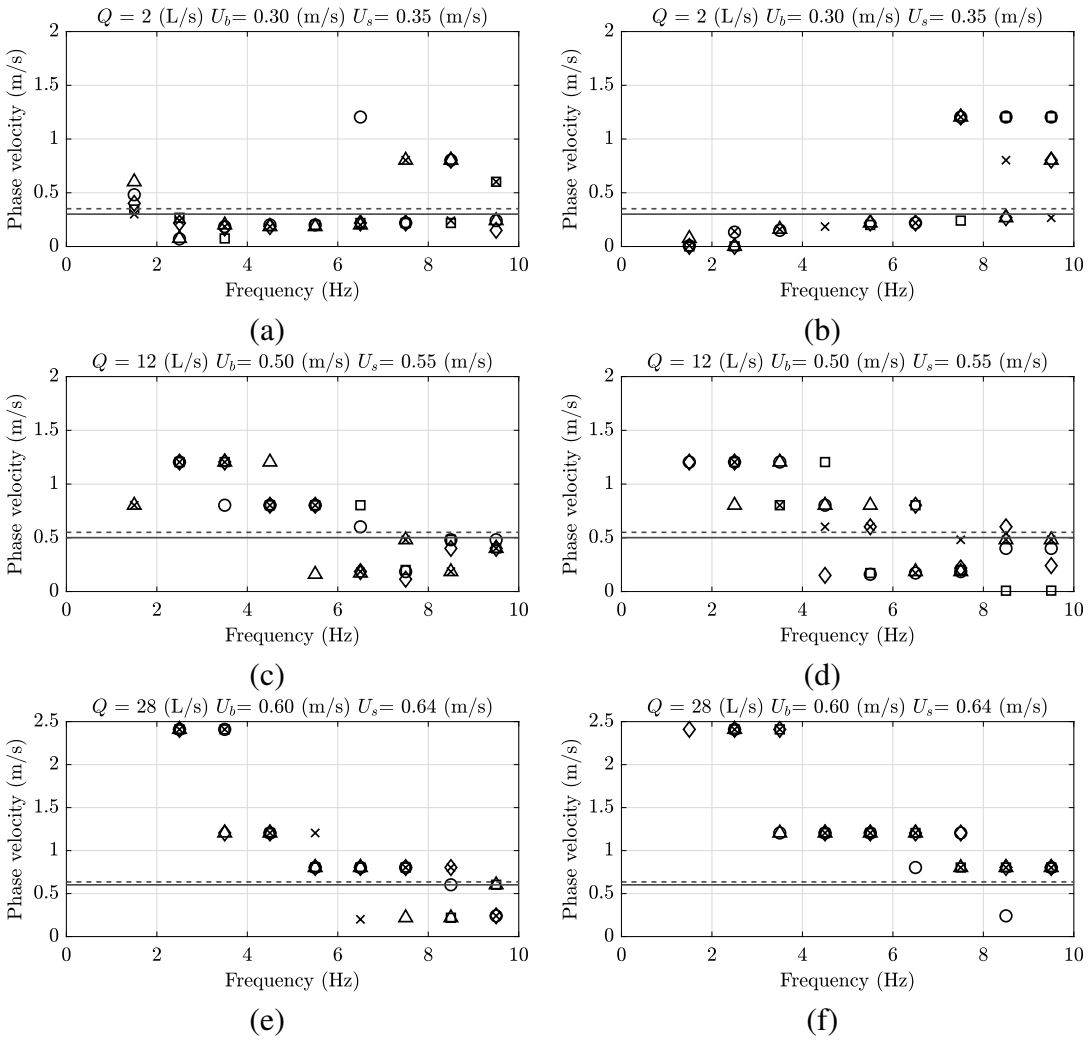

Figure 5.26 Frequency dependence of the phase velocity for flow condition (a)(b) 1, (c)(d) 8 and (e)(f) 14. Left column results obtained from wave probes and right column results obtained from DIC. Solid line represents bulk flow velocity and dashed line represents surface velocity. 5 types of markers represent 5 repeated tests.

It is likely that gravity waves have an impact on the correlation of surface fluctuation between two spatial locations, and hence on the phase velocity extraction. To validate this idea, the phase velocity is extracted from the decomposed turbulence component as shown in Fig. 5.24 middle column. The frequency dependence of phase velocity calculated from the decomposed DIC turbulence component surface fluctuations are shown in Fig. 5.27, and are similar to what Nichols (2014) observed in open channel flows. The velocity at which the surface pattern propagates is relatively independent of frequency, and is close to the flow surface velocity. This relationship is in agreement with observations of Fujita et al. (2011), Nichols (2014), who have found that the free surface roughness patterns travel with a speed almost comparable to the surface velocity experimentally.

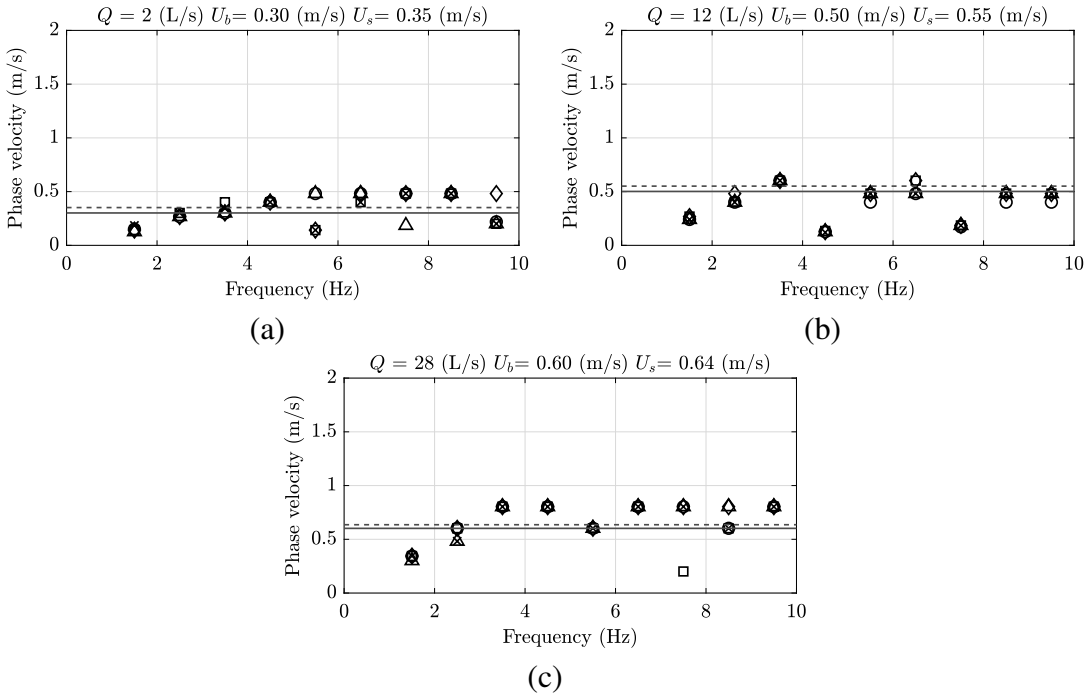

Figure 5.27 Frequency dependence of the phase velocity for flow condition (a) 1, (b) 8 and (c) 14 obtained from masked DIC data. Solid line represents bulk flow velocity and dashed line represents surface velocity. 5 types of markers represent 5 repeated tests.

5.3.3 Correlation characteristics of surface roughness

Subsection 5.3.2 shows that the propagation speed for the surface features is close to the surface velocity and bulk flow velocity. This suggests that the advection of surface pattern is related to underlying turbulent structures. Horoshenkov et al. (2013) have examined the free surface behaviour measured by several non-equally spaced wave probes, using a spatial

correlation function, for rectangular open channel flows. The same analysis is also performed in this study to find the correlation characteristics of surface roughness in a partially filled pipe. The normalised temporal cross-correlation function for flow conditions 1, 4, 8 and 13 are shown in Fig. 5.28, which are calculated from different pairs of wave probes with different spatial separation ρ_{mn}. Four different line types represent four different wave probe pairs 11 (0 mm), 67 (20 mm), 12 (40 mm) and 56 (60 mm). 11 means wave probe 1 correlated against wave probe 1, which also applies to 67, 12 and 56. The cross-correlation coefficient is calculated from the data of two wave probes by the MATLAB 'xcorr' function. The cross-correlation coefficient is then scaled between -1 to +1 with 'normalized' option. It makes more physical sense and is easier to understand the meaning. The cross-correlation, auto-correlation and normaised cross correlation are calculated according to Eq. 5.13.

$$\text{cross-correlation}(\eta_m, \eta_n)(\tau) = \int_{-\infty}^{\infty} \eta_m(t)\eta_n(t+\tau)dt, \tag{5.13a}$$

$$\text{auto-correlation}(\eta_m)(\tau) = \int_{-\infty}^{\infty} \eta_m(t)\eta_m(t+\tau)dt, \tag{5.13b}$$

$$\text{normalised cross-correlation}(\eta_m, \eta_n)(\tau) = \frac{\text{cross-correlation}(\eta_m, \eta_n)(\tau)}{\sqrt{\text{auto-correlation}(\eta_m)(0) \cdot \text{auto-correlation}(\eta_n)(0)}}. \tag{5.13c}$$

In Eq. 5.13, η_m and η_n represent instantaneous surface fluctuations measured by wave probe m and wave probe n, respectively. Correlation coefficient +1 means exactly the same, -1 means exactly opposite and 0 means no correlation. The spatial lag is the product of surface velocity U_s times the time lag τ. The extreme value in correlation coefficient represents the instant when two signals recorded on the two wave probes separated in space are most closely correlated. From Fig. 5.28, it can be seen that the auto-correlation extreme value is equal to 1 for all flow conditions, which is expected. Horoshenkov et al. (2013) have found the position of this extremum is close to the distance by which the two wave probes are separated for some flow conditions and some wave probe lags and the position of this extreme value was shifted for others. Most of the extreme values are not close to the distance by which the two wave probes are separated in this study, except the 20 mm lag for flow condition 4 as shown in Fig. 5.28b. Moreover, Horoshenkov et al. (2013) have found some strong negative correlation coefficient cases, which represent the surface pattern is similar but inverted. Both Romanova (2013) and this study do not observe correlation coefficient values below -0.5, which suggests similar but inverted surface patterns are not strongly observed in partially filled pipe flows. Negative extreme correlation value can only be observed for flow conditions 1 - 5 (see Fig. 5.28a and b) while the remaining flow conditions exhibit positive extreme correlation values. Comparing Fig. 5.28a and b, it can be observed that the

correlation coefficient is higher for higher flows, which means over a certain distance the surface pattern is more consistent for higher flows.

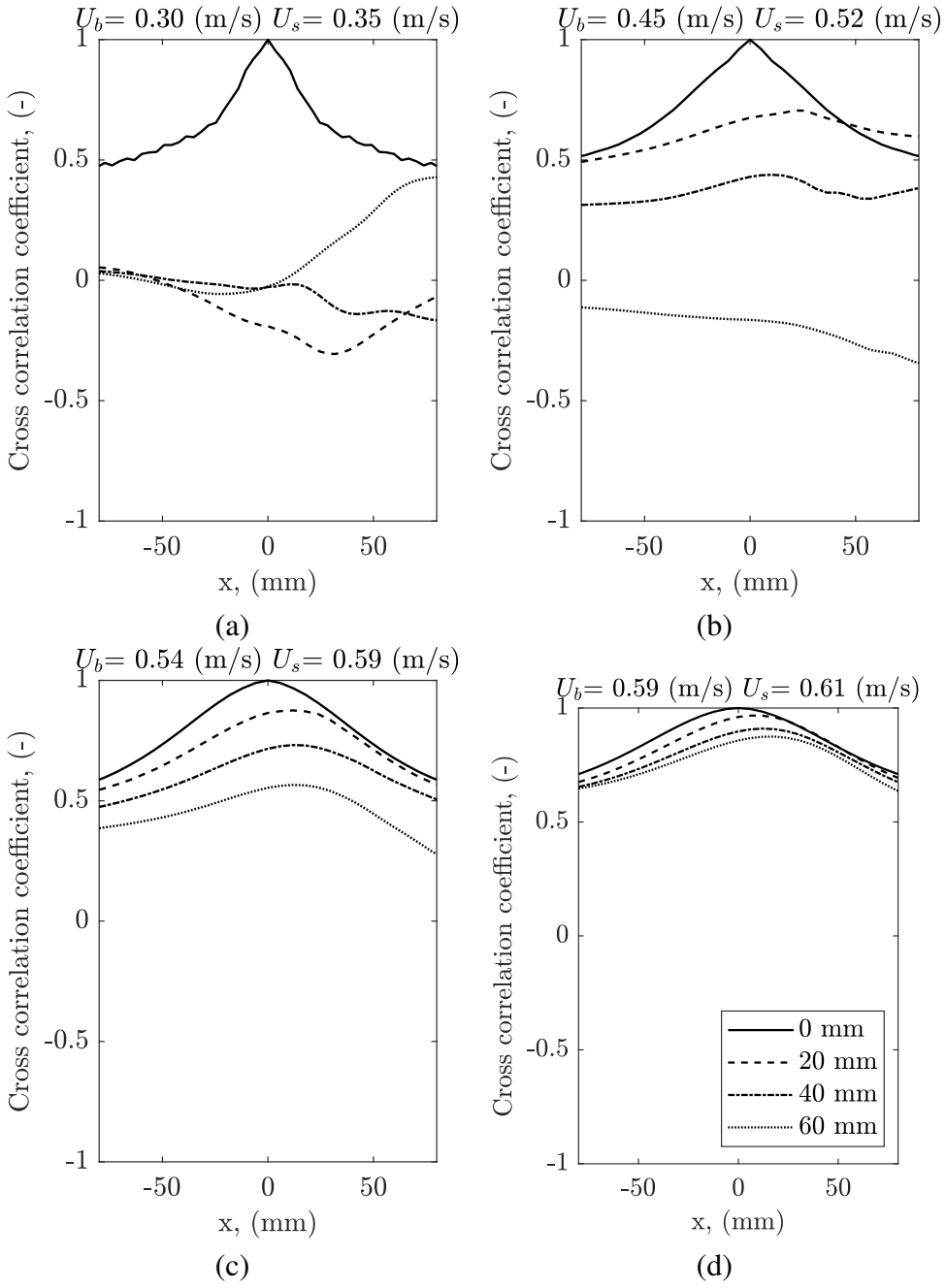

Figure 5.28 The temporal cross-correlation data for flow condition (a) 1, (b) 4, (c) 8 and (d) 13 derived from wave probe free surface measurement. Four line types represent different wave probe spatial separations.

Figure 5.28 shows the temporal cross-correlation functions for 4 wave probe separations, with the time axis converted to spatial lag using the surface velocity. The temporal correlation functions are obtained for all 22 wave probe pairs (listed in Table 3.1) and for all flow conditions. In Fig. 5.29, each circle marker y value corresponds to the extreme y value for each line in Fig. 5.28 and the x value corresponds to the wave probe separation indicated in the legend. The x-axis is the time lag in Eq. 5.13 times the surface velocity measured by floating tracers. It can be observed that measured spatial correlation results do not necessarily follow the spatial correlation function (Eq. 2.30) proposed by Nichols (2014) for all flow conditions, especially for high flow conditions (see Fig. 5.28d and e). The dashed line is obtained by MATLAB 'spline' interpolation to better visualise the pattern of experimental markers. For flow conditions 1 - 7 (see Fig. 5.29a, b and c), there is an oscillating component, a decay in the amplitude of the oscillation, and an overall decay towards a constant value. Previous study in rectangular channels (Horoshenkov et al., 2013) have found the constant value to be zero but it appears non-zero in pipe flow or perhaps takes a longer distance to reach zero. The oscillating component is only apparent for lower flows. For flow conditions 8 - 14 (see Fig. 5.29d and e), the oscillation pattern is hardly seen but only exponential decay and the decay rate generally increases with the flow rate.

Comparing Fig. 5.29a, b and c, higher flow rate flows show larger oscillation period, which agrees with Horoshenkov et al. (2013), Nichols et al. (2016). To estimate the oscillation spatial period for flow conditions 1 - 7, the minima in the spatial correlation function is determined using MATLAB 'islocalmin' function as indicated by blue star markers. The oscillation spatial period is generally consistent for all periods as shown in Fig. 5.28b and c while a bit ambiguous for flow condition 1 large separations as shown in Fig. 5.28a. The characteristic spatial period L_0 is calculated by the distance between first two minima as shown in Fig. 5.29a, b and c first two blue star markers. Figure 5.30 shows that the characteristic spatial period demonstrates a strong consistent nonlinear relationship with bulk flow velocity and hydraulic radius. Nichols (2014) has found a nonlinear relationship between normalised characteristic spatial period L_0/k_s and normalised velocity U_b/U_*. For the smooth bed condition in this study, the equivalent roughness k_s and shear velocity U_* is extremely small. Therefore, non-normalised characteristic spatial period is plotted against bulk flow velocity as shown in Fig. 5.30a. The characteristic spatial period increases with the bulk flow velocity. The relationship between the characteristic spatial period and the hydraulic radius is shown in Fig. 5.30b. A quadratic function $L_0 = 27.61R_h + 0.07$ is fitted to the experimental data as shown in Fig. 5.30b, with a best fit coefficient of determination $R^2 = 0.97$. This equation quantifies length dependency and is valid for flows in the depth range $15.7\ \% < d/D < 43.0\ \%$.

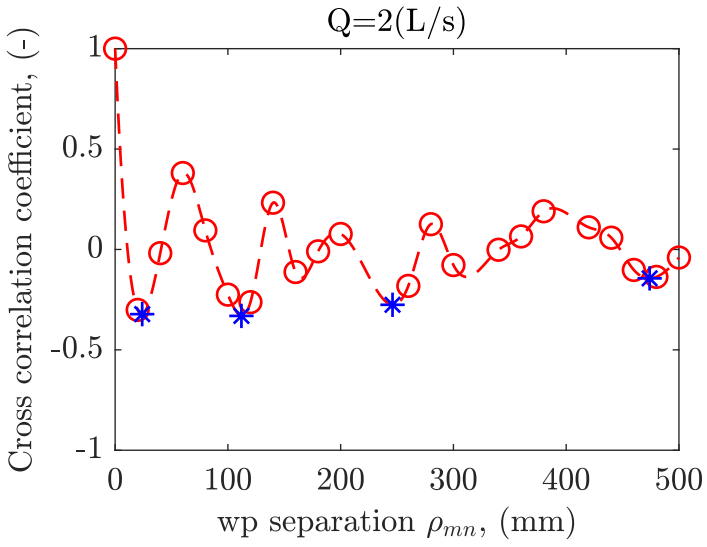
Q=2(L/s)
Cross correlation coefficient, (-)
1
0.5
0
-0.5
-1
0
100
200
300
400
500
wp separation ρ_{mn}, (mm)

(a)

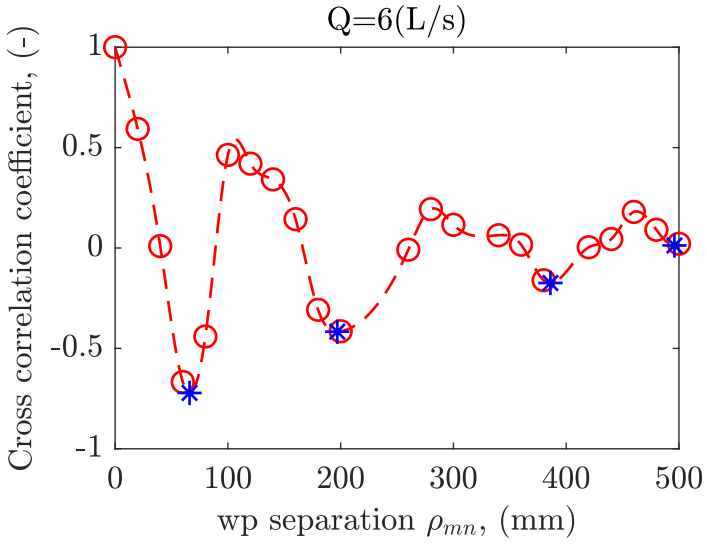
Q=6(L/s)
Cross correlation coefficient, (-)
1
0.5
0
-0.5
-1
0
100
200
300
400
500
wp separation ρ_{mn}, (mm)

(b)

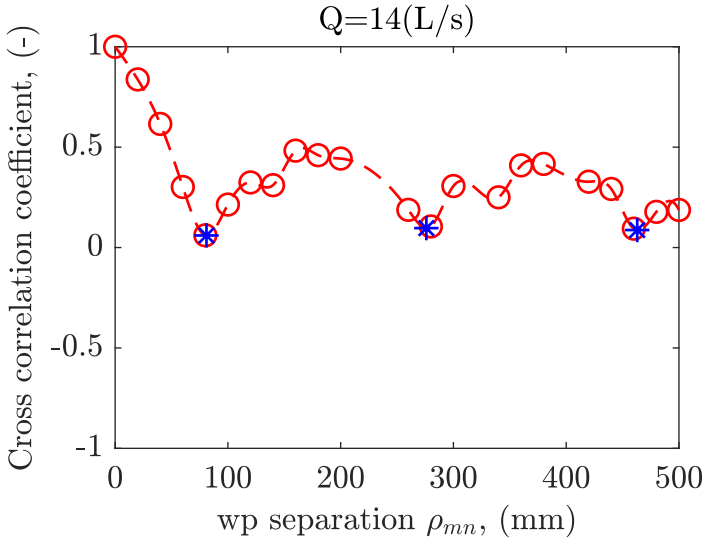
Q=14(L/s)
Cross correlation coefficient, (-)
1
0.5
0
-0.5
-1
0
100
200
300
400
500
wp separation ρ_{mn}, (mm)

(c)

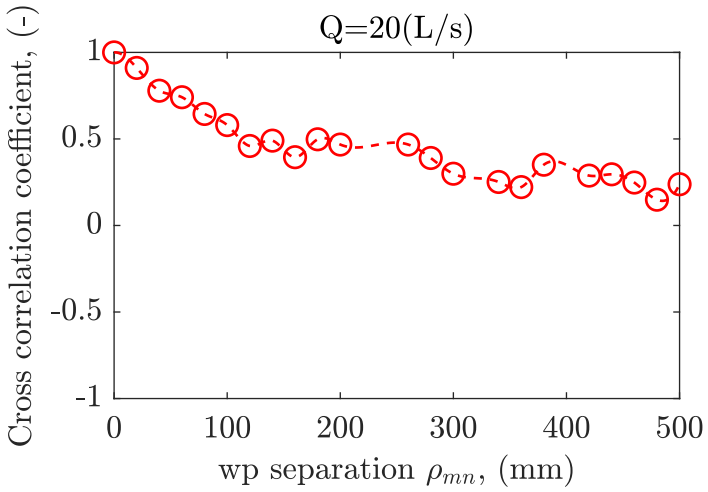

(d)

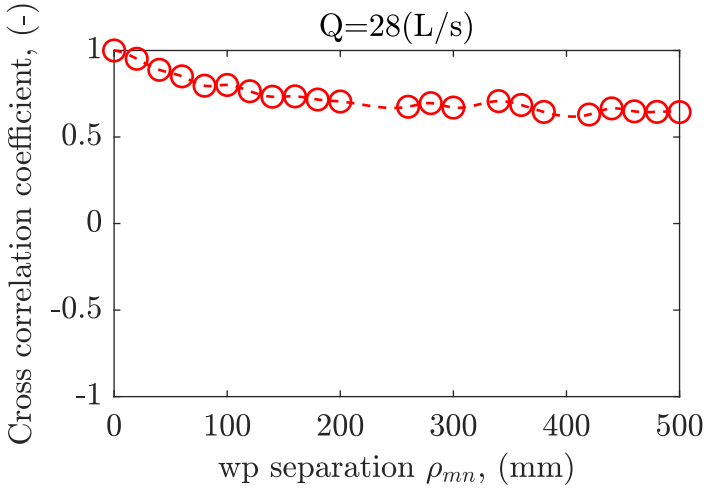

(e)

Figure 5.29 Spatial cross correltaion function for water surface roughness for flow conditions (a) 1, (b) 3, (c) 7, (d) 10 and (e) 14.

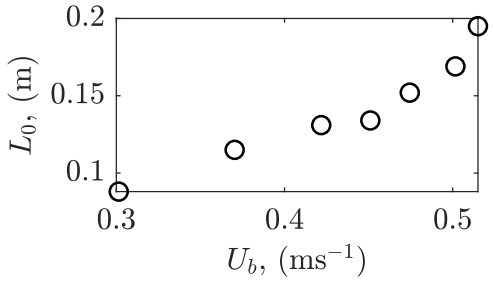

(a)

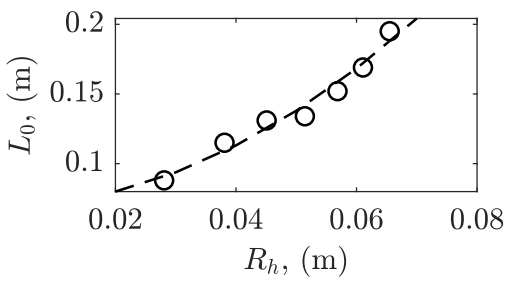

(b)

Figure 5.30 The dependence of the characteristic spatial period against (a) bulk flow velocity U_b and (b) hydraulic radius R_h.

With the estimated surface characteristic spatial period, the relationship between the oscillation frequency and the standard deviation of water surface is further analysed. As discussed in subsection 5.3.1, the surface pattern inverts periodically over time and advects at a speed close to the surface flow velocity. The temporal frequency of oscillation of the free surface pattern f_0 is defined by

$$f_0 = U_s/L_0, \tag{5.14}$$

where L_0 is defined from the spatial correlation function as mentioned in the previous paragraph. Figure 5.31 shows the relationship between oscillation frequency f_0 and the standard deviation of surface fluctuations. The standard deviation surface fluctuation error bars represent variation across 7 wave probes and the oscillation frequency error bars represent variation of 10 repeated surface velocity measurements. The simple harmonic motion model proposed by Nichols et al. (2016) (according to Eq. 2.33) is plotted as a dashed line for reference, with depth of influence factor $N = 28$. It can be noted that the measurement data fit the Nichols et al. (2016) model well when the standard deviation surface fluctuation is 0.34 mm $< \sigma <$ 0.60 mm and slightly smaller than the theory when $\sigma <$ 0.33 mm. The value of the depth of influence factor in the model is optimized using the MATLAB 'fit' function, with an initial guess $N = 28$. The optimised depth of influence factor is found to be $N \approx 37$, as shown in Fig.5.31 as a dotted line. This suggests that the free surface oscillation motion affects a body of water down to 37 average wave heights below the mean free surface level when the pipe is less than 43 % filled. This can further explain the deviation in the close to free surface region as shown in Fig. 5.3 in subsection 5.1.1. The experimental data shows similar trend with the oscillation model. The disparity between the experimental data and the model can be explained by uncertainties when estimating the characteristic spatial period. The characteristic spatial period is only estimated by the first period rather than averaging several periods. Besides, Nichols et al. (2016) model did not take into account the effect of the surface tension, which is negligible in their study. As discussed in subsection 5.3.2, surface tension plays more important role in smooth pipe flows than in rough bed channel flows.

A discontinuity can be observed between the third and fourth experimental data point in Fig. 5.31. The depth of influence factor N calculated directly for each flow condition according to Eq. 2.33, with error bars defined according to the aforementioned uncertainties, is shown in Fig. 5.32. Nichols et al. (2016) has found the value of N is relatively constant in their study. In this study, the value of N is generally constant only when 0.34 mm $< \sigma <$ 0.60 mm while gradually decreasing with increase of flows when $\sigma <$ 0.33 mm.

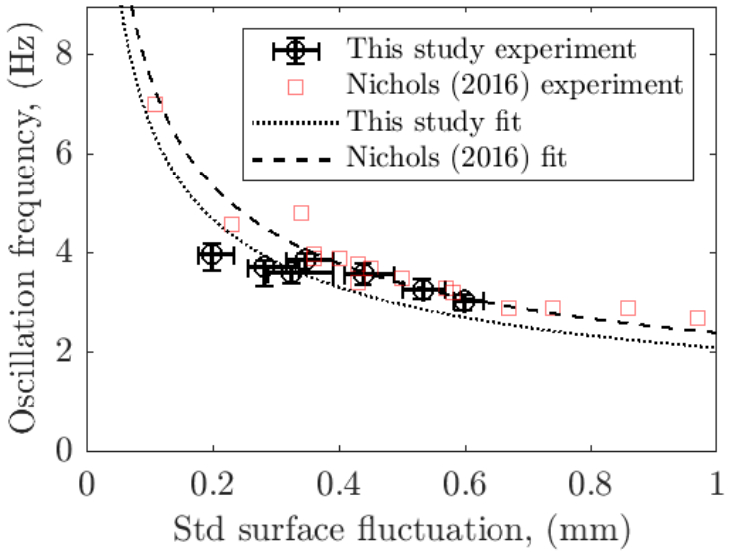

Figure 5.31 Surface oscillation frequency for flow condition 1 - 7 in this study and the study of Nichols et al. (2016) gravel bed flow conditions.

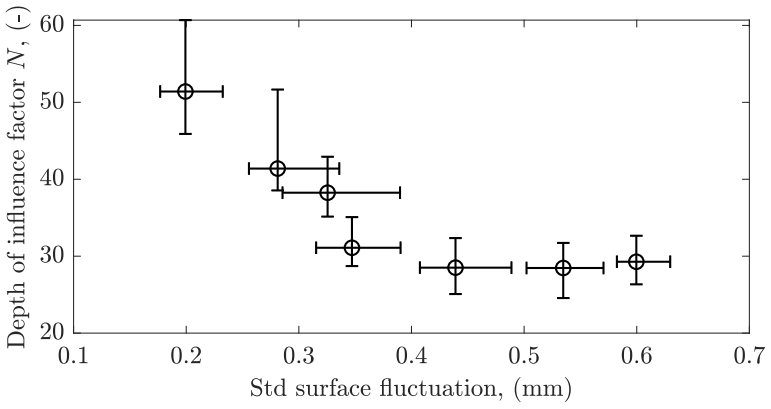

Figure 5.32 Depth of influence factor, N, calculated for flow condition 1 - 7.

The surface oscillation behaviour may relate to bursting and sweeping events (Nichols et al., 2016, Shvidchenko and Pende, 2001). Besides, Liu et al. (2022) has found the linkage between the occurrence of surface boils and bursting motions. Therefore, the oscillation frequency f_0 and the near-bed bursting frequency f_B are plot against flow depth d for comparison in Fig. 5.33. The oscillation frequency f_0 is calculated according to Eq. 5.14. The bursting frequency f_B is obtained from (Nichols et al., 2016)

$$f_B = U_s/(DN_B), \tag{5.15}$$

where N_B is a normalised mean bursting period defined by Nezu and Nakagawa (1993). The value of N_B is optimized to obtain the minimum of the function

$$F(N_B) = \sum_{j=1}^{7} |f_{0j} - f_{Bj}|. \tag{5.16}$$

The N_B is found to be N_B = 1.6 in this study, which is within the region Nezu and Nakagawa (1993) suggested ($1.5 < N_B < 2.5$). This suggests that the free surface oscillation motion has linkage to the near bed busting phenomenon, which agrees with Nichols et al. (2016), Nikora and Goring (2000).

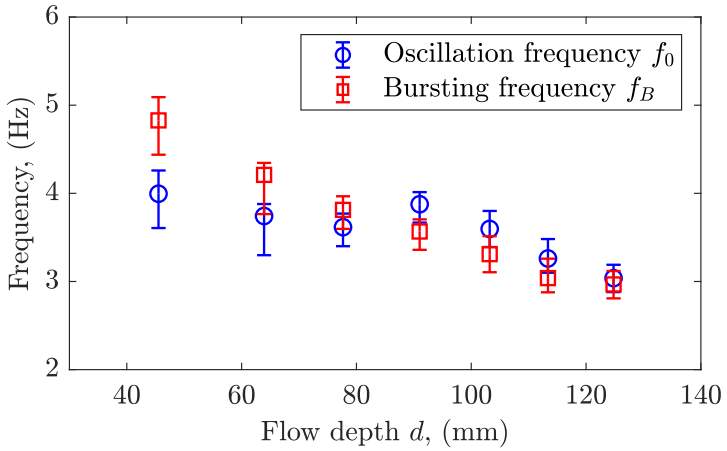

Figure 5.33 Surface oscillation frequency and bursting frequency (calculated according to Nezu and Nakagawa (1993)) as a function of the flow depth for flow condition 1 - 7.

5.3.4 Surface roughness along lateral direction

Subsections 5.3.1, 5.3.2 and 5.3.3 focus on the surface dynamics in the streamwise direction. This subsection investigates the surface dynamics more in the lateral direction. As shown in

Fig. 4.14, some variations can be observed in the lateral direction in the surface fluctuation standard deviation surface. To quantify the variation of the surface roughness along the lateral direction, the surface roughness is averaged over 297 mm streamwise length and plotted against lateral position as shown in Fig. 5.34. The surface roughness are generally symmetrical about the lateral center for all flow conditions, which means the time averaged free surface dynamics are symmetrical. A minima can be observed at the lateral center for all flow conditions, which is more obvious in Fig. 5.34a and b. Two maxima peaks can be observed in Fig. 5.34a, b and c, which can be explained by two secondary currents. Comparing Fig. 5.34a and b, the strength of the secondary currents increases. In Fig. 5.34c, these two peaks are less evident, which indicates two side secondary currents merge to the center. Besides, an increase of standard deviation towards to the wall can be observed in Fig. 5.34b, c and d. This can be explained by corner vortices in the corner region bounded by the pipe wall and free surface. The standard deviation increase towards pipe wall is more evident for higher depth flow, which means the corner vortices' effect is more obvious for higher depth flows. Liu et al. (2022) have found the maximum surface roughness occurs very close to the pipe wall from LES model for $d/D = 37.9$, 56.3 75.1 % cases. However, in this study, this is only valid for flows with relative depth $d/D > 49.3$ % (more than half filled flows) as shown in Fig. 5.34c and d. Besides, the difference of surface roughness along the lateral direction is generally within 0.03 mm in this study. This is the reason that the magnitude of surface fluctuations does not show a distinguishable difference at different lateral positions in the ST matrix as shown in Fig. 5.25.

5.3.5 Frequency wavenumber analysis

Subsections 5.3.2 and 5.3.3 have investigated the free surface dynamics along a relatively large spatial streamwise rnange (500 mm). The free surface behaviour and the role played by turbulence can be inferred from the frequency spectrum of surface fluctuation Dolcetti (2016), Liu et al. (2022), Tani and Fujita (2020). The frequency wavenumber spectrum is calculated by means of a three dimensional Fourier analysis to the DIC measured data with an area of approximately 297 mm $\times$ 198 mm (2D in space and 1D in time). Examples of the streamwise and lateral logarithm of the frequency wavenumber spectra are shown in Fig. 5.35 and 5.36, respectively. The magnitude of the spectra increases with the increase of depth of flow for both streamwise and lateral directions, meaning higher surface fluctuations, which is as expected. For streamwise spectra as shown in Fig. 5.35, three ridges can be observed in the $k_x > 0$ region, corresponding to three types of motion. The dotted line in Fig. 5.35 indicates the surface velocity measured by the floating tracer, with the relationship:

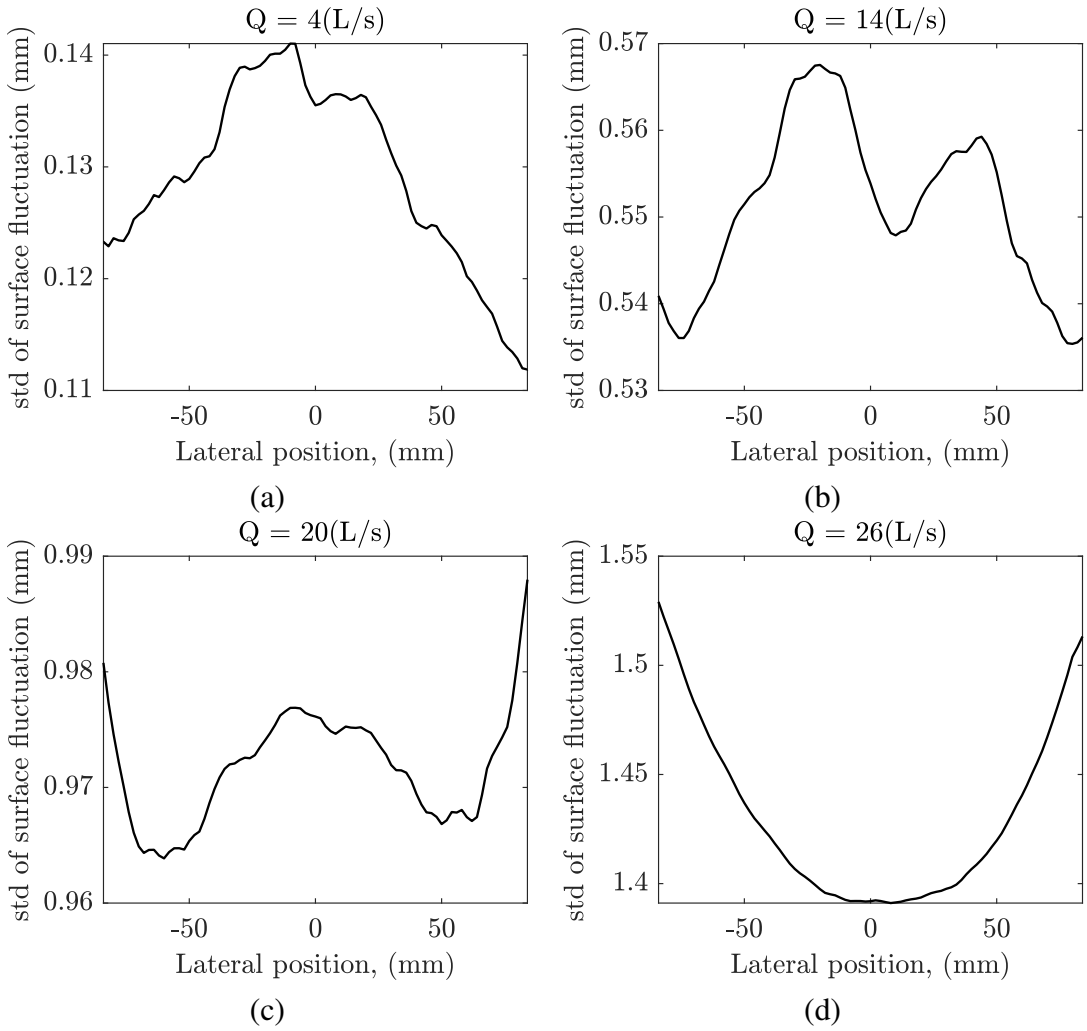

Figure 5.34 Mean Std surface fluctuation along lateral direction for flow conditions (a) 2, (b) 7, (c) 10 and (d) 12 from 2D DIC measurement.

$$\omega(k_x) = U_s k_x. \tag{5.17}$$

The straight line ridge overlaps well with the surface velocity, which indicates the turbulence driven behaviour of free surface fluctuations traveling at a constant speed close to the mean surface velocity. The two dashed lines next to the dotted line represent dispersion relationships of gravity waves by the mean surface flow. The dispersion relationships are described as:

$$\omega(k_x) = k_x U_s \pm k_x \sqrt{(\frac{g}{k_x} + \frac{T k_x}{\rho}) \tan(k_x d)} \tag{5.18}$$

The plus and minus sign in Eq. 5.18 correspond to travelling and receding waves, respectively. Comparing the magnitude of these three ridges, it can be observed that the contribution of three types of motion are comparable. This further explains the multiple gradients observed in the space time matrix as shown in Fig. 5.23 in subsection 5.3.1 and the different phase velocities observed in the dispersion relationship as shown in Fig. 5.26. There are some horizontal ridges for flow condition 4 - 14 in the frequency range 0 - 40 rads^{-1} (corresponds to 0 - 6.4 Hz) as shown in Fig. 5.35b, c and d. The magnitude of these horizontal ridges is higher for higher flow rates. The horizontal ridges in the streamwise spectra means waves travelling at zero velocity, in another words stationary waves.

Two ridges symmetric about k_y = 0 and a horizontal ridge can be observed in the lateral frequency wavenumber spectra as shown in Fig. 5.36. The travelling and receding waves are illustrated as dashed lines calculated by

$$\omega(k_y) = \pm k_y \sqrt{(\frac{g}{k_y} + \frac{T k_y}{\rho_f}) \tan(k_y d)}. \tag{5.19}$$

The symmetric ridges overlap well with the theoretical gravity waves. The magnitude of the gravity waves power spectra increases with increased flow. A horizontal ridge can be observed for all flow conditions in the lateral frequency wavenumber spectra. A constant frequency is also plotted in Fig. 5.36 as a dash-dotted line, calculated by

$$\omega(k_y) = k_y \sqrt{(\frac{g}{k_0} + \frac{T k_0}{\rho_f}) \tan(k_0 d)}, \tag{5.20a}$$

$$k_0 = \frac{2\pi}{2L_w}. \tag{5.20b}$$

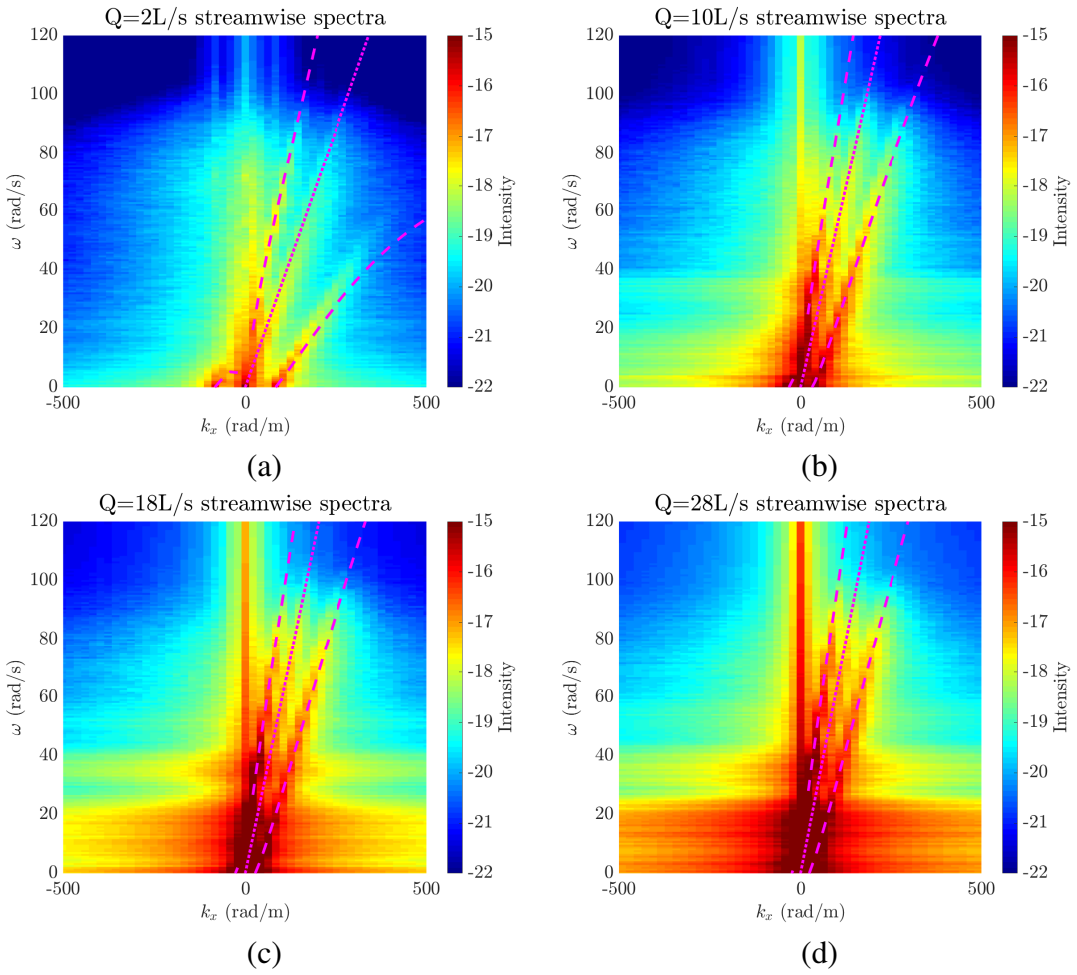

Figure 5.35 Streamwise frequency wavenumber spectra for flow conditions (a) 1, (b) 5, (c) 9 and (d) 14 from 2D DIC measurement.

The horizontal ridge overlaps well with the constant velocity calculated according to Eq. 5.20 for all flow conditions, except flow condition 1. This indicates water sloshing from side to side in the partially filled pipe, with a wavelength of 2 times of surface width L_w. This is a feature of pipe flow since the inlet flow was carefully controlled to have no lateral component and the flow was allowed to stabilise for a long time before measurements were taken.

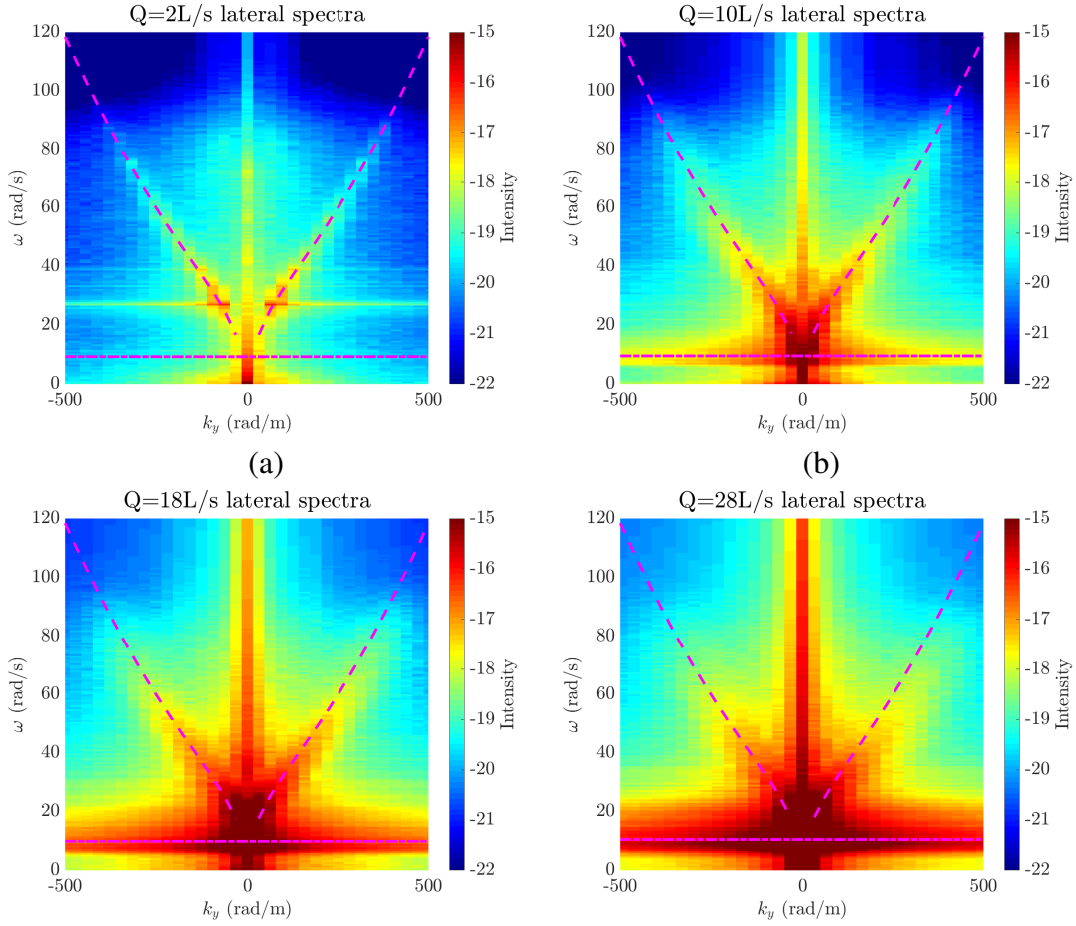

Figure 5.36 Lateral frequency wavenumber spectra for flow conditions (a) 1, (b) 5, (c) 9 and (d) 14 from 2D DIC measurement.

5.4 The relationship between free surface and turbulent flow

5.4.1 Water depth and flow rate

Figure 5.37 shows the relation between the water depth and flow rate for all 14 flow conditions and smooth pipe results from Romanova (2013) as circle and square markers, respectively. Apparently, both studies show water depth increases with the flow rate. Romanova (2013) has found the relationship follows the equation

$$d = 47Q^{0.47}, \tag{5.21}$$

with a best fit coefficient of determination R^2 = 0.99. The pipe slope in this study is two times steeper than the study of Romanova (2013), thus with similar flow rate, the water depth is lower in this study. For the pipe slope 1/1000 smooth pipe flow conditions, the relationship is found to be

$$d = 28Q^{0.58}, \tag{5.22}$$

with a best fit coefficient of determination R^2 = 0.996.

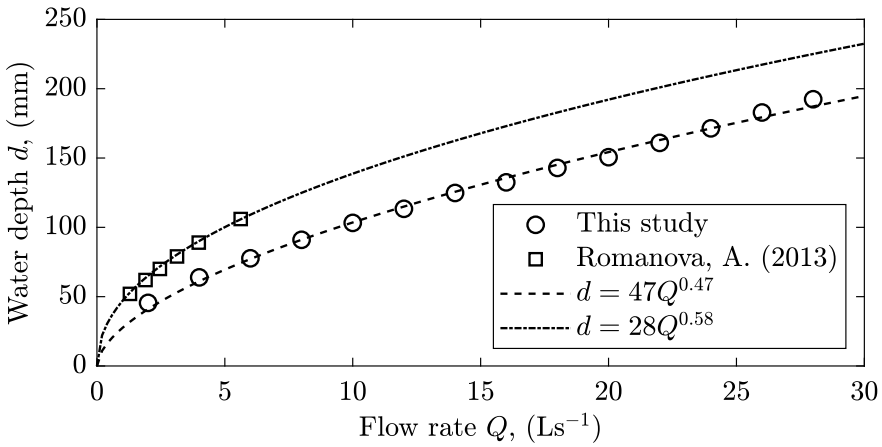

Figure 5.37 Water depth as a function of flow discharge for all smooth pipe flow conditions with R^2 = 0.996. Circle markers are from this study and square markers are from study of Roy et al. (2004), which used a smooth pipe flow but with a different slope

5.4.2 Bulk flow velocity and friction factor

Figure. 5.38 shows the bulk flow velocity as a function of friction factor for all 14 flow conditions and smooth pipe results from Romanova (2013) as circle and square markers, respectively. Romanova (2013) has found the bulk flow velocity always decreases with the increase of friction factor. In this study, the bulk flow velocity always decreases with the increase of friction factor only when the relative depth d/D is less than 35.6 %, beyond that this trend is less obvious. Romanova (2013) has fitted an equation

$$U_b = 0.0089 f^{-1}, \tag{5.23}$$

with a best fit coefficient of determination R^2 = 0.98 for smooth pipe conditions. In this study, the relationship of bulk flow velocity and friction factor is found to be

$$U_b = 0.0001 f^{-2.2}, \tag{5.24}$$

with a best fit coefficient of determination R^2 = 0.92.

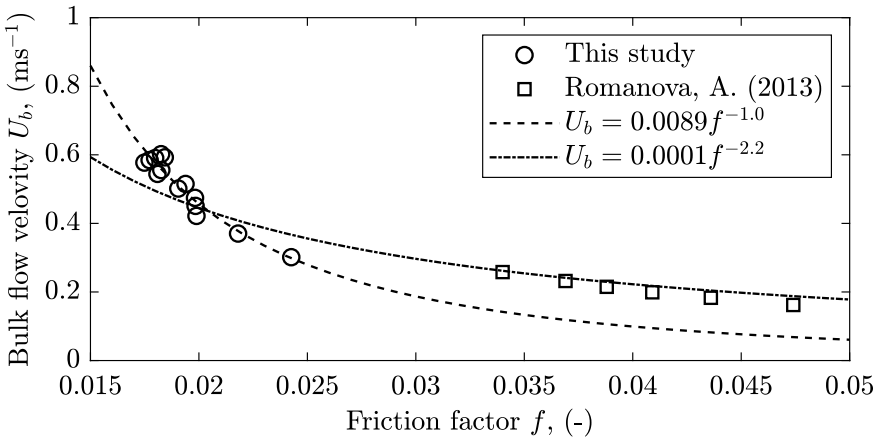

Figure 5.38 Bulk flow velocity as a function of friction factor for all smooth pipe flow conditions with R^2 = 0.92.

5.4.3 Surface velocity

The relationship between surface velocity from the floating tracer and the mean bulk flow velocity is shown in Fig. 5.39. Round markers represent the mean surface velocity and error bars correspond to maximum and minimum values from 10 repeated tracer tests. The average variance of surface velocity by 10 repeated tests for all flow conditions is 0.019 m/s^2. The variance likely arises from uncertainties in timing of the floating tracer and the floating tracer

not flowing exactly along the lateral center of the pipe. A 1:1 line is plotted in Fig. 5.39 in blue for reference. It can be noted that surface velocity is always greater than bulk flow velocity for all flow conditions examined. Surface velocity appears proportional to bulk flow velocity up to a certain flow rate and the proportional ratio decreases after that. A best fit line through the origin is fitted to the first 7 data points (when the relative depth is below 43%). As shown by the red dashed line in Fig. 5.39, surface velocity is approximately 1.14 times the bulk flow velocity when the flow depth is less than 43% of the pipe diameter. For higher flow rate flows, the ratios of surface and bulk flow velocity become smaller than 1.14. This can be explained by the streamwise velocity profile in Fig. 4.22b. For higher flow rate (higher flow depth) conditions, the velocity profile does not follow a simple parabolic shape and the maximum velocity no longer occurs at the free surface. This confirms the existence of the dip phenomenon in the partially filled pipes (Guo et al., 2015, Wu et al., 2018).

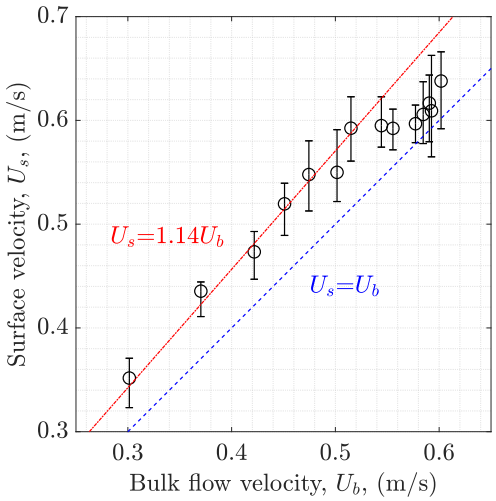

Figure 5.39 Surface velocity versus bulk flow velocity.

5.4.4 Free surface and sub-surface quantitative analysis

The proposed phase-space 1D detection method is described in detail in section. 5.2. Profiles of the size of turbulent structures and number of structures per meter, obtained from sub-surface streamwise ADV data using both U-level and phase-space methods, are compared in Fig. 5.21 and Fig. 5.22. Turbulent profiles obtained from the phase-space method show similar results as from the U-level method while phase-space method takes account of the physical reality that a coherent structure. With the turbulence properties quantified with the sub-surface data, it is necessary to perform the same analysis on the free surface data. The phase-space method is applied to the surface vertical velocity, which is obtained by

taking the time derivative of the wave probe measured surface fluctuation data. Figure. 5.40 show profiles of size of turbulent structures and number of structures per meter for both free surface and sub-surface data using the phase-space method. The sub-surface size of turbulent structures is the product of the mean event duration from ADV vertical data and local time-averaged streamwise velocity and the free surface size of turbulent structures is the product of (a) the mean event duration from wave probe vertical velocity data and (b) mean free surface velocity measured by floating tracer. The sub-surface number of structures per meter is the reciprocal of the product of (a) the mean event period from ADV vertical data and (b) local time-averaged streamwise velocity. The free surface number of structures per meter is the reciprocal of the product of (a) the mean event period from wave probe vertical velocity data and (b) mean free surface velocity measured by floating tracer. Comparing Fig. 5.40a, Fig. 5.21a, Fig. 5.40b and Fig. 5.21b, it can be noted that the sub-surface profiles (markers at $z/d < 1$) calculated from vertical and streamwise ADV data are similar. With the increasing flow, the size of turbulent structures are larger and a fewer number of turbulent structures are apparent per meter. The free surface markers (markers at $z/d = 1$) are all in the trend of the sub-surface profiles, even though they are measured by two different pieces of equipment out of synchronisation.

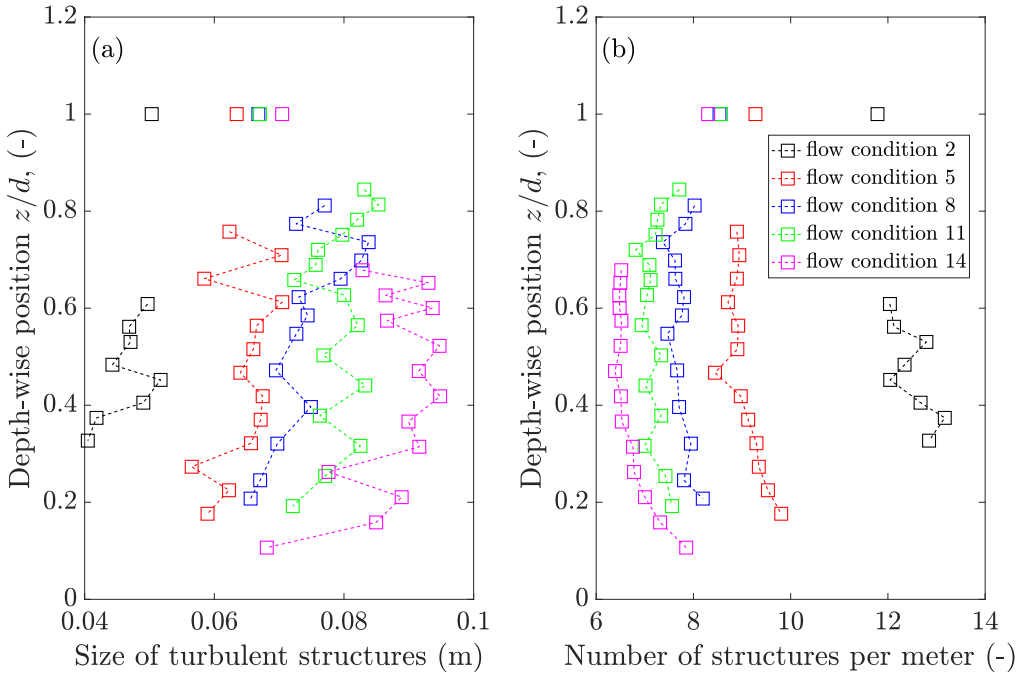

Figure 5.40 Free surface and sub-surface phase-space analysis (a) size of turbulent structure profile and (b) number of structures per meter.

Since the size of free surface features and number of structures per meter can be observed changing with different flow conditions in Fig. 5.40, these two free surface feature properties are plotted against flow depth for all flow conditions in Fig. 5.41 and 5.42, respectively. Circle and square markers correspond to results obtained from wave probes and DIC, respectively. Results from wave probes and DIC generally overlap, showing a similar pattern. As shown in Fig. 5.41, the size of free surface turbulent structures generally increases with flow depth, which agrees with the literature for rectangular channels Nichols (2014), Roy et al. (2004). This finding further supports the observation of Smolentsev and Miraghaie (2005) that the average size of the turbulent patch at the surface decreases as Froude number increases (higher Froude number corresponds to low flow depth in this study as illustrated in Table 3.2). Interestingly, instead of a single gradient linear trend, two linear trends can be observed in Fig. 5.41 for flow conditions 1-4 and 5-14 as indicated by a dashed line and dash dotted line, respectively. The scale is smaller for higher flow conditions than lower flow conditions. In this study, the size of free surface features is approximately 0.74 times the flow depth when the relative flow depth is less than 32 % and 0.45 times the flow depth when the relative flow depth is more than 35 %. Two different turbulence intensity profiles can be observed as well for flow conditions 1-4 and 5-14 as illustrated in Fig. 5.10. This suggests that flows with similar sub-surface turbulence intensity profiles have similar free surface feature size scale.

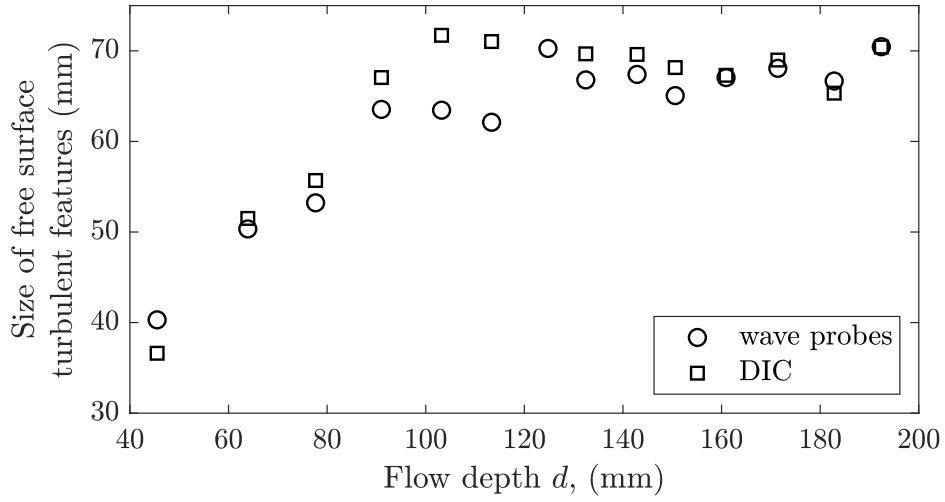

Figure 5.41 The correlation between the size of the free surface features at the lateral center and the depth of the flowing water was investigated using wave probes and DIC, and analysed using a phase-space method.

Figure. 5.42 shows that the number of free surface features per meter decreases with the flow depth.

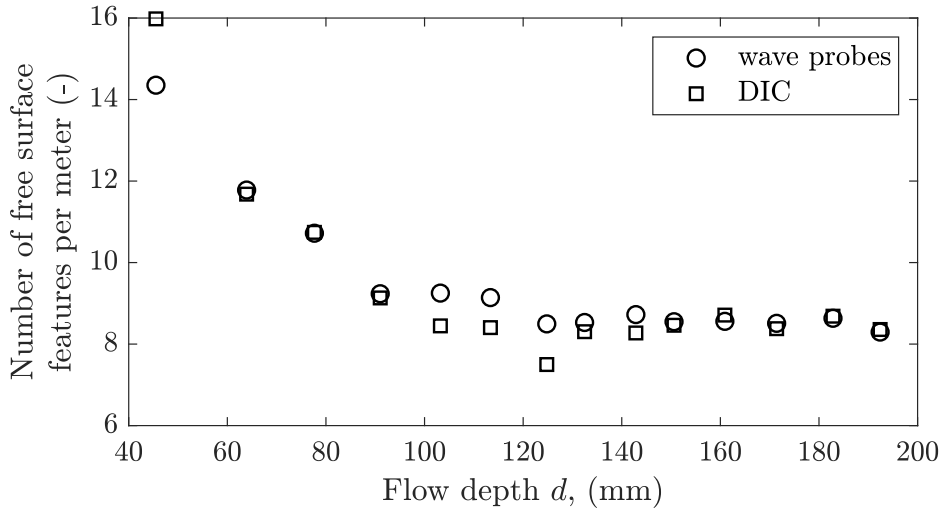

Figure 5.42 The correlation between number of free surface features per meter scale at the lateral center and the depth of the flowing water was investigated using wave probes and DIC, and analysed using a phase-space method.

The free surface lateral centerline analysis from wave probes and DIC show comparable results. The phase-space analysis is then applied to all 7 wave probes and different lateral positions in the DIC measured surface fluctuations. Figure. 5.43 and 5.44 show the size of free surface turbulent features and number of free surface turbulent features per meter against lateral position, respectively. All profiles are generally symmetrical about the lateral center. Example of 6 flow conditions are shown in Fig. 5.43, with Fig. 5.43a and b representative for flow conditions 1 - 5 and Fig. 5.43c - f representative for flow conditions 6 - 14. As shown in Fig. 5.43a and b, the size of free surface turbulent features peak at the lateral center with two additional small peaks offset from the lateral center. It can be seen from Fig. 5.43c - f that these two small offset peaks still exist while showing a minimum in the lateral center. These two peaks likely correspond to what Ng et al. (2018) observed in a partially filled pipe, described as a pair of rolls reflected about the pipe vertical bisector, which is a line dividing the pipe into two equal halves vertically. A concave in the lateral center can start to be observed when flow depth is greater than $d/D > 39.1$ % as shown in Fig. 5.43c - f. An 'M' shape can be evidently visible in Fig. 5.43c and d. For the fixed gradient and roughness pipe condition in this study, higher depth flows correspond to higher Reynolds number flows and thus stronger secondary currents. Two strong secondary currents at both lateral sides appear to interact at the lateral center and reduce the size of free surface features when the Reynolds number greater than 3.05×10^4.

Figure. 5.44 shows 6 examples of number of free surface turbulent features per meter against lateral position. Shapes of these profiles are generally opposite to the profiles in

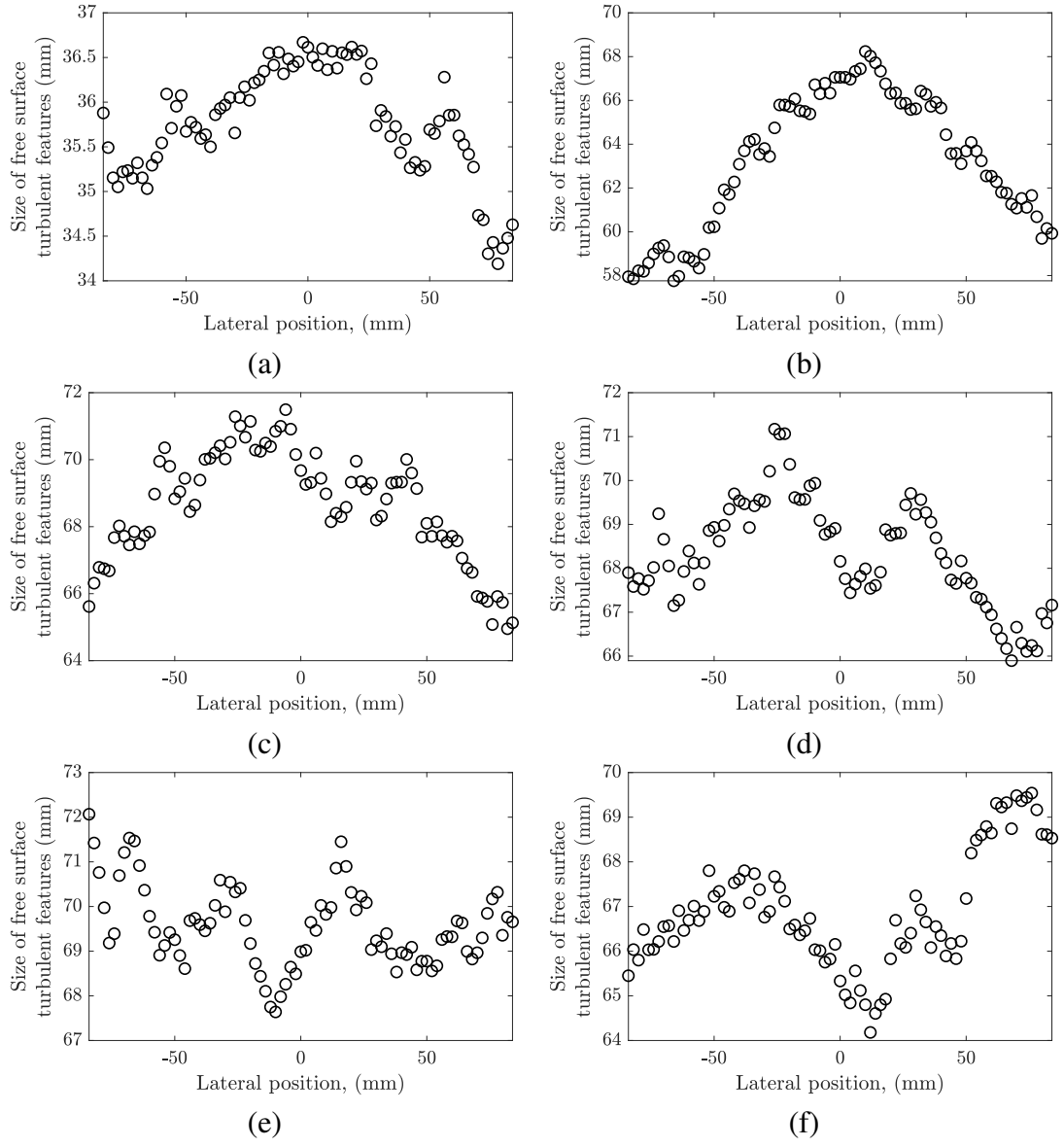

Figure 5.43 Size of free surface feature along lateral positionfor flow conditions (a) 1, (b) 4, (c) 8, (d) 10, (e)12 and (f) 13 from 2D DIC measurement.

Fig. 5.43. It makes sense as when the free surface feature size is larger, the number of features would be fewer per meter.

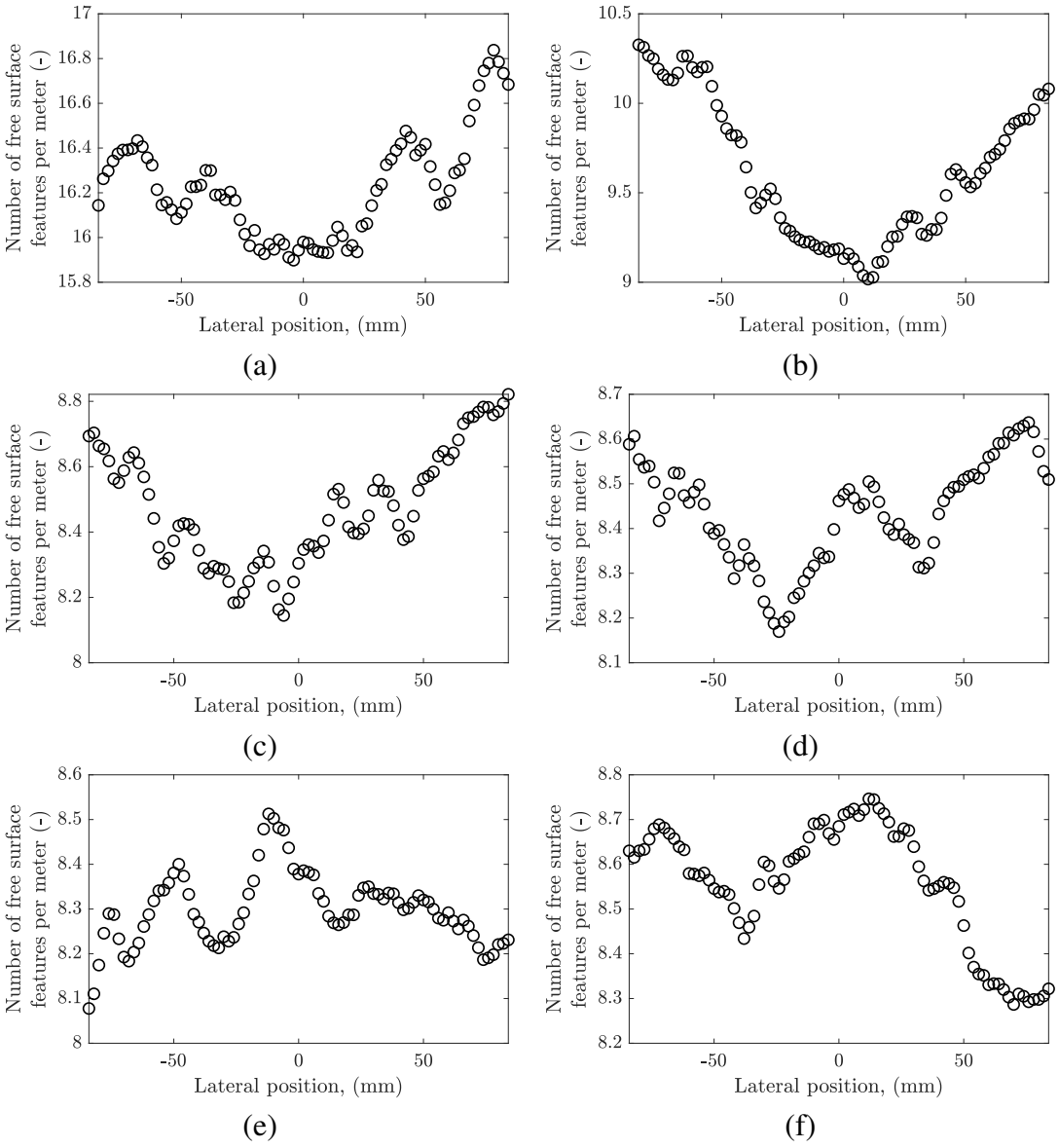

Figure 5.44 Number of free surface features per meter along lateral position for flow conditions (a) 1, (b) 4, (c) 8, (d) 10, (e)12 and (f) 13 from 2D DIC measurement.

5.5 Doppler radar sensing

Preceding sections 5.3 - 5.4 indicate that free surface features can be used to understand the behaviour of flow, turbulence, and secondary currents below the surface. Therefore, radar method may have value if it can allow the surface reconstruction non-intrusively. This section investigates how the response of radar to the dynamics of water surface.

5.5.1 Radar non-linear demodulation and calibration

As mentioned in subsection 4.5.3, the compensation function obtained from the electric circuit can reduce the I/Q signal distortion. However, the given function results in under or over compensation of the signal as shown in Fig. 4.31. Therefore, there is a need to find an optimal compensation function. The coefficient a_1 in the compensation function H_{D1} is optimised through 'EVM optimisation' Guo et al. (2015). Mechanical motion No. 44 with motion amplitude 2.45 mm and frequency 3.2 Hz in Table. 4.3, a motion with frequency less than the cutoff frequency of the high pass filter and total displacement more than three quarter of the half radar wavelength, is chosen for the calibration and optimisation. The chosen 4.9 mm total displacement motion signal response can form a 78.9% ellipse arc perimeter, which ensures the good ellipse fitting. The dominant frequency 3.2 Hz of the mechanical motion is below the high pass filter cutoff frequency 4.1 Hz, which means existence of signal distortion in the interest region.

The I/Q constellation from experiment measurement for mechanical motion No. 44 is shown in Fig. 5.45a with value of EVM -7.64 dB calculated from Eq. 2.48. The experiment measured I/Q signals are compensated with the modified compensation function $H_{D1} \cdot H_{D1} \cdot H_{HP}$ as discussed in subsection 4.5.3, with coefficient a_1 swept in a predefined range (0.94 - 0.98) around the electric circuit calculated value (0.974). The compensated I/Q constellation is then normalised to a unit circle arc by algebraic ellipse fitting (Zakrzewski et al., 2014). The compensated and normalised I/Q constellations by different values of coefficient a_1 are shown in Fig. 5.45b -f, with unit circle drawn in grey line. The EVM value is a measure of the degree of distortion and the quality of the I/Q signals (Gu et al., 2016). Smaller EVM values represent better fit of I/Q signals to the unit circle, thus less signal distortion. It can be noted that the compensated signals (Fig. 5.45b - f) show smaller value of EVM compared with the uncompensated signals (Fig. 5.45a). Among all the compensated signal I/Q constellations, Fig. 5.45e shows the best fit to the unit circle, with the smallest EVM value -19.76 dB.

In order to accurately recover the free-surface displacement information in the I/Q signals, the value of EVM needs to be minimised. The relationship between EVM and the value of coefficient a_1 is shown in Fig. 5.46 on the left y axis. The relative difference

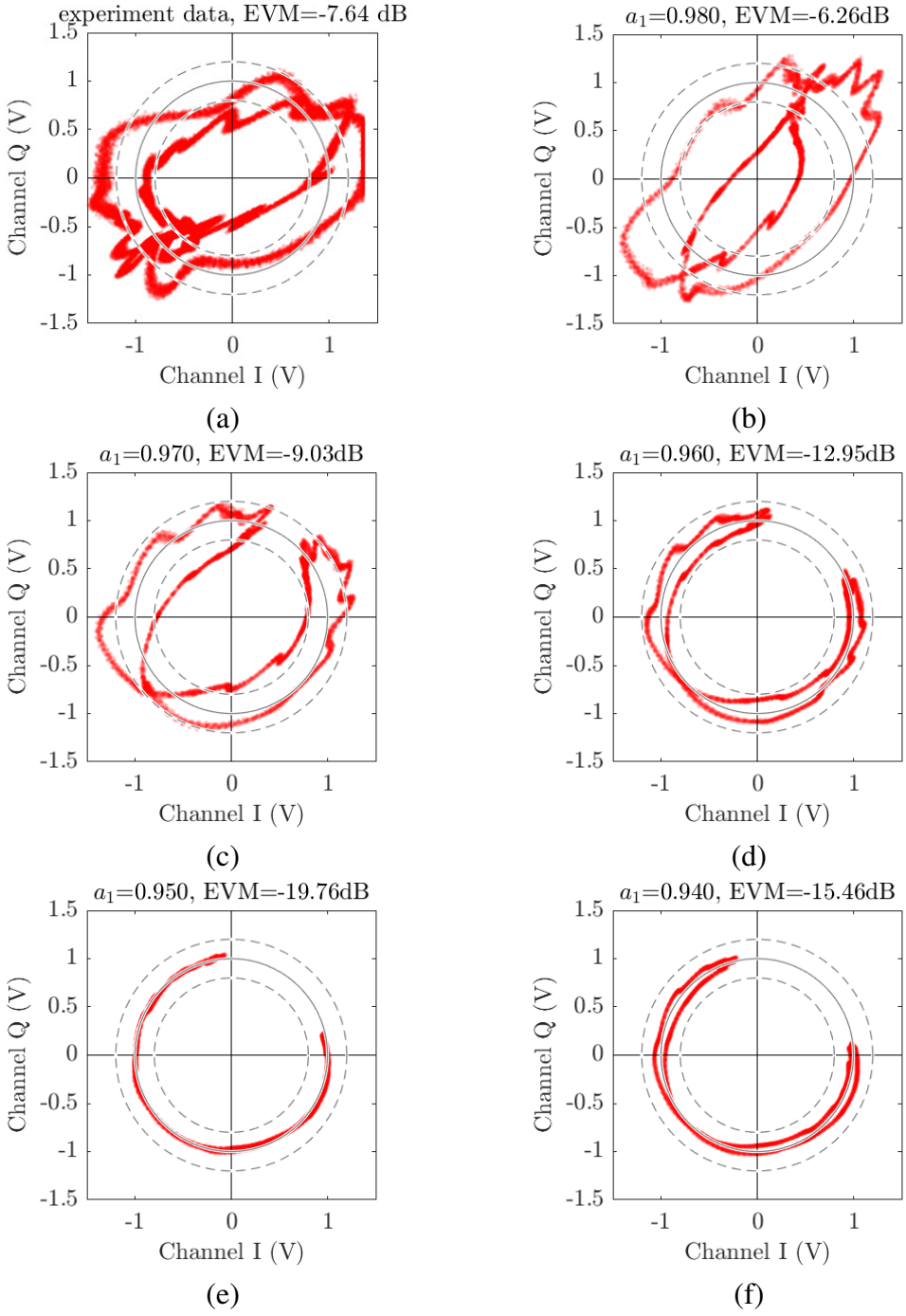

Figure 5.45 (a) Distorted I/Q signals from experiment in the I/Q plane. Compensated I/Q signals in the I/Q plane. The experiment result is compensated using different coefficient a_1: (b) $a_1 = 0.98$, (c) $a_1 = 0.97$, (d) $a_1 = 0.96$, (e) $a_1 = 0.95$ and (f) $a_1 = 0.94$.

between demodulated displacement from compensated DRS signals and displacement directly measured by LDS is shown in Fig. 5.46 on the right y axis. It can be noted that both EVM and relative difference decrease and then increase with a_1. This is reasonable as when a_1 is smaller than the optimum a_1, the signal is over compensated and when a_1 is larger than the optimum a_1, the signal is under compensated. The optimum a_1 is found to be 0.95, with which the EVM is -19.76 dB and relative difference of 0.6 % to LDS. Therefore the compensation function in this study is $H_D \cdot H_D \cdot H_{HP}$, with $H_D(z) = (1 - 0.95z^{-1})/(1 - z^{-1})$.

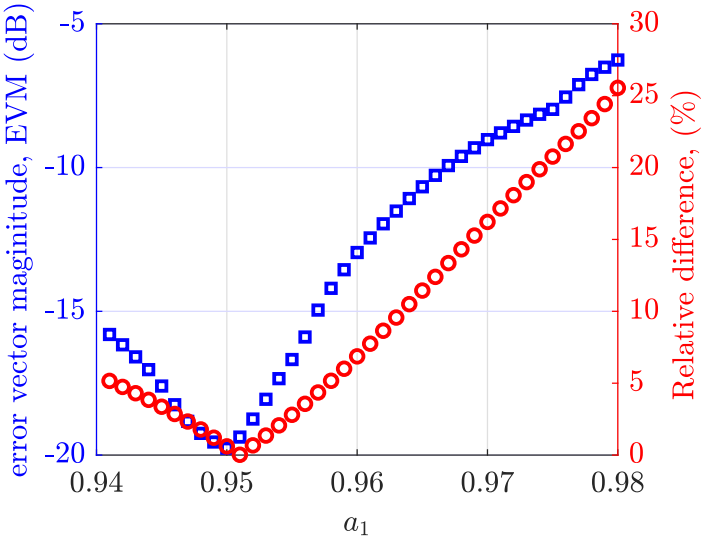

Figure 5.46 EVM and measured displacement relative error in response of coefficient a_1.

The amplitude imbalance A_e and phase imbalance ϕ_e are found to be 0.7601 and -0.1992, respectively from the ellipse fitting of constellation in Fig. 5.45e when a_1 is optimum. The imbalances of compensated signals are then corrected with the Gramm-Schmidt (GS) procedure (Zakrzewski et al., 2014). After the signal distortion compensation and the imbalances correction, the I/Q constellation forms a circle arc or a full circle shape. The DC offset (center of the arc or circle) is calibrated according to Zakrzewski et al. (2012) to bring the arc or circle to the origin. The procedure of recovering motion information from the amplified baseband signals is summarised in Fig. 5.47. The displacement is non-linearly demodulated by extended DACM algorithm Wang et al. (2014) and compared with displacement measured by LDS as mentioned in subsection 4.5.1.

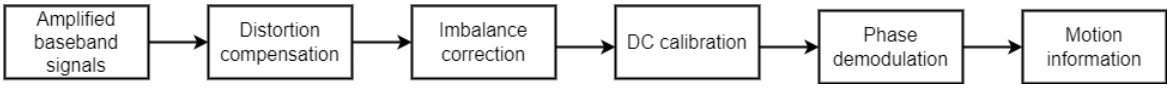

Figure 5.47 The framework of signal post processing in non-contact motion detect system.

The relative difference of measured sinusoidal motion amplitude by DRS and LDS is calculated according to

$$\text{relative error} = \frac{|A_{mDRS} - A_{mLDS}|}{A_{mLDS}} \tag{5.25}$$

where A_{mDRS} is the motion amplitude measured by DRS and A_{mLDS} is the motion amplitude measured by LDS. It can be seen from Fig. 5.48 that all 100 motions' measured relative difference being below 20 %. As shown in Fig. 5.48a, the relative difference is not affected by the dominant frequency of the motion, except some outliers in $f_m = 4$ Hz. In general, the relative difference decreases with the amplitude of the motion as shown in Fig. 5.48b. The accuracy is improved when the ratio of the amplitude and radar wavelength A_m/λ is greater than 0.2. Overall, 96 % ,78% and 36% of motions show relative difference within 10 % , 5% and 1%, respectively. Figure 5.48c shows the relative error for different motion amplitudes and motion frequencies. It can be seen that relative error reduced with the increase of motion amplitude and not affected by motion frequencies.

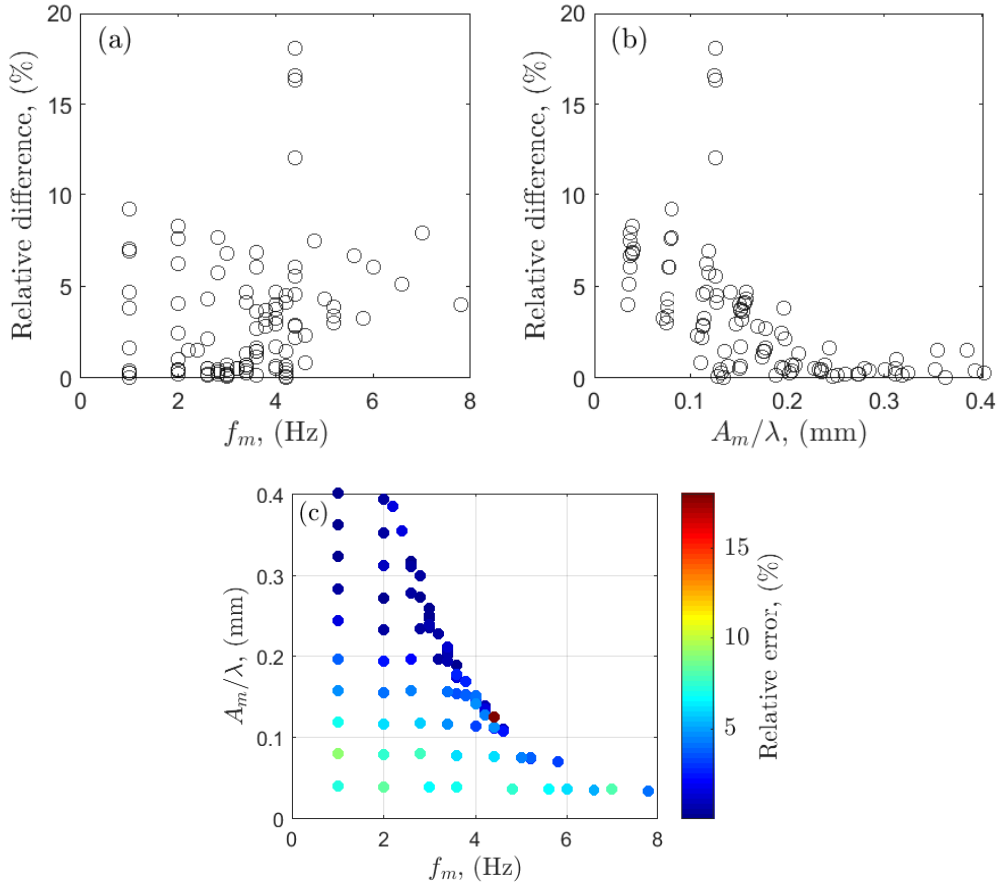

Figure 5.48 Relative error of measured motion amplitude between DRS and LDS vary with (a) different motion frequencies f_m, (b) different scaled motion amplitudes A_m/λ and (c) different motion frequencies f_m and scaled motion amplitudes A_m/λ.

5.5.2 Radar linear demodulation simulation

The non-linear demodulation from both I/Q channel outputs was used in the preceeding subsection 5.5.1 to recover the motion of the plate. When the detected motion displacement is small enough ($x_m \ll \lambda$) and the sensor is not placed at 'null point' (see subsection 2.5.2 for more details), the small angle approximation is valid. The baseband output is proportional to the motion displacement summed with the residual phase noise (Wang et al., 2014, Droitcour, 2006), resulting in the linear demodulation method, which will be used later in this subsection. As mentioned in subsection 2.5.2, when the nominal distance d_0 dependent on phase shift is an odd multiple of $\pi/2$, the radar is at optimum point and when it is an even multiple of $\pi/2$, the radar is at null point. As the I/Q channel has $\pi/2$ phase shift, when the channel I is at optimum point, the channel Q is at null point. Therefore, there is always one channel that is not in the null point.

In order to study the phenomenon of the null point and its effect on the linear demodulation, the ideal I/Q channel response to a 3 mm amplitude of 3 Hz sinusoidal motion is simulated in the following form:

$$I(t) = A_I \cos\left(\frac{4\pi x(t)}{\lambda} + \phi_I\right) + DC_I \tag{5.26a}$$

$$\begin{aligned} Q(t) &= A_Q \sin\left(\frac{4\pi x(t)}{\lambda} + \phi_Q\right) + DC_Q \\ &= A_Q \cos\left(\frac{4\pi x(t)}{\lambda} + \phi_I + \frac{\pi}{2}\right) + DC_Q \end{aligned} \tag{5.26b}$$

$$x_m = 1.5\cos(2\pi 3t) \tag{5.26c}$$

$$A_I = A_Q = 1,\ DC_I = DC_Q = 0 \tag{5.26d}$$

The displacement time series of the sinusoidal motion is illustrated in Fig. 5.49. The response of both channels with different phase shifts are shown in Fig. 5.50, with each upper subfigure in the time domain and each lower subfigure in the frequency domain. When the channel I is at optimum point, with phase shift being odd multiple times of $\pi/2$, channel Q is at null point (Li and Lin, 2008). As is shown in Fig. 5.50b time series, Channel I shows a sinusoidal pattern that is proportional to the motion illustrated in Fig. 5.49. Similarly, when channel Q is at optimum point, channel I is at null point with phase shift equal to even multiples of $\pi/2$ (see Fig. 5.50d). When the radar is at the null detection point, for example Channel Q output in Fig. 5.50b and Channel I output in Fig. 5.50d, the channel shows a periodic signal that has twice the frequency of the motion. This agrees with observations from Park et al. (2007a) who measured human chest movements and found that the measured respiration

rate is actually twice the real value when measured at the null point. As shown in Fig. 5.50d time series, channel Q is at optimum point and signal response is proportional to the motion. When the radar is at the position between optimum and null points, the time series response is partly distorted. The power spectra in Fig. 5.50a and c shows that the dominant frequency of the motion can be detected while some additional spikes still occur, corresponding to the distortion in the signal.

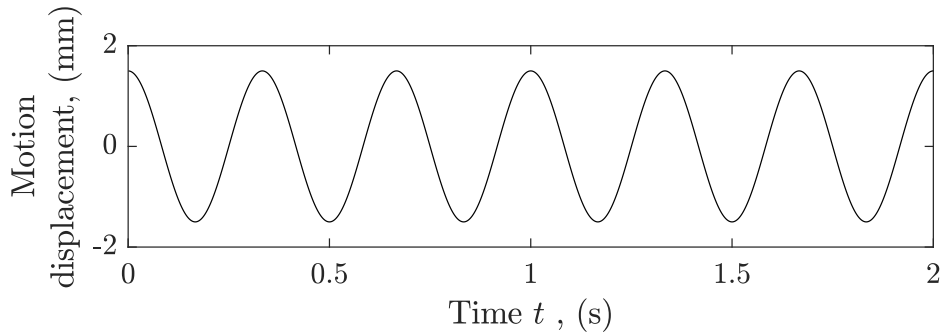

Figure 5.49 Displacement time series of the $x_m = 1.5\cos(2\pi 3t)$ sinusoidal motion.

As illustrated in Fig. 5.50 time series, the response of I/Q channel to the same motion but different phase shift (related to different nominal distance) are different. Therefore, the standard deviation of both channel outputs should be different for different phase shifts. The standard deviation of I/Q channel output for the motion of Eq. 5.26c is shown in Fig. 5.51. The standard deviation of the channel output varies periodically with the phase shift, with the period of $2 \times \pi/2$. The variation for I channel has $\pi/2$ phase shift with Q channel.

The preceding paragraph described how the standard deviation of channel output varies with the phase shift to a single amplitude and frequency sinusoidal motion. Figure 5.52 illustrates the standard deviation of channel output response to different amplitude motions. The horizontal axis means the normalised motion displacement $2A_m/\lambda$, which is calculated by 2 times of sinusoidal amplitude normalised by the radar wavelength. Different lines represent the channel I response with different phase shift. It can be noted that when the normalised motion displacement is smaller than a certain value, the standard deviation of channel output can be assumed to be proportional to the motion displacement for all phase shift conditions. Hence the standard deviation of channel output can give an estimate of standard deviation of motion. The range for the small angle approximation to be valid is different for different phase shifts. For example, when the phase shift $\phi_I = 1 \times \pi/8$, the linear approximation is valid when $2A_m/\lambda > 0.35$. The linear approximation is valid for shorter range of motions when the phase shift is $\phi_I = 4 \times \pi/8$.

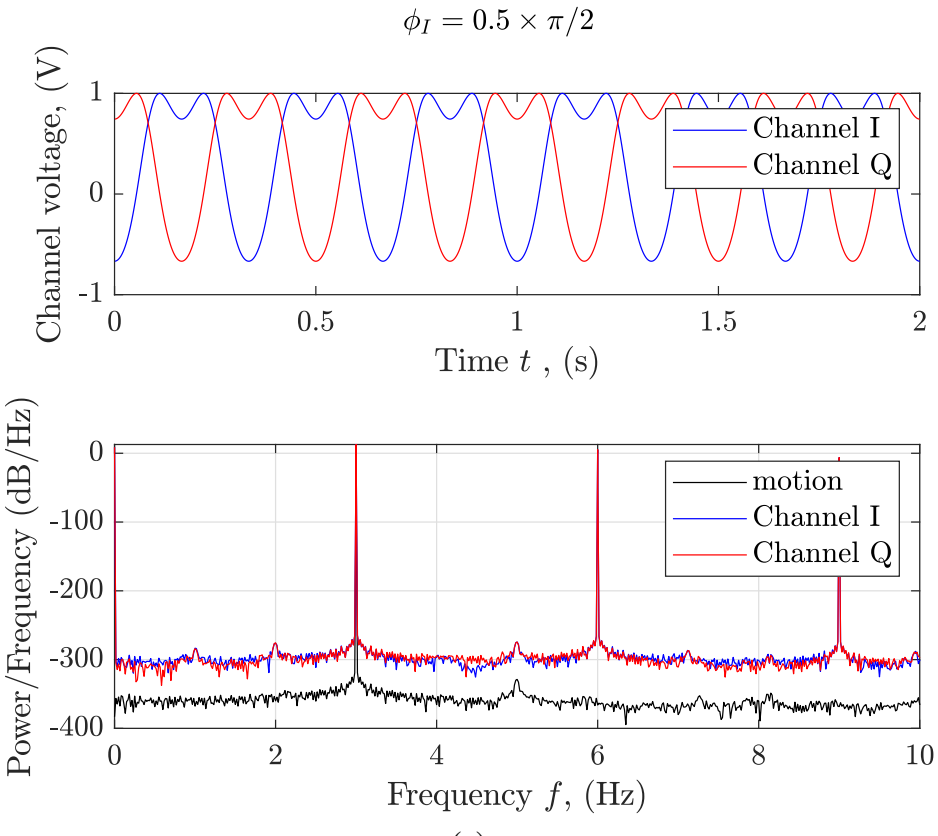
$\phi_I = 0.5 \times \pi/2$
Channel voltage, (V)
Time t , (s)
Channel I
Channel Q
Power/Frequency (dB/Hz)
Frequency f, (Hz)
motion
Channel I
Channel Q

(a)

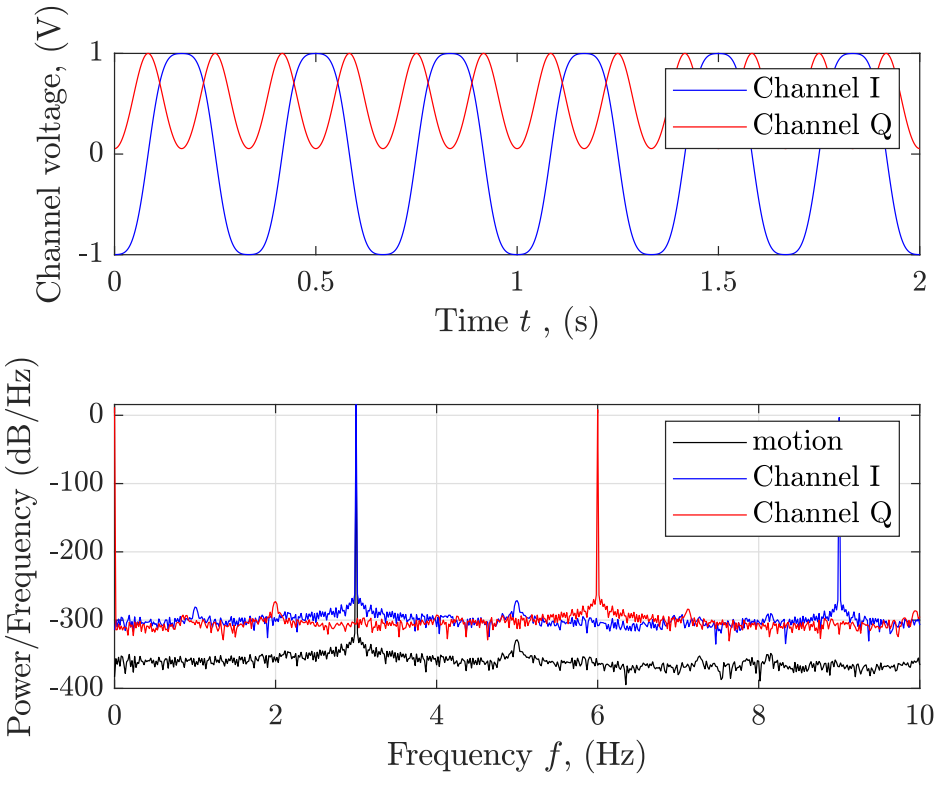
$\phi_I = 1.0 \times \pi/2$
Channel voltage, (V)
Time t , (s)
Channel I
Channel Q
Power/Frequency (dB/Hz)
Frequency f, (Hz)
motion
Channel I
Channel Q

(b)

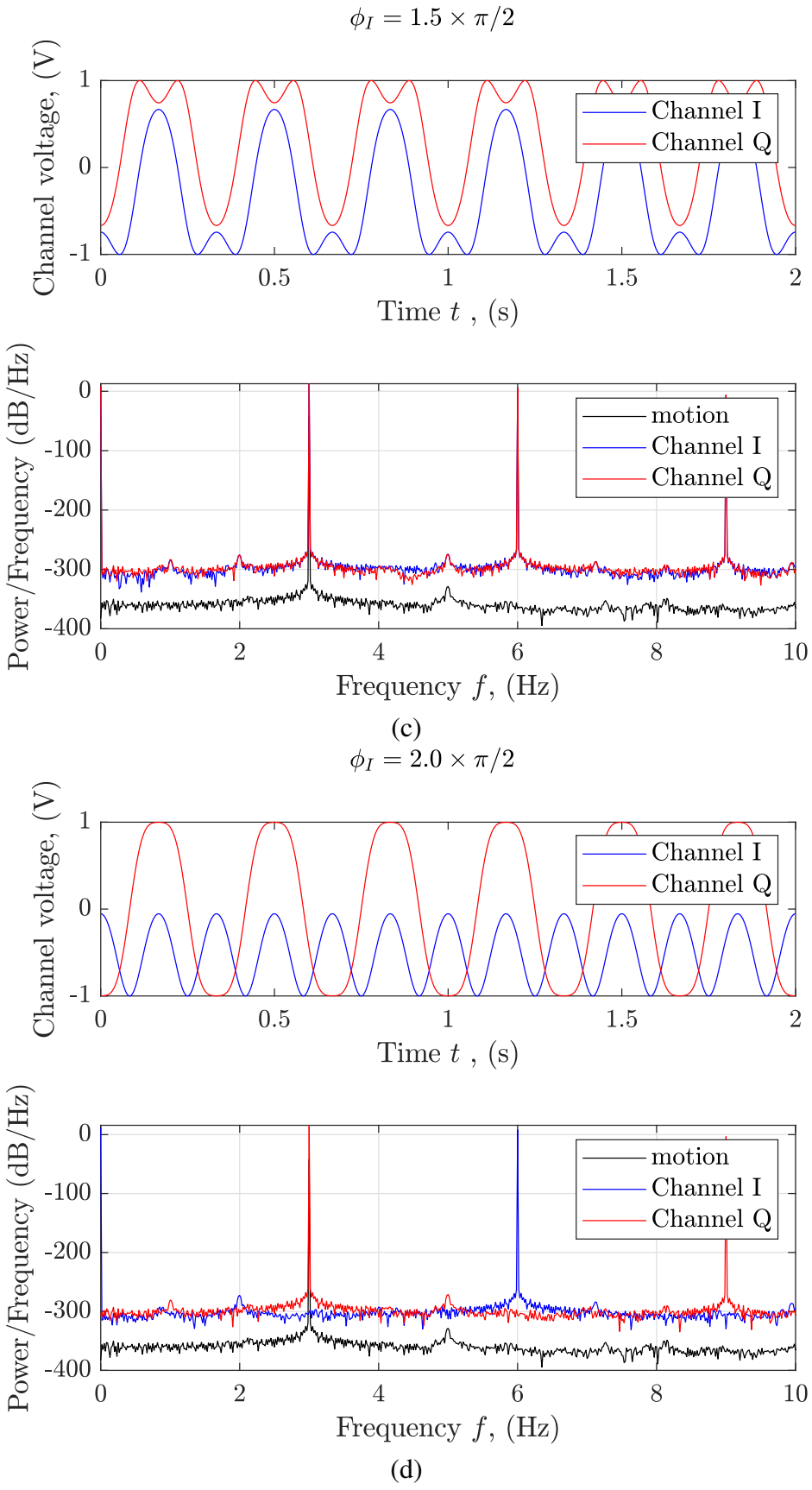

Figure 5.50 I/Q channel response for a A_m = 1.5 mm, f_m = 3 Hz sinusoidal motion with different phase shift, (a) $\phi_I = 0.5 \times \pi/2$, (b) $\phi_I = 1.0 \times \pi/2$, (c) $\phi_I = 1.5 \times \pi/2$ and (d) $\phi_I = 2.0 \times \pi/2$. The upper subfigures are in time domain and the lower subfigures are in frequency domain.

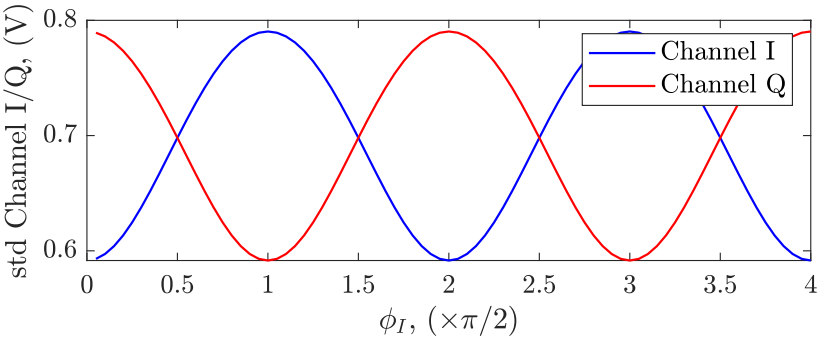

Figure 5.51 The relationship between the channel output variation with the phase shift to a 3 mm amplitude 3 Hz sinusoidal motion.

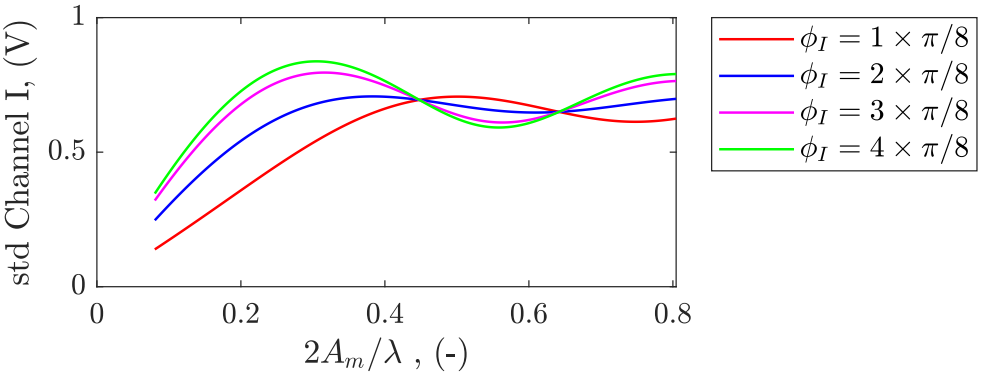

Figure 5.52 The relationship between the channel I fluctuation and the normalised motion displacement with different phase shifts.

5.5.3 Radar linear demodulation experiment

After the I/Q channel output simulation analysis, the radar sensor experiment results for the metal plate motions as summarised in Table 4.3 are analysed. The distance between the radar sensor and the metal plate is fixed as shown in Fig. 4.23, which means ϕ_I is the same for all experiments. The relationship between the standard deviation of the output channel I and the normalised motion displacement (2 times motion amplitude normalised by the radar wavelength) from 100 metal plate calibration tests is shown in Fig. 5.53. Motions with different dominant frequencies are represented by different markers. Fig. 5.53a shows the standard deviation of the raw channel I output and Fig. 5.53b shows the signal distortion compensated channel I output. It can be seen from Fig. 5.53a that the approximate linear relationship exists for motions with the same frequency. The gradient of the approximate linear relationship is smaller for smaller frequency motions. As can be seen from the magnitude response of the 2 high pass filters in Fig.4.28 as a red line, frequency components below 4 Hz are rolled off and lower frequency components have larger deduction. Therefore, results for motions with dominant frequency in the range 4 - 8 Hz show a similar approximate linear relationship while dominant frequencies in range 0 - 4 Hz show smaller gradient in Fig. 5.53a. When the high pass filter effect is compensated, all frequencies' motions show a similar approximate linear relationship when $x_m = 2A_m/\lambda < 0.3$, which is similar to simulation results as shown in Fig. 5.52. The dashed line in Fig. 5.53b is the simulated result according to the following equation:

$$I(t) = A_I \cos\left(\frac{4\pi x(t)}{\lambda} + \phi_I\right) + DC_I \tag{5.27a}$$

$$\phi_I = \frac{4\pi d_0}{\lambda}, \tag{5.27b}$$

$$x_m = A_m \cos(2\pi f_m t), \tag{5.27c}$$

$$A_I = 5,\ DC_I = DC_Q = 0, \tag{5.27d}$$

$$\lambda = 12.43, d_0 = 300. \tag{5.27e}$$

The phase shift ϕ_I is obtained from the nominal distance d_0, which is 300 mm for this experiment setup, with Eq. 5.27b. Strong agreement with 2.54 % relative difference between experiment results (markers) and simulation results (dashed line) can be found in Fig. 5.53b, which means the proposed AC coupling signal distortion compensation adequately restores the harmonic motion of the metal plate.

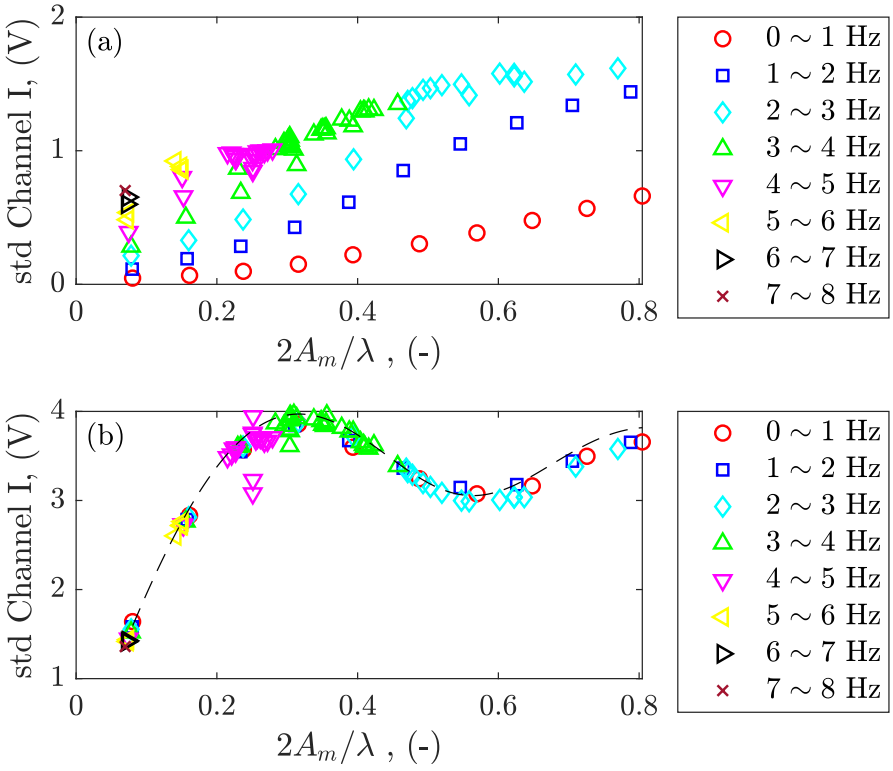

Figure 5.53 The relationship between the channel I fluctuation and the motion fluctuation for motions with different dominant frequencies. (a) raw channel I output and (b) compensated channel I.

5.5.4 Radar sensing large gravity waves

In this subsection response of the radar to the large gravity waves obtained in the wave tank experiment (see subsection 4.5.2 for more details about the experiment) is analysed. The size of the gravity waves is characterised by their wave amplitude A_m which is much bigger than the wavelength of the radar waves λ.

As small angle approximation is only valid when $x_m \ll \lambda$, non-linear demodulation is implemented in this large gravity wave analysis. The post-processed I/Q signals followed by the procedure explained in Fig. 5.47 are plotted in I/Q plane for four wave conditions (wave condition 3, 7, 13 and 20 in Table. 4.4) as shown in Fig. 5.54. Comparing Fig. 4.27c and Fig. 5.54b, the I/Q constellation for the same gravity wave is significantly improved by the signal post-processing, with the post-processed I/Q constellation forming an approximately circular pattern resembling a unit circle. Still some signal distortion can be observed, especially in Fig. 5.54a. This is because the dominant frequency of this motion $f_m = 0.25$, is well below the cut-off frequency 4.1 Hz, which corresponds to the largest signal distortion.

The wave probe measured, DRS raw signal demodulated, DRS signal with distortion compensation demodulated, distortion compensated DRS signal with imbalances corrected demodulated and distortion compensated imbalances corrected DRS signal with DC calibrated demodulated surface fluctuation time series for two gravity wave conditions are shown in Fig.5.55. From the 6 s segment time series in Fig.5.55a and c, all DRS demodulated surface fluctuation shows the same dominant frequency as wave probe measured one. The raw DRS signal demodulated surface fluctuation evidently show some discrepancy with wave probe measurement. As shown from the zoomed time series in Fig.5.55b and d, the signal distortion compensation evidently reduces the discrepancy between the DRS demodulated result and wave probe result. The imbalance correction does not improve the demodulation evidently in this experiment by comparing the blue and green lines in Fig.5.55. Besides, the DC calibration has slightly improved the demodulation by comparing the red and blue lines in Fig.5.55. Similar results were obtained for other wave conditions. To quantify the effect of the post processing in this experiment, the displacement measured by wave probes and DRS with different stages of post processing for all 20 wave conditions are compared. On average, the relative error compared with wave probes measured displacements (black line in Fig. 5.55) is 21.26 % for the raw signal demodulated displacements (magenta line in Fig. 5.55), 8.58 % for with distortion compensation demodulated displacements (green line in Fig. 5.55)), 8.59% for with imbalances corrected displacements (blue line in Fig. 5.55) and 7.89 % for DC calibrated demodulated displacements (red line in Fig. 5.55).

The standard deviation of the surface fluctuations for 20 different gravity waves measured with wave probes is plotted against DRS post-processed results in Fig. 5.56, with a 1:1 linear

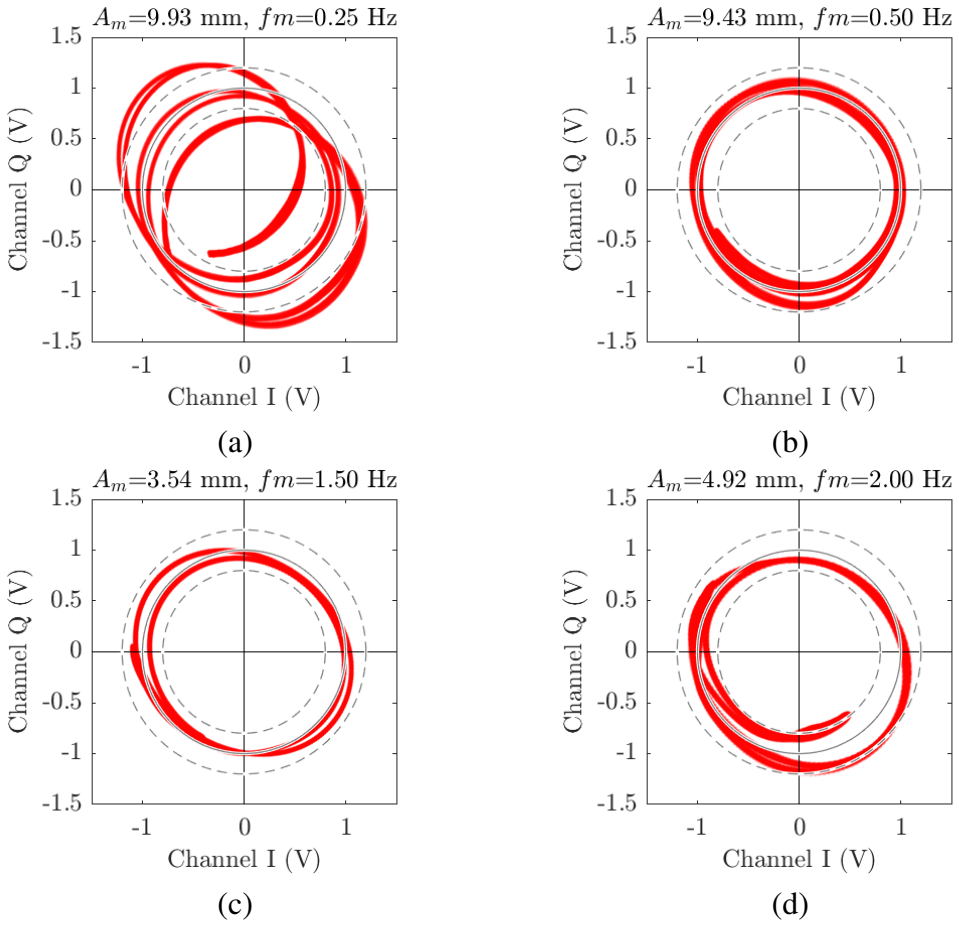

Figure 5.54 Corrected I/Q constellation for large gravity waves (a) wave condition 3 A_m = 9.93 mm f_m=0.25 Hz, (b) wave condition 7 A_m = 9.43 mm f_m = 0.50 Hz, (c) wave condition 13 A_m = 3.54 mm f_m = 1.50 Hz, (d) wave condition 20 A_m = 4.92 mm f_m = 2.00 Hz.

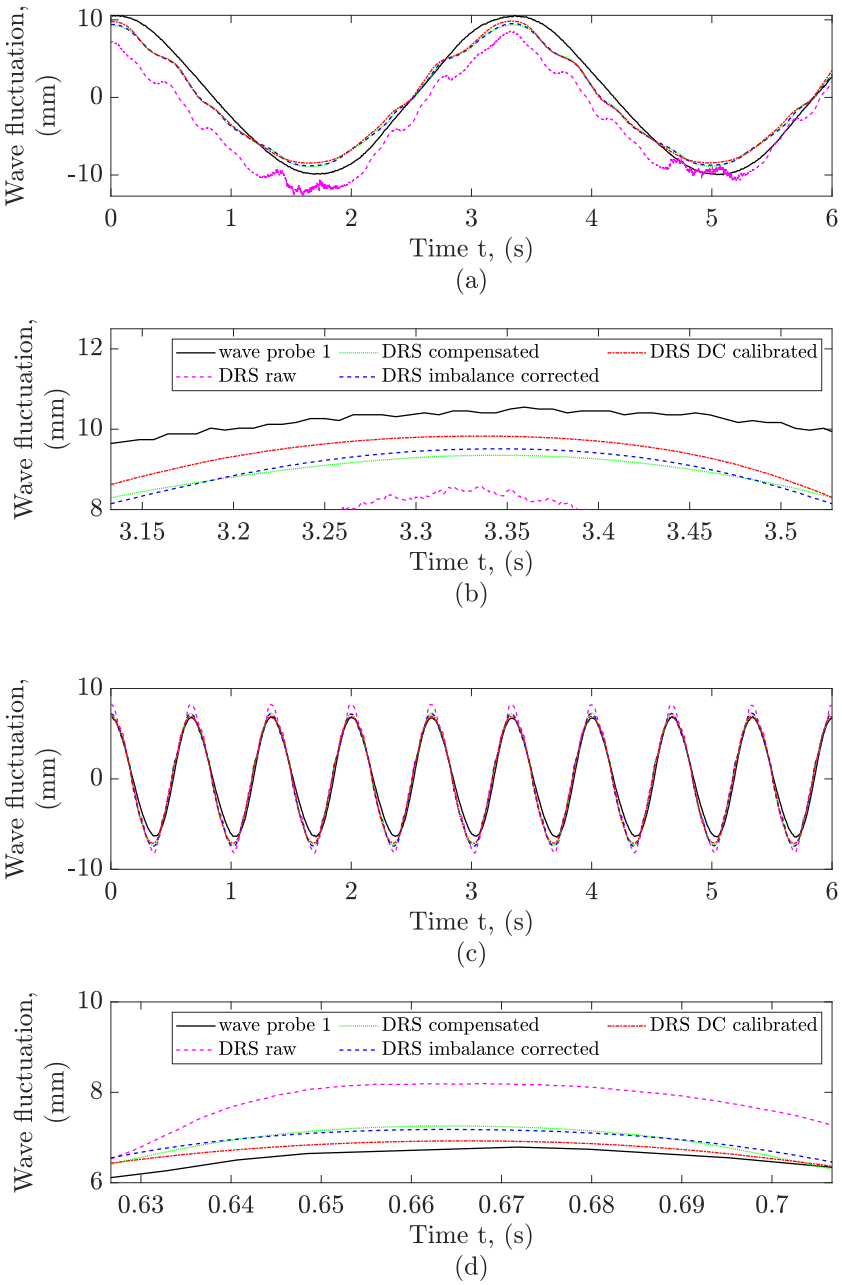

Figure 5.55 Large gravity wave surface fluctuation measured by wave probe 1 and DRS for (a)(b) wave condition 3 A_m = 9.93 mm f_m = 0.25 Hz and (c)(d) wave condition 15 A_m = 6.59 mm f_m = 1.50 Hz. (a)(c) shows a time period of 6 s and (b)(d) shows a zoomed time interval.

line for reference. Error bars represent the variations in three wave probes. This figure also shows the regression line σ_{WP} = 1.03σ_{DRS}-0.08 with the coefficient of determination R^2 = 0.96. This suggests that the radar method can be calibrated and used to deduce the mean roughness height with relative error of 1.9 % for the wave conditions studied in this experiment.

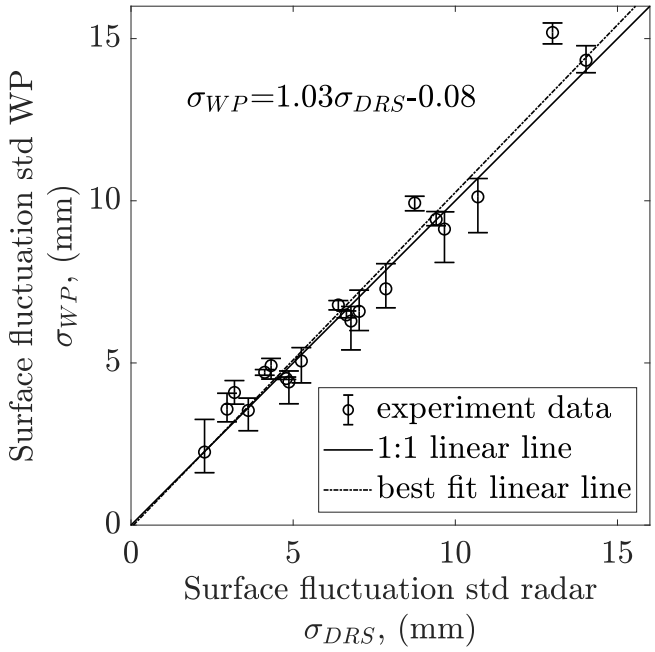

Figure 5.56 Standard deviation of surface fluctuation measured by wave probes and Doppler radar in a rectangular channel.

5.5.5 Radar sensing of small water waves

As is shown in Fig. 5.53, the standard deviation of I/Q channel output is generally proportional to the motion amplitude when $2A_m/\lambda < 0.3$ for all phase shifts. The experiment as mentioned in subsection 4.5.1 shown in Fig. 4.25 are analysed in this subsection using the linear demodulation technique. The standard deviation of I/Q channel is affected by the amplitude imbalance according to Eq. 2.45. Therefore, the I/Q channel outputs are calibrated first with the use of GS method as shown in Eq. 2.58. The amplitude and phase imbalances are obtained through the metal plate calibration tests as mentioned in subsection 5.5.1 with A_e = 0.7601 and ϕ_e = -0.1992. The standard deviation of both imbalances calibrated I/Q channels are plotted against normalised wave amplitude as shown in Fig. 5.57. The wave amplitude is obtained from the wave probes measured water surface fluctuations. A linear relationship can be observed in Fig. 5.57, which confirms the small angle approximation is valid for both sinusoidal motions and random motions.

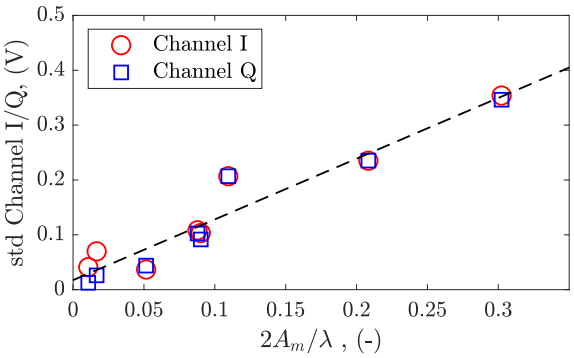

Figure 5.57 The relationship between the channel I fluctuation and the motion fluctuation for small waves.

5.5.6 Radar sensing turbulent waves

As mentioned in subsection 5.5.2, the linear demodulation is valid when the motion displacement is small compared with the radar wavelength at non null points. As the radar used in this study has quadrature receivers (see subsection 2.5.2 for more details), there is always one channel that is not at a null point. In addition, preliminary experiment results as discussed in subsection 5.5.5 further proves that the standard deviation of I/Q channels has a linear relationship with the water wave motion standard deviation for both small sinusoidal motions and small random motions. The surface roughness is below 1.5 mm for this study as shown in Fig. 4.11, which means the motion displacement ($\sim$ 3 mm) is small compared with the radar wavelength (λ = 12.43 mm). The imbalances in the measured I/Q channel signals are adjusted first according to the GS method. The standard deviation of calibrated I/Q channels are then compared with the standard deviation surface fluctuation measured by DIC as shown in Fig. 5.58. The horizontal error bars represent maximum and minimum values from DIC 5 repeated 66 s measurements and the vertical error bars represent maximum and minimum values from DRS 3 repeated 300 s measurements. A best fit linear regression was found for experimental data using MATLAB 'polyfit' function as shown in Fig. 5.58 as dashed line. The standard deviation of DRS channel outputs are generally linearly proportional to the surface roughness.

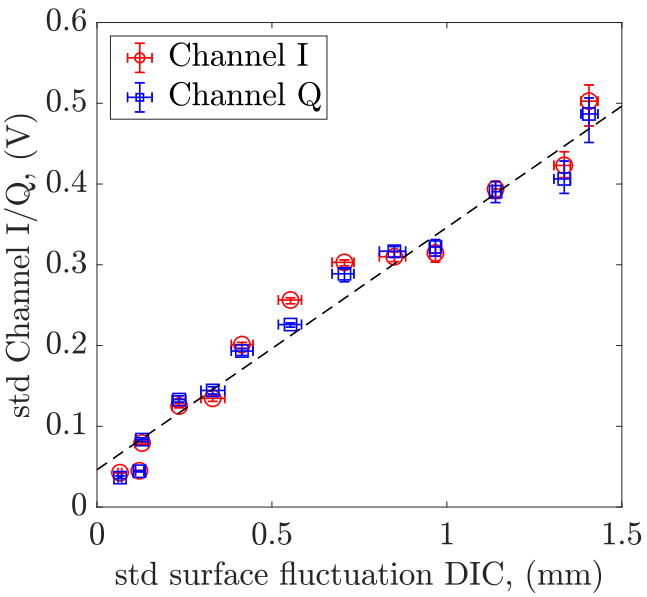

Figure 5.58 The relationship between the channel I/Q fluctuation and the motion fluctuation for pipe turbulent flows.

The preceding paragraph proves the linear relationship between the DRS channel outputs fluctuations and the water surface fluctuations. As the water surface fluctuations are related to

the turbulent properties (Nichols, 2014, Dolcetti, 2016), the DRS channel outputs fluctuations are compared with water depth d, flow rate Q, bulk flow velocity U_b and Reynolds number Re as shown in Figs. 5.59(a)-(d). The standard deviation of channel fluctuations increase as all four flow parameters d, Q, U_b and Re. A best fit linear line is fit in Fig. 5.59b and best fit quadratic lines are fit in Fig. 5.59a, c and d. It can be observed that the standard deviation of DRS channel outputs is linearly proportional to flow rate and has quadratic relationship with water depth, bulk flow velocity and Reynolds number. These DRS channel outputs correlation with turbulent flow properties infer that the non-contact compact DRS sensor is able to infer the information of the turbulent flow.

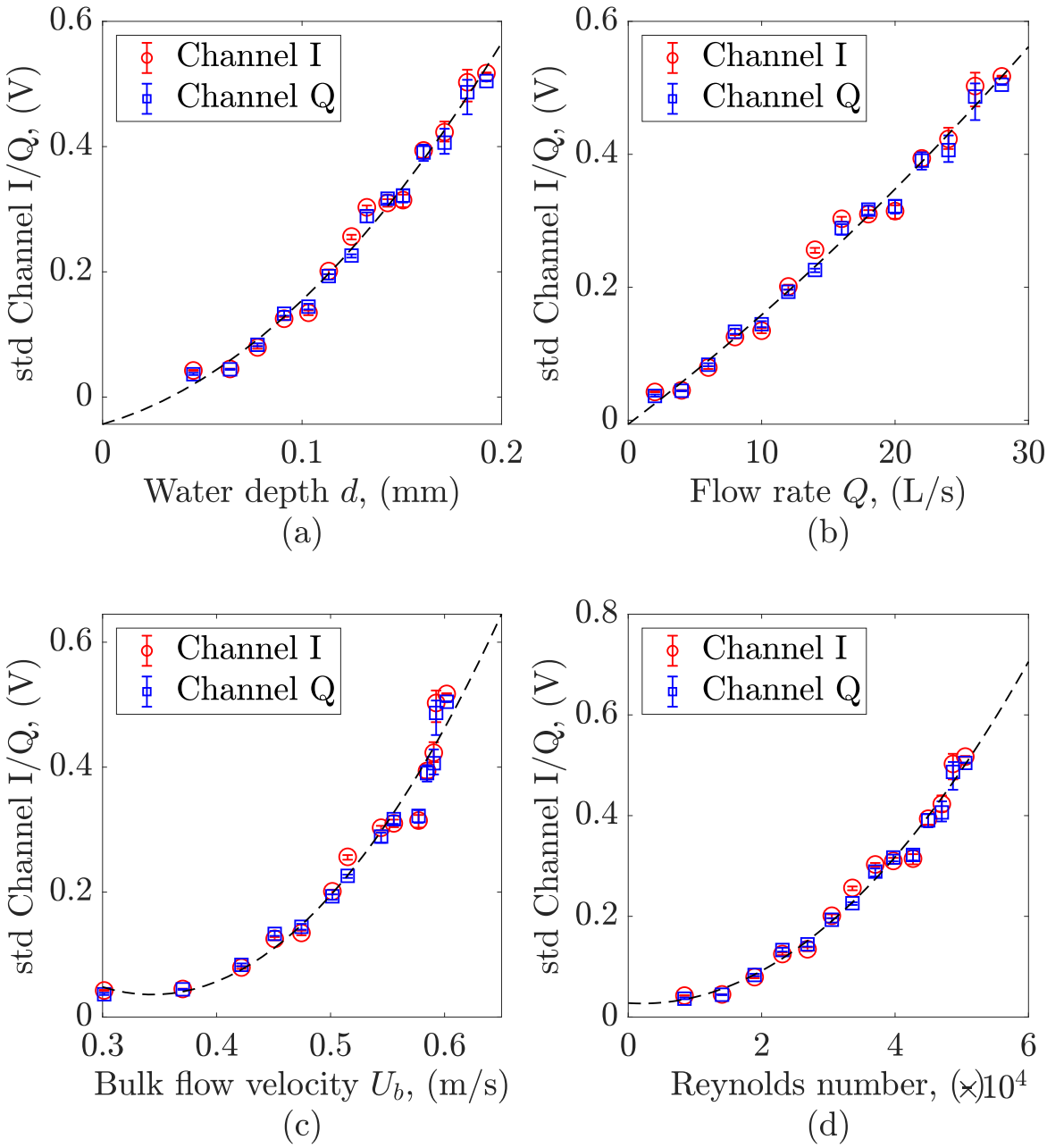

Figure 5.59 The relationship between the channel I/Q fluctuation and pipe turbulent flows properties (a) water depth d, (b) flow rate Q, (c) bulk flow velocity U_b and (d) Reynolds number Re.

Chapter 6

Thesis conclusion

6.1 Key conclusions

In reviewing the literature, no data was found on the 2D surface fluctuations in partially filled pipes. The aim of this thesis is to extend knowledge of the hydrodynamics in partially filled pipes and relate the flow hydraulic properties with a Doppler radar sensor.

In this study, a unique experiment facility was built, which is able to measure the free surface properties and sub-surface properties as shown in Fig. 3.2. The equipment and the type of measured data are summarised in Table 3.3. A non-equidistantly spaced wave probe array was set up, which consists of 7 wave probes. A guitar tuner system was implemented to tension the wave probe wires instead of the bolt screw system used in previous literature (Nichols, 2014, Romanova, 2013), which can more sensitively control the tension in the wires. A novel application of the DIC system was proposed to measure 3D water surface dynamics, in which stochastic speckle pattern is projected onto the tinted opaque water surface and the surface is then imaged by two cameras above. The displacement of each small facet can be evaluated and thus the fluctuations across the whole surface can be determined. This technique is able to measure surface fluctuations in a 2D area with approximate size 297 $\times$ 198 mm at high frequency ($\sim$ 120 Hz). In the present study, a mass concentration of 0.06 % TiO_2 was found adequate to make the water opaque enough for optical measurement via DIC, while not significantly changing the turbulent surface dynamics in partially filled pipes. It is demonstrated that spikes in data caused by both air bubbles and the gaps reflection of light can be easily filtered out and interpolated. The consistency of the data collected with the novel DIC system was validated against wave probe measured data in terms of the PDF, standard deviation and power spectrum of the water surface fluctuations. A side-looking and a downward-looking ADV were used for sub-surface 1D 3C velocity measurement. The phase-space despiking technique proposed by Goring and Nikora (2002) was used to

remove spikes in the raw ADV data, which efficiently removes the erroneous data points while not alternating the turbulence information. The high quality ADV data are objectively selected according to correlation value and PDF of ADV data. The accuracy of both ADV are compared with each other and compared with the surface velocity and bulk flow velocity. Due to the curvature of the pipe, the downward-looking ADV is more reliable than the side-looking ADV, especially the vertical velocity measurement (see Table B.1 - B.3).

The streamwise velocity profile in a rectangular open channel can be well described by the conventional log law (Nezu and Nakagawa, 1993). The mean velocity at a certain depth-wise position is proportional to the logarithm of the distance from the wall of the channel. The single point mean velocity increases with the depth-wise position of the point, and the maximum velocity occurs at the surface of the flow. However, in circular cross section flows, the maximum velocity does not occur at the free surface in every case. The centerline streamwise mean velocity profile usually follows the log-law up to a certain depth-wise position, and then deviates downward from the log-law as shown in Fig. 5.3 and 5.4. The streamwise mean velocity profile follows the modified pipe velocity distribution model proposed by Guo et al. (2015). This is the velocity dip phenomenon, which was also observed by Ead et al. (2000), Clark and Kehler (2011), Guo et al. (2015), Wu et al. (2018). Guo and Meroney (2013), Yoon et al. (2012), Wu et al. (2018), Ng et al. (2021), Guo et al. (2015) observed the velocity dip phenomenon for flows with filling ratio d/D greater than 87 %, 50 %, 50 %, 44 % and 34 %, respectively in partially filled pipes. In this study, the velocity dip phenomenon occurs when the filling ratio is over 35 %. It confirms that the velocity dip phenomenon can occur in turbulent pipe flows that are less than half filled. For flows over 35 % filled, the ratio of the velocity dip position from the bottom and the water depth δ/d generally decreases with water depth, which means the position of the maximum velocity point gradually moves downward from the free surface. The ratio of the velocity dip position from the bottom and the pipe diameter δ/D is almost constant (~ 0.28), which means the maximum velocity point remains at a similar position in the pipe independent of the filling ratio. The centerline streamwise velocity profiles were normalised by the maximum velocity and bulk flow velocity in z/d, z/D_h and z/D coordinates. It can be noted that the normalised velocity profiles generally overlap near the bottom of the pipe, and deviate towards to the free surface, which indicates the impact of the free surface. Both bulk flow velocity and maximum velocity increase with the filling ratio. However, the ratio of the bulk flow velocity and maximum velocity remains almost constant when the dip phenomenon occurs.

The turbulence intensity in three directions show two different profiles when the filling ratio is below and above $\sim$ 35 %. When the pipe is less than $\sim$ 35 % filled with water, the turbulence intensity profiles more closely resemble results obtained by Nezu and Nakagawa

(1993) for rectangular channels. However, when the velocity dip phenomenon occurs ($d/D >$ 35%), the turbulence intensity profiles do not follow Nezu and Nakagawa (1993), especially in the region near the water surface. Instead of continuously decreasing turbulence intensities towards the water surface, the turbulence intensities start to increase at approximately $z/d = 0.5$. This observation is also reported by Clark and Kehler (2011) in corrugated circular pipes. A set of empirical turbulence intensity equations for smooth circular pipes is proposed, which is modified from Clark and Kehler (2011) empirical equations. The Reynolds normal shear stress in three directions and TKE (see Fig. 5.11 and 5.12) all show a peak at approximately $z/d = 0.5$, which agrees with observations from Clark and Kehler (2011), Ng et al. (2021). In the Reynolds shear stress profile, a change of sign can be observed at $z/d \approx 0.5$. The Reynolds shear stress is positive below $z/d = 0.5$ and becomes negative when over $z/d = 0.5$, which is also observed by Ng et al. (2021) in a partially filled pipe and is a phenomenon not observed in rectangular open channels (Nichols, 2014).

To understand the size, shape, timescale and dynamics of coherent structures, an objective 1D phase-space detection method, modified from Goring and Nikora (2002), is proposed in this study. This method requires no calibration or subjective input, and identifies structures based on extremes in velocity, acceleration and jerk. This method gives turbulence statistics comparable with previous methods while recognising a broader and more realistic definition of the physical properties of coherent structures by considering also the first and second derivative of velocity. This algorithm was compared with the U-level algorithm and evaluated in terms of the time series, phase-space axes, individual event duration, individual event period, quadrant contribution, binary series statistical similarities and turbulent event profiles. The phase-space detected binary series is statistically comparable with U-level detected result. Turbulent event parameters can be obtained through the phase-space detected binary series and are also comparable with U-level results. The relation between turbulent event parameters and flow conditions can be observed by the proposed method. The phase-space method accounts for the physical reality that a coherent structure consists of extremes in velocity, acceleration and jerk, and that these properties should be considered together when identifying extreme behaviour.

Two types of motion can be observed within the free surface dynamics: turbulence waves, and gravity capillary waves travelling in all directions relative to the surface velocity. Evidence of this observation are the surface space time matrix, dispersion relationship and frequency wavenumber spectrum. In the streamwise direction gravity waves move both at a speed faster than the turbulence wave (travelling) and at a speed slower than the turbulence wave (receding). To accurately extract the travelling speed of the turbulence waves, the mask function proposed by Tani and Fujita (2020) can be used to exclude gravity capillary

waves. The magnitude of the turbulence waves are generally below 1 mm and the magnitude of gravity capillary waves are much higher (1 - 5 mm) in this study. When correlating the masked surface fluctuations at two spatial points, the phase velocity derived from the maximum correlation lag is close to the surface velocity measured by floating tracer. From the lateral frequency wavenumber spectrum, gravity capillary waves can be also observed and are moving laterally across the flow. Besides, waves moving at constant velocity in the lateral direction can be observed. It indicates that the water is sloshing from side to side with wavelength equal to two times of surface width. This can explain the uneven secondary currents and the meandering of the main secondary currents observed by Liu et al. (2022). The size of the two main secondary currents change with the sloshing of the water. Due to these two main secondary currents, two maxima can be observed from the standard deviation of surface fluctuations along lateral direction. As the Reynolds number increases, the secondary currents are stronger and merge at the center. Besides, the corner vortices are stronger for more turbulent flows, causing the standard deviation of the surface fluctuations to be higher towards the wall. The periodic oscillating pattern observed by Nichols et al. (2013) can also be observed in the spatial correlation function for flows $d/D \leq 43\%$ in this study. The spatial correlation coefficient continuously decays over distance for flows in partially filled pipes with filling ratios bigger than 43 %. The oscillation frequencies for flows $d/D \leq 43\%$ agree well with Nichols et al. (2016) simple harmonic motion model. The depth of influence factor is $N \approx 37$, which means the surface oscillons affect the bulk flow to a depth of about 37 times the average wave height. This shows a strong interdependence between turbulence and surface dynamics for these flows. The oscillation frequencies are comparable with the bursting frequency as shown in Fig. 5.33, which proves that the surface oscillation dynamics are related to the busting phenomenon from the bottom.

The empirical relationships between water depth and flow rate, bulk flow velocity and friction factor, surface velocity and bulk flow velocity for flows tested in this study have been found. The proposed phase-space detection method has been applied to the surface fluctuation data from both DIC and wave probes. The change in size of free surface features and number of free surface features per meter follow the same trend as the change in sub-surface size of turbulent structures and number of sub-surface structures per meter, respectively. The size of free surface features increases with flow depth until 1/3 filling ratio and then remains almost constant. On the contrary, the number of free surface features decreases with flow depth up to approximately 1/3 filling ratio and then remains almost constant. Similar to the standard deviation of surface fluctuations along the lateral profile, two peaks are observed in the size of free surface features along lateral direction, which corresponds to the effect of the two main secondary currents.

A novel 24 GHz FMCW Doppler radar sensor system has been built and applied for water surface measurement in this study. The characteristics and performance of the radar in measuring fluctuations have been investigated using an oscillating metal plate test. The amplifier board in this study consists of two cascaded high pass filters, which could cause signal distortion and potentially inaccurate signal demodulation. The inverse high pass filter transfer function, or so called compensation function, can effectively recover the filtered low frequency components. The optimum coefficient a_1 is found to be 0.95 for the circuit in this study. By applying the ellipse fitting to the I/Q constellation, the amplitude and phase imbalances are found to be 0.7601 and -0.1992, respectively as discussed in subsection 5.5.1. With the known compensation transfer function and imbalance values, the non-linear demodulation technique based on both channel outputs (I/Q channel outputs) can be used to recover the actual motions. In the metal plate calibration tests, the relative difference between the radar and the laser displacement sensor measured motions is no greater than 20 %. The relative difference decreases to 5 % when the amplitude of motion is greater than 0.15 times the radar wavelength. The linear demodulation technique with the small angle approximation assumption is also investigated. This technique is not able to recover the exact motion displacement but is able to give a linear approximation if the motion is small enough. In the metal plate calibration tests, the standard deviation of the radar channel output fluctuation is approximately proportional to the standard deviation of the motion when the ratio of the total displacement of motion and the radar wavelength is below 0.3.

After the characterisation of the DRS from the metal plate calibration tests, preliminary tests were carried out in a rectangular open channel as mentioned in subsection 4.5.2. For large gravity waves (waves with amplitude greater than 2 mm), the DPoD signal compensation technique together with the non-linear demodulation technique successfully recovers the motion of the surface fluctuations as presented in subsection 5.5.4. The recovered gravity wave displacement from DRS is within 1.9 % of the wave probe measurement. The linear demodulation technique is used for measurement data of small water waves (waves with standard deviation below 1 mm). A linear relationship can be observed between the standard deviation of DRS channel output and the standard deviation of the wave motion.

For turbulent waves in a partially filled pipe, it was not possible to exactly recover the surface shape because the highpass filter effect is not easy to compensate for broad spectrum motions. However, the voltage fluctuation of the DRS is approximately linearly proportional to the DIC measured surface fluctuation. This suggests that the DRS channel output links well to the surface roughness in a partially filled pipe and provides capability for non-contact sensing in sewer systems using the radar technique. As mentioned in preceding paragraphs, the surface roughness has relationships with other flow information, such as water depth, flow

rate, bulk flow velocity and Reynolds number. Empirical relationships between the listed flow properties and standard deviation of radar channel outputs were found in this study.

6.2 Recommendations for further work

The recommendations for further work are mainly on three areas: (i) hydraulic experiment design improvement, (ii) radar design improvement and (iii) extension to two phase flows study.

Whilst the hydraulic measurement setup has been carefully designed based on previous research studies (Nichols, 2014, Dolcetti, 2016, Romanova, 2013), this work has also identified some aspects that could be improved. The distance between the third and fourth wave probes is 160 mm as shown in Fig. 3.10, causing a large gap in the spatial correlation function and streamwise frequency wavenumber spectrum. Comparing frequency wavenumber spectra in this study (Fig. 5.35, 5.36) and in Dolcetti (2016) study, it can be observed that the spatial resolution (i.e. x-axis resolution) of the frequency wavenumber spectrum from DIC in this study is smaller than that of the wave probes in Dolcetti (2016) study. This is because the DIC measured a total distance of 297 mm in the streamwise direction, while the wave probes in Dolcetti (2016) have a total distance of 762.5 mm. Two extra cameras can be added to the DIC system to increase the measuring area. Four cameras can be arranged as a 2 by 2 array, which can improve the measurement area both in streamwise and vertical directions. Besides, two extra cameras can potentially reduce the occurrence of gaps in the data caused by light reflections. Furthermore, the DIC system used in this study requires opaque water, and thus the simultaneous optical measurement of sub-surface properties such as the velocity field is difficult. ADV was used in this study for the sub-surface 1D 3C velocity field measurement. Only sub-surface lateral center velocities have been measured by ADV in this study. Besides, near free surface and near bottom ADV data are usually noisy due to the reflection from boundaries. It is of great interest to measure the whole 3D 3C velocity field below the free surface by a PTV system, which would be able to confirm the sloshing of water from side to side. The correlation between peaks in the size of turbulence surface features along lateral direction profile (Fig. 5.43) and two main secondary current cells could also then be investigated. In addition, the corner vortices near the free surface could be visualised and correlated to the higher surface roughness near the pipe wall in Fig. 5.34.

For the radar design, one possible improvement is to adjust the value of the 3.9 kΩ resistor in the amplifier circuit (Fig. 3.24). Doubling or tripling the resistor value would result in a lower high-pass filter cutoff frequency, such as 2.04 Hz or 1.36 Hz, respectively. This modification would preserve the turbulence frequency components of interest while reducing

any potential impact on the desired signals. Additionally, advancements in integrated circuit technologies have led to improved quadrature balance in mixers. Modern quadrature mixers, such as the Skyworks73009 (Skyworks, 2019) used in the work of Gu et al. (2016), exhibit minimal amplitude and phase imbalances of only 0.3 dB and 1°, respectively. To ensure the robustness of the findings, the radar system employed in this study has undergone testing in controlled environments, including experiments with a metal plate, a precisely controlled rectangular channel, and a laboratory partially filled pipe. To further validate the relationships depicted in Fig. 5.59, field studies using this radar system would be valuable. Conducting experiments in real-world conditions would help verify if the observed relationships hold true. Furthermore, the Doppler radar sensor shows potential for application in inferring hydraulic parameters in sewer systems, offering non-contact monitoring capabilities. To facilitate field studies, the same sliding frame used in this study (Fig. 3.25) can be directly employed, assuming the pipe size remains the same. However, modifications should be made to the data acquisition system and cables to ensure their waterproofing and field-study safety. This would enable the deployment of the radar sensor in practical scenarios and expand its application in hydraulic parameter inference.

All experiments in this study were carried out in a pipe with several openings at the top, which is basically an open channel flume with circular shape cross section. In real world sewer system, pipes are usually closed and involve two phase flows. Study on two phase flows in a closed pipe conduit can be extended from this study on one phase flow in an open pipe conduit. This is important because Hydrogen sulphide (H_2S) can be generated in sewer systems and transported by the air in the sewer headspace (Åse Dalseth Austigard and Heldal, 2018). It is a toxic gas with odour and can cause infrastructure corrosion (Zhang et al., 2008). Nowadays, sewer design mainly aims to meet hydraulic requirements. However, less attention has been paid to the air phase transport in sewer pipes. Rita Ventura Matos and Matos (2019) have investigated the effect of sewerage system ventilation in H_2S dynamics. They have highlighted the importance of accurately predicting gas movement within sewers under different conditions. Air water flows in hydraulic structures have great potential for aeration enhancement of flow. It would be interesting to find out if there is a correlation between the in sewer gas movement and gas pollution concentrations. Furthermore, it is recommended to look at how the free surface shape, dynamics and area affect the transfer of gases across the interface. This could contribute to the sewer pipe design to meet both hydraulic and chemical requirements in the future and hence minimise sewer corrosion and reduce health risk.

6.3 Conclusion summary

In conclusion, this study has led to several key findings, which are summarised in Table 6.1.

Table 6.1 Thesis conclusion summary

Objective	Observed/Derived Novelties
Develop novel facility enable to measure free surface and subsurface turbulence	Novel facility enable to measure free surface and subsurface turbulence was developed - ADV (1D 3C) used to measure subsurface velocity field - DIC (2D) combined with WP (1D) to measure free surface
Collect novel water surface fluctuation data over a 2D area	Implemented DIC to collect a large novel dataset in partially filled pipes
Identify the linkage between flow conditions, turbulence and free surface dynamics	The linkage between flow conditions, turbulence, and free surface dynamics were identified - Observed velocity and TKE dip in the subsurface - Identified three waves on the free surface - Established the relationship between surface oscillation frequency and bursting frequency - Explored the relationship between free surface feature size and subsurface turbulent structure size
Find the linkage between radar signal response to free surface and flow conditions	The linkage between radar signal response to free surface and flow conditions were identified - Radar signal links the surface fluctuation roughness

In this conclusion summary, Table 6.1 presents a summary of the key objectives and the observed or derived novelties for each objective. The first objective involved the development of a novel facility for measuring free surface and subsurface turbulence, utilizing ADV and DIC combined with WP. The second objective involved collecting a significant dataset of water surface fluctuation using DIC in partially filled pipes. The third objective focused on quantifying the linkage between flow conditions, turbulence, and free surface dynamics, which resulted in the identification of various relationships and phenomena. Lastly, the third objective aimed to establish the linkage between radar signal response to the free surface and flow conditions, highlighting the sensitivity of the radar signal to surface fluctuation roughness. This insight has important implications for the development of advanced monitoring systems, potentially revolutionising drainage system monitoring and enhancing its effectiveness. The outcomes of this study not only address critical knowledge gaps in the field of free surface dynamics in partially filled pipes but also present opportunities for transformative advancements in the monitoring and management of fluid systems. By bridging theoretical understanding with practical applications, these findings lay a foundation for future research and innovation in the field of pipe flow fluid dynamics.

References

On the dynamical theory of incompressible viscous fluids and the determination of the criterion. *Philosophical Transactions of the Royal Society of London*, 186:123–164, 1895. ISSN 15580644. doi: 10.1098/rsta.1895.0004.

Center tracking quadrature demodulation for a Doppler radar motion detector. *IEEE MTT-S International Microwave Symposium Digest*, pages 1323–1326, 2007. ISSN 0149645X. doi: 10.1109/MWSYM.2007.380438.

Coherent structures and their interactions in smooth open channel flows. *Environmental Fluid Mechanics*, 15:653–672, 2015. doi: 10.1007/s10652-014-9390-z.

Effects of respiration depth on human body radar cross section Using 2.4GHz continuous wave radar. *Proceedings of the Annual International Conference of the IEEE Engineering in Medicine and Biology Society, EMBS*, pages 4070–4073, 2017. ISSN 1557170X. doi: 10.1109/EMBC.2017.8037750.

Flow correlations and transport behaviour of turbulent slurries in partially filled pipes. *Chemical Engineering Science*, 235:116465, 2021. ISSN 00092509. doi: 10.1016/j.ces.2021.116465. URL https://doi.org/10.1016/j.ces.2021.116465.

G. B. Airy. *Tides and waves*. Encyclopedia Metropolitan, London, 1845.

F. Alimenti, S. Bonafoni, E. Gallo, V. Palazzi, R. Vincenti Gatti, P. Mezzanotte, L. Roselli, D. Zito, S. Barbetta, C. Corradini, D. Termini, and T. Moramarco. Noncontact measurement of river surface velocity and discharge estimation with a low-cost doppler radar sensor. *IEEE Transactions on Geoscience and Remote Sensing*, 58(7):5195–5207, 2020. ISSN 15580644.

R. A. Antonia A N and D. D. K. Bisset. Spanwise structure in the near-wall region of a turbulent boundary layer. *Journal of Fluid Mechanics*, pages 437–458, 1990. doi: 10.1017/S0022112090001355.

M. Arsalan, A. Santra, and C. Will. Improved Contactless Heartbeat Estimation in FMCW Radar via Kalman Filter Tracking. *IEEE Sensors Letters*, 4(5), 2020. ISSN 24751472. doi: 10.1109/LSENS.2020.2983706.

A. Balabel and A. Alzaed. Computational Fluid Dynamics of Dam-Break Problem with Different Fluid Properties Using the Level Set Method. *Energy Research*, 2(1):52, 2018. doi: 10.31058/j.er.2018.21005.

A. Baron and M. Quadrio. Turbulent boundary layer over riblets: Conditional analysis of ejection-like events. *International Journal of Heat and Fluid Flow*, 18(2):188–196, 1997. doi: 10.1016/S0142-727X(96)00087-2.

J. Bevan. Climate Change: Too True to be Good, 2018. URL https://www.thersa.org/events/2018/09/climate-change-too-true-to-be-good.

A. Bjorck. Solving linear least squares problems by gram-schmidt orthogonalization. *Math*, 7(1):1–21, 1967.

D. G. Bogardt and W. G. Tiederman. Burst detection with single-point velocity measurements. *Journal of Fluid Mechanics*, 162:38–51, 1986. doi: 10.1017/S0022112086002094.

R. S. Boppe and W. L. Neu. Quasi-coherent structures in the marine atmospheric surface layer. *Journal of Geophysical Research: Oceans*, 100(C10):20,635–20,648, 1995. doi: 10.1029/95JC02305.

R. S. Boppe, W. L. Neu, and H. Shuai. Large-scale motions in the marine atmospheric surface layer. *Boundary-Layer Meteorology*, 92:165–183, 1999. doi: 10.1023/A:1001837729368.

O. Boric-Lubecke, V. M. Lubecke, I. Mostafanezhad, B.-K. Park, W. Massagram, and B. Jokanovic. Doppler Radar Architectures and Signal Processing for Heart Rate Extraction. *Microwave Review*, 15(2):12–17, 2009.

M. Brocchini and D. H. Peregrine. The dynamics of strong turbulence at free surfaces. Part 1. Description. *Journal of Fluid Mechanics*, 449:225–254, 2001. ISSN 00221120. doi: 10.1017/S0022112001006012. URL https://doi.org/10.1017/S0022112001006012http://www.journals.cambridge.org/abstract_S0022112001006012https://www.researchgate.net/publication/231945770.

J. C. Burns. Long waves in running water. *Journal of Fluid Mechanics*, 49(4):695 – 706, 1953. doi: https://doi.org/10.1017/S0305004100028899.

T. R. Camp. Design of sewers to facilitate flow. *Sewage works journal*, 18(1):3–16, 1946. ISSN 00969362.

H. Capart, X. Sillen, and Y. Zech. Numerical and experimental water transients in sewer pipes. *Journal of Hydraulic Research*, 35(5):659–672, 1997. ISSN 00221686. doi: 10.1080/00221689709498400.

P. A. Carling, Z. Cao, M. J. Holland, D. A. Ervine, and K. Babaeyan-Koopaei. Turbulent flow across a natural compound channel. *Water Resources Research*, 38(12):6–1–6–11, 2002. ISSN 00431397. doi: 10.1029/2001wr000902.

L. Cea, A. J. Puertas, and A. L. Pena. Velocity measurements on highly turbulent free surface flow using ADV. *Experiments in Fluids*, 42:333–348, 2007. doi: 10.1007/s00348-006-0237-3.

S. P. Clark and N. Kehler. Turbulent flow characteristics in circular corrugated culverts at mild slopes. *Journal of Hydraulic Research*, 49(5):676–684, oct 2011. doi: 10.1080/00221686.2011.596399.

D. Clegg, A. R. Eadon, and D. Fiddes. UK State-of-the-Art – Sewerage Rehabilitation. *Water Science and Technology*, 21(10-11):1101–1112, oct 1989. ISSN 0273-1223. doi: 10.2166/wst.1989.0311.

P. J. Cobelli, A. E. Agnè, M. Ae, V. P. Ae, P. Petitjeans, A. Maurel, V. Pagneux, and P. Petitjeans. Global measurement of water waves by Fourier transform profilometry. *Experiments in Fluids*, 46(6):1037–1047, 2009. ISSN 07234864. doi: 10.1007/s00348-009-0611-z.

J. R. Cooper, S. J. Tait, and K. V. Horoshenkov. Determining hydraulic resistance in gravel-bed rivers from the dynamics of their water surfaces. *Earth Surface Processes and Landforms*, 31(14):1839–1848, dec 2006. ISSN 01979337. doi: 10.1002/esp.1447.

S. Costanzo. Software-defined doppler radar sensor for human breathing detection. *Sensors (Switzerland)*, 19(14), jul 2019. ISSN 14248220. doi: 10.3390/s19143085.

DantecDynamics. *ISTRA 4D software Manual Q-400 system*, 2018.

L. J. De Chant. The venerable 1/7th power law turbulent velocity profile: A classical nonlinear boundary value problem solution and its relationship to stochastic processes. *Applied Mathematics and Computation*, 161(2):463–474, 2005. ISSN 00963003. doi: 10.1016/j.amc.2003.12.109.

G. Dolcetti. *Remote monitoring of shallow turbulent flows based on the Doppler spectra of airborne ultrasound*. PhD thesis, The University of Sheffield Faculty, 2016.

G. Dolcetti, B. Hortobágyi, M. Perks, and S. J. Tait. The effect of surface gravity waves on the measurement of river surface velocity. *River Flow 2020 - Proceedings of the 10th Conference on Fluvial Hydraulics*, pages 862–871, 2020. doi: 10.1201/b22619-122.

D. Douxchamps, A. D. Devriendt, A. H. Capart, A. C. Craeye, B. Macq, and A. Y. Zech. Stereoscopic and velocimetric reconstructions of the free surface topography of antidune flows. *Experiments in Fluids*, 2005. doi: 10.1007/s00348-005-0983-7.

A. Droitcour. *Non-contact measurement ofheart and respiration rates with single-chip microwave Doppler radar*. PhD thesis, Stanford Univ., 2006.

A. D. Droitcour, O. Boric-Lubecke, V. M. Lubecke, J. Lin, and G. T. Kovacs. Range correlation and I/Q performance benefits in single-chip silicon Doppler radars for noncontact cardiopulmonary monitoring. *IEEE Transactions on Microwave Theory and Techniques*, 52(3):838–848, 2004. ISSN 00189480. doi: 10.1109/TMTT.2004.823552.

EA. Environment Agency sets out roadmap for more flood and climate-resilient nation. 2022. URL https://www.gov.uk/government/news/environment-agency-sets-out-roadmap-for-more-flood-and-climate-resilient-nation.

S. Ead, N. Rajaratnam, C. Katopodis, and F. Ade. Turbulent open-channel flow in circular corrugated culverts. *Journal of Hydraulic Engineering*, 126(10):750–757, 2000. doi: 10.1061/(ASCE)0733-9429(2000)126:10(750).

EMS. FLO-DAR AV sensor. 2022. URL https://www.em-solutions.co.uk/wp-content/uploads/EMS-Hach-Flo-Dar-non-contact-flow-meter-datasheet.pdf.

E. Falcon and N. Mordant. Experiments in Surface Gravity–Capillary Wave Turbulence. *Annual Review of Fluid Mechanics*, 54(1), 2022. ISSN 0066-4189. doi: 10.1146/annurev-fluid-021021-102043.

T. Fan, C. Ma, Z. Gu, Q. Lv, J. Chen, D. Ye, J. Huangfu, Y. Sun, C. Li, and L. Ran. Wireless Hand Gesture Recognition Based on Continuous-Wave Doppler Radar Sensors. *IEEE Transactions on Microwave Theory and Techniques*, 64(11):4012–4020, 2016. ISSN 00189480. doi: 10.1109/TMTT.2016.2610427.

D. Ferraro, F. Coscarella, and R. Gaudio. Scales of turbulence in open-channel flows with low relative submergence. *Phys. Fluids*, 31:125114, 2019. doi: 10.1063/1.5127562.

O. Flores, J. J. Riley, and A. R. Horner-Devine. On the dynamics of turbulence near a free surface. *Journal of Fluid Mechanics*, 821:248–265, 2017. ISSN 14697645. doi: 10.1017/jfm.2017.209.

B. Freeze, S. Smolentsev, N. Morley, and M. Abdou. Characterization of the effect of Froude number on surface waves and heat transfer in inclined turbulent open channel water flows. *International Journal of Heat and Mass Transfer*, 46(20):3765–3775, 2003. ISSN 00179310. doi: 10.1016/S0017-9310(03)00197-2.

I. Fujita. Discharge measurements of snowmelt flood by space-time image velocimetry during the night using far-infrared camera. *Water (Switzerland)*, 9(4):269, 2017. ISSN 20734441. doi: 10.3390/w9040269.

I. Fujita and R. Tsubaki. A Novel Free-Surface Velocity Measurement Method Using Spatio-Temporal Images. *Hydraulic Measurements and Experimental Methods*, pages 375–381, 2002. doi: 10.1061/40655(2002)85.

I. Fujita, H. Watanabe, and Tsubaki. Development of a non-intrusive and efficient flow monitoring technique: The space-time image velocimetry (STIV). *International Journal of River Basin Management*, 5(2):105–114, 2007. ISSN 1814-2060. doi: 10.1080/15715124.2007.9635310.

I. Fujita, Y. Furutani, and T. Okanishi. Advection Features of Water Surface Profile in Turbulent Open-Channel Flow With Hemisphere Roughness Elements. *Visualization of Mechanical Processes*, 1(4):1–8, 2011. ISSN 2152-209X. doi: 10.1615/VisMechProc.v1.i3.70.

F. G. Bass and I. M. Fuks. *Wave Scatttering from Statstically Rough Surfaces*. Pergamon Press, Oxford, 1979. ISBN 0080198961.

X. Gao and O. Boric-Lubecke. AC Coupled Quadrature Doppler Radar Displacement Estimation. *IEEE MTT-S International Microwave Symposium*, pages 1–4, 2015. doi: 10.1109/MWSYM.2015.7167039.

D. Girbau, A. Lázaro, Á. Ramos, and R. Villarino. Remote sensing of vital signs using a doppler radar and diversity to overcome null detection. *IEEE Sensors Journal*, 12(3):512–518, 2012. ISSN 1530437X. doi: 10.1109/JSEN.2011.2107736.

G. Gomit, L. Chatellier, D. Calluaud, L. David, D. Fréchou, R. Boucheron, O. Perelman, and C. Hubert. Large-scale free surface measurement for the analysis of ship waves in a towing tank. *Experiments in Fluids*, 56(10):1–13, 2015. ISSN 07234864. doi: 10.1007/s00348-015-2054-z.

D. G. Goring and V. I. Nikora. Despiking acoustic doppler velocimeter data. *Journal of Hydraulic Engineering*, 128(1):117–126, 2002. doi: 10.1061/(ASCE)0733-9429(2002)128:1(117).

M. Gschwandl, M. Frewein, P. F. Fuchs, T. Antretter, G. Pinter, and P. Novak. Evaluation of Digital Image Correlation Techniques for the Determination of Coefficients of Thermal Expansion for Thin Reinforced Polymers. *20th International Conference on Electronic Materials and Packaging*, pages 3–6, 2019. doi: 10.1109/EMAP.2018.8660763.

C. Gu. Short-range noncontact sensors for healthcare and other emerging applications: A review. *Sensors (Switzerland)*, 16(8), 2016. ISSN 14248220. doi: 10.3390/s16081169.

C. Gu, Z. Peng, and C. Li. High-Precision Motion Detection Using Low-Complexity Doppler Radar with Digital Post-Distortion Technique. *IEEE Transactions on Microwave Theory and Techniques*, 64(3):961–971, 2016. ISSN 00189480. doi: 10.1109/TMTT.2016.2519881.

M. Guala, S. E. Hommema, and R. J. Adrian. Large-scale and very-large-scale motions in turbulent pipe flow. *J. Fluid Mech*, 554:521–542, 2021. doi: 10.1017/S0022112006008871. URL https://doi.org/10.1017/S0022112006008871.

S. Guan, J. A. Rice, C. Li, and C. Gu. Automated DC offset calibration strategy for structural health monitoring based on portable CW radar sensor. *IEEE Transactions on Instrumentation and Measurement*, 63(12):3111–3118, 2014. ISSN 00189456. doi: 10.1109/TIM.2014.2317298.

M. Guerra and J. Thomson. Turbulence measurements from five-beam acoustic doppler current profilers. *Journal of Atmospheric and Oceanic Technology*, 34(6):1267–1284, 2017. ISSN 15200426. doi: 10.1175/JTECH-D-16-0148.1.

J. Guo and R. N. Meroney. Theoretical solution for laminar flow in partially-filled pipes. *Journal of Hydraulic Research*, 51(4):408–416, 2013. ISSN 00221686. doi: 10.1080/00221686.2013.784881.

J. Guo, A. Mohebbi, Y. Zhai, and S. P. Clark. Turbulent velocity distribution with dip phenomenon in conic open channels. *Journal of Hydraulic Research*, 53(1):73–82, 2015. ISSN 00221686. doi: 10.1080/00221686.2014.928807.

X. Guo and L. Shen. Interaction of a deformable free surface with statistically steady homogeneous turbulence. *Journal of fluid mechanics*, 658:33–62, 2010. doi: 10.1017/S0022112010001539.

J. Harband. Three dimensional flow over a submerged object. *Journal of Engineering Mathematics*, 10(1), 1976.

K. V. Horoshenkov, A. Nichols, S. J. Tait, and G. A. Maximov. The pattern of surface waves in a shallow free surface flow. *Journal of Geophysical Research: Earth Surface*, 118(3): 1864–1876, sep 2013. ISSN 21699011. doi: 10.1002/jgrf.20117.

J.-W. Hu and H.-J. Kim. Discussion of "Despiking Acoustic Doppler Velocimeter Data" by Derek G. Goring and Vladimir I. Nikora. *JOURNAL OF HYDRAULIC ENGINEERING*, 13(2):379–383, 2013. ISSN 1598-2351. doi: 10.1007/s13296-013-2015-4.

W. Hu, Z. Zhao, Y. Wang, H. Zhang, and F. Lin. Noncontact accurate measurement of cardiopulmonary activity using a compact quadrature doppler radar sensor. *IEEE Transactions on Biomedical Engineering*, 61(3):725–735, 2014. ISSN 00189294. doi: 10.1109/TBME.2013.2288319.

M. C. Huang, J. J. Liu, W. Xu, C. Gu, C. Li, and M. Sarrafzadeh. A Self-Calibrating Radar Sensor System for Measuring Vital Signs. *IEEE Transactions on Biomedical Circuits and Systems*, 10(2):352–363, 2016. ISSN 19324545. doi: 10.1109/TBCAS.2015.2411732.

A. Hussain. Coherent structures and turbulence. *Journal of Fluid Mechanics*, 173:303–356, 1986. ISSN 14697645. doi: 10.1017/S0022112086001192. URL https://www.cambridge.org/core/journals/journal-of-fluid-mechanics/article/abs/coherent-structures-and-turbulence/4B9538E410B2D70C412DD1A4CB7BE154.

R. Islam, D. Z. Zhu, and M. Asce. Kernel Density-Based Algorithm for Despiking ADV Data. 2013. doi: 10.1061/(ASCE)HY.

R. G. Jackson. Sedimentological and fluid-dynamic implications of the turbulent bursting phenomenon in geophysical flows. *Journal of Fluid Mechanics*, 77(3):531–560, 1976. ISSN 14697645. doi: 10.1017/S0022112076002243.

Y. Jiang, Q. Pu, and W. Ding. Reconstruction of Velocity Distribution in Partially-Filled Pipe Based on Non-Uniform Under-Sampling. *Advances in Mathematical Physics*, 4:1–10, 2020. ISSN 16879139. doi: 10.1155/2020/6961286.

E. Johnson and E. A. Cowen. Estimating bed shear stress from remotely measured surface turbulent dissipation fields in open channel flows. *Journal of the American Water Resources Association*, 53:1982–1996, 2017. ISSN 1093-474X. doi: 10.1111/j.1752-1688.1969.tb04897.x.

E. D. Johnson and E. A. Cowen. Remote Estimation of Turbulence Intensity Variation in Open Channels. *Journal of Hydraulic Engineering*, 146(9):04020062, 2020. ISSN 0733-9429. doi: 10.1061/(asce)hy.1943-7900.0001774.

P. Karsmakers, T. Croonenborghs, M. Mercuri, D. Schreurs, and P. Leroux. Automatic indoor fall detection based on microwave radar measurements. *European Microwave Week 2012: "Space for Microwaves", EuMW 2012, Conference Proceedings - 9th European Radar Conference, EuRAD 2012*, pages 202–205, 2012.

Katronic. KATflow200 Hand-held clamp-on ultrasonic flowmeter. 2020. URL https://www.flowquip.co.uk/wp-content/uploads/2014/09/DS_KF200.pdf.

S. J. Kline, W. C. Reynolds, F. A. Schraubt, and P. W. Runstadlers. The structure of turbulent boundary layers. *Journal of Fluid Mechanics*, 30:741–773, 1967. doi: 10.1017/S0022112067001740.

D. W. Knight and K. Shiono. Turbulence measurements in a shear layer region of a compound channel. *Journal of Hydraulic Research*, 28(2):175–196, 1990. ISSN 00221686. doi: 10.1080/00221689009499085.

D. W. Knight and M. Sterling. Boundary Shear in Circular Pipes Running Partially Full. *Journal of Hydraulic Engineering*, 126(April):263–275, 2000.

S. Komori, Y. Murakami, and H. Ueda. The Relationship between Surface-Renewal and Bursting Motions in an Open-Channel Flow. *Journal of Fluid Mechanics*, 203(103): 103–123, 1989. ISSN 14697645. doi: 10.1017/S0022112089001394.

P.-A. Krogstad and J. H. Kaspersen. Methods to detect coherent structures - a comparison. In *Australasian Fluid Mechanics Conference*, pages 1269–1272, Australia, 1992.

P.-Å. Krogstad, J. H. Kaspersen, and S. Rimestad. Convection velocities in turbulent boundary layers. *Physics of Fluids*, 10:949, 1998. doi: 10.1063/1.869617.

KRUSS. Wilhelmy plate method. 2022. URL https://www.kruss-scientific.com/en/know-how/glossary/wilhelmy-plate-method.

A. Krynkin, K. V. Horoshenkov, A. Nichols, and S. J. Tait. A non-invasive acoustical method to measure the mean roughness height of the free surface of a turbulent shallow water flow. *Review of Scientific Instruments*, 85(11):114902, 2014. ISSN 10897623. doi: 10.1063/1.4901932. URL http://aip.scitation.org/toc/rsi/85/11http://dx.doi.org/10.1063/1.4901932.

S. Kumar, R. Gupta, and S. Banerjee. An experimental investigation of the characteristics of free-surface turbulence in channel flow. *Physics of Fluids*, 10(2):437–456, 1998. ISSN 1070-6631. doi: 10.1063/1.869573. URL http://aip.scitation.org/doi/10.1063/1.869573.

A. Laiadi and A. Merzougui. Free surface flows over a successive obstacles with surface tension and gravity effects. *AIMS Mathematics*, 4(2):316–326, 2019. ISSN 24736988. doi: 10.3934/math.2019.2.316.

Y. S. Lee, P. N. Pathirana, and C. L. Steinfort. Respiration rate and breathing patterns from Doppler radar measurements. *IECBES 2014, Conference Proceedings - 2014 IEEE Conference on Biomedical Engineering and Sciences: "Miri, Where Engineering in Medicine and Biology and Humanity Meet"*, (December):235–240, 2014. doi: 10.1109/IECBES.2014.7047493.

C. J. Legleiter, C. D. Mobley, and B. T. Overstreet. A framework for modeling connections between hydraulics, water surface roughness, and surface reflectance in open channel flows. *Journal of Geophysical Research: Earth Surface*, 122(9):1715–1741, 2017. ISSN 21699011. doi: 10.1002/2017JF004323.

C. Li and J. Lin. Complex signal demodulation and random body movement cancellation techniques for non-contact vital sign detection. *IEEE MTT-S International Microwave Symposium Digest*, pages 567–570, 2008. ISSN 0149645X. doi: 10.1109/MWSYM.2008.4633229.

C. Li, V. M. Lubecke, O. Boric-Lubecke, and J. Lin. A review on recent advances in doppler radar sensors for noncontact healthcare monitoring. *IEEE Transactions on Microwave Theory and Techniques*, 61(5):2046–2060, 2013. ISSN 00189480. doi: 10.1109/TMTT.2013.2256924.

S. Linz, G. Vinci, S. Lindner, S. Mann, F. Lurz, F. Barbon, R. Weigel, and A. Koelpin. I/Q imbalance compensation for Six-port interferometers in radar applications. *European Microwave Week 2014: Connecting the Future, EuMW 2014 - Conference Proceedings; EuMC 2014: 44th European Microwave Conference*, (2):746–749, 2014. doi: 10.1109/EuMC.2014.6986542.

Y. Liu, T. Stoesser, and H. Fang. Impact of turbulence and secondary flow on the water surface in partially filled pipes. *Physics of Fluids*, 34(3):035123, 2022. ISSN 1070-6631. doi: 10.1063/5.0078564.

S. Longo. Experiments on turbulence beneath a free surface in a stationary field generated by a Crump weir: Free-surface characteristics and the relevant scales. *Experiments in Fluids*, 49(6):1325–1338, 2010. ISSN 07234864. doi: 10.1007/s00348-010-0881-5.

S. S. Lu and W. W. Willmarth. Measurements of the structure of the Reynolds stress in a turbulent boundary layer. *Journal of Fluid Mechanics*, 60(3):481–511, 1973. doi: 10.1017/S0022112073000315.

T. S. Luchiktand, W. G. Tiederman, T. S. Luchik, and W. G. Tiederman. Timescale and structure of ejections and bursts in turbulent channel flows. *Journal of Fluid Mechanics*, 174:529, 1987. doi: 10.1017/S0022112087000235.

Q. Lv, D. Ye, S. Qiao, Y. Salamin, J. Huangfu, C. Li, and L. Ran. High dynamic-range motion imaging based on linearized doppler radar sensor. *IEEE Transactions on Microwave Theory and Techniques*, 62(9):1837–1846, 2014. ISSN 00189480. doi: 10.1109/TMTT.2014.2342663.

Q. Lv, L. Chen, K. An, J. Wang, H. Li, D. Ye, J. Huangfu, C. Li, and L. Ran. Doppler Vital Signs Detection in the Presence of Large-Scale Random Body Movements. *IEEE Transactions on Microwave Theory and Techniques*, 66(9):4261–4270, 2018. ISSN 00189480. doi: 10.1109/TMTT.2018.2852625.

T. B. Maddux, S. R. McLean, and J. M. Nelson. Turbulent flow over three-dimensional dunes: 2. Fluid and bed stresses. *Journal of Geophysical Research: Earth Surface*, 108 (F1):n/a–n/a, dec 2003. doi: 10.1029/2003jf000018.

T. Mandel, S. Gakhar, H. Chung, J. Koseff, T. L. Mandel, I. Rosenzweig, and J. R. Koseff. On the surface expression of a canopy-generated shear instability. *Article in Journal of Fluid Mechanics*, 867:633–660, 2019. doi: 10.1017/jfm.2019.170. URL https://doi.org/10.1017/jfm.2019.170.

H. Martin and P. Miroslav. A complex review of the possibles of residual stress analysis using moving 2D and 3D digital image correlation system. *Journal of Mechanical Engineerunn*, 71(1):61–78, 2021. ISSN 2450-5471. doi: 10.2478/scjme-2021-0006.

S. Martínez-Aranda, J. Fernández-Pato, D. Caviedes-Voullième, I. García-Palacín, and P. García-Navarro. Towards transient experimental water surfaces: A new benchmark dataset for 2D shallow water solvers. *Advances in Water Resources*, 121(August):130–149, 2018. ISSN 03091708. doi: 10.1016/j.advwatres.2018.08.013.

MATLAB. scatteredinterpolant. *MATLAB version 9.6.0.1150989 (R2019a)*, 2019. URL https://uk.mathworks.com/help/matlab/ref/scatteredinterpolant.html.

G. H. Matthes. Macroturbulence in natural stream flow. *Transactions American Geophysical Union*, 28(2):255–265, 1947. ISSN 23249250. doi: 10.1029/TR028i002p00255.

M. Mercuri, P. J. Soh, G. Pandey, P. Karsmakers, G. A. Vandenbosch, P. Leroux, and D. Schreurs. Analysis of an indoor biomedical radar-based system for health monitoring. *IEEE Transactions on Microwave Theory and Techniques*, 61(5):2061–2068, 2013. ISSN 00189480. doi: 10.1109/TMTT.2013.2247619.

M. Metzger, B. McKeon, and E. Arce-Larreta. Scaling the characteristic time of the bursting process in the turbulent boundary layer. *Physica D: Nonlinear Phenomena*, 239(14): 1296–1304, 2010. doi: 10.1016/j.physd.2009.09.004.

S. Michell. Flow in Pipes. *Fluid and Particle Mechanics*, pages 82–127, 1970. doi: 10.1016/b978-0-08-013312-6.50006-4.

Micro-Epsilon. Micro-Epsilon Laser displacement sensors mannual. 2010.

F. Moisy, M. Rabaud, and K. Salsac. A synthetic Schlieren method for the measurement of the topography of a liquid interface. *Experiments in Fluids*, 46(6):1021–1036, 2009. ISSN 07234864. doi: 10.1007/s00348-008-0608-z.

M. Mrówka, T. Machoczek, P. Jureczko, K. Joszko, M. Gzik, W. Wolański, and K. Wilk. Mechanical, chemical, and processing properties of specimens manufactured from polyether-ether-ketone (Peek) using 3d printing. *Materials*, 14(11), 2021. ISSN 19961944. doi: 10.3390/ma14112717.

F. Muraro, G. Dolcetti, A. Nichols, S. J. Tait, K. V. Horoshenkov, and P. of Water Engineering. Free-surface behaviour of shallow turbulent flows State-of-the-art paper Free-surface behaviour of shallow turbulent flows. *Journal of Hydraulic Research*, 59(1):1–20, 2021. doi: 10.1080/00221686.2020.1870007. URL https://www.tandfonline.com/action/journalInformation?journalCode=tjhr20.

I. Nezu and H. Nakagawa. *Turbulence in open-channel flows*. IAHR Monograph, Balkema, Rotterdam NL, 1993. ISBN 9054101180 9789054101185.

H. C. Ng, H. L. F. Cregan, and J. M. Dodds. Partially filled pipes : experiments in laminar and turbulent flow. *Journal of Fluid Mechanics*, pages 467–507, 2018. doi: 10.1017/jfm.2018.345.

H. C. Ng, E. Collignon, R. J. Poole, and D. J. Dennis. Energetic motions in turbulent partially filled pipe flow. *Physics of Fluids*, 33(2), 2021. ISSN 10897666. doi: 10.1063/5.0031639.

A. Nichols. *Free surface dynamics in shallow turbulent flows*. PhD thesis, University of Bradford, 2014.

A. Nichols, S. Tait, K. Horoshenkov, and S. Shepherd. A non-invasive airborne wave monitor. *Flow Measurement and Instrumentation*, 34:118–126, 2013. ISSN 09555986. doi: 10.1016/j.flowmeasinst.2013.09.006. URL http://dx.doi.org/10.1016/j.flowmeasinst.2013.09.006.

A. Nichols, S. J. Tait, K. V. Horoshenkov, and S. J. Shepherd. A model of the free surface dynamics of shallow turbulent flows. *Journal of Hydraulic Research*, 54(5):516–526, 2016. ISSN 00221686. doi: 10.1080/00221686.2016.1176607.

A. Nichols, M. Rubinato, Y. H. Cho, and J. Wu. Optimal use of titanium dioxide colourant to enable water surfaces to be measured by kinect sensors. *Sensors (Switzerland)*, 20(12): 1–17, 2020. ISSN 14248220. doi: 10.3390/s20123507.

V. Nikora and D. Goring. Flow turbulence over fixed and weakly mobile gravel beds. *Journal of Hydraulic Engineering*, 126(9):679–690, 2000.

Nortek. The Comprehensive Manual for Velocimeters. *Nortek Manuals*, 2021.

C. Noss, K. Koca, P. Zinke, P.-Y. Henry, C. Ushanth Navaratnam, J. Aberle, A. Lorke, P. Researcher, and P.-y. Henry. A Lagrangian drifter for surveys of water surface roughness in streams. *Journal of Hydraulic Research*, 58(3):471–488, 2019. doi: 10.1080/00221686.2019.1623930. URL https://www.tandfonline.com/action/journalInformation?journalCode=tjhr20.

P. G. Novo and Y. Kyozuka. Analysis of turbulence and extreme current velocity values in a tidal channel. *Journal of Marine Science and Technology*, 24:659–672, 2019. doi: 10.1007/s00773-018-0601-z.

Ofwat. Service delivery report 2020 - 2021. 2021. URL https://www.ofwat.gov.uk/wp-content/uploads/2021/11/Service-Delivery-Report-2020-2021.pdf.

B. Pan, K. Qian, H. Xie, and A. Asundi. Two-dimensional digital image correlation for in-plane displacement and strain measurement: A review. *Measurement Science and Technology*, 20(6), 2009. ISSN 13616501. doi: 10.1088/0957-0233/20/6/062001.

B. K. Park, O. Boric-Lubecke, and V. M. Lubecke. Arctangent demodulation with DC offset compensation in quadrature Doppler radar receiver systems. *IEEE Transactions on Microwave Theory and Techniques*, 55(5):1073–1078, 2007a. ISSN 00189480. doi: 10.1109/TMTT.2007.895653.

B.-k. Park, A. Vergara, O. Boric-Lubecke, Victor M Lubecke, and A. Høst-Madsen. Quadrature Demodulation with DC Cancellation for a Doppler Radar Motion Detector. *October*, pages 1–7, 2007b.

B. K. Park, S. Yamada, and V. Lubecke. Measurement method for imbalance factors in direct-conversion quadrature radar systems. *IEEE Microwave and Wireless Components Letters*, 17(5):403–405, 2007c. ISSN 15311309. doi: 10.1109/LMWC.2007.895742.

Z. Peng and C. Li. Portable microwave radar systems for short-range localization and life tracking: A review. *Sensors (Switzerland)*, 19(5):1–19, 2019. ISSN 14248220. doi: 10.3390/s12051136.

A. Przadka, B. Cabane, V. Pagneux, A. Maurel, and P. Petitjeans. Fourier transform profilometry for water waves: how to achieve clean water attenuation with diffusive reflection at the water surface? *Experiments in Fluids*, 52:519–527, 2012. doi: 10.1007/s00348-011-1240-x.

M. Rashidi. Burst-interface interactions in free surface turbulent flows. *Physics of Fluids*, 9: 3485, 1997. doi: 10.1063/1.869457. URL https://doi.org/10.1063/1.869457.

L. Rayleigh. The form of standing waves on the surface of running water. *Proceedings of the London Mathematical Society*, s1-15 (1):69–78, 1883.

P. L. Reu and T. J. Miller. The application of high-speed digital image correlation. *Journal of Strain Analysis for Engineering Design*, 43(8):673–688, 2008. ISSN 03093247. doi: 10.1243/03093247JSA414.

C. G. Rita Ventura Matos, Filipa Ferreira and J. S. Matos. Understanding the effect of ventilation, intermittent pumping and seasonality in hydrogen sulfide and methane concentrations in a coastal sewerage system. *Environmental Science and Pollution Research*, 26: 3404–3414, 2019. doi: 10.1007/s11356-018-3856-3.

D. V. Q. Rodrigues, D. Rodriguez, V. Pugliese, M. Watson, and C. Li. Air Bubble Detection Based on Portable mm-Wave Doppler Radars. pages 1–3, 2021.

D. Rodriguez and C. Li. Sensitivity and Distortion Analysis of a 125-GHz Interferometry Radar for Submicrometer Motion Sensing Applications. *IEEE Transactions on Microwave Theory and Techniques*, 67(12):5384–5395, 2019. ISSN 15579670. doi: 10.1109/TMTT.2019.2951142.

A. Romanova. *Acoustic Monitoring of Hydraulic Resistance in Partially Full Pipes*. PhD thesis, University of Bradford, 2013.

A. V. Romanova, K. V. Horoshenkov, and A. Krynkin. Dynamically rough boundary scattering effect on a propagating continuous acoustical wave in a circular pipe with flow. *Sensors*, 18(4), 2018. ISSN 14248220. doi: 10.3390/s18041098.

A. G. Roy, T. Buffin-Belanger, H. Lamarre, and A. Kirkbride. Size, shape and dynamics of large-scale turbulent flow structures in a gravel-bed river. *Journal of Fluid Mechanics*, 500:1–27, 2004. doi: 10.1017/S0022112003006396.

S. K Som and G. Biswas. *Introduction To Fluid Mechanics And Fluid Machines*. Tata McGraw-Hill Education, New Delhi, 2010. ISBN 8121916666.

A. Salama. Velocity profile representation for fully developed turbulent flows in pipes: A modified power law. *Fluids*, 6(10), 2021. ISSN 23115521. doi: 10.3390/fluids6100369.

K. Satoru, U. Hiromasa, O. Fumimaru, and M. Tokuro. Turbulence structure and transport mechanism at the free surface in an open channel flow. *International Journal of Heat and Mass Transfer*, 25(4):513–521, 1982. ISSN 00179310. doi: 10.1016/0017-9310(82)90054-0.

R. Savelsberg and W. Van De Water. Turbulence of a Free Surface. *Physical review letters*, 100(3), 2008. doi: 10.1103/PhysRevLett.100.034501.

R. Savelsberg and W. Van De Water. Experiments on free-surface turbulence. *Journal of Fluid Mechanics*, 619:95, 2009. ISSN 0022-1120. doi: 10.1017/S0022112008004369. URL http://www.journals.cambridge.org/abstract_S0022112008004369.

R. Savelsberg, A. Holten, and W. Van De Water. Measurement of the gradient field of a turbulent free surface. *Experiments in Fluids*, 41(4):629–640, 2006. ISSN 07234864. doi: 10.1007/s00348-006-0186-x.

H. Schlichting. *Boundary Layer Theory*. McGraw-Hill, New York, 1979. ISBN 978-3-662-52919-5.

D. A. Shah and R. A. Antonia. Scaling of the "bursting" period in turbulent boundary layer and duct flows. *hysics of Fluids A: Fluid Dynamics*, 1:318, 1989. doi: 10.1063/1.857450.

A. B. Shvidchenko and G. Pende. Macroturbulent structure of open-channel flow over gravel beds. *Water Resources Research*, 37(3):709–719, 2001.

J. Y. Sim, J. H. Park, and J. R. Yang. Vital-signs detector based on frequency-shift keying radar. *Sensors (Switzerland)*, 20(19):1–17, 2020. ISSN 14248220. doi: 10.3390/s20195516.

A. Simonini, D. Fontanarosa, M. G. De Giorgi, and M. R. Vetrano. Mode characterization and damping measurement of liquid sloshing in cylindrical containers by means of Reference Image Topography. *Experimental Thermal and Fluid Science*, 120(July 2020):110232, 2021. ISSN 08941777. doi: 10.1016/j.expthermflusci.2020.110232. URL https://doi.org/10.1016/j.expthermflusci.2020.110232.

A. Singh, X. Gao, E. Yavari, M. Zakrzewski, X. H. Cao, V. M. Lubecke, and O. Boric-Lubecke. Data-based quadrature imbalance compensation for a CW doppler radar system. *IEEE Transactions on Microwave Theory and Techniques*, 61(4):1718–1724, 2013. ISSN 00189480. doi: 10.1109/TMTT.2013.2249525.

S. Skaria, A. Al-Hourani, M. Lech, and R. J. Evans. Hand-Gesture Recognition Using Two-Antenna Doppler Radar with Deep Convolutional Neural Networks. *IEEE Sensors Journal*, 19(8):3041–3048, 2019. ISSN 1530437X. doi: 10.1109/JSEN.2019.2892073.

Skyworks. SKY73009-11:400 to 3000 MHz Direct Quadrature Demodulator. 2019. URL https://www.skyworksinc.com/-/media/SkyWorks/Documents/Products/101-200/SKY73009_11_103034I.pdf.

A. J. Smits. *Flow Visualization - Techniques and Examples*. Imperial College Press, London, 2012. ISBN 9781848167919. doi: 10.1142/9781848160361.

S. Smolentsev and R. Miraghaie. Study of a free surface in open-channel water flows in the regime from "weak" to "strong" turbulence. *International Journal of Multiphase Flow*, 31 (8):921–939, 2005. ISSN 03019322. doi: 10.1016/j.ijmultiphaseflow.2005.05.008.

S. Smolentsev, N. Morley, B. Freeze, R. Miraghaic, J. C. Nave, S. Banerjee, A. Ying, and M. Abdou. Thermofluid modeling and experiments for free surface flows of low-conductivity fluid in fusion systems. *Fusion Engineering and Design*, 72(1-3 SPEC. ISS.): 63–81, 2004. ISSN 09203796. doi: 10.1016/j.fusengdes.2004.07.003.

M. Sterling and D. W. Knight. Resistance and boundary shear in circular conduits with flat beds running part full. *Proceedings of the Institution of Civil Engineers - Water and Maritime Engineering*, 142(4):229–240, 2000. ISSN 1472-4561. doi: 10.1680/wame.2000.142.4.229.

G. Strang. *Introduction to Linear Algebra*. Wellesley-Cambridge Press, Wellesley, MA, fourth edition, 2009. ISBN 9780980232714 0980232716 9780980232721 0980232724 9788175968110 8175968117.

A. N. Sukhodolov, J. J. Fedele, and B. L. Rhoads. Structure of flow over alluvial bedforms: An experiment on linking field and laboratory methods. *Earth Surface Processes and Landforms*, 31(10):1292–1310, 2006. ISSN 01979337. doi: 10.1002/esp.1330.

A. Tamburrino and J. S. Gulliver. Free-surface visualization of streamwise vortices in a channel flow. *Water Resources Research*, 43(11):1–12, nov 2007. ISSN 00431397. doi: 10.1029/2007WR005988.

L. Tan and J. Jiang. *Digital Signal Processing: Fundamentals and Applications*, volume 42. Elsevier Science, United Kingdom, 3rd editio edition, 2018. ISBN 9780128150719. doi: 10.5860/choice.42-6523.

Z. Tang, N. Jiang, ·. X. Zheng, and Y. Wu. Bursting process of large- and small-scale structures in turbulent boundary layer perturbed by a cylinder roughness element. *Experiments in Fluids*, 57:79, 2016. doi: 10.1007/s00348-016-2174-0.

K. Tani and I. Fujita. Wavenumber-frequency analysis of river surface texture to improve accuracy of image-based velocimetry. *E3S Web of Conferences*, 40, 2018. doi: 10.1051/e3sconf/20184006012. URL https://doi.org/10.1051/e3sconf/20184006012.

K. Tani and I. Fujita. Application of the sampling moiré method to shallow open-channel flows with circular roughness elements. *Flow Measurement and Instrumentation*, 76 (October):101845, 2020. ISSN 09555986. doi: 10.1016/j.flowmeasinst.2020.101845.

G. Taubin. Estimation of planar curves, surfaces, and nonplanar space curves defined by implicit equations with applications to edge and range image segmentation. *IEEE transactions on pattern analysis and machine intelligenc*, 13(11):1115–1138, 1991. doi: 10.1109/34.103273.

G. Tchobanoglous. *Wastewater engineering : collection and pumping of wastewater*. McGraw-Hill, New York, 1981. ISBN 007041680X 9780070416802.

C. Techens, M. Palanca, P. E. Éltes, Á. Lazáry, and L. Cristofolini. Testing the impact of discoplasty on the biomechanics of the intervertebral disc with simulated degeneration: An in vitro study. *Medical Engineering and Physics*, 84:51–59, 2020. ISSN 18734030. doi: 10.1016/j.medengphy.2020.07.024.

M. A. C. Teixeira. Comment on Wavelet spectral analysis of the free surface of turbulent flows. *Journal of Hydraulic Research*, 57(4):603–604, 2019. ISSN 00221686. doi: 10.1080/00221686.2018.1555561.

TELEDYNE. TIENet 350 area velocity sensor installation and operation guide. 2016. URL https://www.rshydro.co.uk/files/TIENet-350-AV-Sensor-User-Manual.pdf.

R. Tsubaki, I. Fujita, I. Fujuta, and I. Fujita. Stereoscopic measurement of a fluctuating free surface with discontinuities. *Measurement Science and Technology*, 16(10):1894–1902, 2005. ISSN 09570233. doi: 10.1088/0957-0233/16/10/003.

J. P. Tullis, R. Watkins, and S. L. Barfuss. Innovative new drainage pipe. In *Proceedings of the International Conference on Pipeline Design and Installation*, ASCE, 1990.

D. E. Turney, A. Anderer, and S. Banerjee. A method for three-dimensional interfacial particle image velocimetry (3D-IPIV) of an air-water interface. *Measurement Science and Technology*, 20(4), 2009. ISSN 13616501. doi: 10.1088/0957-0233/20/4/045403.

R. Vinuesa, M. H. Hites, C. E. Wark, and H. M. Nagib. Documentation of the role of large-scale structures in the bursting process in turbulent boundary layers. *Phys. Fluids*, 27:105107, 2015. doi: 10.1063/1.4934625.

J. M. Wallace. Quadrant Analysis in Turbulence Research: History and Evolution. *Fluid Mechanics*, 48:131–158, 2016. doi: 10.1146/annurev-fluid-122414-034550.

J. M. Wallace, R. S. Brodkey, and H. Eckelmann. Pattern-recognized structures in bounded turbulent shear flows. *Journal of Fluid Mechanics*, 4:673–693, 1977. doi: 10.1017/S0022112077001402.

J. Wang, X. Wang, L. Chen, J. Huangfu, C. Li, and L. Ran. Noncontact distance and amplitude-independent vibration measurement based on an extended dacm algorithm. *IEEE Transactions on Instrumentation and Measurement*, 63(1):145–153, 2014. ISSN 00189456. doi: 10.1109/TIM.2013.2277530.

W. C. Wang, Y. A. Chiang, K. J. Yu, Y. C. Ho, H. T. Shen, T. Y. Chang, Y. H. Chang, and C. S. Tsao. Three-dimensional digital image correlation measurement of mechanical properties of soft materials. *EXPERIMENTAL SOLID MECHANICS*, 50(2):419–428, 2015. ISSN 15729648. doi: 10.1007/s11012-014-9947-4.

Y. Wang, C. Mingotaud, and L. K. Patterson. Noncontact monitoring of liquid surface levels with a precision of 10 micrometers: A simple ultrasound device. *Review of Scientific Instruments*, 62(6):1640–1641, 1991. ISSN 00346748. doi: 10.1063/1.1142445.

Y. Wang, W. Wang, M. Zhou, A. Ren, and Z. Tian. Remote monitoring of human vital signs based on 77-GHZ MM-WAVE FMCW radar. *Sensors (Switzerland)*, 20(10), 2020. ISSN 14248220. doi: 10.3390/s20102999.

R. Watson-Watt. Radar in war and in peace. *Nature*, 156:319–324, 1945.

F. White. *Viscous Fluid Flow*. McGraw-Hill, New York, 1991. ISBN 007124493X, 9780071244930.

B. Wu, H. Bao, J. Ou, and S. Tian. Stability and accuracy analysis of the central difference method for real-time substructure testing. *Earthquake Engineering and Structural Dynamics*, 34(7):705–718, 2005. doi: 10.1002/eqe.451.

Y. Wu, Z. Liu, Y. Chen, and M. Li. Investigation of velocity distribution and turbulence characteristics in subcritical circular open channel flows using a modified Reynolds stress model. *Journal of Hydro-Environment Research*, 19(February):68–77, 2018. ISSN 15706443. doi: 10.1016/j.jher.2018.02.002.

S. Yan, X. Zeng, and A. Long. Meso-scale modelling of 3D woven composite T-joints with weave variations. *Composites Science and Technology*, 171(July 2018):171–179, 2019. ISSN 02663538. doi: 10.1016/j.compscitech.2018.12.024.

E. Yavari, V. Lubecke, and O. Boric-Lubecke. AC/DC coupling effects on CW and pulse transmission modes in Doppler radar physiological monitoring system. *RWW 2012 - Proceedings: 2012 IEEE Topical Conference on Biomedical Wireless Technologies, Networks, and Sensing Systems, BioWireleSS 2012*, pages 25–28, 2012. doi: 10.1109/BioWireless.2012.6172739.

J.-i. I. Yoon, J. Sung, M. Ho Lee, J.-i. I. Yoon, G. Student, and M. H. Lee. Velocity profiles and friction coefficients in circular open channels. *Journal of Hydraulic Research*, 50(3):304–311, 2012. ISSN 00221686. doi: 10.1080/00221686.2012.673745. URL https://www.tandfonline.com/action/journalInformation?journalCode=tjhr20http://dx.doi.org/10.1080/00221686.2012.673745.

W. R. Young and C. L. Wolfe. Generation of surface waves by shear-flow instability. *J. Fluid Mech*, 739:276, 2014. doi: 10.1017/jfm.2013.617.

M. Zakrzewski, H. Raittinen, and J. Vanhala. Comparison of center estimation algorithms for heart and respiration monitoring with microwave doppler radar. *IEEE Sensors Journal*, 12(3):627–634, 2012. ISSN 1530437X. doi: 10.1109/JSEN.2011.2119299.

M. Zakrzewski, A. Singh, E. Yavari, X. Gao, O. Boric-Lubecke, J. Vanhala, and K. Palovuori. Quadrature imbalance compensation with ellipse-fitting methods for microwave radar physiological sensing. *IEEE Transactions on Microwave Theory and Techniques*, 62(6):1400–1408, 2014. ISSN 00189480. doi: 10.1109/TMTT.2014.2321738.

M. Zakrzewski, K. Palovuori, and J. Vanhala. Quadrature channel calibration with a pendulum for accurate displacement measurement with CW Doppler radar. *Conference Proceedings - 2014 IEEE MTT-S International Microwave Workshop Series on: RF and Wireless Technologies for Biomedical and Healthcare Applications, IMWS-Bio 2014*, pages 16–18, 2015a. doi: 10.1109/IMWS-BIO.2014.7032441.

M. Zakrzewski, A. Vehkaoja, A. S. Joutsen, K. T. Palovuori, and J. J. Vanhala. Noncontact Respiration Monitoring during Sleep with Microwave Doppler Radar. *IEEE Sensors Journal*, 15(10):5683–5693, 2015b. ISSN 1530437X. doi: 10.1109/JSEN.2015.2446616.

L. Zhang, P. De Schryver, B. De Gusseme, W. De Muynck, N. Boon, and W. Verstraete. Chemical and biological technologies for hydrogen sulfide emission control in sewer systems: A review. *Water Research*, 42(1):1–12, 2008. ISSN 0043-1354. doi: 10.1016/j.watres.2007.07.013.

X. Zhang and C. S. Cox. Measuring the two-dimensional structure of a wavy water surface optically: A surface gradient detector. *Experiments in Fluids*, 17(4):225–237, 1994. ISSN 07234864. doi: 10.1007/BF00203041.

K. S. Åse Dalseth Austigard and K. K. Heldal. Hydrogen sulphide exposure in waste water treatment. *J Occup Med Toxicol*, 13, 2018. doi: 10.1186/s12995-018-0191-z.

Appendix A

Illustration of the calibration in Istra4D

This appendix presents three calibration examples within the Istra4D software. In Fig.A.1a, green circles indicate successful corner detection, indicating a good search. Fig.A.1b shows red circles, which indicate that an insufficient number of corners were detected in the image. This typically occurs when the calibration plate is titled excessively. It is important to position the calibration plate at different angles, but the angle should not be too large to ensure accurate corner detection. In Fig. A.1c, blue circles represent the inability to locate the center marker. This can occur when there is overexposure in the image. If the marker cannot be found due to lighting conditions, the brightness settings can be adjusted for calibration purposes. It is crucial to ensure proper exposure levels to enable successful marker detection during the calibration process. For more detailed information about the calibration procedure, please refer to the manual provided by Dantec Dynamics, which can be requested at https://www.dantecdynamics.com/solutions/stress-strain-espi-dic/digital-image-correlation-dic/dic-standard-3d/.

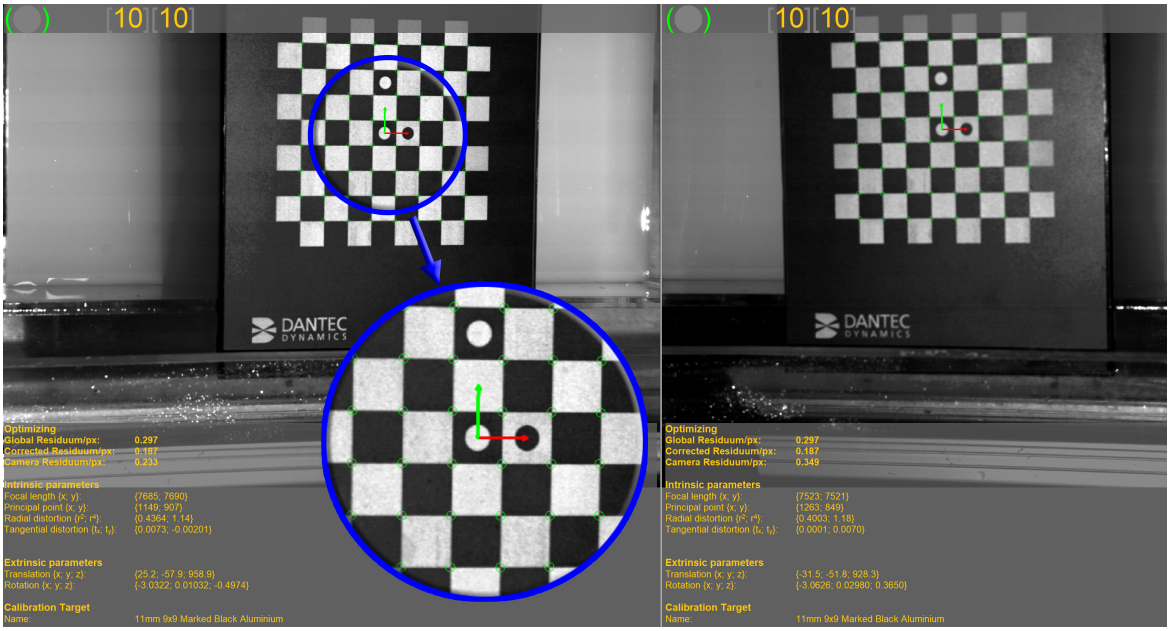
10 10
DANTEC DYNAMICS
Optimizing
Global Residuum/px: 0.297
Corrected Residuum/px: 0.187
Camera Residuum/px: 0.233
Intrinsic parameters
Focal length {x, y}: {7685; 7690}
Principal point {x, y}: {1149; 907}
Radial distortion {r²; r⁴}: {0.4364; 1.14}
Tangential distortion {t_x, t_y}: {0.0073; -0.00201}
Extrinsic parameters
Translation {x; y; z}: {25.2; -57.9; 958.9}
Rotation {x; y; z}: {-3.0322; 0.01032; -0.4974}
Calibration Target
Name: 11mm 9x9 Marked Black Aluminium
10 10
DANTEC DYNAMICS
Optimizing
Global Residuum/px: 0.297
Corrected Residuum/px: 0.187
Camera Residuum/px: 0.349
Intrinsic parameters
Focal length {x, y}: {7523; 7521}
Principal point {x, y}: {1263; 849}
Radial distortion {r²; r⁴}: {0.4003; 1.18}
Tangential distortion {t_x, t_y}: {0.0001; 0.0070}
Extrinsic parameters
Translation {x; y; z}: {-31.5; -51.8; 928.3}
Rotation {x; y; z}: {-3.0626; 0.02980; 0.3650}
Calibration Target
Name: 11mm 9x9 Marked Black Aluminium

(a)

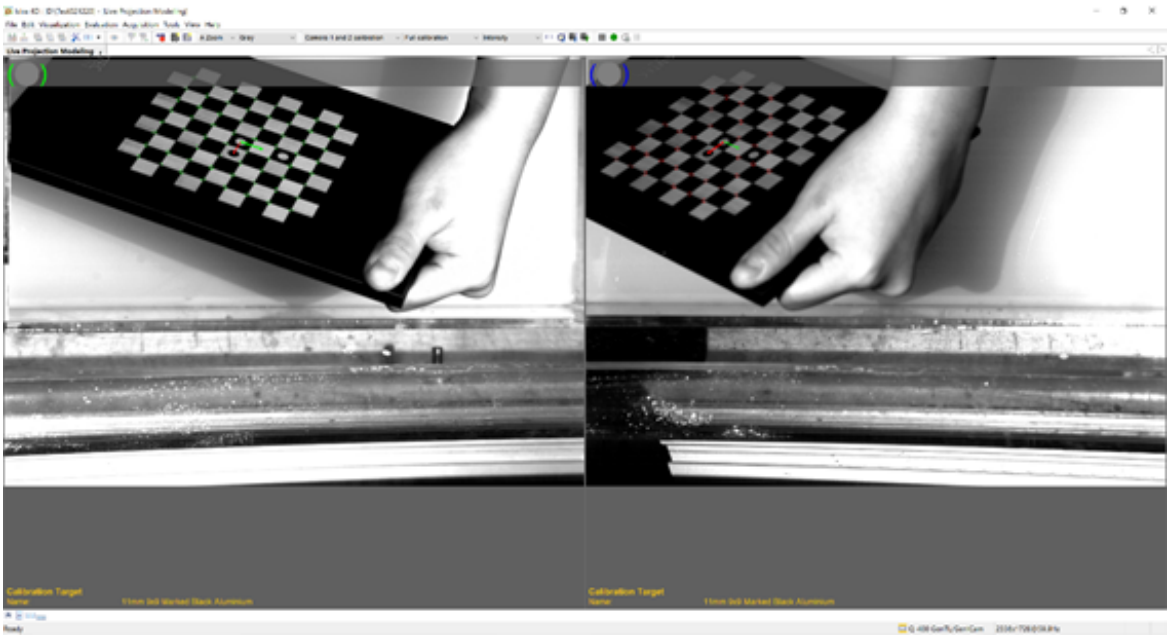

(b)

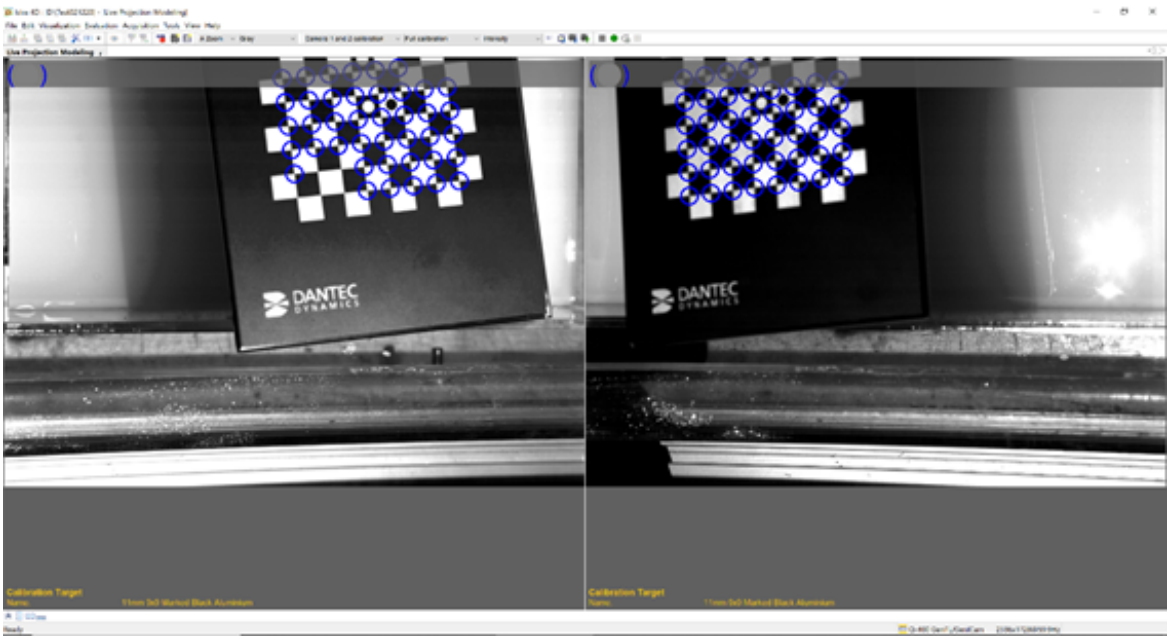

(c)

Figure A.1 Illustration of the calibration in Istra4D , with the upstream camera view on the left and the downstream camera view on the right, (a) good calibration with green markers, (b) bad calibration with red markers and (c) bad calibration with blue markers.

Appendix B

ADV measurement depth-wise positions

Table B.1 ADV measurement streamwise velocity depth-wise positions

FC		y/d																	
1	S	0.49	0.48	0.47	0.46	0.45	0.44	0.43	0.42	0.41									
	B																		
2	S	0.61	0.56	0.53	0.48	0.45	0.41	0.37	0.33	~~0.30~~									
	B	~~0.14~~	0.12	0.11	0.09	0.08	0.06	0.05	0.03	0.01									
3	S	0.68	0.64	0.61	0.58	0.55	0.51	0.49	0.45	0.42	0.38	0.36	0.32	0.29	0.27	0.24			
	B	0.29	0.27	~~0.23~~	~~0.18~~	0.16	~~0.15~~	~~0.09~~	0.06	0.03	0.01								
4	S	0.73	0.67	0.62	0.56	0.51	0.45	0.40	0.34	0.29	0.23	0.18							
	B	0.40	0.34	0.29	~~0.23~~	0.14	0.09	0.07	0.01										
5	S	0.76	0.71	0.66	0.61	0.56	0.52	0.47	0.42	0.37	0.32	0.27	0.22	0.18	0.13				
	B	0.47	0.39	0.34	~~0.32~~	0.22	0.13	0.05	0.03										

6	S	0.78	0.74	0.69	0.65	0.60	0.56	0.52	0.47	0.43	0.34	0.25	0.21	0.16					
	B	0.52	0.50	~~0.43~~	~~0.32~~	0.29	0.21	~~0.16~~	~~0.12~~	0.07	~~0.03~~	~~0.01~~							
7	S	0.80	0.76	0.72	0.68	0.64	0.60	0.56	0.52	0.48	0.40	0.32	0.24	0.20	~~0.12~~				
	B	0.56	0.52	0.48	0.44	0.36	0.28	0.20	0.18	0.13	0.11	0.04	0.02						
8	S	0.81	0.77	0.74	0.70	0.66	0.62	0.59	0.55	0.47	0.40	0.32	0.25	0.21	0.17				
	B	0.59	0.55	0.51	0.43	~~0.36~~	0.28	0.21	0.17	~~0.13~~	0.09	0.06	0.02						
9	S	0.83	0.79	0.76	0.72	0.69	0.65	0.62	0.58	0.51	0.44	0.37	0.30	0.23	0.16				
	B	0.62	0.58	0.55	0.48	0.41	~~0.34~~	0.27	0.20	~~0.13~~	~~0.09~~	0.06	0.02	0.02					
10	S	0.84	0.81	0.77	0.74	0.71	0.67	0.64	0.57	0.51	0.44	0.37	0.31	0.24	0.21	0.17	0.14		
	B	0.64	0.61	0.57	0.54	~~0.47~~	0.41	0.34	~~0.27~~	0.21	0.14	~~0.11~~	0.08	0.04	0.01				
11	S	0.84	0.81	0.78	0.75	0.72	0.69	0.66	0.63	0.56	0.50	0.44	0.38	0.32	0.25	0.19	0.13		
	B	0.66	0.63	0.61	0.52	0.48	0.42	0.36	0.30	0.24	0.17	0.13	0.10	0.07	0.05	0.01			
12	S	0.88	0.85	0.82	0.80	0.77	0.71	0.65	0.59	0.53	0.47	0.42	0.36	0.30	0.24	0.18	0.12		
	B	~~0.68~~	0.65	0.62	0.56	0.47	0.45	0.39	0.33	~~0.24~~	~~0.21~~	0.15	0.12	~~0.08~~	~~0.07~~	0.02	0.01		
13	S	0.86	0.83	0.80	0.78	0.75	0.72	0.69	0.67	0.61	0.56	0.50	0.45	0.39	0.34	0.28	0.23	0.17	0.12
	B	~~0.69~~	~~0.67~~	0.64	0.61	0.56	0.50	0.45	0.39	~~0.34~~	~~0.26~~	0.23	0.17	~~0.12~~	0.06	0.04			
14	S	0.68	0.65	0.63	0.60	0.57	0.52	0.47	0.42	0.37	0.31	0.26	0.21	0.16	0.11	0.10			
	B	~~0.70~~	~~0.65~~	0.59	0.52	0.49	0.44	0.39	0.33	0.28	~~0.26~~	0.18	0.13	~~0.07~~	0.02				

Table B.2 ADV measurement lateral velocity depth-wise positions

FC		y/d																	
1	S	0.49	0.48	0.47	0.46	0.45	0.44	0.43	0.42	0.41									
	B																		
2	S	0.61	0.56	0.53	0.48	0.45	0.41	0.37	0.33	~~0.30~~									
	B	~~0.14~~	~~0.12~~	~~0.11~~	~~0.09~~	~~0.08~~	~~0.06~~	~~0.05~~	~~0.03~~	~~0.01~~									
3	S	0.68	0.64	0.61	0.58	0.55	0.51	0.49	0.45	0.42	0.38	0.36	0.32	0.29	0.27	0.24			
	B	0.29	~~0.27~~	~~0.23~~	~~0.18~~	~~0.16~~	~~0.15~~	~~0.09~~	~~0.06~~	~~0.03~~	0.01								
4	S	0.73	0.67	0.62	0.56	0.51	0.45	0.40	0.34	0.29	0.23	0.18							
	B	~~0.40~~	0.34	0.29	~~0.23~~	~~0.14~~	~~0.09~~	0.07	0.01										
5	S	0.76	0.71	0.66	0.61	0.56	0.52	0.47	0.42	0.37	0.32	0.27	0.22	0.18	0.13				
	B	~~0.47~~	0.39	0.34	~~0.32~~	~~0.22~~	~~0.13~~	0.05	0.03										
6	S	0.78	0.74	0.69	0.65	0.60	0.56	0.52	0.47	0.43	0.34	0.25	0.21	0.16					
	B	0.52	0.50	~~0.43~~	~~0.32~~	0.29	0.21	~~0.16~~	~~0.12~~	~~0.07~~	~~0.03~~	~~0.01~~							
7	S	0.80	0.76	0.72	0.68	0.64	0.60	0.56	0.52	0.48	0.40	0.32	0.24	0.20	~~0.12~~				
	B	0.56	0.52	0.48	0.44	~~0.36~~	0.28	0.20	0.18	~~0.13~~	~~0.11~~	0.04	0.02						
8	S	0.81	0.77	0.74	0.70	0.66	0.62	0.59	0.55	0.47	0.40	0.32	0.25	0.21	0.17				
	B	0.59	0.55	0.51	0.43	~~0.36~~	0.28	0.21	0.17	~~0.13~~	~~0.09~~	0.06	0.02						
9	S	0.83	0.79	0.76	0.72	0.69	0.65	0.62	0.58	0.51	0.44	0.37	0.30	0.23	0.16				
	B	0.62	~~0.58~~	0.55	0.48	0.41	~~0.34~~	0.27	0.20	~~0.13~~	~~0.09~~	~~0.06~~	0.02	0.02					
10	S	0.84	0.81	0.77	0.74	0.71	0.67	0.64	0.57	0.51	0.44	0.37	0.31	0.24	0.21	0.17	0.14		
	B	0.64	0.61	0.57	~~0.54~~	0.47	0.41	0.34	~~0.27~~	0.21	0.14	~~0.11~~	~~0.08~~	0.04	0.01				
11	S	0.84	0.81	0.78	0.75	0.72	0.69	0.66	0.63	0.56	0.50	0.44	0.38	0.32	0.25	0.19	0.13		
	B	0.66	0.63	0.61	0.52	0.48	0.42	0.36	~~0.30~~	~~0.24~~	0.17	~~0.13~~	~~0.10~~	~~0.07~~	0.05	0.01			

12	S	0.88	0.85	0.82	0.80	0.77	0.71	0.65	0.59	0.53	0.47	0.42	0.36	0.30	0.24	0.18	0.12		
	B	~~0.68~~	~~0.65~~	0.62	0.56	0.47	0.45	0.39	0.33	~~0.24~~	0.21	0.15	0.12	~~0.08~~	~~0.07~~	0.02	0.01		
13	S	0.86	0.83	0.80	0.78	0.75	0.72	0.69	0.67	0.61	0.56	0.50	0.45	0.39	0.34	0.28	0.23	0.17	0.12
	B	~~0.69~~	~~0.67~~	0.64	~~0.61~~	0.56	~~0.50~~	0.45	0.39	~~0.34~~	~~0.26~~	0.23	0.17	~~0.12~~	~~0.06~~	0.04			
14	S	0.68	0.65	0.63	0.60	0.57	0.52	0.47	0.42	0.37	0.31	0.26	0.21	0.16	0.11	0.10			
	B	~~0.70~~	~~0.65~~	~~0.59~~	0.52	0.49	~~0.44~~	0.39	0.33	0.28	~~0.26~~	~~0.18~~	0.13	~~0.07~~	0.02				

Table B.3 ADV measurement vertical velocity depth-wise positions

FC	y/d																	
1	S	0.49	0.48	0.47	0.46	0.45	0.44	0.43	0.42	0.41								
	B																	
2	S	0.61	0.56	0.53	0.48	0.45	0.41	0.37	0.33	~~0.30~~								
	B	~~0.14~~	0.12	0.11	0.09	0.08	0.06	0.05	0.03	0.01								
3	S	0.68	0.64	0.61	0.58	0.55	0.51	0.49	~~0.45~~	0.42	0.38	0.36	0.32	0.29	0.27	0.24		
	B	0.29	0.27	~~0.23~~	~~0.18~~	0.16	~~0.15~~	~~0.09~~	0.06	0.03	0.01							
4	S	0.73	0.67	0.62	0.56	0.51	0.45	0.40	0.34	0.29	0.23	0.18						
	B	0.40	0.34	0.29	~~0.23~~	0.14	0.09	0.07	0.01									
5	S	0.76	0.71	0.66	0.61	0.56	0.52	0.47	0.42	0.37	0.32	0.27	0.22	0.18	0.13			
	B	0.47	0.39	0.34	~~0.32~~	0.22	0.13	0.05	0.03									
6	S	0.78	0.74	0.69	0.65	0.60	0.56	0.52	0.47	0.43	0.34	0.25	0.21	0.16				
	B	0.52	0.50	~~0.43~~	~~0.32~~	0.29	0.21	~~0.16~~	~~0.12~~	0.07	~~0.03~~	~~0.01~~						
7	S	0.80	0.76	0.72	0.68	0.64	0.60	0.56	0.52	0.48	0.40	0.32	0.24	0.20	~~0.12~~			
	B	0.56	0.52	0.48	0.44	~~0.36~~	0.28	0.20	0.18	~~0.13~~	~~0.11~~	0.04	0.02					

8	S	0.81	0.77	0.74	0.70	0.66	0.62	0.59	0.55	0.47	0.40	0.32	0.25	0.21	0.17				
	B	0.59	0.55	0.51	0.43	~~0.36~~	0.28	0.21	0.17	~~0.13~~	0.09	0.06	0.02						
9	S	0.83	0.79	0.76	0.72	0.69	0.65	0.62	0.58	0.51	0.44	0.37	0.30	0.23	0.16				
	B	0.62	0.58	0.55	0.48	0.41	~~0.34~~	0.27	0.20	~~0.13~~	~~0.09~~	0.06	0.02	0.02					
10	S	0.84	0.81	0.77	0.74	0.71	0.67	0.64	0.57	0.51	0.44	0.37	0.31	0.24	0.21	0.17	0.14		
	B	0.64	0.61	0.57	0.54	0.47	0.41	0.34	~~0.27~~	0.21	0.14	~~0.11~~	0.08	0.04	0.01				
11	S	0.84	0.81	0.78	0.75	0.72	0.69	0.66	0.63	0.56	0.50	0.44	0.38	0.32	0.25	0.19	0.13		
	B	0.66	0.63	0.61	0.52	0.48	0.42	0.36	~~0.30~~	0.24	0.17	~~0.13~~	~~0.10~~	0.07	0.05	0.01			
12	S	0.88	0.85	0.82	0.80	0.77	0.71	0.65	0.59	0.53	0.47	0.42	0.36	0.30	0.24	0.18	0.12		
	B	~~0.68~~	0.65	0.62	0.56	0.47	0.45	0.39	0.33	~~0.24~~	0.21	0.15	0.12	~~0.08~~	~~0.07~~	0.02	0.01		
13	S	0.86	0.83	0.80	0.78	0.75	0.72	0.69	0.67	0.61	0.56	0.50	0.45	0.39	0.34	0.28	0.23	0.17	0.12
	B	~~0.69~~	0.67	0.64	0.61	0.56	0.50	0.45	0.39	~~0.34~~	~~0.26~~	0.23	0.17	~~0.12~~	0.06	0.04			
14	S	0.68	0.65	0.63	0.60	0.57	0.52	0.47	0.42	0.37	0.31	0.26	0.21	0.16	0.11	0.10			
	B	0.70	~~0.65~~	0.59	0.52	0.49	0.44	0.39	0.33	0.28	~~0.26~~	0.18	0.13	~~0.07~~	0.02				

FC represents flow condition

S represents side-looking ADV

B represents bottom-looking ADV

~~0.xx~~ represents discarded measurement

Appendix C

Microwave sensor components

The photography of Doppler Radar sensor components and accessories are illustrated in this appendix.

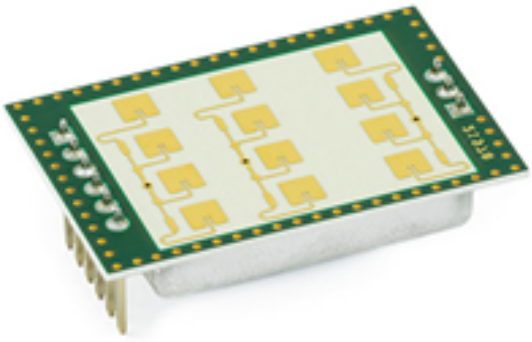

Figure C.1 The radar sensor: RF beam K-LC7 radar transceiver.

Figure C.2 The 10V power supply for two microwave sensors.

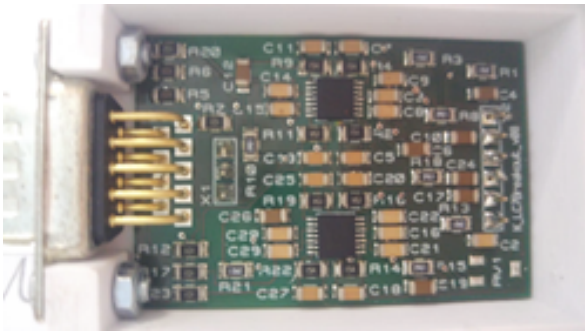

Figure C.3 The photo of amplifier module.

Figure C.4 The National Instruments for two microwave sensors.